

NORTHWESTERN UNIVERSITY

Resonant Localized Surface Plasmon Resonance Spectroscopy: Fundamentals and Applications

A DISSERTATION

SUBMITTED TO THE GRADUATE SCHOOL  
IN PARTIAL FULFILLMENT OF THE REQUIREMENTS

for the degree

DOCTOR OF PHILOSOPHY

Field of Chemistry

By

Jing Zhao

EVANSTON, ILLINOIS

June 2008

© Copyright by Jing Zhao 2008

All Rights Reserved

## **Abstract**

### **Resonant Localized Surface Plasmon Resonance Spectroscopy: Fundamentals and Applications**

Jing Zhao

The work presented here describes investigations into the interaction of resonant molecules with metallic nanoparticles by localized surface plasmon resonance (LSPR) spectroscopy. The contents of this thesis include the study of the coupling mechanism between molecular resonance and plasmon resonance from experimental and theoretical perspectives and applications of this mechanism to biological sensing. From these studies, LSPR spectroscopy is shown to be a powerful tool to study the electronic structures of resonant molecules adsorbed on nanostructured metallic surfaces.

In studies of the dye molecule Rhodamine 6G on Ag nanoparticles, we find that Rhodamine 6G is prone to aggregation on the Ag nanoparticle surface, leading to electronic structure changes that can be detected by LSPR and simulated by electrodynamics and density functional theory. It is further shown that resonant LSPR spectroscopy is able to detect the electronic resonance changes in heme-containing proteins caused by small molecules binding to the protein. Moreover, for the resonant analyte tris(bipyridine)ruthenium(II) with two electronic resonances polarized in different directions, the LSPR couples strongly to only one of the electronic resonances that is in-plane with the plasmon resonance.

The correlation between the molecular resonance, LSPR and the wavelength-scanned surface-enhanced resonance Raman scattering (WS-SERRS) excitation profile is investigated using the tris(bipyridine)ruthenium(II)/Ag nanoparticle system. In combination with electrodynamics modeling, it is demonstrated that the WS-SERRS excitation profiles involve

multiplicative electromagnetic and resonance Raman enhancement. Lastly, the optical properties of new plasmonic materials are explored by a numerical electrodynamics method and compared with experimental results. LSPR of truncated tetrahedral copper and aluminum nanoparticles of different sizes and in different media are studied by the discrete dipole approximation method. Since copper and aluminum are very active and prone to oxidize, the effect of oxides on the LSPR nanoparticles is also examined.

---

Prof. George C. Schatz  
Prof. Richard P. Van Duyne  
Research Advisors

## **Acknowledgements**

I would like to thank first and foremost my research advisors Professor Richard P. Van Duyne and Professor George C. Schatz for their advice, availability and support during the past five years. I was extremely lucky to have the opportunity to do joint experiment/theory projects with them and learn from them. Their encouragement and guidance helped me to go through tough times during my graduate studies. Their passion for science and education strongly inspired me to continue pursuing my interest in scientific research. My experience at Northwestern University will be an unforgettable and invaluable one.

I owe a great deal to Dr. Shengli Zou and Dr. Xiaoyu Zhang who have always been there to offer great advice in research and in life. I am grateful to the mentoring of Dr. Amanda Haes, who helped me get started on my projects. I would like to give special thanks to Dr. Jeff Anker, Dr. George Chan, Jon Dieringer, Dr. Erin Hicks, Dr. Shouzhou Li, Dr. Leif Sherry, Dr. Lasse Jensen, Dr. Jiha Sung, Dr. Kallie Willets and Dr. Chanda Yonzon who helped me with various aspects of research. I would also like to thank my collaborators Professor Stephen G. Sligar and Dr. Aditi Das from University of Illinois at Urbana-Champaign. Without all these people's efforts, none of our work would have come to fruition.

I would like to thank the entire Van Duyne and Schatz groups, all the past and present members (2003-2008) for providing a wonderful and enthusiastic working atmosphere. Especially my colleagues in my office, Hai, Wenfang, Bisu, Christine, Martin and Maricris, it was enjoyable working and talking with all of you. Thanks to the newly formed electrodynamics subgroup, Ariel, Ana, Anatoliy, David, Jeff, Jon, Logan, and Shouzhou, the interesting discussion with you deepened my understanding of electrodynamics. I would also like to thank

the rest of the Van Duyne and Schatz groups for help with my research and the fun we had together.

Thanks to my thesis defense committee members, Professor Peter Stair and Professor Eric Weitz for your time, patience and valuable comments during my qualifying exam, research proposal exam and thesis defense.

Last, but not least, I would like to thank my family and friends for their support throughout my graduate studies at Northwestern University. I was extremely lucky to meet Xiaoyu Zhang, Hai Long, George Chan, Shengli Zou, Shuzhou Li and my five-year long roommate Zixiao Pan, and have them as my friends. Thank you all for being there for me and sharing my happiness and listening to my complaints, and most of all thanks for being my friend. I am greatly indebted to my parents whose love and encouragement made me through my failures and my successes. Thanks for your consideration and advice in all aspects of life. Thanks my grandma for your care and interest. Unfortunately, we only managed to meet a couple times in the past five years. I miss you all and will always love you. Finally, to my fiancée and best friend Lian, who kept me going through the ups and downs by always being confident and positive about life and keeping up with our goals and dreams.

Jing Zhao  
Evanston, Illinois  
April 2008

## TABLE OF CONTENTS

<b>Abstract</b>		<b>Page 3</b>
<b>Acknowledgments</b>		<b>5</b>
<b>List of Illustrations</b>		<b>13</b>
<b>List of Tables</b>		<b>22</b>
<b>Chapter 1</b>	<b>Introduction to the Localized Surface Plasmon Resonance and Its Interaction with Molecular Resonance</b>	<b>23</b>
1.1	Introduction to Plasmonics	24
1.2	Theoretical Approaches to the Optical Properties of Nanoparticles	27
1.3	Interaction of Resonant Molecules with Metallic Nanoparticles and Resonant Localized Surface Plasmon Resonance Spectroscopy	30
1.4	Goals and Organization	39
<b>Chapter 2</b>	<b>Interaction of Plasmon and Molecular Resonances for Rhodamine 6G Adsorbed on Silver Nanoparticles</b>	<b>41</b>
2.1	Introduction	42
2.2	Experimental Methods	44
2.2.1	Materials	44
2.2.2	Substrate Preparation	45
2.2.3	Nanoparticle Preparation	45
2.2.4	Nanoparticle Solvent Annealing and Functionalization	45
2.2.5	Ultraviolet-Visible Extinction Spectroscopy	46
2.2.6	Ultraviolet-Visible Surface Absorption Spectroscopy of R6G	46

2.3	Results and Discussion	46
2.3.1	Wavelength Dependence of Benzenethiol Induced LSPR Shift	47
2.3.2	Wavelength Dependence of the R6G Induced LSPR Shift	47
2.3.3	Empirical Model of the Wavelength Shift	52
2.3.4	Concentration Dependence of the R6G Absorbance on Ag film and Analysis	55
2.3.5	Concentration Dependence of the R6G Induced LSPR Shift	59
2.3.6	Electrodynamics Model of the Wavelength Shift	61
2.3.7	Quantum Chemical Modeling of the Absorption Spectra of Rhodamine 6G	68
2.4	Conclusions	75
<b>Chapter 3</b>	<b>Resonance Localized Surface Plasmon Spectroscopy: Low Molecular Weight Substrate Binding to Cytochrome P450</b>	<b>77</b>
3.1	Introduction	78
3.2	Experimental Methods	79
3.2.1	Materials	79
3.2.2	Protein expression and purification	79
3.2.3	Glass Substrate Preparation	80
3.2.4	Nanoparticle Preparation	80
3.2.5	Nanoparticle Solvent Annealing and Functional Immobilization	81
3.2.6	Ultraviolet-Visible Spectroscopy	81
3.3	Results and Discussion	81



3.3.1	UV-Vis Spectra and Experimental Scheme	81
3.3.2	Representative LSPR Spectra and Wavelength-Dependent LSPR Shift	82
3.3.3	Control experiments	86
	3.3.3.1 Camphor-MUA Adsorption	86
	3.3.3.2 Camphor-bound CYP101 Adsorption to MUA	88
3.3	Conclusions	90
<b>Chapter 4</b>	<b>Resonance Localized Surface Plasmon Spectroscopy: Sensing Substrate and Inhibitor Binding to Cytochrome P450</b>	<b>91</b>
4.1	Introduction	92
4.2	Experimental Methods	94
4.2.1	Materials	94
4.2.2	Protein Expression and Purification	95
4.2.3	Glass Substrate Preparation	95
4.2.4	Nanoparticle Preparation	95
4.2.5	Nanoparticle Solvent Annealing and Functional Immobilization	96
4.2.6	Ultraviolet-Visible Spectroscopy	96
4.3	Results and Discussion	97
4.3.1	Coupling between P450 resonances and LSPR	97
4.3.2	P450 LSPR Sensor Response to Low Molecular Weight Substrate and Inhibitor	101
4.4	Conclusions	104
<b>Chapter 5</b>	<b>Wavelength-Scanned Surface-Enhanced Resonance Raman</b>	<b>106</b>

	<b>Excitation Spectroscopy of Tris(bipyridine)ruthenium(II) on Ag Nanoparticles</b>	
5.1	Introduction	107
5.2	Experimental Methods	109
5.2.1	Materials	109
5.2.2	Nanoparticle Sample Preparation	110
5.2.3	Electrochemistry of $\text{Ru}(\text{bpy})_3^{2+}$ coverage on Ag electrode	112
5.2.4	LSPR shift induced by $\text{Ru}(\text{bpy})_3^{2+}$ on Ag nanoparticles	112
5.2.5	SERS excitation profile of $\text{Ru}(\text{bpy})_3^{2+}$ on Ag nanoparticles	113
5.3	Results and Discussion	115
5.3.1	Electrochemistry of $\text{Ru}(\text{bpy})_3^{2+}$ coverage on Ag electrode	115
5.3.2	LSPR shift induced by $\text{Ru}(\text{bpy})_3^{2+}$ on Ag nanoparticles	116
5.3.3	Kramers-Kronig Transformation and Refractive Index of $\text{Ru}(\text{bpy})_3^{2+}$	118
5.3.4	Theoretical modeling of LSPR shift	122
5.3.5	SERS excitation profile of $\text{Ru}(\text{bpy})_3^{2+}$ on Ag nanoparticles	127
5.3.6	Theoretical modeling of SERRS excitation profile	132
5.3.7	An Example of SERRS EF Calculation	137
5.4	Conclusions	138
<b>Chapter 6</b>	<b>Theoretical Study of Plasmonic Properties of Copper and Aluminum Nanoparticles Fabricated by Nanosphere Lithography</b>	<b>140</b>

6.1	Introduction	141
6.2	Plasmonic properties of Copper Nanoparticles	144
6.2.1	Effect of Copper Oxides on the LSPR of Copper Nanoparticles	144
6.2.2	Tuning the LSPR of Copper Nanoparticles by Width and Height	146
6.3	Plasmonic properties of Aluminum Nanoparticles	150
6.3.1	Effect of Aluminum Oxides on the LSPR of Aluminum Nanoparticles	150
6.3.2	Tuning the LSPR of Aluminum Nanoparticles by Nanosphere Diameter	154
6.3.3	Refractive Index Sensitivity of Aluminum Nanoparticles	156
6.3.4	Refractive Index Sensitivity Studied by Quasistatic Theory	156
6.3.5	LSPR of Al, Ag, Au and Cu NSL-Nanoparticles with Similar Geometry	160
6.4	Conclusions	162
	<b>References</b>	<b>164</b>
<b>Appendix A</b>	<b>Detection of Drug binding to Human Cytochrome P450-3A4 in Nanodisc using Resonant Localized Surface Plasmon Resonance</b>	<b>190</b>
A.1	Introduction	181
A.2	Experimental Methods	194
A.2.1	Materials	194
A.2.2	Ultraviolet-Visible Spectroscopy	194
A.2.3	Expression and Purification of CYP3A4 Nanodiscs	194

A.2.4	Substrate Binding to CYP3A4 Nanodiscs	196
A.2.5	Nanoparticle Fabrication and Functional Immobilization	196
A.3	Results and Discussions	197
A.3.1	Drug Binding to CYP3A4-ND	197
A.3.2	LSPR Coupling of CYP3A4-Nanodisc to Silver Nanoparticle	199
A.3.3	Drug Binding to CYP3A4-Nanodisc monitored using Localized Surface Plasmon Resonance	199
<b>Vita</b>		<b>204</b>

## List of Illustrations

		<b>Page</b>
Figure 1.1	Schematic illustration of SPR (A) and LSPR (B)	25
Figure 1.2	(A) Schematic illustration of the experimental procedure. (B) Wavelength dependent LSPR shifts induced by MgPz adsorption to Ag nanoparticles. Inset shows the molecular structure of MgPz. The solid green line is the solution absorption spectrum of MgPz. The black solid line with dots presents the induced LSPR shifts from a monolayer of MgPz versus the LSPR of bare Ag nanoparticles.	36
Figure 1.3	Extinction spectra of Ag spheroid/MgPz and LSPR shift induced by MgPz. (A) Extinction spectra of bare Ag spheroid (solid lines) and Ag spheroid with MgPz (dashed lines) with varying $\chi$ parameters. Each pair of spectra of the same color was calculated with the same $\chi$ . (B) LSPR shift of Ag nanoparticles induced by MgPz versus LSPR wavelength of bare Ag nanoparticles. The black line with dots is experimental LSPR shift data and the red curve is the calculated LSPR shift.	38
Figure 2.1	Wavelength-dependent LSPR shift induced by a monolayer of benzenethiol vs. the LSPR wavelength of bare Ag nanoparticles.	48
Figure 2.2	(A) Molecular structure of Rhodamine 6G. (B) Absorption spectrum of R6G in ethanol solution.	49
Figure 2.3	Influence of R6G on the LSPR shift of Ag nanoparticles and representative LSPR spectra. (A) Wavelength-dependent LSPR shift induced by a monolayer of R6G vs. the LSPR wavelength of bare Ag nanoparticles. Solid black line with filled dots is a plot of the LSPR shift (nm) vs. LSPR position of Ag nanoparticles. The green solid and dashed lines are the absorption spectrum of the R6G in ethanol solution and on a 200 nm Ag film (arbitrary scaling), respectively. (B)-(E) LSPR spectra of Ag nanoparticles (associated with points B-E in Figure A) before (black line, 1) and after (red line 2) chemical modification. (B) (1), $\lambda_{\max} = 535.9$ nm and (2), $\lambda_{\max} = 530.3$ nm. The LSPR shift = -5.6 nm, %FWHM = 1.1%, and %I = -5.9%. (C) (1), $\lambda_{\max} = 575.0$ nm and (2), $\lambda_{\max} = 629.7$ nm. The LSPR shift = 54.7 nm, %FWHM = 3.4%, and %I = +11.9%. (D) (1), $\lambda_{\max} = 598.0$ nm and (2), $\lambda_{\max} = 647.4$ nm. The LSPR shift = 49.4 nm, %FWHM = 8.9%, and %I = +1.5%. (E) (1), $\lambda_{\max} = 717.8$ nm and (2), $\lambda_{\max} = 723.1$ nm. The LSPR shift = 5.3 nm, %FWHM = 8.6%, and %I = -1.8%.	50

Figure 2.4	Predicted LSPR shift (using Eq. 1) with a scaled refractive index from Kramers-Kronig analysis. The solid black line with filled dots is a plot of the experimental LSPR shift (nm) vs. spectral position of the bare Ag nanoparticles.	54
Figure 2.5	Absorption spectra of R6G in ethanol solution and different concentrations of R6G on a Ag surface. Dashed lines represent deconvolution of the spectra into Gaussian bands. (A) R6G in ethanol (B) 0.6 $\mu$ M R6G on Ag surface (C) 6 $\mu$ M R6G on Ag surface (D) 0.1 mM R6G on Ag surface.	56
Figure 2.6	Exciton splitting diagram of the electronic states for R6G monomer and two types (H or J) of dimers, according to the arrangement of the dipole moments. M represents the R6G monomer excitation. H-type and J-type splitting results in an increase or decrease in the excitation energy. The thickest arrow represents the strongest transition.	57
Figure 2.7	LSPR shift vs. concentrations of R6G dosing solutions at constant LSPR of the bare Ag nanoparticles. (A) The LSPR of the bare Ag nanoparticles is $\sim$ 540 nm. (B) The LSPR of the bare Ag nanoparticles is $\sim$ 560 nm.	60
Figure 2.8	Predicted LSPR shift (using Eq. 2.1) with arbitrarily scaled refractive indices from Kramers-Kronig analysis. The solid black line with filled dots is a plot of the experimental LSPR shift (nm) vs. spectral position of the Ag nanoparticles. The blue dashed-dotted line, red dotted line and green dashed line represent the predicted LSPR shift using the refractive indices of the R6G H-dimer, monomer and J-dimer, respectively.	63
Figure 2.9	Predicted LSPR shift using Eq. 2.3. The solid black line with filled dots is a plot of the experimental LSPR shift (nm) vs. spectral position of the Ag nanoparticles. The blue dashed-dotted line, red dotted line and green dashed line represent the predicted LSPR shift using the dielectric constants of the R6G H-dimer, monomer and J-dimer, respectively.	66
Figure 2.10	Optimized structure and simulated absorption spectrum of R6G in solution. Solvent effects accounted for by a red-shift of 56 nm.	69
Figure 2.11	Simulated structure of R6G dimers and absorption spectra. (A) Structure of H-type dimer. (B) Structure of J-type dimer. (C) Calculated absorption spectra of R6G monomer (black line), H-type dimer (blue line) and J-type dimer (red line). Solution effects are	70

accounted for by a red shift of 56 nm.

- Figure 2.12 Simulated absorption spectra of R6G with an Ag<sub>2</sub> cluster and neutral R6G. (A) Calculated absorption of R6G with an Ag<sub>2</sub> cluster. Inset is the optimized structure of R6G-Ag<sub>2</sub>. The distance between the N atom of R6G and Ag atom is 3.08 Å. (B) Calculated absorption of neutral R6G. Solution effects are accounted for by a red shift of 56 nm. 73
- Figure 2.13 S1 absorption maximum as a function of the angle ( $\Omega$ ) between the xanthenep plane and the phenyl substituent. Solvent effects accounted for by a red shift of 56 nm. (A) Side-view of the structure of R6G. (B) Plot of the S1 absorption maximum as a function of the angle ( $\Omega$ ). (C) Schematic illustration of the two possible adsorption sites.  $\Omega-1 = 88^\circ$ ,  $\Omega-2 = 66^\circ$  74
- Figure 3.1 (A) UV-vis absorption spectra of CYP101(Fe<sup>3+</sup>) (green solid line) with a Soret band at 417 nm (low spin) and camphor-bound CYP101(Fe<sup>3+</sup>) (pink dashed line) with a Soret band at 391 nm (high spin). (B) Schematic notations of 11-MUA, CYP101 and camphor. (C) Schematic representation of CYP101 protein immobilized Ag nanobiosensor, followed by binding of camphor. The Ag nanoparticles are fabricated using NSL (nanosphere lithography) on a glass substrate. 83
- Figure 3.2 UV-vis extinction spectra of each step in the surface modification of NSL fabricated Ag nanoparticles and the wavelength-dependent LSPR shift plots. All extinction measurements were collected in a N<sub>2</sub> environment. A 200  $\mu$ M camphor buffer solution was used. (A) A series of UV-vis extinction spectra of Ag nanoparticles (a)  $\lambda_{\max, \text{SAM}} = 636.1$  nm, (b)  $\lambda_{\max, \text{CYP101}} = 649.3$  nm, and (c)  $\lambda_{\max, \text{CYP101-Cam}} = 640.1$  nm. (B) A series of UV-vis extinction spectra of Ag nanoparticles (a)  $\lambda_{\max, \text{SAM}} = 421.4$  nm, (b)  $\lambda_{\max, \text{CYP101}} = 487.6$  nm, and (c)  $\lambda_{\max, \text{CYP101-Cam}} = 452.9$  nm. (C) Plots of LSPR shifts versus  $\lambda_{\max, \text{SAM}}$  where  $\Delta\lambda_1 = \lambda_{\max, \text{CYP101}} - \lambda_{\max, \text{SAM}}$  (shift on binding CYP101), and  $\Delta\lambda_2 = \lambda_{\max, \text{CYP101-Cam}} - \lambda_{\max, \text{CYP101}}$  (shift on binding camphor). The vertical black dotted line denotes the molecular resonance of Fe<sup>3+</sup>CYP101 at 417 nm. 84
- Figure 3.3 Camphor adsorption to MUA functionalized Ag nanoparticles. Black solid line is the extinction spectrum of MUA-functionalized Ag nanoparticles in N<sub>2</sub> before exposure to camphor; while red dashed line is after exposure to camphor. All the spectra were measured in N<sub>2</sub>. 87

- Figure 3.4      The LSPR shifts experiments following two different protocols. (A) Schematic illustration of protocol A. (B) Schematic illustration of protocol B. (C) Extinction spectra of functionalized Ag nanoparticles at each step following protocol A. Black solid line is the LSPR of MUA-Ag nanoparticles. Blue dotted line is the LSPR of the sample after exposure to camphor-free CYP101. Red dashed line is the LSPR of the sample after exposure to camphor. (D) Extinction spectra of functionalized Ag nanoparticles at each step following protocol B. Black solid line is the LSPR of MUA-Ag nanoparticles. Red dashed line is the LSPR of the sample after exposure to camphor-bound CYP101. All the spectra were measured in N<sub>2</sub>. 89
- Figure 4.1      UV-vis absorption spectrum of CYP101 (green solid line), imidazole-bound CYP101 (red dotted line) and camphor-bound CYP101 (blue dashed line). 98
- Figure 4.2      Influence of CYP101 on the LSPR shift of 11-MUA SAM functionalized Ag nanoparticles and representative LSPR spectra. (A-D) LSPR spectra of Ag nanoparticles (associated with points A-D in Figure E) before (black line) and after CYP101 binding (red dotted line). Labeled are the LSPR peak positions of the spectra. (E) Wavelength-dependent LSPR shift induced by CYP101 vs. the LSPR wavelength of 11-MUA SAM functionalized Ag nanoparticles. Solid black line with filled dots is a plot of the LSPR shift (nm) vs. LSPR position of 11-MUA Ag nanoparticles. The green solid line is the absorption spectrum of the CYP101 (arbitrary scaling). 99
- Figure 4.3      (A) Schematic illustration of small molecule binding to CYP101 receptors on 11-MUA functionalized Ag nanoparticles. Inset shows the molecular structure of camphor and imidazole. (B) The wavelength-dependent LSPR shift induced by imidazole (red line with red dots) and camphor (blue line with squares). (C) Representative LSPR spectra of nanoparticles with CYP101 before (a, pink dashed line) and after (b, green dotted line) camphor binding. (D) Representative LSPR spectra of nanoparticles with CYP101 before (a, pink dashed line) and after (b, green dotted line) imidazole binding. 103
- Figure 5.1      The structure (left) and absorption spectrum of Ru(bpy)<sub>3</sub><sup>2+</sup> (right). The absorption spectrum is 0.01 mM Ru(bpy)<sub>3</sub>(PF<sub>6</sub>)<sub>2</sub> in 0.1 M TBAH acetonitrile solution. 111
- Figure 5.2      Schematic diagram of the WS SERES apparatus. 114



- Figure 5.3 (A) Cyclic voltammogram of 0.10 mM  $\text{Ru}(\text{bpy})_3^{2+}$  in acetonitrile at a silver electrode with 0.10 M TBAH as the supporting electrolyte. The scan begins at 0 mV and first moves in the negative direction at 100 mV/sec. The three electron reductions of  $\text{Ru}(\text{bpy})_3^{2+}$  occur at -1347, -1539, and -1769 mV. (B) A representative double potential step chronocoulogram in acetonitrile at the silver electrode with 0.10 M TBAH as the supporting electrolyte. Prior to the measurement, the electrode was incubated in 0.10 mM  $\text{Ru}(\text{bpy})_3^{2+}$  solution for 5min. Starting potential:-800 mV. Ending potential:-2000mV. Step width: 250 ms. (C) Anson plots of  $Q_f$  vs  $t^{1/2}$  (forward) and  $Q_r$  vs  $\theta$  (reverse) for (B). (D) The plot of  $\text{Ru}(\text{bpy})_3^{2+}$  adsorbate coverage vs incubation time. As the incubation time is increased from 5 to 140 min, the surface concentration increases from  $0.20 \times 10^{14}$  to  $0.94 \times 10^{14}$  molecules/cm<sup>2</sup>. 117
- Figure 5.4 Effect of a monolayer of  $\text{Ru}(\text{bpy})_3^{2+}$  on the LSPR shift of Ag nanoparticles. (A) Wavelength-dependent LSPR shift induced by a monolayer of  $\text{Ru}(\text{bpy})_3^{2+}$  vs. the LSPR wavelength of bare Ag nanoparticles. Black line with filled dots is a plot of the LSPR shift (nm) vs. LSPR position of Ag nanoparticles. The orange line is the absorption spectrum of  $\text{Ru}(\text{bpy})_3^{2+}$  (arbitrary scaling). (B) Predicted LSPR shift (red line) using Eq. 1 and 2 and experimental LSPR shift (the solid black line with filled dots). 119
- Figure 5.5 Deconvolution of the absorption band of  $\text{Ru}(\text{bpy})_3^{2+}$  into two Gaussian curves at 452 and 425 nm (dashed lines). 121
- Figure 5.6 Calculated extinction spectra of bare Ag spheroid (solid lines) and Ag spheroid with  $\text{Ru}(\text{bpy})_3^{2+}$  (dashed lines) with varying  $\chi$  parameters. Each pair of spectra of the same color was calculated with the same  $\chi$ . 126
- Figure 5.7 Representative SERS spectrum of  $\text{Ru}(\text{bpy})_3^{2+}$  on NSL-fabricated Ag nanoparticle substrate.  $\lambda_{\text{ex}} = 457.9$  nm, power= 0.131 mW, acquisition time = 60 s. An atomic force micrograph image of the sample is shown in the inset. 128
- Figure 5.8 LSPR and surface-enhanced Raman excitation spectra of the 1487 cm<sup>-1</sup> peak(A, C and E) and 1602 cm<sup>-1</sup> peak (B, D and F) of  $\text{Ru}(\text{bpy})_3^{2+}$  with cyclohexane as intensity standard. (A-B) LSPR  $\lambda_{\text{max}} = 434.7$  nm, profile fit maximum at (A)  $\lambda_{\text{ex,max}} = 445.1$  nm and (B)  $\lambda_{\text{ex,max}} = 428.1$  nm. (C-D) LSPR  $\lambda_{\text{max}} = 465.2$  nm, profile fit maximum at (C)  $\lambda_{\text{ex,max}} = 466.4$  nm and (D)  $\lambda_{\text{ex,max}} = 454.3$  nm. (E-F) LSPR  $\lambda_{\text{max}} = 480.1$  nm, profile fit maximum at (E)  $\lambda_{\text{ex,max}} = 464.1$  129

nm and (F)  $\lambda_{\text{ex,max}} = 460.6$  nm.

- Figure 5.9 SERR spectra of  $\text{Ru}(\text{bpy})_3^{2+}$  on NSL-fabricated Ag nanoparticle substrate at two different excitation wavelengths.  $\lambda_{\text{ex1}} = 457.9$  nm (top purple curve).  $\lambda_{\text{ex2}} = 420$  nm (bottom blue curve). 131
- Figure 5.10 Predicted (blue dashed line) and experimental (black dots and red curve) surface-enhanced Raman excitation spectra of the  $1487\text{ cm}^{-1}$  peak. (A-C) correspond to three samples (A, C and E) in Figure 5.8. 134
- Figure 5.11 Calculated  $\langle |E|^2 \rangle / |E_0|^2$  of a bare Ag spheroid (solid lines) and Ag spheroid with  $\text{Ru}(\text{bpy})_3^{2+}$  (dashed lines) with the same  $\chi$  parameter. 136
- Figure 6.1 Dielectric constants of Cu (A) and  $\text{Cu}_2\text{O}$  (B). The solid line represents the real part and the dashed line represents the imaginary part. 142
- Figure 6.2 Dielectric constants of Al. The solid line represents the real part and the dashed line represents the imaginary part. 143
- Figure 6.3 (A) Extinction spectra of copper nanoparticles before treatment with glacial acetic acid in  $\text{N}_2$  (black), during the treatment in real time in acetic acid (pink, blue, green) and after the treatment in  $\text{N}_2$ . Inset is an AFM image of the copper nanoparticles. (B) DDA simulations of the effect of oxidation of copper ( $\text{Cu}_2\text{O}$ ) on a NSL Cu nanoparticle. Calculations were performed for a nanoparticle with a Cu core surrounded by a  $\text{Cu}_2\text{O}$  shell. The inset shows a side view of the core-shell nanoparticle. The total height and width of the nanoparticle was fixed at 50 and 100 nm, respectively. The thicknesses (T) of the  $\text{Cu}_2\text{O}$  shell were varied from 0 to 6 nm. 145
- Figure 6.4 (A) Extinction spectra of Cu nanoparticle with varying widths calculated by DDA. Spectrum 1 (black),  $D = 280$  nm,  $\lambda_{\text{max}} = 635$  nm; spectrum 2 (blue),  $D = 390$  nm,  $\lambda_{\text{max}} = 655$  nm; spectrum 3 (red),  $D = 450$  nm,  $\lambda_{\text{max}} = 665$  nm; spectrum 4 (green),  $D = 510$  nm,  $\lambda_{\text{max}} = 680$  nm; and spectrum 5 (purple),  $D = 590$  nm,  $\lambda_{\text{max}} = 720$  nm. (B) LSPR  $\lambda_{\text{max}}$  versus diameter is shown for the calculated results. (C) Extinction spectra of Cu nanoparticle arrays with varying widths after acetic acid treatment ( $D = 280 - 590$  nm;  $d_m = 50$  nm) measured with UV-vis spectroscopy. All spectra were collected in a  $\text{N}_2$  environment. Spectrum 1 (red),  $D = 590$  nm,  $\lambda_{\text{max}} = 876$  nm; spectrum 2 (green),  $D = 500$  nm,  $\lambda_{\text{max}} = 789$  nm; spectrum 3 (blue),  $D = 450$  nm,  $\lambda_{\text{max}} = 750$  nm; spectrum 4 (orange),  $D = 390$  nm,  $\lambda_{\text{max}} = 698$  nm, and spectrum 5 (purple),  $D = 280$  nm, and  $\lambda_{\text{max}} = 643$  nm. (D) LSPR  $\lambda_{\text{max}}$  versus diameter is shown for the 147

experimental results.

- Figure 6.5 (A) Extinction spectra of Cu nanoparticle with varying heights calculated by DDA. Spectrum 1 (grey),  $h = 70$  nm,  $\lambda_{\max} = 652$  nm; spectrum 2 (black),  $h = 60$  nm,  $\lambda_{\max} = 653$  nm; spectrum 3 (light blue),  $h = 50$  nm,  $\lambda_{\max} = 655$  nm; spectrum 4 (green),  $h = 40$  nm,  $\lambda_{\max} = 660$  nm; spectrum 5 (dark blue),  $h = 30$  nm,  $\lambda_{\max} = 670$  nm; and spectrum 6 (red),  $h = 20$  nm,  $\lambda_{\max} = 705$  nm. (B) LSPR  $\lambda_{\max}$  versus nanoparticle height ( $h$ ) is shown for calculated results. (C) Extinction spectra of the Cu nanoparticle arrays after acetic acid treatment ( $D = 390$  nm;  $h = 20 - 70$  nm) measured with UV-vis spectroscopy. All spectra were collected in a  $N_2$  environment. Spectrum 1 (red),  $h = 20$  nm,  $\lambda_{\max} = 764$  nm; spectrum 2 (dark blue),  $h = 30$  nm,  $\lambda_{\max} = 730$  nm; spectrum 3 (green),  $h = 40$  nm,  $\lambda_{\max} = 713$  nm; spectrum 4 (light blue),  $d_h = 50$  nm,  $\lambda_{\max} = 698$  nm; spectrum 5 (black),  $h = 60$  nm,  $\lambda_{\max} = 685$  nm; and spectrum 6 (light gray),  $h = 70$  nm,  $\lambda_{\max} = 670$  nm. (D) LSPR  $\lambda_{\max}$  versus nanoparticle height ( $h$ ) is shown for the experimental results. 149
- Figure 6.6 (A) SEM image of Al nanoparticles on a Si substrate where  $D = 390$  nm and  $h = 50$  nm. (B) AFM image of the same size Al nanoparticles on a glass substrate. (C) AFM linescan profile of particle 1 and 2 in (B). 151
- Figure 6.7 DDA simulations of the effect of oxidation of aluminum ( $Al_2O_3$ ) on a NSL Al nanoparticle at room temperature. Calculations were performed for a nanoparticle with Al core surrounded an  $Al_2O_3$  shell. The inset shows a side view of the core-shell nanoparticle. The thicknesses ( $T$ ) of the  $Al_2O_3$  shell were varied from 0 to 10 nm. 153
- Figure 6.8 (A) Extinction spectra of Al nanoparticle with varying widths calculated by DDA. Spectrum 1 (purple), width = 95 nm, spectrum 2 (blue), width = 136 nm; spectrum 3 (red), width = 174 nm; spectrum 4 (green), width = 206 nm; spectrum 5 (pink), width = 230 nm. (B) Extinction spectra of Al nanoparticle with varying widths measured with UV-vis spectroscopy. All spectra were collected in a  $N_2$  environment. Spectrum 1 (black),  $D = 280$  nm,  $\lambda_{\max} = 390$  nm; spectrum 2 (blue),  $D = 390$  nm,  $\lambda_{\max} = 508$  nm; spectrum 3 (green),  $D = 410$  nm,  $\lambda_{\max} = 579$  nm; spectrum 4 (yellow),  $D = 500$  nm,  $\lambda_{\max} = 667$  nm; and spectrum 5 (red),  $D = 590$  nm,  $\lambda_{\max} = 806$  nm. 155
- Figure 6.9 (A) Extinction spectra of Al nanoparticle ( $D = 390$  nm,  $h = 50$  nm) on a glass substrate in different external environments calculated by DDA. Spectrum 1 (black), in  $N_2$ ,  $\lambda_{\max} = 380$  nm; spectrum 2 (blue), in  $H_2O$ ,  $\lambda_{\max} = 450$  nm; spectrum 3 (red), in ethanol,  $\lambda_{\max} = 460$  nm; 157

spectrum 4 (green), in chloroform,  $\lambda_{\max} = 480$  nm; and spectrum 5 (pink), in benzene,  $\lambda_{\max} = 490$  nm. (B) The change in  $\lambda_{\max}$  (eV) versus the refractive index of the surroundings. Black line with triangles is for a bare Al nanoparticle and red line with circles is for Al nanoparticle with a 2 nm aluminum oxide layer.

- Figure 6.10 (A) LSPR  $\lambda_{\max}$  of Ag and Al spheroid versus the refractive index of surroundings calculated by Eq. 6.1 with different  $\chi$  parameters. Red line with circles is for Ag and blue line with triangles is for Al. (B) LSPR  $\lambda_{\max}$  of Ag, Al, Au and Cu spheroid versus the refractive index of surroundings calculated by Eq. 6.1 with different  $\chi$  parameters. Red line with circles is for Ag, blue line with triangles is for Al, purple line with squares is for Au and green line with diamonds is for Cu. 159
- Figure 6.11 Comparison of the LSPR of Cu, Ag, Au, and Al for a similar size and shape obtained from experiment (A) and DDA calculations (B) ( $D = 390$  nm;  $h = 50$  nm; glass substrate;  $N_2$  environment). 161
- Figure A.1 (A) Schematic representation of CYP3A4-Nanodisc immobilized Ag nanobiosensor, followed by binding of drug molecule. The Ag nanoparticles are fabricated using NSL (nanosphere lithography) on a glass substrate. (B) UV-vis absorption spectra of CYP3A4-Nanodisc in the following states: (1) low spin substrate free ferric state of with a Soret band at 415 nm (blue solid line) (2) high spin type I drug bound ferric state with a Soret band at 391 nm (red dotted line) and (3) low spin type II drug bound ferric state with Soret band at 425 nm. The inset shows the detailed changes in the Q-bands region. (C) Schematic notations of 11-MUA, CYP3A4-Nanodisc and drug. 193
- Figure A.2 (Top panel) (A) (B) (C) UV-vis absorption spectrum of CYP3A4-Nanodisc with testosterone (TST) bound (type I substrate), Ketoconazole (KTC) bound (Type II drug) and Erythromycin (ERY) bound (shows a very small type I shift). (Bottom panel) UV-vis extinction spectra of each step in the surface modification of NSL fabricated Ag nanoparticles for the different drug molecules. (D) For testosterone (representative type I substrate) binding,  $\lambda_{\max, \text{MuA}} = 547$  nm,  $\lambda_{\max, \text{CYP3A4-ND}} = 596$  nm, and  $\lambda_{\max, \text{CYP3A4-ND-TypeI}} = 589$  nm (blue shift). The direction of shift is same as in top panel A. (E) For ketoconazole (representative type II substrate),  $\lambda_{\max, \text{MuA}} = 553$  nm,  $\lambda_{\max, \text{CYP3A4-ND}} = 566$  nm, and  $\lambda_{\max, \text{CYP3A4-ND-KTC}} = 570$  nm (red shift). The direction of shift in same as top panel B. (F) For erythromycin binding,  $\lambda_{\max, \text{MuA}} = 591$  nm,  $\lambda_{\max, \text{CYP3A4-ND}} = 610$  nm and  $\lambda_{\max, \text{CYP3A4-ND-ERY}} = 609$  nm. All extinction measurements were collected in a 200

N<sub>2</sub> environment. A typical concentration of 100  $\mu$ M drug molecule was used to saturate all the binding sites.

**List of Tables**

		<b>Page</b>
Table 2.1	Refractive indices of Rhodamine 6G monomer, H-dimer and J-dimer transformed from Rhodamine 6G absorption spectra on Ag surface	62
Table A.1	Drug name, structure, binding type to CYP3A4 and spectral change they produce on binding CYP3A4 Nanodisc	198

## **Chapter One**

### **Introduction to the Localized Surface Plasmon Resonance and Its Interaction with Molecular Resonance**

## 1.1 Introduction to Plasmonics

PLASMONICS, an emerging branch of nanophotonics, is the study of light interacting with nanostructured materials that can support surface plasmon resonance excitation. Plasmon resonance excitation is a coherent oscillation of the surface conduction electrons excited by electromagnetic (EM) radiation<sup>1-8</sup>. The excitations are very intense, and strongly dependent on the shape, size and arrangement of the nanoparticles.<sup>8-15</sup> Unlike fluorescence, plasmon resonance excitation is not subject to blinking or irreversible loss,<sup>16</sup> thus making the nanoparticles exquisite reporters of their local dielectric environment. The rapidly growing interest in plasmonics lies in its potential applications for highly miniaturized and sensitive photonic devices by controlling, manipulating, and amplifying light on the nanoscale<sup>17,18</sup>. To date, a variety of plasmonic devices have been demonstrated, such as waveguides<sup>18-21</sup>, photonic circuits<sup>22,23</sup>, filters<sup>21</sup>, and nanoscopic light sources<sup>24</sup>. Furthermore, our rapidly improving understanding of the interactions between adsorbed molecules and plasmonic nanostructures (i.e., molecular plasmonics) is having a significant impact on a broad spectrum of other applications, including nanoscale optical spectroscopy<sup>25,26</sup>, surface-enhanced Raman spectroscopy (SERS)<sup>4,27-31</sup>, and surface plasmon resonance sensing<sup>31-37</sup>.

There are two types of surface plasmon excitations —surface plasmon polaritons (SPPs) and localized surface plasmon resonances (LSPRs) (schematic shown in Figure 1.1). SPPs are propagating excitations, which move along the metal-dielectric interface, for distances on the order of tens to hundreds of microns. SPPs are associated with smooth, thin metal films with thicknesses in the 10–200 nm range. The interaction between the metal surface-confined EM wave and an adsorbate layer leads to angle shifts in the plasmon resonance condition that are measured in surface plasmon resonance (SPR) measurements. LSPR excitation, by contrast,



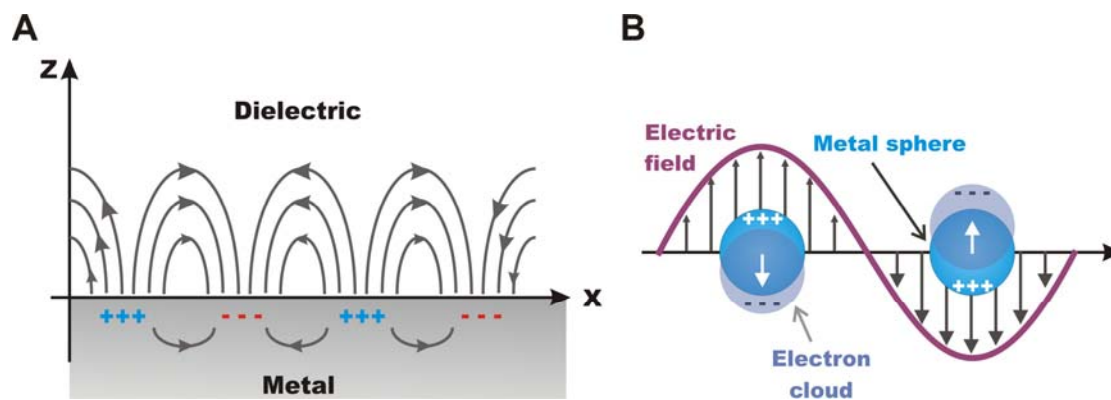


**Figure 1.1** Schematic illustration of SPR (A) and LSPR (B).

occurs in metal nanoparticles that are much smaller than the incident wavelength. Here the induced polarization oscillates locally around the nanoparticle at a certain frequency. The LSPR wavelength ( $\lambda_{\text{max}}$ ) and peak width of the nanoparticles are extremely sensitive to nanoparticle composition,<sup>9,38</sup> size,<sup>26,39,40</sup> shape,<sup>13,39,41-45</sup> dielectric environment,<sup>12,36,44,46,47</sup> and proximity to other nanoparticles,<sup>48-51</sup>

Both SPR and LSPR are sensitive to the local refractive index changes that occur when a target analyte binds to the metal film or nanoparticles; therefore, a variety of chemical/biological sensors have been developed based on SPR and LSPR. These sensors are highly sensitive, label-free, and can provide real-time kinetic information for binding processes.<sup>32,52-56</sup> In addition, LSPR sensing elements are intrinsically at the single nanoparticle level,<sup>26,44,45</sup> making the LSPR sensors possible for in situ detection in biological systems. Furthermore, advances in synthetic and lithographic fabrication techniques allow for tuning the LSPR wavelength throughout the visible, near-infrared, and into the infrared region of the EM spectrum, by varying the shape, size, and material of the nanoparticles<sup>9,41,44,45,57-60</sup>. This gives flexibility in designing and optimizing LSPR sensors.

In addition to high environmental sensitivity, LSPR also results in enhanced local electromagnetic field around the nanostructures. Experimental and theoretical studies over the last thirty years show that the enhanced electromagnetic field is the origin of the majority of the enhancement in surface-enhanced spectroscopies. Surface-enhanced Raman scattering (SERS) is one of the most studied surface-enhanced spectroscopic techniques to date.<sup>61-65</sup> When molecules are absorbed on metallic nanoparticles or thin films, the Raman signal can be enhanced by several orders of magnitude due to the local field enhancement. The enormous amount of SERS

enhancement from the plasmon resonance in combination with molecular resonance enhancement allows for SERS detection at single molecule level.<sup>62,64,65</sup>

Well-defined and uniform nanostructures are critical to the reproducibility of LSPR and SERS spectra. A commonly used method in the Van Duyne group to fabricate nanostructures is known as nanosphere lithography (NSL). NSL is an inexpensive and simple method to fabricate large arrays of nanoparticles of well-controlled size and shape.<sup>39,42,43</sup> NSL fabrication begins with the self-assembly of size-monodisperse polystyrene nanospheres on a substrate to form a deposition mask. Then, metal is deposited through the nanosphere masks using thermal or electron beam evaporation. After removal of the polystyrene nanospheres, well-ordered two-dimensional triangular nanoparticle arrays remain on the substrates. By changing the nanosphere diameter,  $D$ , and the deposited metal thickness,  $d_m$ , nanoparticles with different in-plane width, out-of-plane height, and interparticle spacing can be produced. Since the LSPR of nanoparticles is sensitive to its geometry, the NSL technique allows for fabricated nanostructures with tunable LSPR wavelengths. It has been demonstrated that NSL-fabricated Ag nanoparticles can exhibit tunable LSPR all through visible wavelength range.<sup>13,39,42</sup> NSL-fabricated nanotriangles have sharp tips that are responsible for extremely high electromagnetic fields around the nanoparticles.<sup>66,67</sup> Therefore, NSL-fabricated nanoparticles are an excellent platform for sensing applications and surface-enhanced spectroscopies.

## 1.2 Theoretical Approaches to the Optical Properties of Nanoparticles

In addition to the experimental advances described above, theory has long played an important role in the modeling of metal nanoparticle optical properties. 100 years ago, the celebrated work of Mie<sup>68</sup> (along with important contributions from many others<sup>69</sup>), revealed that

classical electromagnetic theory (i.e., solving Maxwell's equations for light interacting with the particles) provides a quantitative description of the extinction and scattering spectra of a sphere of arbitrary sizes. Mie's solution is of great interest to researcher even now, and it provides a good approximation in a lot of applications even when the particles are not spherical. Other particle shapes, such as spheroids, do admit to exact solutions,<sup>70</sup> but the solutions are harder to use. For anisotropic nanoparticles, one of the most useful approaches has been the quasistatic approximation, in which Maxwell's equations are replaced by electrostatics (LaPlace equation), but still using frequency dependent dielectric functions.

For a prolate spheroid oriented along the  $z$  direction ( $\frac{x^2 + y^2}{a^2} + \frac{z^2}{b^2} = 1$ ,  $a < b$ ), parallel to the direction of the applied electric field, in the quasistatic limit where the dimension of a spheroid is much smaller than the incident wavelength, the extinction cross-section ( $C_{ext}$ ) of a spheroidal using spheroid coordinates is expressed by the following equation:<sup>10,71,72</sup>

$$C_{ext} \propto \frac{1}{3} f^3 \frac{\xi_0}{Q_1(\xi_0)} \frac{1}{\lambda} \text{Im} \left\{ \frac{\epsilon_i - \epsilon_o}{\epsilon_i + \chi \epsilon_o} \right\} \quad (1.1)$$

where  $\epsilon_o$  is the dielectric constant of the medium outside the spheroid,  $\epsilon_i$  is the dielectric function of the spheroid, and  $f$  is the focus of the spheroid given by:

$$f = (b^2 - a^2)^{1/2} \quad (1.2)$$

$\xi_0$  is the value of  $\xi$  at the spheroid surface where:

$$\xi_0 = \frac{1}{\sqrt{1 - \frac{a^2}{b^2}}} \quad (1.3)$$

$Q_1$  is a Legendre function of the second kind where:

$$Q_1(\xi_0) = \frac{\xi_0}{2} \ln\left(\frac{\xi_0 - 1}{\xi_0 + 1}\right) - 1 \quad (1.4)$$

and the function  $\chi$  is given by:

$$\chi = -1 + \frac{1}{(\xi_0^2 - 1)Q_1(\xi_0)} \quad (1.5)$$

From this primitive estimation, it can be concluded that the extinction of a sphere or spheroid depends on its size and shape ( $f$ ,  $\xi_0$ ,  $Q_1$ , and  $\chi$ ), material ( $\varepsilon_i$ ) and the surrounding environment ( $\varepsilon_o$ ). For metals that can support surface plasmons, the dielectric function  $\varepsilon_i$  is complex and wavelength-dependent, and has a large negative real part and a small positive imaginary part. Usually,  $\varepsilon_o$  is a real constant, and it is small compared to the real part of  $\varepsilon_i$ . Therefore, when  $\text{Re}(\varepsilon_i) + \chi\varepsilon_o = 0$ ,  $C_{\text{ext}}$  reaches its maximum, known as the resonant condition.  $\varepsilon_o$  is not limited to a real constant but can be complex and wavelength-dependent, eg., that of dye molecules. In this case, the resonant condition and  $C_{\text{ext}}$  profile versus wavelength become more complicated. Recently, we applied this approach to the treatment of spheroids interacting with dye molecule adsorbates,<sup>73</sup> which will be discussed in the next section and Chapter Two.

Recent experimental advances in colloid chemistry enable making colloidal nanostructures with narrow distributions of particle shape and size. The most commonly prepared shapes are spheroids,<sup>70,74</sup> disks,<sup>75</sup> triangular prisms,<sup>41,60</sup> rods<sup>76,77</sup> and cubes,<sup>78</sup> which are produced by the reduction of a metal salt. In addition, the colloidal nanoparticle forms aggregates upon addition of electrolytes. The nanoparticle aggregates are responsible for the extremely high enhancement observed in surface-enhanced Raman spectroscopy at the single molecule level.<sup>79-81</sup> A quantitative electromagnetic description was needed to study these arbitrarily shaped colloidal nanoparticles and nanoparticle aggregates. On the other hand,

progress in lithographic methods for making surface-bound and released nanoparticles results in interest in describing the optical properties of nonspherical nanoparticles and nanoparticle arrays,<sup>82-88</sup> particles on substrates and/or coated with dielectric/molecular layers,<sup>89-92</sup> holes in metal films<sup>93,94</sup> and many other complex nanostructures. Therefore, it is important to have more powerful numerical approaches for these problems.

One of the most commonly used numerical methods for solving Maxwell's equations is the discrete dipole approximation (DDA) method. DDA was first developed in the field of astrophysics by Purcell and Pennypacker,<sup>95</sup> and has proved to be a powerful tool in studies of light scattering from nonmetallic dust particles of astrophysical interest. In this approach, one represents the object of interest as a cubic lattice having a finite number of polarizable dipoles, each of which is small enough that only dipole interactions with an applied electromagnetic field and with induced fields in other elements need to be considered.<sup>96,97</sup> The number of dipoles is determined by the dimension of the object and the cubic lattice grid spacing. The polarizabilities of the dipoles can be chosen so that bulk materials will behave the same as the continuum solution to Maxwell's equations. In the limit of a large enough number of elements, the electric fields determined by the DDA method will match the analytical solutions quantitatively.<sup>98</sup> With appropriate choice of the grid spacing, DDA is accurate enough for many applications, and therefore, has been widely used to simulate the optical spectra of nanostructures.<sup>14,15,66,67,86,99,100</sup>

### **1.3 Interaction of Resonant Molecules with Metallic Nanoparticles and Resonant Localized Surface Plasmon Resonance Spectroscopy**

The interaction between chromophores and metallic nanoparticles or thin films has gained growing interest in the past ten years. The study is driven by applications ranging from

chemical and biological sensing and imaging,<sup>101-103</sup> surface-enhanced spectroscopies,<sup>4,63,104</sup> to dye-sensitized solar cells,<sup>105-111</sup> and so on. In this section, I will introduce recent experimental and theoretical studies of dye molecules interacting with single nanoparticles and nanoparticle arrays, and compare them with the studies done in the Van Duyne and Schatz groups.

When chromophores adsorb onto metallic nanostructures that can support surface plasmon resonance, there is coupling between the plasmon resonance modes and chromophore molecular resonances. The strength of the coupling between molecular resonance and LSPR depends on the degree of overlap in the absorption spectrum of the molecules and the extinction (or scattering) spectrum of the nanoparticles. When the LSPR of the nanoparticles is on resonant with the molecular resonance, there is strong coupling between the molecular resonance and LSPR; and both the intensity and line shape of the extinction (or scattering) spectrum of the nanoparticle change significantly. When the LSPR of the nanoparticles is off molecular resonance, the coupling between LSPR and molecular resonance becomes weaker; and the molecular resonance shows up in the LSPR of the nanoparticles as an extra peak. This was verified by several studies with systems of organic dyes and biological analytes interacting with Au and Ag nanoparticles, and also theoretical modeling using electrodynamics and quantum mechanics.<sup>73,103,112-117</sup>

In 2004, Wiederrecht et. al. studied the coupling between organic molecular J-aggregated dyes and plasmon resonance of colloidal nanoparticles by UV-vis spectroscopy and electrodynamics simulation.<sup>114</sup> Ag and Au nanoparticles were used in this study to control the LSPR of the nanoparticles to be off and on molecular resonance so one can compare the weak and strong coupling cases. The absorption spectra of the J-aggregate coated nanoparticles are different from that of the bare nanoparticles. For Ag nanoparticles, an extra band from the J-

aggregate absorption was observed (weak coupling); while for Au nanoparticles, a decrease in the extinction spectrum intensity was observed (strong coupling). From electrodynamics simulation, the different coupling behavior was attributed to constructive and destructive coherence effects between the nanoparticle electronic polarization and that of the exciton transition dipole. Moreover, in 2007, Wurtz et. al. studied coupling of the J-aggregate coating with a Au nanorod assembly in an alumina template on a glass substrate.<sup>115</sup> The coupling strength was controlled by the geometry of the Au nanorod assembly and the thickness of the J-aggregate layer. The change in the extinction spectra of the Au nanorods after coating with the J-aggregates is similar as what was observed by Wiederrecht and coworkers, in both the weak and strong coupling cases.<sup>114</sup> In addition, in the strong coupling case, a split in the extinction band of the Au nanorods was also observed. Quantum mechanics interpreted the nature the coupled states as hybrid states from the plasmon resonance of the Au nanorods and the J-aggregate excitonic states.

From a theoretical perspective, Ambjörnsson et. al. reported study of the resonant coupling between anisotropic molecular layer and localized plasmons in ellipsoidal metal nanoparticles using electrodynamics methods in 2005.<sup>112</sup> The molecular resonance of the coating was tuned to be close-to or far-off the ellipsoid plasmon resonances to study strong and weak couplings. From the calculations, for the off-resonance case (weak coupling), the extinction spectrum of the coated-nanoparticle is the summation of the LSPR of the bare nanoparticle and the molecular resonance peak, where the magnitude of the molecular resonance peak is enhanced by the presence of the metallic surface. For the case when the molecular resonance is degenerate with the plasmon resonance, the plasmon resonance peak is split into two hybridized resonance peaks, consistent with experimental observation of the strong coupling between dye molecules



and Au nanorods. Recently, in 2007, A. M. Kelley described the optical spectra of J-Aggregated dyes on Au nanospheres by quantum mechanics.<sup>117</sup> She solved the Schrödinger equation for the wave functions and energies of new states that result from the coupling of the molecular states to the nanoparticle states through dipole-dipole interaction. The coupling strength is controlled by the distance between the molecular dipole and the nanoparticle dipole, and the molecular resonance of the dye molecules. The calculations showed the same coupling behavior in the dye-nanoparticle structures as in the aforementioned experiments and electrodynamics simulations.

The measurements performed by Wiederrecht et. al. and Wurtz et. al. are ensemble extinction spectra of organic dye molecules on colloidal nanoparticles and nanoparticle arrays.<sup>114,115</sup> Recently, Lee and coworkers explored the interaction between biological analytes with visible chromophores and single nanoparticles by dark-field microscopy.<sup>116</sup> It was found that when the LSPR of Au nanoparticles overlaps with the Q absorption bands of heme-protein Cytochrome c, quenching dips were observed in the scattering of single Au nanoparticles rising from the absorption of Cytochrome c. The authors claimed that the quenching dips resulted from plasmon resonance energy transfer (PRET) process. When tuning the Au nanoparticle size, the LSPR of the Au nanoparticles changes; therefore, the intensity of the PRET bands varies, depending on the degree of spectral overlap of Cytochrome c and the nanoparticle LSPR. The experimental observations are similar to the experimental and theoretical studies discussed above. The results open up the possibility of using the biomolecule-conjugated nanoparticle sensors to detect local environment changes in living cells with potentially nanoscale spatial resolution.

The work presented above all demonstrate that the coupling between the molecular resonances of chromophores and the localized surface plasmon resonances of metallic

nanoparticles leads to spectral line shape and intensity changes. However, there is a lack of analysis of the LSPR spectral shift caused by resonant adsorbates, which is crucial in LSPR sensing applications. The Van Duyne group studied the coupling between molecular resonances and LSPR using a different approach named resonant LSPR spectroscopy where we use Ag nanoparticles fabricated by NSL with varying LSPR wavelength, and monitor the effect of the resonant adsorbates on this wavelength, leading to a wavelength shift ( $\Delta\lambda_{\text{max}}$ ) at different LSPR wavelengths.<sup>73,103,113</sup>

As mentioned in section 1.1, the NSL fabricated Ag nanoparticles are triangular shape with sharp tips while the previously discussed studies were mostly performed on Au nanoparticles with no sharp features. It was demonstrated by several theoretical and experimental studies that the sharp tips in nanoparticles are responsible for the majority of the electric field enhancement around the nanoparticles and their sensitivity to environment.<sup>56,67</sup> Therefore, comparing with the aforementioned work, the resonant LSPR study on the NSL nanotriangles should lead to different spectral changes that may result from the sharp features in their structure. In addition, even though Au nanoparticles are more stable at ambient conditions than Ag nanoparticles, the LSPR band of the Au nanoparticles is usually broader and less intense in the visible wavelength range than the Ag nanoparticles due to the intrinsic dielectric properties of Au. And Au has interband transitions at  $\sim 500$  nm which limits the tunable range of the LSPR of the Au nanoparticles to be above 500 nm.<sup>9,66,118</sup> Using Ag nanoparticles extends the LSPR tuning range down to 400 nm, and this that allows us to study the coupling of the chromophores with molecular resonances below 500 nm to the LSPR of the Ag nanoparticles.

In 2006, Haes et. al. studied the effect of a monolayer of [2, 3, 7, 8, 12, 13, 17, 18-Octakis(propyl) porphyrazinato] magnesium (II) (MgPz) on the LSPR of the NSL-fabricated Ag

nanoparticles, nanoparticles with varying LSPR throughout the 450 ~ 700 nm range (experimental scheme shown in Figure 1.2 A).<sup>113</sup> The structure of MgPz was shown in Figure 1.2 B (inset) and the green line is the absorption spectrum of MgPz in ethanol. The LSPR shift ( $\Delta\lambda_{\max}$ ) upon adsorption of MgPz is shown in Figure 1.2 B as the black solid line with dots. At an off-molecular-resonance wavelength (weak coupling), a LSPR shift of ~ 20 nm was observed. However, when the LSPR peak maximum directly overlaps with the molecular resonance (strong coupling), the LSPR shift is reduced to less than 2 nm. When the LSPR maximum is slightly red-shifted from the molecular resonance, the LSPR shift is amplified by 300% over the average LSPR shift (20 nm) to 60 nm. It is apparent that the LSPR shifts exhibit highly wavelength-dependent behavior. Comparing to the results of dye molecules on the Au nanospheres and nanorods, no significant change in the LSPR spectral line shape and width was observed in both the weak or strongly coupling cases. Possible reasons for this difference compared to the earlier work on Au nanoparticles are that the intrinsic dielectric property difference between Ag and Au is responsible, the sharp tip features of the Ag nanotriangles are involved, or the NSL-fabricated particle inhomogeneity is obscuring the linshapes.<sup>103,113</sup>

In section 1.2, we discussed that for a particle with size much smaller than the wavelength of the incident light, the electrostatics (quasistatic) approximation can be applied to simplify the calculation of the absorption and scattering efficiency. We can use this approach to approximately simulate the extinction of nanoparticles coated with a layer of molecules. The extinction cross section of a metallic spheroid embedded in a homogeneous medium is given by Eq.1.6 (which is a simplification of Eqs. 1.1):<sup>1,2,68</sup>

$$C_{ext} \propto \frac{1}{\lambda} \text{Im} \left\{ \frac{\epsilon_i - \epsilon_o}{\epsilon_i + \chi \epsilon_o} \right\} \quad (1.6)$$

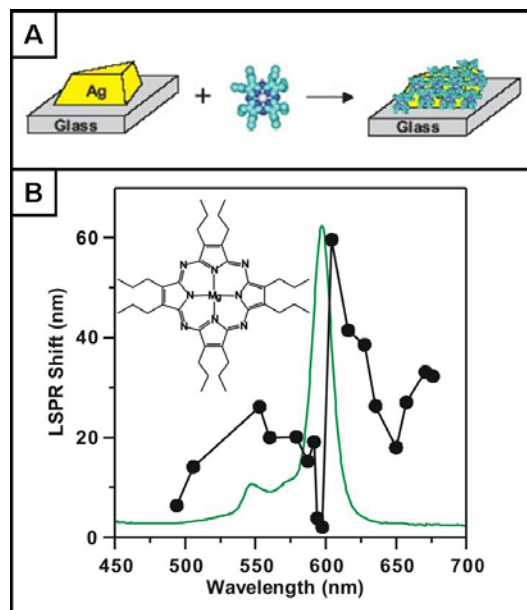


**Figure 1.2.** (A) Schematic illustration of the experimental procedure. (B) Wavelength dependent LSPR shifts induced by MgPz adsorption to Ag nanoparticles. Inset shows the molecular structure of MgPz. The solid green line is the solution absorption spectrum of MgPz. The black solid line with dots presents the induced LSPR shifts from a monolayer of MgPz versus the LSPR of bare Ag nanoparticles.

The shape factor  $\chi$  for the particle has the value 2 for a sphere, and increases with increasing aspect ratio (thereby describing the shape dependence of the plasmon resonance). To treat an inhomogeneous medium consisting of a layer of molecules surrounded by a solvent, an effective medium theory can be developed wherein the effective dielectric function of the surrounding medium is assumed to be of the form:

$$\varepsilon_{o, \text{effect}} = \varepsilon_{mol} \cdot x + \varepsilon_o \cdot (1 - x) \quad (1.7)$$

where  $\varepsilon_{mol}$  is the dielectric function of the molecule, and  $x$  is an empirical parameter (between 0 and 1) which is determined by the relative amounts of molecules and solvent that are contained within the range of the electromagnetic field around the particle. To model the wavelength shift induced by resonant molecules in the extinction of Ag nanoparticle arrays, one evaluates this equation using the dielectric function of  $N_2$  and the effective dielectric function of  $N_2$  with a thin layer of resonant molecules.

Eqs 1.6 and 1.7 are used to calculate the extinction wavelength shift induced by MgPz as a function of the plasmon resonance wavelength. The dielectric functions of MgPz were taken from Haes et al<sup>113</sup> and parameter  $x$  in the effective medium theory was chosen as 0.01 to match the experimental data. Figure 1.3 A shows the calculated extinction spectra of bare (solid lines) and MgPz-coated (dashed lines) Ag spheroids. Here the extinction wavelength of the Ag spheroid is varied by varying  $\chi$ . Each pair of spectra with the same colors is calculated using the same  $\chi$ . When the extinction maximum of the Ag spheroid is separated by more than 50 nm from the absorption peak of MgPz, the extinction maximum of the MgPz-coated Ag nanoparticle is red-shifted from that of the bare Ag nanoparticle. In addition, there is a small peak at  $\sim 600$  nm in the spectrum due to absorption by MgPz. When the extinction wavelength of the Ag

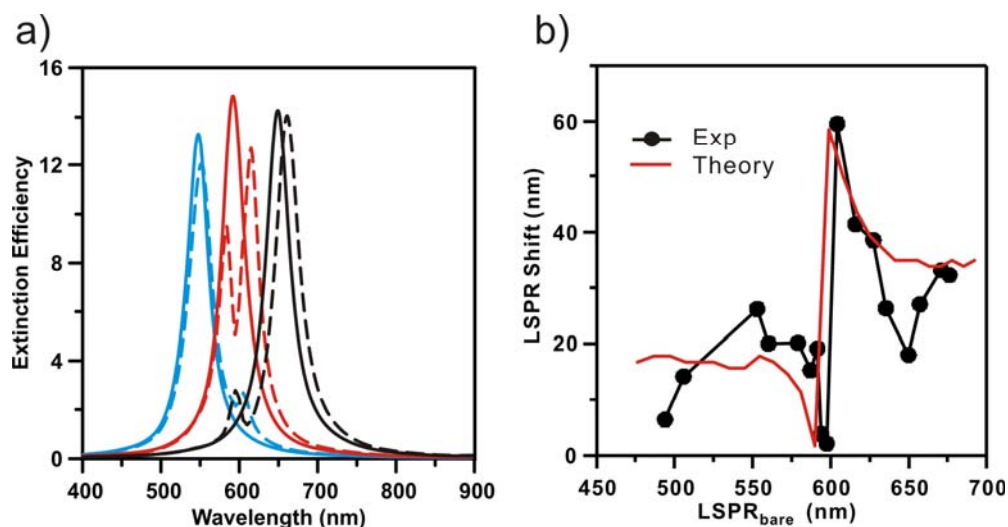


**Figure 1.3.** Extinction spectra of Ag spheroid/MgPz and LSPR shift induced by MgPz. (A) Extinction spectra of bare Ag spheroid (solid lines) and Ag spheroid with MgPz (dashed lines) with varying  $\chi$  parameters. Each pair of spectra of the same color was calculated with the same  $\chi$ . (B) LSPR shift of the Ag nanoparticles induced by MgPz versus LSPR wavelength of bare Ag nanoparticles. The black line with dots is experimental LSPR shift data and the red curve is the calculated LSPR shift.

nanoparticle is close to the MgPz absorption peak, a dip in the extinction spectrum of the MgPz-coated Ag nanoparticle is found due to MgPz absorption, and the extinction is split into two bands. This result is consistent with the experimental and theoretical studies from several other groups discussed previously. Figure 1.3 B shows the predicted LSPR wavelength shift (red solid line) in comparison with the experimental data (black solid line with dots). The modeling agrees well with the experiments, confirming that this method can be used to calculate the LSPR of metal nanoparticles coated with a resonant molecular layer.

Results shown in Figure 1.2 reveal that resonant LSPR spectroscopy is a powerful tool to study the interaction between dye molecules and metallic nanoparticles. The LSPR is extremely sensitive to the electronic resonances of the dye molecules so it can be used to detect small changes in the dye molecular resonances due to environmental change (such as pH,<sup>119-123</sup> polarity of the solvent<sup>124-127</sup>), aggregation,<sup>128-130</sup> and binding of other analytes,<sup>131-134</sup> etc. The results also provide guidance to design and optimization of resonant LSPR sensors.

## 1.4 Goals and Organization

The work presented in this thesis focuses on the fundamentals of resonant chromophores interacting with metallic nanoparticles by monitoring the localized surface plasmon resonance of the nanoparticles, modeling the results with electrodynamics theory, and exploring applications in biological detection. The goal of this work is to understand the coupling mechanism of the molecular and plasmon resonances, to learn its role in surface-enhanced Raman scattering (SERS) spectroscopy, and to get optimized conditions for resonant biological target sensing.

In Chapter Two, we consider the coupling of the LSPR of the NSL-fabricated Ag nanoparticles and Rhodamine 6G, a widely used molecular probe for (single-molecule) SERS.

The LSPR shift induced by Rhodamine 6G has complicated features, that are related to the electronic resonances of the Rhodamine 6G monomer and dimers formed on the nanoparticle surface. The findings show the extreme sensitivity of the LSPR in elucidating the detailed electronic structure of a resonant adsorbate. In Chapters Three and Four, the coupling mechanism of resonant molecules with LSPR is applied to the detection of small molecules binding to cytochrome P450 proteins. When small substrate or inhibitor molecules bind to cytochrome P450 proteins, they induce a shift in the wavelength of the Soret and Q absorption bands of the protein. Resonant LSPR spectroscopy was used to detect this electronic resonance change. In Chapter Five, we study the correlation between LSPR, molecular resonance and SERS enhancement. Wavelength-scanned surface-enhanced resonance Raman excitation spectroscopy profiles of Tris-(2,2'-bipyridine)-ruthenium(II) ( $\text{Ru}(\text{bpy})_3^{2+}$ ) adsorbed on Ag nanoparticle arrays were taken and correlated to the LSPR of Ag nanoparticles. Quasi-static electrostatics modeling was applied to simulate the WS-SERRES profiles, demonstrating that the WS-SERRES profiles involve multiplicative electromagnetic and resonance Raman enhancement. Finally, in Chapter Six, we explore new plasmonic materials. The discrete dipole approximation method was used to study the plasmonic properties of Cu and Al nanoparticles fabricated by nanosphere lithography. A comparison of the calculated results with the experiments is presented.



## **Chapter Two**

### **Interaction of Plasmon and Molecular Resonances for Rhodamine 6G Adsorbed on Silver Nanoparticles**

## 2.1 Introduction

The last two decades have witnessed a rapid growth in the development of highly selective and sensitive optical chemical and biological nanosensors.<sup>33,102</sup> Fluorescent and colorimetric dyes are widely used in these applications, where they can be immunoassay labels, tissue stains, and chemical indicators.<sup>135</sup> However, individual dye molecules produce a relatively weak signal (e.g. fluorescein has an absorbance cross section of  $3.5 \times 10^{-16} \text{ cm}^2$ )<sup>16</sup>, and most fluorescent dyes photobleach, providing only a limited “photon budget.”<sup>136</sup> Nanoparticles do not have the same limitations. Noble metal nanoparticles produce extremely intense scattering and extinction signals (e.g. a single 60 nm silver nanosphere has an extinction cross section of  $2.5 \times 10^{-10} \text{ cm}^2$ )<sup>16</sup> and do not photobleach. Adding chemically sensitive dyes to these metal nanostructures produces integrated chemical sensors with bright, low bleaching extinction and scattering signal. This paper describes, for the first time, a metal nanoparticle/chromophore coupling with multiple resonant states.

When metal nanoparticles are excited by electromagnetic radiation, they exhibit collective oscillations of their conduction electrons known as localized surface plasmon resonance (LSPR).<sup>2,4,137</sup> The wavelength ( $\lambda_{\text{max}}$ ) associated with maximum LSPR extinction of the nanoparticles can be measured with UV-Vis spectroscopy. It has been well established that the LSPR maximum of the nanoparticles strongly depends on the composition, size, shape and local dielectric environment.<sup>12,14,39</sup> Therefore, nanoparticles can sense the change in the local refractive index that accompanies molecular binding. Such nanoparticle-based optical sensing techniques are effective for quantitative detection of chemical and biological targets.<sup>26,32,56,113,138-141</sup> This is achieved by monitoring the shift in  $\lambda_{\text{max}}$  upon binding of the probe analytes onto the nanoparticles.

Most LSPR sensing experiments have been performed with electronically nonresonant adsorbates, which do not have electronic transitions in the visible wavelength range. However, since many biological targets have visible chromophores, it is worthwhile to broaden the scope of LSPR sensing by exploring electronically resonant adsorbates. Recent progress has revealed the correlation between the molecular resonances and the nanoparticles' surface plasmon resonances for two different resonant adsorbates, [2, 3, 7, 8, 12, 13, 17, 18-Octakis(propyl) porphyrizinato] magnesium (II) and Iron (II) Tris 2,2'-bipyridine.<sup>113</sup> When resonant molecules are adsorbed on the nanoparticles, strong coupling between the molecular resonance and nanoparticle LSPR has been observed experimentally and simulated by electrodynamics theory.<sup>112-114</sup> The induced LSPR shift due to this coupling is found to be strongly dependent on the spectral overlap between the molecular resonances and the LSPR. Specifically, a large red shift occurs when the LSPR is located at a slightly longer wavelength than the molecular resonance, i.e., a factor of 3 greater than when the LSPR is distant from the molecular resonance. On the basis of this amplification mechanism, a nanoparticle-based biosensor has been successfully developed to detect the binding of a low molecular weight substrate to cytochrome P450 proteins.<sup>103</sup> By coupling LSPR with the resonant states of these heme-containing proteins, one can monitor the LSPR response to the change in the Soret band of these proteins upon substrate binding.

Rhodamine 6G (R6G) has been chosen in this study because of its active role in surface-enhanced Raman spectroscopy (SERS). It was one of the first molecules used for single-molecule SERS (SMSERS) studies with enhancement as large as  $10^{14}$  to  $10^{15}$  being observed.<sup>62,80,142</sup> It has been demonstrated that the SERS enhancement factor is closely related to the plasmon resonance of the nanoparticle, laser excitation wavelength and the molecular

resonance.<sup>4,28,29,143-145</sup> However, the single molecule SERS mechanism is not fully understood.

Therefore, understanding the coupling of R6G molecular resonances with LSPR is crucial for elucidating the single molecule SERS mechanism.

In this work, the coupling between the molecular resonances of R6G and the nanoparticles' LSPR is systematically studied by monitoring the change in  $\lambda_{\text{max}}$  before and after R6G binding. To explore the wavelength-dependent LSPR shift, nanoparticles with varying  $\lambda_{\text{max}}$  through the visible region are fabricated using nanosphere lithography (NSL).<sup>39,43</sup> It is found that the LSPR response is highly wavelength and concentration dependent. In addition, the LSPR response shows extreme sensitivity to all resonant states of the adsorbed species, revealing features difficult to observe using standard absorption methods. By combining theoretical modeling with the experimental observations, a microscopic understanding of the complicated LSPR response is obtained.

## 2.2 Experimental Methods

### 2.2.1 Materials

Absolute ethanol was obtained from Pharmco (Brookfield, CT). Methanol was purchased from Fisher Scientific (Pittsburgh, PA). Silver wire (99.99%, 0.5 mm diameter) was purchased from D.F. Goldsmith (Evanston, IL). Tungsten vapor deposition boats were acquired from R.D. Mathis (Long Beach, CA). Polystyrene nanospheres with diameters of 280, 390, 450, and 510 nm were received as a suspension in water (Interfacial Dynamics Corporation, Portland, OR or Duke Scientific, Palo Alto, CA) and were used without further treatment. Millipore cartridges (Marlborough, MA) were used to purify water to a resistivity of 18.2 M $\Omega$ ·cm. Fisherbrand No. 2 glass coverslips with 18 mm diameters were obtained from Fisher Scientific (Pittsburgh, PA).

Benzenethiol and Rhodamine 6G was obtained from Sigma Aldrich (St. Louis, MO) and used as received.

### 2.2.2 Substrate Preparation

Glass substrates were cleaned in piranha solution (1:3 30%  $\text{H}_2\text{O}_2/\text{H}_2\text{SO}_4$ ) for 30 minutes at 80°C. (Warning: Piranha reacts violently with organic compounds and should be handled with caution.) Samples were allowed to cool and were then rinsed profusely with water. Samples were then sonicated in 5:1:1  $\text{H}_2\text{O}/\text{NH}_4\text{OH}/30\% \text{H}_2\text{O}_2$  and rinsed with water. The samples were stored in ultrapure water prior to use.

### 2.2.3 Nanoparticle Preparation

NSL was used to create monodispersed, surface-confined Ag nanotriangles.<sup>43</sup> Polystyrene nanospheres ( $\sim 2.2 \mu\text{L}$ ) were drop-coated onto the glass substrates and allowed to dry, forming a monolayer in a close-packed hexagonal formation. This close-packed layer of nanospheres served as a lithographic mask to deposit Ag in the triangular voids between the spheres. The samples were mounted into a Consolidated Vacuum Corporation vapor deposition chamber. A Leybold Inficon XTM/2 quartz crystal microbalance (East Syracuse, NY) was used to measure the thickness of the Ag film deposited over the nanosphere mask,  $d_m$ . Following metal deposition, the samples were sonicated for 3-5 minutes in ethanol to remove the polystyrene nanosphere mask. The perpendicular bisector of the nanoparticles was varied by changing the diameter of the nanospheres used. The height of the nanoparticles was varied by depositing varying amounts of Ag onto the sample. These two parameters were varied to alter the LSPR peak position throughout the visible region of the spectrum. In general, an increase in nanosphere diameter and/or a decrease in metal film thickness result in a red shift in LSPR.

### 2.2.4 Nanoparticle Solvent Annealing and Functionalization

For each experiment, the sample was stabilized and functionalized in a home built flow cell.<sup>36</sup> Prior to modification, the Ag nanoparticles were solvent annealed<sup>36</sup> with methanol. Dry N<sub>2</sub> gas and solvent were cycled through the flow cell until the  $\lambda_{\text{max}}$  of the sample stabilized. Samples were then incubated in 0.6  $\mu\text{M}$  R6G ethanolic solutions for 1 hour. After incubation, the nanoparticle samples were rinsed with 10-20 mL ethanol and dried by flowing N<sub>2</sub> gas through the sample cell.

### 2.2.5 Ultraviolet-Visible Extinction Spectroscopy

UV-vis extinction spectra were collected using an Ocean Optics (Dunedin, FL) SD2000 or HR2000 fiber optically coupled spectrometer with a CCD detector. All spectra in this study are macroscopic measurements performed in standard transmission geometry with unpolarized light. The probe spot size was approximately 2 mm in diameter.

### 2.2.6 Ultraviolet-Visible Surface Absorption Spectroscopy of R6G

UV-vis surface absorption spectra of R6G on thin metal films were collected using an integrating sphere (RSA-HP-84, LabSphere) and fiber-optic coupled spectrometer (USB2000-VIS-NIR, Ocean Optics) with a CCD detector. R6G was adsorbed onto a 200 nm thick Ag film (vapor deposited onto a glass substrate) by immersion in R6G ethanolic solutions at room temperature for 12 h, followed by thorough rinsing in ethanol. Two reflectance spectra were measured. The reference spectrum, reference ( $\lambda$ ), was that of an identical 200 nm thick Ag film on glass with no R6G adsorbed. The sample spectrum, sample ( $\lambda$ ), was that of R6G on a 200 nm thick Ag film. The surface absorption spectrum was then calculated as  $A_{\text{surf}}(\lambda) = -\log_{10}(\text{sample}(\lambda)/\text{reference}(\lambda))$ . All the measurements were conducted in air at room temperature.

## **2.3 Results and Discussion**

### 2.3.1 Wavelength Dependence of Benzenethiol Induced LSPR Shift

To explore the wavelength dependence of the adsorbate-induced LSPR shift, a non-resonant adsorbate, benzenethiol was investigated. Nanoparticles with various heights and widths were fabricated by NSL.<sup>13</sup> The extinction spectra of the nanoparticles before and after exposure to benzenethiol were collected in a N<sub>2</sub> environment. As the aspect ratio (in-plane width/out-of-plane height) of the nanoparticles increase from 1.3 to 2.9, the LSPR of bare nanoparticles varies from ~ 460 nm to ~ 730 nm. The effect of a monolayer of benzenethiol on the LSPR ( $\Delta\lambda_{\text{max}}$ ) versus the LSPR wavelength of bare nanoparticles ( $\lambda_{\text{max,bare}}$ ) was monitored and plotted in Figure 2.1. From Figure 2.1, the LSPR shift increases monotonically from 35 nm to 55 nm with increasing  $\lambda_{\text{max,bare}}$ . This agrees with previous observations, showing that with increasing aspect ratio of the nanoparticle, the LSPR shift increases.<sup>56</sup>

### 2.3.2 Wavelength Dependence of the R6G Induced LSPR Shift

Figure 2.2 A-B shows the structure of R6G and its solution absorption spectrum, respectively. In ethanol solution (solid green line in Figure 2.2 B), R6G exhibits a peak at 530 nm from the S<sub>0</sub>-S<sub>1</sub> electronic transition (extinction coefficient  $\epsilon_{\text{max}} = 105 \text{ mM}^{-1} \cdot \text{cm}^{-1}$ , FWHM = 31.85 nm, 1145 cm<sup>-1</sup>) and a shoulder at 495 nm from vibronic S<sub>0</sub>-S<sub>1</sub> transition.<sup>144,146</sup>

The LSRP shift induced by resonant adsorbates is known to be highly wavelength-dependent. Figure 2.3A reveals the influence of a monolayer of R6G on the LSPR wavelength of Ag nanoparticles. The electronic absorption spectrum of R6G has been included for direct comparison with the experimental data points. The LSPR shift displays interesting behavior when scanning  $\lambda_{\text{max,bare}}$  from 450 to 750 nm. When  $\lambda_{\text{max,bare}}$  is much bluer (i.e. 450 ~ 470 nm) than the molecular resonance, a small LSPR shift (less than 5 nm) is observed. As  $\lambda_{\text{max,bare}}$  is

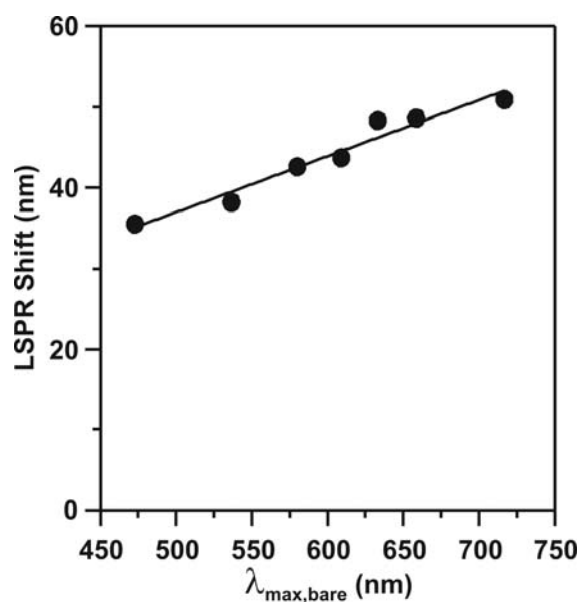


**Figure 2.1** Wavelength-dependent LSPR shift induced by a monolayer of benzenethiol vs. the LSPR wavelength of bare Ag nanoparticles.



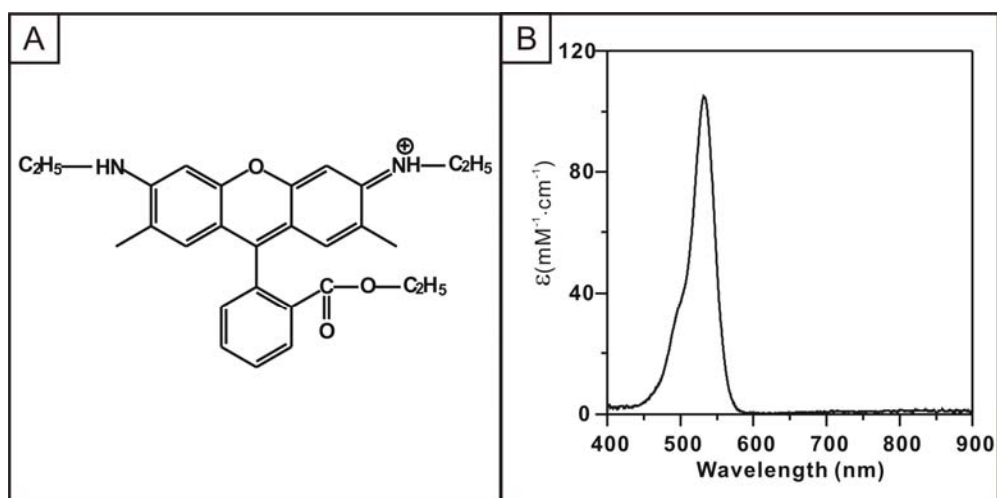


**Figure 2.2** (A) Molecular structure of Rhodamine 6G. (B) Absorption spectrum of R6G in ethanol solution.

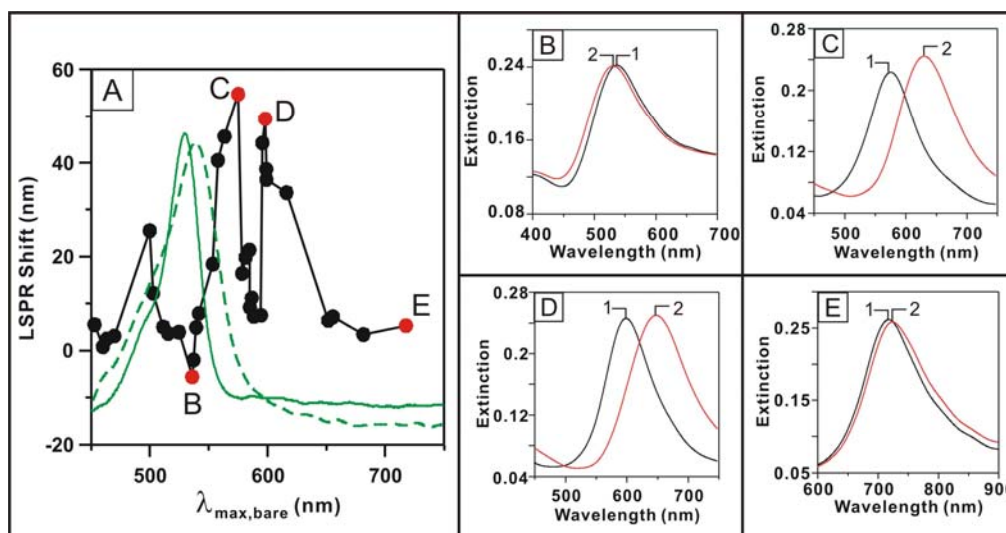


**Figure 2.3** Influence of R6G on the LSPR shift of Ag nanoparticles and representative LSPR spectra. (A) Wavelength-dependent LSPR shift induced by a monolayer of R6G vs. the LSPR wavelength of bare Ag nanoparticles. Solid black line with filled dots is a plot of the LSPR shift (nm) vs. LSPR position of Ag nanoparticles. The green solid and dashed lines are the absorption spectrum of the R6G in ethanol solution and on a 200 nm Ag film (arbitrary scaling), respectively. (B)-(E) LSPR spectra of Ag nanoparticles (associated with points B-E in Figure A) before (black line, 1) and after (red line 2) chemical modification. (B) (1),  $\lambda_{\text{max}} = 535.9$  nm and (2),  $\lambda_{\text{max}} = 530.3$  nm. The LSPR shift = -5.6 nm, %FWHM = 1.1%, and %I = -5.9%. (C) (1),  $\lambda_{\text{max}} = 575.0$  nm and (2),  $\lambda_{\text{max}} = 629.7$  nm. The LSPR shift = 54.7 nm, %FWHM = 3.4%, and %I = +11.9%. (D) (1),  $\lambda_{\text{max}} = 598.0$  nm and (2),  $\lambda_{\text{max}} = 647.4$  nm. The LSPR shift = 49.4 nm, %FWHM = 8.9%, and %I = +1.5%. (E) (1),  $\lambda_{\text{max}} = 717.8$  nm and (2),  $\lambda_{\text{max}} = 723.1$  nm. The LSPR shift = 5.3 nm, %FWHM = 8.6%, and %I = -1.8%.

gradually tuned to the red, an increase in the induced shift is found. A local LSPR shift maximum of 25 nm occurs at  $\lambda_{\text{max,bare}} \sim 500$  nm. When  $\lambda_{\text{max,bare}}$  approaches the molecular resonance at 530 nm, the induced LSPR shift gradually decreases in the range of 500 ~ 530 nm. When  $\lambda_{\text{max,bare}}$  is very close to the molecular resonance, the LSPR shift drops and a slight blue shift ( $\sim 5$  nm) is observed (Figure 2.3B). Although minima in wavelength shift plots similar to what we find in the 520-530 nm range were seen in an earlier study of resonant chromophores on metal particles,<sup>113</sup> this is the first time that a blue-shift has been observed. In the past work it was noted that minima are found on the blue side of the molecular resonance as this is where the molecular polarizability is negative, leading to an induced polarization that destructively interferes with the oscillating polarization associated with plasmon resonance excitation. Whether this leads to a blue shift or not is likely determined by the size of the adsorbate polarizability, and whether this dominates over other contributions to the adlayer polarizability (from molecules that are not in resonance) which would typically be positive.

When  $\lambda_{\text{max,bare}}$  is shifted red from the molecular resonance at 530 nm, the LSPR shift gradually recovers from 530 ~ 575 nm and reaches a maximum value of 55 nm at  $\lambda_{\text{max,bare}} \sim 575$  nm. This maximum response is amplified by  $\sim 300\%$  over the average LSPR shift ( $\sim 20$  nm) (Figure 2.3C). Maxima similar to this were seen previously for other molecules<sup>103,113</sup> and their occurrence was explained based on the fact that both the molecular and metal polarizability is positive on the red side of the molecular resonance.

As  $\lambda_{\text{max,bare}}$  is further red-shifted from 575 to 590 nm, the LSPR shift sharply drops to a less than 10 nm shift followed by another LSPR shift maximum ( $\sim 50$  nm) at  $\lambda_{\text{max,bare}} \sim 595$  nm (Figure 2.3D). Finally, when  $\lambda_{\text{max,bare}}$  is red-shifted past 595 nm, the LSPR shift slowly

decreases to less than 10 nm at  $\lambda_{\text{max,bare}}$  close to 700 nm (Figure 2.3E). Notice that the LSPR shifts induced by R6G at an off-resonance wavelengths ( $< 470$  nm and  $> 650$  nm) are small compared to the shifts induced by benzenethiol. This simply reflects the lower packing density of R6G compared to benzenethiol due to its larger size. Furthermore, unlike the previously reported studies,<sup>113</sup> the LSPR peak intensity and width do not change significantly over the scanned wavelength region.

It is especially noteworthy that three LSPR shift maxima have been observed while there are only two absorption features in the molecular electronic transitions. This phenomenon is different from what was observed in previous wavelength shift spectroscopy studies near molecular resonances, where only one LSPR shift maximum was observed.<sup>113</sup>

### 2.3.3 Empirical Model of the Wavelength Shift

The LSPR shift is dependent on the refractive index of the surrounding medium of the nanoparticle. For non-resonant adsorbates, the LSPR wavelength shift ( $\Delta\lambda_{\text{max}}$ ) can be estimated from the following empirical equation:<sup>113,138,147,148</sup>

$$\Delta\lambda_{\text{max}} = m(n_{\text{ads}} - n_{\text{N}_2})(1 - e^{-2d/l_d}) \quad (2.1)$$

where  $m$  is the refractive index sensitivity of the nanoparticles ( $\sim 200$  nm/RIU),<sup>36,147</sup>  $n_{\text{ads}}$  is the real part of the refractive index of the adsorbate,  $n_{\text{N}_2}$  is the refractive index of the  $\text{N}_2$  surroundings (1.0),  $d$  is the molecular thickness (experimentally determined to be 1.0 nm by measuring the particle height before and after R6G adsorption using Atomic Force Microscopy, data not shown), and  $l_d$  is the characteristic electromagnetic field decay length of the nanoparticles (approximately 6 nm).<sup>147</sup> For resonant adsorbates, it has been demonstrated

that  $\Delta\lambda_{\max}$  near molecular resonance can be estimated from the real part of the refractive index using a Kramers-Kronig transformation<sup>149</sup> and Eq. 2.1. Using the same treatment as in the previous studies,  $n_{\text{ads}}$  is expressed as the sum of the nonresonant part of the refractive index ( $n_{\text{non,ads}}$ ) and the resonant contribution ( $\Delta n_{\text{res,ads}}$ ). From Eq.2.1, the refractive index of the adsorbate layer can be estimated. Since the average  $\Delta\lambda_{\max}$  at off-molecular resonance wavelengths is 10 nm, the  $n_{\text{non,ads}}$  of the R6G monolayer is calculated to be  $\sim 1.3$ .

Using a Kramers-Kronig transformation,  $\Delta n_{\text{res,ads}}$  of R6G was transformed from its solution absorption spectrum (Figure 2.2B) using the following equation:<sup>10,149</sup>

$$\Delta n_{\text{res,ads}}(\omega) = \frac{c}{\pi} \int_0^{\infty} \frac{\Delta\alpha(\omega')}{(\omega')^2 - \omega^2} d\omega' \quad (2.2)$$

where  $\Delta\alpha$  is the change in the absorption coefficient ( $2.303 * A(\lambda)/T$  in which  $A(\lambda)$  is the molecular absorbance at a given wavelength and  $T$  is the effective molecular thickness),  $c$  is the speed of light,  $\lambda$  is the wavelength of light, and  $\omega$  is the angular frequency ( $2\pi c/\lambda$ ). The Kramers-Kronig transformation expresses the real part of the refractive indices as an integral of the absorption coefficients. Notice that the integral in this formula has a singularity, which was treated numerically by excluding the singular point in the integral. This treatment will lead to some uncertainty in the absolute value of the refractive indices; however, it will simply result in a different scaling factor than what is used in the following sections to predict the LSPR shift. Therefore, the overall line shape of the predicted LSPR shift will not be affected.

Figure 2.4 shows the LSPR shift predicted using Eq. 2.1. The predicted LSPR shift has a maximum at 550 nm and a minimum at 520 nm associated with the  $S_0$ - $S_1$  transition. And the very small peak at 500 nm (indicated by the arrow in Figure 2.4) is associated with the vibronic band. This model fails to predict the complicated LSPR shift features. Although it captures two

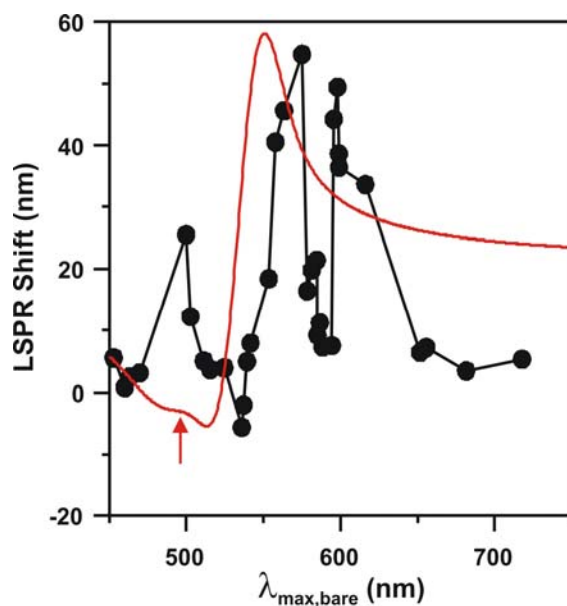


**Figure 2.4** Predicted LSPR shift (using Eq. 1) with a scaled refractive index from Kramers-Kronig analysis. The solid black line with filled dots is a plot of the experimental LSPR shift (nm) vs. spectral position of the bare Ag nanoparticles.

of the experimental LSPR shift features to some extent, the position and magnitude of the two features do not agree with the experiments. The additional LSPR shift maximum at  $\sim 595$  nm is not predicted using this empirical model. According to the empirical analysis, another absorption feature at  $\sim 570$  nm is necessary to generate such LSPR shift results.

#### 2.3.4 Concentration Dependence of the R6G Absorbance on Ag film and Analysis

As discussed, R6G has two absorption features in ethanol solution -- an  $S_0-S_1$  electronic transition and a vibronic shoulder. Figure 2.5A shows the deconvolution of the R6G solution phase absorption spectrum with two Gaussian curves at 532 and 504 nm. Since all the R6G induced LSPR shift measurements were conducted on an Ag surface with nanoscale patterns, it is important to examine the absorption behavior of R6G on an Ag surface. Ideally, one should study the R6G absorbance on Ag nanoparticles. However, the LSPR extinction always would interfere with the measurements. Instead, an alternative approach is to conduct the optical absorbance measurement of R6G on a continuous Ag film.

Figures 2.5(B-D) show the absorbance of different dosing concentrations of R6G (0.6  $\mu$ M, 6  $\mu$ M and 0.1 mM, respectively) on an Ag surface. R6G is known to form dimers in solution at high concentrations and when intercalated in heterogeneous materials like clays, silica and colloidal gold nanoparticles.<sup>130,150-154</sup> R6G can form both J-type (head-to-tail dipole moments) and H-type dimers (parallel dipole moments). The latter conformer is expected to be more likely on a surface due to the adsorption of R6G through one of its N atoms. The formation of dimers will affect the absorption characteristics of R6G by inducing spectral shifts and band splitting. These changes can be qualitatively explained by exciton theory<sup>155,156</sup> based on interactions between the dipole moments of the monomeric units. The dipole-dipole interactions result in a

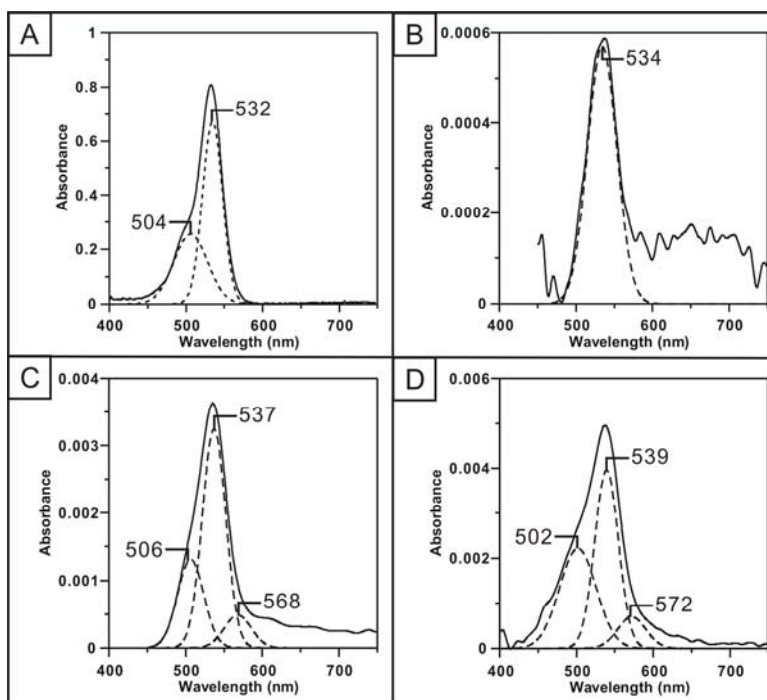


**Figure 2.5** Absorption spectra of R6G in ethanol solution and different concentrations of R6G on a Ag surface. Dashed lines represent deconvolution of the spectra into Gaussian bands. (A) R6G in ethanol (B) 0.6  $\mu\text{M}$  R6G on Ag surface (C) 6  $\mu\text{M}$  R6G on Ag surface (D) 0.1 mM R6G on Ag surface.



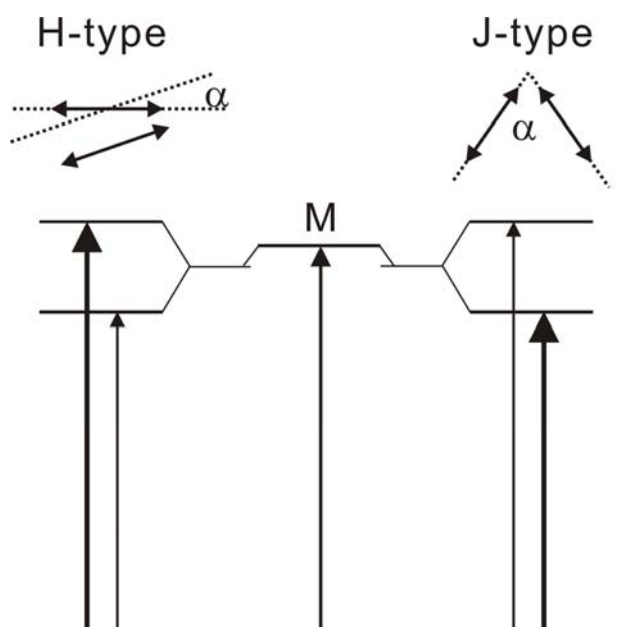


**Figure 2.6.** Exciton splitting diagram of the electronic states for R6G monomer and two types (H or J) of dimers, according to the arrangement of the dipole moments. M represents the R6G monomer excitation. H-type and J-type splitting results in an increase or decrease in the excitation energy. The thickest arrow represents the strongest transition.

splitting of the monomer excitation which depends on the geometry of the aggregates. The geometry with the head-to-tail transition dipoles leads to a decrease in energy, and the geometry with the parallel transition dipoles leads to an increase in energy (see the exciton energy diagram in Figure 2.6). Therefore, the absorption of H-type dimers is predicted to blue-shift the R6G absorption whereas for J-dimers the absorption is predicted to red-shift. To examine whether there is R6G dimer formation on the Ag surface, each absorption spectrum is deconvoluted by different numbers of Gaussian curves with correlation coefficients greater than 0.99. As shown in Figure 2.5B, when the R6G dosing concentration is as low as 0.6  $\mu\text{M}$ , a weak absorption spectrum is collected and the major absorption band can be fitted with one Gaussian curve at 534 nm. Although there are a few longer wavelength features, the signal to noise ratio is not high enough to resolve those peaks. Compared to the R6G solution absorption in Figure 2.5A, the major absorption band is slightly red shifted and broadened. Notice that the  $S_0$ - $S_1$  vibronic shoulder observed in solution can not be resolved when R6G adsorbs on the surface at this dosing concentration. When the R6G dosing concentration is 6  $\mu\text{M}$ , the absorbance of R6G is stronger and broadened compared to the lower concentration case, indicating that the R6G coverage on Ag surface is higher. For the higher R6G dosing concentrations (Figures 2.5C-D), three Gaussian curves are necessary to generate a good deconvolution of the absorption spectra. Figure 2.5C shows the deconvolution of this absorption spectrum using three Gaussian curves at 506, 537 and 568 nm. The curve at 537 nm has the highest intensity, followed by the curve at 506 nm, and the lowest intensity at 568 nm. Notice the major absorption is red-shifted from the R6G solution absorption. The ratio of the 506 to 537 nm bands is 0.41, higher than that of the 504 and 532 nm bands for the solution case (0.38). When the R6G dosing concentration is 0.1 mM, the absorption of R6G increases and broadens further compared to the lower concentrations.

Figure 2.5D shows the deconvolution of the absorption spectrum using three Gaussian curves at 502, 539 and 572 nm. The peak at 539 nm has the highest intensity, followed by the curve at 502 nm, and the lowest intensity at 572 nm. Notice that the major absorption is shifted further to the red from the R6G solution absorption. The ratio of the 502 nm to 539 nm bands further increases to 0.56. Since the spectral positions of the dimer band and the vibronic shoulder of the monomer overlap, it is not possible to distinguish them. However, it is known from the solution and intercalation experiments that an increase in the ratio of the band at  $\sim 500$  nm and the band at  $\sim 540$  nm and a shifting in the position of these bands is evidence for dimer formation.<sup>130,150-154</sup> The increase in the ratio of these two bands with increasing concentration observed here, therefore, suggests that R6G dimer formation is important on the Ag surface. Note that different concentrations of R6G were used to dose the surface due to the morphology difference of the Ag nanoparticles and films. The NSL-fabricated nanoparticles are more likely to encourage the R6G dimer formation at a lower concentration. Higher concentration of R6G dosing solution could be used, but past studies show that R6G tends to form dimers in ethanol solution when its concentration is higher than 0.1 mM thus introducing interference from R6G dimers already formed in the solution.<sup>157</sup>

### 2.3.5 Concentration Dependence of the R6G Induced LSPR Shift

From the above discussion, it is clear that the absorbance of R6G on an Ag surface is concentration-dependent. It is therefore worthwhile to quantitatively study the effect of a sub-monolayer coverage of R6G on the LSPR shift. As described in the experimental section, 0.6  $\mu$ M R6G is used to ensure monolayer coverage with 1 hr incubation time. By keeping the same incubation time, the effect of sub-monolayer R6G on the LSPR of the Ag nanoparticles is studied

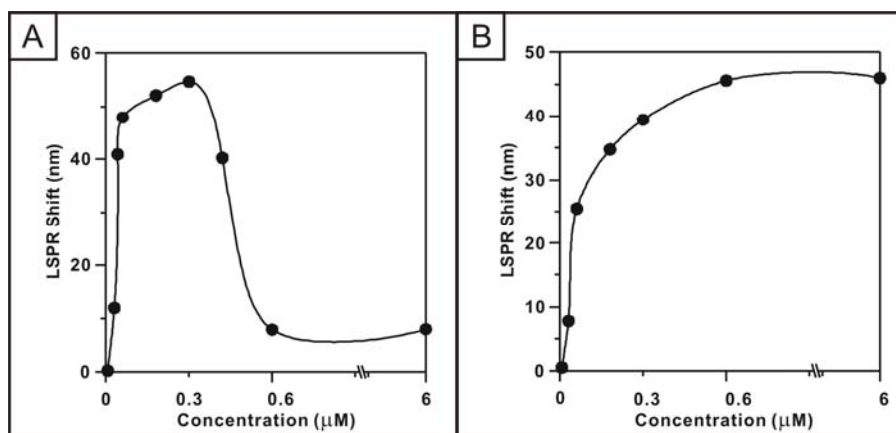


**Figure 2.7** LSPR shift vs. concentrations of R6G dosing solutions at constant LSPR of the bare Ag nanoparticles. (A) The LSPR of the bare Ag nanoparticles is  $\sim 540$  nm. (B) The LSPR of the bare Ag nanoparticles is  $\sim 560$  nm.

by varying the R6G concentration. Since the LSPR shift is highly wavelength dependent, two representative plasmon wavelengths of the bare nanoparticles are chosen: one at  $\sim 540$  nm, which is slightly red of the molecular resonance; the other at  $\sim 560$  nm, which is close to the wavelength of the maximum LSPR shift observed in Figure 2.3A.

The LSPR shift versus the concentration of R6G is plotted in Figure 2.7. The data shown in Figure 2.7A represent the LSPR shift when  $\lambda_{\text{max,bare}}$  is at 540 nm and that in Figure 2.7B represents the LSPR shift when  $\lambda_{\text{max,bare}}$  is at 560 nm. From Figure 2.7A, when the concentration of R6G is as low as 0.006  $\mu\text{M}$ , no shift is observed. As the concentration is gradually increased, the induced LSPR shift increases. When the R6G concentration is 0.3  $\mu\text{M}$ , a maximum LSPR shift of 55 nm is observed. Interestingly, as the concentration further increases, the LSPR shift gradually decreases to less than 10 nm at a concentration of 0.6  $\mu\text{M}$ . Further increase in concentration gives the same LSPR shift which confirms that the nanoparticle surface is saturated with a R6G monolayer. By contrast, the LSPR shifts plotted in Figure 2.7B do not exhibit such behavior. As the concentration increases, the LSPR shift gradually increases and saturates at 0.6  $\mu\text{M}$ . An explanation for the concentration dependence of LSPR shifts will be presented in the following section.

### 2.3.6 Electrodynamics Model of the Wavelength Shift

Three R6G absorption bands are observed on the Ag surface, which are probably associated with different R6G monomer and dimers. We calculated refractive indices of the R6G monomer and dimers from the Kramers-Kronig analysis using the deconvoluted curves in Figure 2.5D. This set of refractive indices is chosen to match these experimental results because they best represent the saturated R6G surface absorption response. Two types of R6G dimers,

**Table 2.1** Refractive indices of Rhodamine 6G monomer, H-dimer and J-dimer transformed from Rhodamine 6G absorption spectra on Ag surface.

Wavelength (nm)	Monomer		H-dimer		J-dimer	
	Real	Imaginary	Real	Imaginary	Real	Imaginary
450	1.31E+00	1.85E-08	1.27E+00	1.75E-02	1.34E+00	1.59E-11
460	1.30E+00	6.46E-07	1.25E+00	4.05E-02	1.34E+00	5.16E-10
470	1.29E+00	1.48E-05	1.24E+00	7.89E-02	1.34E+00	1.25E-08
480	1.28E+00	2.24E-04	1.25E+00	1.29E-01	1.34E+00	2.24E-07
490	1.25E+00	2.22E-03	1.28E+00	1.76E-01	1.34E+00	3.00E-06
500	1.21E+00	1.44E-02	1.34E+00	2.02E-01	1.34E+00	2.98E-05
510	1.16E+00	6.18E-02	1.41E+00	1.95E-01	1.33E+00	2.21E-04
520	1.12E+00	1.74E-01	1.46E+00	1.58E-01	1.33E+00	1.21E-03
530	1.19E+00	3.22E-01	1.48E+00	1.07E-01	1.32E+00	4.97E-03
540	1.37E+00	3.91E-01	1.48E+00	6.09E-02	1.31E+00	1.51E-02
550	1.54E+00	3.12E-01	1.47E+00	2.91E-02	1.31E+00	3.42E-02
560	1.60E+00	1.64E-01	1.45E+00	1.16E-02	1.32E+00	5.76E-02
570	1.57E+00	5.65E-02	1.43E+00	3.91E-03	1.34E+00	7.22E-02
580	1.51E+00	1.28E-02	1.42E+00	1.10E-03	1.37E+00	6.73E-02
590	1.47E+00	1.91E-03	1.41E+00	2.61E-04	1.39E+00	4.66E-02
600	1.45E+00	1.87E-04	1.41E+00	5.18E-05	1.40E+00	2.40E-02
610	1.44E+00	1.20E-05	1.40E+00	8.63E-06	1.39E+00	9.22E-03
620	1.43E+00	5.09E-07	1.40E+00	1.21E-06	1.38E+00	2.63E-03
630	1.42E+00	1.42E-08	1.39E+00	1.41E-07	1.37E+00	5.58E-04
640	1.41E+00	2.59E-10	1.39E+00	1.39E-08	1.37E+00	8.81E-05
650	1.41E+00	3.11E-12	1.39E+00	1.15E-09	1.37E+00	1.03E-05
660	1.40E+00	2.45E-14	1.39E+00	7.95E-11	1.37E+00	9.03E-07
670	1.40E+00	1.27E-16	1.39E+00	4.62E-12	1.36E+00	5.87E-08
680	1.40E+00	4.35E-19	1.38E+00	2.25E-13	1.36E+00	2.84E-09
690	1.40E+00	9.74E-22	1.38E+00	9.21E-15	1.36E+00	1.02E-10
700	1.39E+00	1.44E-24	1.38E+00	3.16E-16	1.36E+00	2.73E-12
710	1.39E+00	1.39E-27	1.38E+00	9.11E-18	1.36E+00	5.43E-14
720	1.39E+00	8.86E-31	1.38E+00	2.20E-19	1.36E+00	8.04E-16
730	1.39E+00	3.71E-34	1.38E+00	4.46E-21	1.36E+00	8.86E-18
740	1.39E+00	1.02E-37	1.38E+00	7.60E-23	1.36E+00	7.26E-20
750	1.39E+00	1.84E-41	1.38E+00	1.08E-24	1.36E+00	4.43E-22

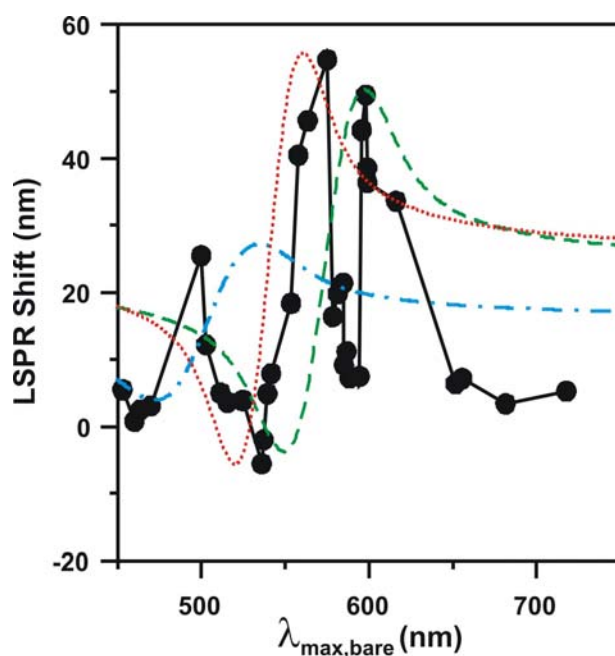


**Figure 2.8** Predicted LSPR shift (using Eq. 2.1) with arbitrarily scaled refractive indices from Kramers-Kronig analysis. The solid black line with filled dots is a plot of the experimental LSPR shift (nm) vs. spectral position of the Ag nanoparticles. The blue dashed-dotted line, red dotted line and green dashed line represent the predicted LSPR shift using the refractive indices of the R6G H-dimer, monomer and J-dimer, respectively.

the H-dimer and J-dimer, are assumed to form on the surface, and these lead to a blue and red shift of the absorption peak, respectively, relative to the monomer wavelength. We assign the blue shifted peak of the deconvoluted curves in Figure 2.5D as an H-dimer absorption, and the red-shifted peak as a J-dimer absorption. Figure 2.8 shows the predicted LSPR wavelength shift ( $\Delta\lambda_{\max}$ ) from Eq 2.1 using the real parts of the refractive indices of the R6G monomer and two dimers. (The refractive indices of R6G monomer and two dimers are available in Table 2.1) The three curves in Figure 2.8 are arbitrarily scaled (with a scaling factor of 2, 2, and 10 for monomer, H-dimer and J-dimer, respectively) due to the uncertainty of the coverage of R6G monomer and dimers on the surface. From Figure 2.8, it is clear that the curves associated with the R6G monomer and dimers correspond to the three experimental LSPR shift features. Nevertheless, the line shape and peak position of the predicted LSPR shift curves do not track the details of the experimental results.

The above empirical model only considered the contribution from the real part of the refractive indices of the R6G monomer and dimers. An advanced electromagnetic method, such as the Discrete Dipole Approximation method,<sup>11,95,96</sup> including both the real and imaginary parts of the adsorbates' dielectric constants, is needed to reveal the overall effect of the adsorbates. However, such calculations are very compute intensive and time-consuming. As an alternative, we use quasistatic (Gans) theory as a simplified model wherein the particle shape is assumed to be an oblate spheroid.<sup>68</sup> This approach leads to the following expression for the extinction cross section  $C_{ext}$  of a metallic particle in a homogenous medium:<sup>10,68</sup>

$$C_{ext} \propto \text{Im} \left\{ \frac{\epsilon_{Ag} - \epsilon_m}{\epsilon_{Ag} + \chi \epsilon_m} \right\} \quad (2.3)$$



where  $\varepsilon_{Ag}$  is the dielectric constant of Ag,  $\varepsilon_m$  is the dielectric constant of the surrounding medium, and  $\chi$  is a shape factor for the particle that has the value 2 for a sphere, and increases with increasing aspect ratio. In the present application, we use  $\chi$  as a parameter to tune the plasmon resonance wavelength, so the quantitative connection between  $\chi$  and the structure of the particle is not needed.

For the bare Ag particle,  $\varepsilon_m$  is set to be 1 for  $N_2$ . When  $\chi$  varies from 2.0 to 24.0, the extinction maximum wavelength of the bare Ag particle ( $\lambda_{max,bare}$ ) varies from 400 to 750 nm. It is hypothesized that one of the three R6G structures, i.e., the monomer or one of the two dimers, dominates the LSPR shift at each wavelength; therefore,  $\varepsilon_m$  for the adsorbates ( $\varepsilon_{m,ads}$ ) is expressed using the following function,

$$\varepsilon_{m,ads} = \begin{cases} \varepsilon_H, & 400 < \lambda_{max,bare} < 530 \\ \varepsilon_{mon}, & 530 < \lambda_{max,bare} < 570 \\ \varepsilon_J, & 570 < \lambda_{max,bare} < 750 \end{cases} \quad (2.4)$$

where  $\varepsilon_H$ ,  $\varepsilon_{mon}$ , and  $\varepsilon_J$  are the dielectric constants of the R6G H-dimer, monomer and J-dimer, respectively. Values for these dielectric constants were obtained by Kramers-Kronig transformation as noted above. Furthermore, Eq. 3 applies when the particle is in a homogenous environment; however, in the experiments, the particles are coated with a very thin layer of R6G, and the rest of the medium is  $N_2$ . This inhomogeneous medium is treated using effective medium theory<sup>2,37</sup> ( $\varepsilon_{m,effective} = \varepsilon_m \cdot x + (1-x) \cdot \varepsilon_{N_2}$ , where  $0 < x < 1$ , and  $x$  is chosen differently for  $\varepsilon_H$ ,  $\varepsilon_{mon}$ , and  $\varepsilon_J$  to match the experiments.  $x$  is chosen as for 0.3, 0.05, and 0.9 for  $\varepsilon_H$ ,  $\varepsilon_{mon}$ , and  $\varepsilon_J$  to match the experimental LSPR shifts line shape). Plugging  $\varepsilon_{m,effective}$  into Eq 2.3, the extinction maximum of the Ag particle embedded in R6G ( $\lambda_{max,R6G}$ ) for each  $\chi$  value is obtained. The LSPR

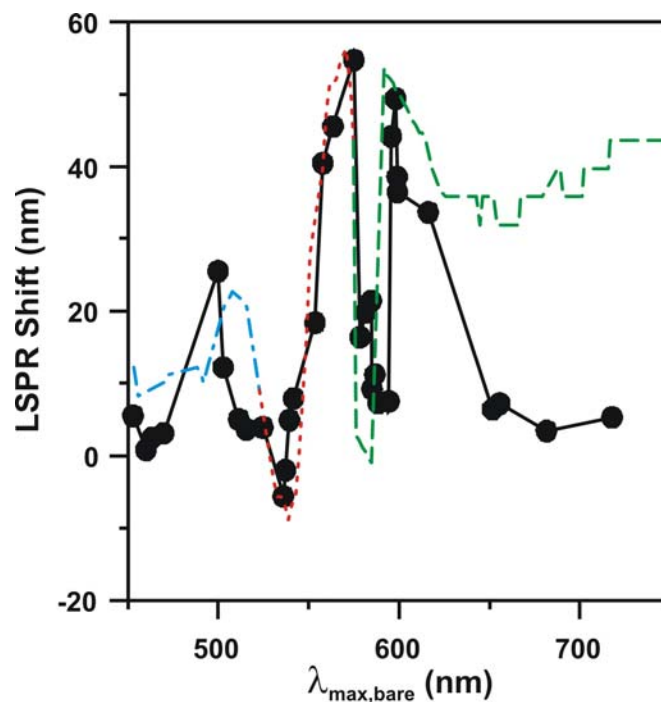


**Figure 2.9** Predicted LSPR shift using Eq. 2.3.

The solid black line with filled dots is a plot of the experimental LSPR shift (nm) vs. spectral position of the Ag nanoparticles. The blue dashed-dotted line, red dotted line and green dashed line represent the predicted LSPR shift using the dielectric constants of the R6G H-dimer, monomer and J-dimer, respectively.

shift is then calculated from the difference between  $\lambda_{max,bare}$  and  $\lambda_{max,R6G}$ , then scaled up to match the magnitude of the experimental LSPR shifts by factors of 6, 1 and 2 for R6G monomer, H-dimer and J-dimer, respectively. This scaling corrects for deficiencies of the Gans model which typically will underestimate dielectric shifts since there are no sharp features on the spheroidal particles.

Figure 2.9 shows the resulting LSPR shift versus  $\lambda_{max,bare}$ . The blue dashed-dotted line, red dotted line and green dashed line represent the predicted LSPR shift using the dielectric constants of the R6G H-dimer, monomer and J-dimer, respectively. From Figure 2.9, the predicted LSPR shift agrees well with the experimental data. This illustrates that the three LSPR shift features are associated with R6G in the three different forms. This can be understood if we assume that each particle is primarily coated with one of the three forms of R6G, and then there is a random mixture of the three different kinds of particles. We also considered an effective medium model in which each particle is assumed to be coated with a random mixture of the three R6G's, so that the adsorbate dielectric constant is a weighted average of the three values, however this did not match the measurements.

The quasistatic model can also be applied to simulate the concentration dependent LSPR shifts in Figure 2.7 by fixing  $\chi$  for two different initial LSPR wavelengths and varying  $x$  in the effective medium treatment. When this is applied at 560 nm, where the R6G monomer absorption dominates, we find that the LSPR shift increases with increasing concentration much as in Figure 2.7B, as increasing concentration produces a higher effective dielectric constant in the surrounding medium. On the other hand, the complicated concentration dependence at 540 nm (Figure 2.7A) can only be understood if we assume that there is a switch in the dominant adsorbed species as concentration is increased. Thus the portion of the curve in Figure 2.7A

below 0.4  $\mu\text{M}$  would correspond to one species (such as the H dimer) and then there is a switch to another species (such as the monomer) at high concentration.

### 2.3.7 Quantum Chemical Modeling of the Absorption Spectra of Rhodamine 6G

Although the empirical modeling qualitatively reproduces the LSPR shift, it is worthwhile to study the microscopic origin of the R6G absorption features using electronic structure theory. The electronic states of R6G were calculated within time-dependent density functional theory (TD-DFT) using the Amsterdam Density Functional (ADF) program package.<sup>158,159</sup> The Becke-Perdew (BP86) XC-potential<sup>160,161</sup> and a triple- $\zeta$  polarized Slater type (TZP) basis set from the ADF basis set library have been used. The following possible origins of the LSPR shift maximum at  $\sim 595$  nm have been examined (1) formation of R6G dimers; (2) metal molecule charge-transfer transitions; (3) the change of the angle between the xanthene plane and the phenyl substituent of R6G.

The optimized R6G structure (shown in Figure 2.10A) was taken from previous work,<sup>162</sup> where the simulated Raman spectrum is in good agreement with the experimental spectrum. The  $S_0$ - $S_1$  transition of R6G corresponds to an excitation from the highest occupied molecular orbital (HOMO) to the lowest unoccupied molecular orbital (LUMO), where both orbitals are localized in the xanthene chromophore and the nitrogen of the ethylamino side groups. The transition is therefore expected to be sensitive to any perturbation on the xanthene ring. The  $S_0$ - $S_1$  transition is calculated to be at 474 nm in vacuum, and a weaker  $S_0$ - $S_2$  transition is at 416 nm. Notice that the calculated  $S_0$ - $S_1$  transition is  $\sim 60$  nm blue-shifted from the experimental measurement in solution at 530 nm. Only small changes in the simulated absorption spectrum were found by using larger basis sets and different functionals. Previously, we found that the agreement with

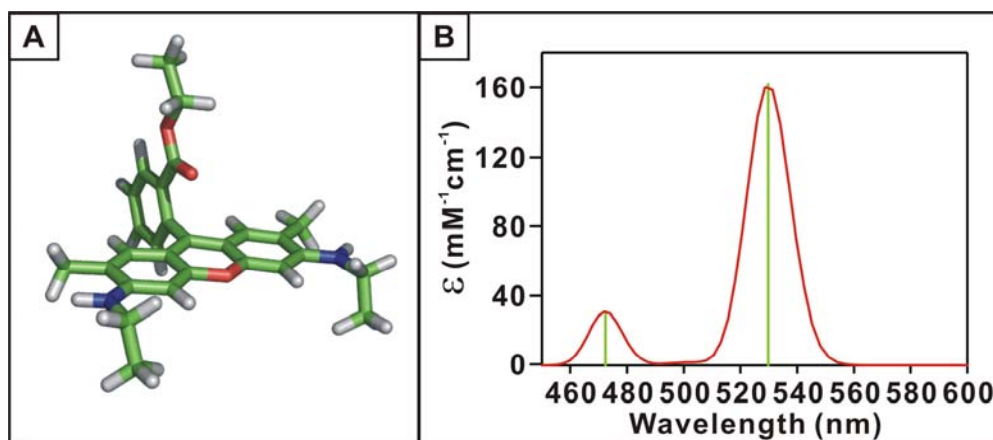


**Figure 2.10** Optimized structure and simulated absorption spectrum of R6G in solution. Solvent effects accounted for by a red-shift of 56 nm.

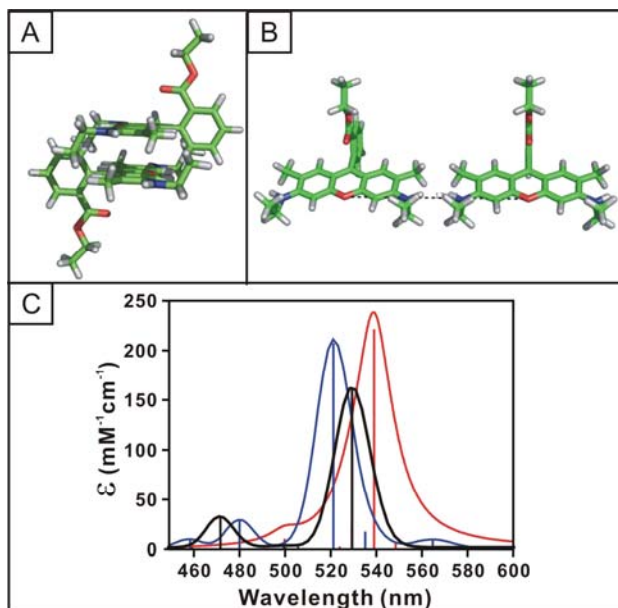


**Figure 2.11** Simulated structure of R6G dimers and absorption spectra. (A) Structure of H-type dimer. (B) Structure of J-type dimer. (C) Calculated absorption spectra of R6G monomer (black line), H-type dimer (blue line) and J-type dimer (red line). Solution effects are accounted for by a red shift of 56 nm.

experiments was significantly improved by considering solvent effects directly in the calculations.<sup>162</sup> For simplicity, the solvent effects in this work are accounted for by applying a constant red shift of 56 nm to the calculated values (simulated spectrum shown in Figure 2.10B). This value is added to all the calculated spectra discussed below.

To examine the exciton splitting in R6G, we calculated the absorption spectra of an anti-parallel H-dimer separated by 3.5 Å and a J-dimer with a center-to-center separation of 13.5 Å (structures and spectra shown in Figure 2.11). For the H-dimer a slight blue shift (less than 10 nm) of the main transition is observed which agrees with the shift direction observed experimentally, but underestimates the shift magnitude. In addition, a small band at 565 nm is found in the simulated dimer absorption spectrum; however, it has very small oscillator strength. In the case of the J-dimer an 8 nm red shift of the main transition is found with a weaker transition around 500 nm. In addition, the main J-dimer transition is stronger than the corresponding H-dimer transition. These results are in very good agreement with the expectation from the simple exciton theory. For both dimers, the calculated exciton splitting is smaller than the experimental observation.<sup>130,150-154</sup> However, the structures for the dimers adopted in the calculation are highly idealized and it is quite likely one would obtain a better agreement with the experiments by optimizing the dimer structures. The calculations support the findings in the concentration-dependent absorption study of R6G adsorbed on an Ag film. Therefore, the formation of dimers provides a very plausible explanation for the LSPR shift experiments, especially considering that R6G tends to form dimers in constrained systems.

As a second explanation of the results in Figure 2.3, we consider the possibility that new transitions, metal molecule charge-transfer transitions, arise when R6G adsorbs onto the metal surface. To examine this possibility we calculated the absorption spectrum of R6G interacting

with an  $\text{Ag}_2$  cluster (structure and spectrum shown in Figure 2.12A). The  $\text{Ag}_2$  is used as a model for the ad-atom adsorption site. Because such a small cluster can not represent the full effect of an Ag surface, we shifted the spectrum in Figure 2.12A by 56 nm. Therefore, the modeling should provide a reasonable description of the CT transitions. The interactions of R6G with the  $\text{Ag}_2$  cluster cause a red shift of the main transition to 544 nm, which is a 14 nm shift compared to that in solution. Two CT transitions red of the main peak are found at 1010 and 617 nm, corresponding to transitions from the HOMO of  $\text{Ag}_2$  to the LUMO and LUMO+1 of R6G, respectively. Since both transitions have small oscillator strength and are more than 100 nm red of the main transition, it is not likely that they are responsible for the LSPR shift feature at  $\sim 595$  nm.

Another possibility is that the interaction between R6G and the surface may cause a complete charge transfer from the metal to R6G since it is a cationic dye. Therefore, we calculated the absorption spectrum of neutral R6G (see Figure 2.12B). The main absorption peak is at 498 nm with a weaker band at around 530 nm. Both bands are blue shifted relative to the cationic R6G absorption with smaller oscillator strength. This makes it unlikely that the formation of the neutral R6G is the cause for the LSPR shift feature at  $\sim 595$  nm.

The last explanation that we considered is that the adsorption of R6G onto the surface causes the angle,  $\Omega$ , between the xanthene plane and the phenyl substituent to change (see Figure 2.13A for definition of  $\Omega$ ). Notice that the optimized structure of R6G (shown in Figure 2.10A) from the calculations has an angle of  $88^\circ$  while in the experimental crystal structure R6G has an angle of  $63^\circ$ .<sup>163</sup> We calculated the absorption spectra of R6G as a function of  $\Omega$  to show how the  $\text{S}_0\text{-S}_1$  transition is sensitive to the perturbation on the xanthene ring. The resulting absorption



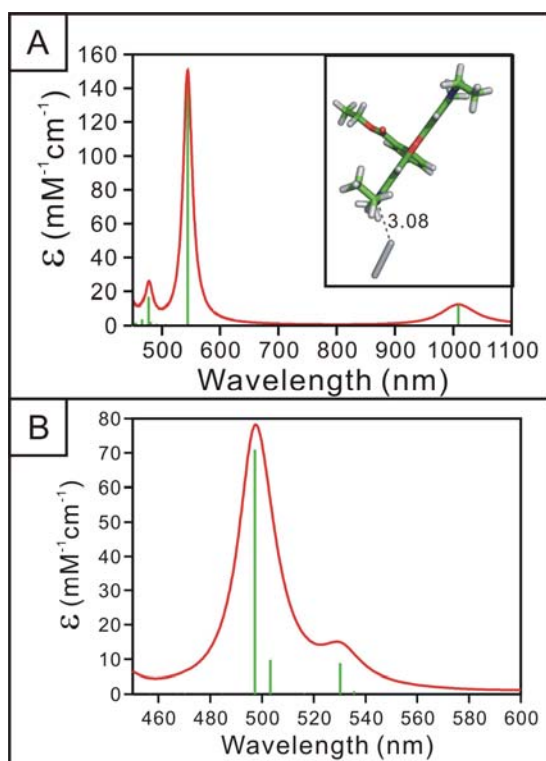


**Figure 2.12** Simulated absorption spectra of R6G with an  $\text{Ag}_2$  cluster and neutral R6G. (A) Calculated absorption of R6G with an  $\text{Ag}_2$  cluster. Inset is the optimized structure of R6G- $\text{Ag}_2$ . The distance between the N atom of R6G and Ag atom is 3.08 Å. (B) Calculated absorption of neutral R6G. Solution effects are accounted for by a red shift of 56 nm.

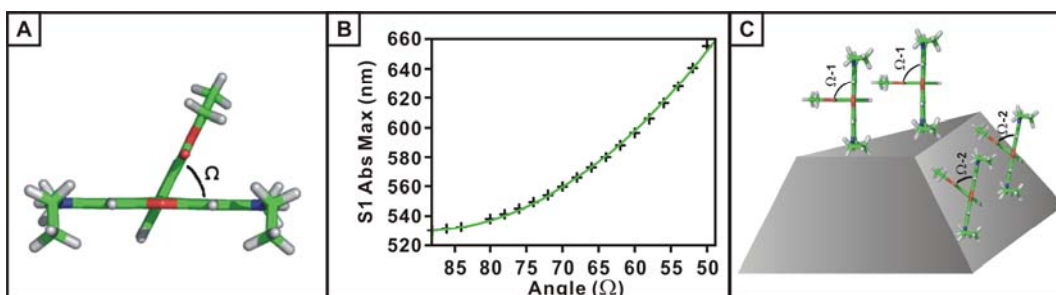


**Figure 2.13** S1 absorption maximum as a function of the angle ( $\Omega$ ) between the xantheneplane and the phenyl substituent. Solvent effects accounted for by a red shift of 56 nm. (A) Side-view of the structure of R6G. (B) Plot of the S1 absorption maximum as a function of the angle ( $\Omega$ ). (C) Schematic illustration of the two possible adsorption sites.  $\Omega-1 = 88^\circ$ ,  $\Omega-2 = 66^\circ$

maximum of the  $S_0$ - $S_1$  transition is plotted (see Figure 2.13B) as a function of  $\Omega$ . When  $\Omega$  decreases, the excitation energy of the  $S_0$ - $S_1$  transition increases, leading to a red shift of the main absorption peak. In order to explain the LSPR shift maximum at  $\sim 595$  nm, an absorption feature around 570 nm is required. Figure 2.13B shows that such an absorption feature can be achieved when  $\Omega$  is decreased by  $20$ - $25^\circ$ . The corresponding  $\Omega$  is then close to the value found for R6G in the crystal structure. The strain caused by decreasing  $\Omega$  to this value amounts to  $\sim 15$ - $17$  Kcal/mol. Furthermore, the strain reduces the oscillator strength of the  $S_0$ - $S_1$  transition. One could speculate that if two distinct absorption sites exist, for example, the top and sides of the NSL-nanoparticle (cartoon shown in Figure 2.11C), one of these sites could then cause  $\Omega$  to twist thereby red shifting the  $S_0$ - $S_1$  transition. However, it requires a significant amount of energy to bend  $\Omega$  by around  $20$ - $25^\circ$ , making it a less likely explanation than the dimer formation.

## 2.4 Conclusions

The coupling between the R6G molecular resonances and the LSPR of Ag nanoparticles has been systematically probed. This is achieved by monitoring the shift in LSPR wavelength of Ag nanoparticles upon R6G binding. The LSPR shift depends on the relative spectral position between the LSPR of the Ag nanoparticles and the molecular resonances of R6G. The LSPR shifts show several complicated features – indeed three local maxima have been observed. In contrast, there are only two features in the R6G solution absorption spectrum. To understand the change in the R6G resonances when it adsorbs to metal surface, absorption spectra of R6G on an Ag surface have been measured at different R6G concentrations. Detailed deconvolution of the spectra indicates the formation of R6G dimers on the surface, even though the R6G

concentration in solution is low enough to avoid R6G aggregate formation in solution. To understand the unusual LSPR shifts, several different kinds of theoretical modeling were considered, including empirical modeling with dielectric constants from a Kramers-Kronig analysis, electrodynamics modeling using Gans theory, and electronic structure calculations using TDDFT. The combined experimental evidence and theoretical modeling show that dimer formation is responsible for the complex spectral coupling between R6G and the nanoparticles.

The extreme sensitivity of the localized surface plasmon resonance wavelength to small environmental changes has been clearly demonstrated in this work. For the first time, changes in the adsorbates' electronic structure due to aggregation have been detected using LSPR spectroscopy. These findings illustrate that the LSPR sensing technique is particularly suitable for studying molecular level information, such as electronic and structural change of the adsorbates. This discovery has potential applications for chemical sensing, studying excited states at metal surfaces, understanding the mechanism of surface-enhanced Raman spectroscopy, and developing novel plasmonic devices.

### **Chapter Three**

#### **Resonance Localized Surface Plasmon Spectroscopy: Low Molecular Weight Substrate**

#### **Binding to Cytochrome P450**

### 3.1 Introduction

Localized surface plasmon resonance (LSPR) nanosensors have been demonstrated as sensitive platforms for the detection of streptavidin,<sup>35</sup> anti-biotin,<sup>138</sup> concanavalin,<sup>56</sup> Alzheimer disease biomarkers<sup>32</sup> and many other biorecognition event.<sup>139</sup> Sensing is accomplished by monitoring the wavelength shift in the LSPR extinction or scattering maximum ( $\lambda_{\text{max}}$ ) induced by the binding of target analytes to the nanoparticle surface. The concentration of target analytes is quantitatively related to the shift in  $\lambda_{\text{max}}$ . In these cases, however, the analytes in earlier studies were optically transparent; and consequently, the observed shift was only weakly dependent on the LSPR  $\lambda_{\text{max}}$ .<sup>32,35,138,164</sup> Since many biomolecules contain visible chromophores, it is important to broaden the scope of LSPR sensing by exploring electronically resonant adsorbates in biosensing events. When resonant molecules are adsorbed on nanoparticles, the induced LSPR shift is found to be strongly dependent on the spectral overlap between the electronic resonance of the adsorbates and the plasmon resonance of the nanoparticles.<sup>113</sup> Specifically, a large red shift occurs when the nanoparticles' LSPR is located at a slightly longer wavelength than the adsorbate's molecular resonance wavelength, i.e., a factor of 3 greater than when the LSPR is distant from the molecular resonance. This resonant LSPR response opens up the possibility of detecting the binding of a low molecular weight analyte to a protein receptor adsorbed on a nanoparticle. Herein, we present a proof-of-concept experiment for the binding of camphor ( $\text{C}_{10}\text{H}_{16}\text{O}$ , molecular weight =  $152.24 \text{ g}\cdot\text{mol}^{-1}$ ) to cytochrome P450cam protein (CYP101). This system was selected because the electronic structure changes that occur when substrate binds have been well characterized.<sup>131,165</sup>

Cytochrome P450s are essential for steroid hormone biosynthesis and are involved in the metabolism of xenobiotics. Many drug molecules, e.g. metyrapone, fluconazole and

cimetidine,<sup>166</sup> inhibit cytochrome P450, thereby leading to a decrease in metabolism which can cause adverse toxicity. The development of an ultrasensitive, label free detection method for binding of the molecules to cytochrome P450s would, therefore, have a significant impact on drug discovery research.<sup>167-169</sup> CYP101 is a specific member of this P450 superfamily catalyzing the stereospecific hydroxylation of camphor as the first step in the utilization of this terpene as a sole source of carbon and energy in the soil organism *Pseudomonas putida*.

## 3.2 Experimental Methods

### 3.2.1 Materials

Silver shot was purchased from Alfa Aesar (#11357 1-3mm diameter, Premion®, 99.9999%). Tungsten vapor deposition boats were acquired from R.D. Mathis (Long Beach, CA). Polystyrene nanospheres with diameters of  $280 \pm 4$  nm,  $390 \text{ nm} \pm 19.5$  nm, were received as a suspension in water (Interfacial Dynamics Corporation, Portland or Duke Scientific, Palo Alto, CA) and were used without further treatment. Fisherbrand No. 2 glass coverslips with 18 mm diameters and the buffer salts ( $\text{KH}_2\text{PO}_4 \cdot 3\text{H}_2\text{O}$  and  $\text{KH}_2\text{PO}_4$ ) were obtained from Fisher Scientific (Pittsburgh, PA). (1*R*)-camphor and 11-mercaptoundecanoic acid (11-MUA) were purchased from Sigma-Aldrich and used as received. For all steps of substrate preparation, water purified with cartridges from Millipore (Marlborough, MA) to a resistivity of  $18.2 \text{ M}\Omega \cdot \text{cm}$  was used. 1-ethyl-3-[3-dimethylaminopropyl]carbodiimide hydrochloride (EDC) was purchased from Pierce (Rockford, IL).

### 3.2.2 Protein expression and purification

Recombinant wild-type P450cam protein was expressed in *Escherichia coli* and purified as reported<sup>1</sup> and stored at  $-80^\circ\text{C}$  at  $\sim 100 \text{ }\mu\text{M}$  concentrations in 50 mM potassium phosphate buffer containing 150mM potassium chloride salt (pH 7.4), 200  $\mu\text{M}$  camphor and 20

mM  $\beta$ -mercaptoethanol. Concentrations of cytochrome P450cam were determined using extinction coefficients  $\epsilon_{391} = 102 \text{ mM}^{-1}\cdot\text{cm}^{-1}$  (camphor-bound) or  $\epsilon_{417} = 115 \text{ mM}^{-1}\cdot\text{cm}^{-1}$  (substrate-free) in aqueous solution. The proteins were made substrate free by using Superdex G-25 columns.

### 3.2.3 Glass Substrate Preparation

Glass substrates were cleaned in piranha solution (1:3 30%  $\text{H}_2\text{O}_2/\text{H}_2\text{SO}_4$ ) for one hour at  $80^\circ\text{C}$ . Samples were cooled to room temperature and were then rinsed profusely with deionized ( $18.2 \text{ M}\Omega\cdot\text{cm}$ ) water. Samples were then sonicated in 5:1:1  $\text{H}_2\text{O}/\text{NH}_4\text{OH}/30\% \text{ H}_2\text{O}_2$  and thoroughly rinsed with water. The samples were stored in deionized ( $18.2 \text{ M}\Omega\cdot\text{cm}$ ) water prior to use.

### 3.2.4 Nanoparticle Preparation

Nanosphere lithography (NSL) was used to create monodisperse, surface-confined Ag nanoparticles. Polystyrene nanospheres ( $\sim 2.2 \mu\text{L}$ ) were drop-coated onto the glass substrates and allowed to dry, forming a monolayer in a close-packed hexagonal formation, which served as a deposition mask. The samples were then transferred to the evaporation chamber. The pressure in the vacuum chamber was maintained below  $1 \times 10^{-5}$  Torr during the evaporation. A silver film was evaporated on the slides. The deposition rate Ag was  $1.0 \sim 1.5 \text{ \AA/s}$ . A Leybold Inficon XTM/2 quartz crystal microbalance (East Syracuse, NY) was used to measure the thickness of the Ag film deposited over the nanosphere mask,  $d_m$ . Following metal deposition, the samples were sonicated for 3-5 minutes in ethanol to remove the polystyrene nanosphere mask. The perpendicular bisector of the nanoparticles was varied by changing the diameter of the nanospheres used. The height of the nanoparticles was varied by depositing varying amounts of



Ag onto the sample. These two parameters were varied to alter the LSPR peak position throughout the visible region of the spectrum.

### 3.2.5 Nanoparticle Solvent Annealing and Functional Immobilization

For each experiment, the sample was stabilized and functionalized in a home built flow cell. Immediately following nanospheres removal, the samples were placed in 1 mM of 11-MUA ethanol solution for 24 ~ 48 h. This time was determined to produce the repeatable and approximately full monolayer coverage of 11-MUA. After incubation, the nanoparticle samples were rinsed thoroughly with neat ethanol and dried by flowing N<sub>2</sub> gas through the sample cell. Samples were then activated using 10mM EDC and then they were incubated in 8 μM cytochrome P450cam for 1 h. After incubation, the nanoparticle samples were rinsed with MQ water and dried by flowing N<sub>2</sub> gas through the sample cell. Finally, the samples were incubated in 200 μM camphor buffer solution for 30 mins. After incubation, the nanoparticle samples were rinsed with MQ water and dried by flowing N<sub>2</sub> gas through the sample cell.

### 3.2.6 Ultraviolet-Visible Spectroscopy

Macroscale UV-vis extinction measurements were collected using an Ocean Optics (Dunedin, FL) SD2000 fiber optically coupled spectrometer with a CCD detector and a Cary 300 Bio UV-vis spectrophotometer. All spectra in this study are macroscopic measurements performed in standard transmission geometry with unpolarized light. The extinction spectra of the same sample acquired from the two spectrometers have been tested to be consistent.

## **3.3 Results and Discussion**

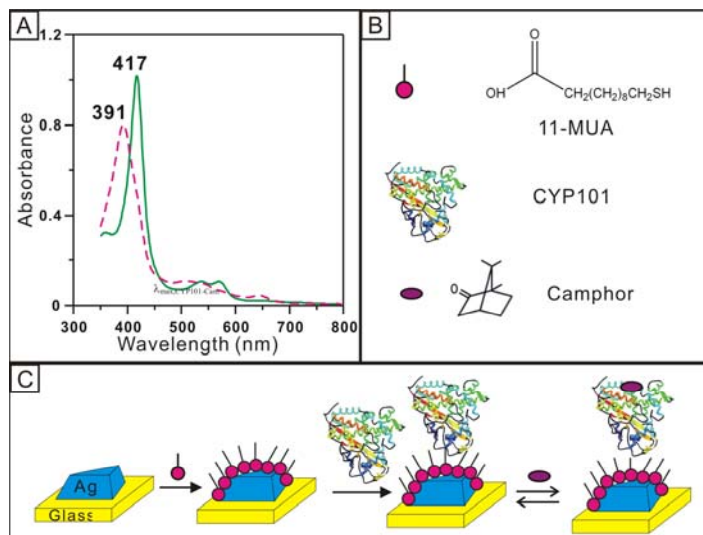
### 3.3.1 UV-Vis Spectra and Experimental Scheme

Figure 3.1A shows the UV-vis absorption spectra of camphor-free (green solid line) and camphor-bound (pink dashed line) oxidized CYP101 in phosphate buffer (pH = 7.4). When camphor binds to CYP101 with the heme iron in its +3 oxidation state, CYP101(Fe<sup>3+</sup>), the Soret absorption band peak of CYP101 blue-shifts by 26 nm from its low spin state at 417 nm (extinction coefficient  $\epsilon$  = 115 mM<sup>-1</sup>cm<sup>-1</sup>) to its high spin state at 391 nm ( $\epsilon$  = 102 mM<sup>-1</sup>cm<sup>-1</sup>). The cause of this peak shift is the displacement of water coordinated with the Fe<sup>3+</sup> in CYP101 by camphor which shifts the spin state of the heme iron from low to high spin.<sup>131,165,170</sup>

Nanosphere lithography (NSL) fabricated Ag nanoparticles were used as the LSPR sensing platform.<sup>32,35,36,138</sup> In order to immobilize Fe<sup>3+</sup>CYP101 onto Ag nanoparticles, a self-assembled monolayer (SAM) of 11-mercaptoundecanoic acid (11-MUA) (Figure 3.1B) was used to modify the nanoparticles. With the aid of 1-Ethyl-3-[3-dimethyl-aminopropyl] carbodiimide hydrochloride, the amine groups on the CYP101(Fe<sup>3+</sup>) were covalently bound to the carboxyl groups on 11-MUA.<sup>35</sup> Then, the samples were exposed to a 200  $\mu$ M camphor solution. Since the dissociation constant  $K_d$  is 0.61  $\mu$ M, this concentration saturates all binding sites in Fe<sup>3+</sup>CYP101.<sup>131,170,171</sup> The experimental procedure is summarized in Figure 3.1C.

### 3.3.2 Representative LSPR Spectra and Wavelength-Dependent LSPR Shift

Each step of the functionalization of the samples was monitored using UV-vis extinction spectroscopy in a N<sub>2</sub> environment. Figures 3.2A and 3.2B show two sets of representative LSPR spectra. In figure 3.2A, after incubation in 11-MUA, the LSPR extinction wavelength,  $\lambda_{\text{max,SAM}}$  was measured to be 636.1 nm. The sample was then incubated in CYP101(Fe<sup>3+</sup>) solution. The LSPR of CYP101(Fe<sup>3+</sup>) modified nanoparticles,  $\lambda_{\text{max,CYP101}}$ , red-shifted by 13.2 nm to 649.3 nm. Next, the sample was exposed to a camphor solution, and the LSPR,  $\lambda_{\text{max,CYP101-Cam}}$ , blue-shifted



**Figure 3.1** (A) UV-vis absorption spectra of CYP101(Fe<sup>3+</sup>) (green solid line) with a Soret band at 417 nm (low spin) and camphor-bound CYP101(Fe<sup>3+</sup>) (pink dashed line) with a Soret band at 391 nm (high spin). (B) Schematic notations of 11-MUA, CYP101 and camphor. (C) Schematic representation of CYP101 protein immobilized Ag nanobiosensor, followed by binding of camphor. The Ag nanoparticles are fabricated using NSL (nanosphere lithography) on a glass substrate.

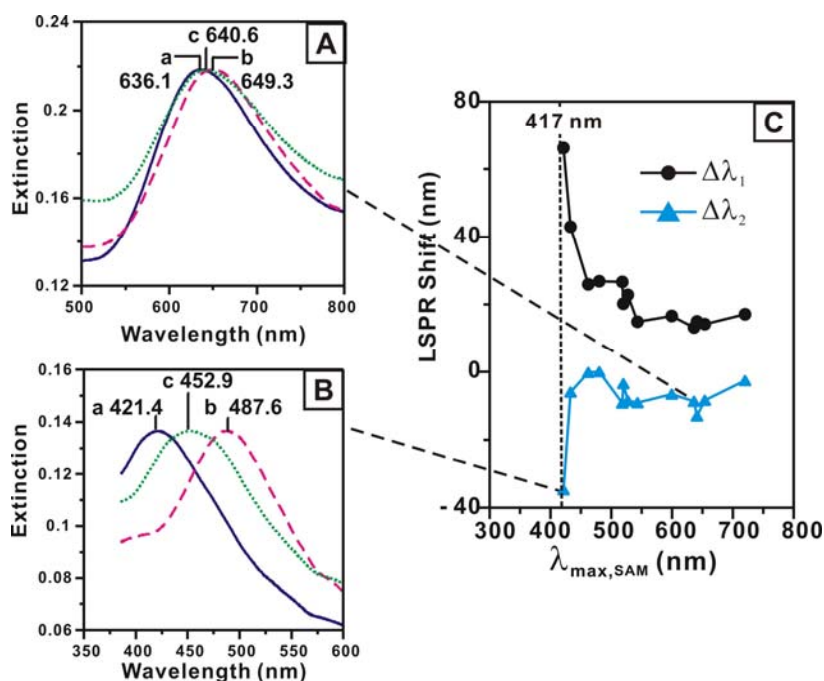


**Figure 3.2** UV-vis extinction spectra of each step in the surface modification of NSL fabricated Ag nanoparticles and the wavelength-dependent LSPR shift plots. All extinction measurements were collected in a N<sub>2</sub> environment. A 200  $\mu$ M camphor buffer solution was used. (A) A series of UV-vis extinction spectra of Ag nanoparticles (a)  $\lambda_{\max, \text{SAM}} = 636.1$  nm, (b)  $\lambda_{\max, \text{CYP101}} = 649.3$  nm, and (c)  $\lambda_{\max, \text{CYP101-Cam}} = 640.1$  nm. (B) A series of UV-vis extinction spectra of Ag nanoparticles (a)  $\lambda_{\max, \text{SAM}} = 421.4$  nm, (b)  $\lambda_{\max, \text{CYP101}} = 487.6$  nm, and (c)  $\lambda_{\max, \text{CYP101-Cam}} = 452.9$  nm. (C) Plots of LSPR shifts versus  $\lambda_{\max, \text{SAM}}$  where  $\Delta\lambda_1 = \lambda_{\max, \text{CYP101}} - \lambda_{\max, \text{SAM}}$  (shift on binding CYP101), and  $\Delta\lambda_2 = \lambda_{\max, \text{CYP101-Cam}} - \lambda_{\max, \text{CYP101}}$  (shift on binding camphor). The vertical black dotted line denotes the molecular resonance of Fe<sup>3+</sup> CYP101 at 417 nm.

by 8.7 nm to 640.6 nm. A parallel experiment was conducted using the nanoparticles with  $\lambda_{\max, \text{SAM}}$  close to but slightly greater than the molecular resonance of the CYP101( $\text{Fe}^{3+}$ ) ( $\lambda_{\max, \text{SAM}} = 420$  nm; the molecular resonance of CYP101( $\text{Fe}^{3+}$ ) is at 417 nm). In this case, dramatic wavelength shifts were observed (shown in Figure 2B). Specifically, the LSPR red-shifted by 66.2 nm to 487.6 nm after incubation in CYP101( $\text{Fe}^{3+}$ ), and then blue-shifted by 34.7 nm to 452.9 nm upon the substrate binding of camphor.

Based on the aforementioned results, it is clear that the LSPR shifts vary strongly with  $\lambda_{\max, \text{SAM}}$ . To study this, experiments were conducted to measure the LSPR response of nanoparticles while varying the initial LSPR wavelength. The LSPR peaks were controlled by changing the nanosphere diameter and the deposited metal film thickness.<sup>39</sup> In general, an increase in nanosphere diameter and/or a decrease in metal film thickness result in a red shift in LSPR. Figure 3.2C shows the wavelength-dependent plots of  $\Delta\lambda_1$  (black line with dots), and  $\Delta\lambda_2$  (blue line with triangles) versus  $\lambda_{\max, \text{SAM}}$ . The values of  $\Delta\lambda$  were calculated from the following equations:

$$\Delta\lambda_1 = \lambda_{\max, \text{CYP101}} - \lambda_{\max, \text{SAM}} \quad (3.1)$$

$$\Delta\lambda_2 = \lambda_{\max, \text{CYP101-Cam}} - \lambda_{\max, \text{CYP101}} \quad (3.2)$$

Here, a positive wavelength shift indicates a red-shift and a negative (-) wavelength shift indicates a blue-shift. When the  $\lambda_{\max, \text{SAM}}$  is located at wavelengths longer than the CYP101( $\text{Fe}^{3+}$ ) resonance ( $> 460$  nm), an average shift of  $\sim 19$  nm is observed for  $\Delta\lambda_1$ , and  $\sim -6$  nm for  $\Delta\lambda_2$ . However, when  $\lambda_{\max, \text{SAM}}$  is at a slightly longer wavelength than the CYP101( $\text{Fe}^{3+}$ ) resonance (the results shown in figure 3.2B), amplified shifts are observed for  $\Delta\lambda_1$  (amplified magnitude  $\sim 340\%$ ) and  $\Delta\lambda_2$  ( $\sim 550\%$ ).

These results are remarkable due to both the magnitude of the shifts and the shift direction. In previously reported studies of LSPR response to the binding of non-resonant proteins to the nanoparticles, we always observed a red-shift in LSPR wavelength.<sup>32,35</sup> Similarly, we observe that the LSPR red-shifts from  $\lambda_{\max, \text{SAM}}$  upon binding of either CYP101( $\text{Fe}^{3+}$ ), or camphor bound CYP101( $\text{Fe}^{3+}$ ). However, the exposure of CYP101( $\text{Fe}^{3+}$ ) modified nanoparticles to camphor results in a blue-shift (i.e.,  $\Delta\lambda_2$ ). If camphor were a noninteracting adsorbate added to CYP101( $\text{Fe}^{3+}$ ), the local refractive index around the nanoparticles would increase, resulting in a red shift in the LSPR peaks. However, blue shifts are found for a variety of nanoparticles with different  $\lambda_{\max, \text{SAM}}$  (Figure 3.2C). This shows that substrate binding to CYP101( $\text{Fe}^{3+}$ ) involves a change in the electronic state of the protein, and since this state is at a shorter wavelength than in CYP101( $\text{Fe}^{3+}$ ), the  $\lambda_{\max, \text{CYP101-Cam}}$  is blue-shifted relative to  $\lambda_{\max, \text{CYP101}}$ .

### 3.3.3 Control experiments

To further verify the blue shift in the LSPR of CYP101-functionalized Ag nanoparticles is not from surface displacement of CYP101 or MUA upon exposure to camphor analyte, two control experiments were performed.

#### 3.3.3.1. Camphor-MUA Adsorption

A control experiment was performed on MUA-functionalized Ag nanoparticles with camphor solution. Ag nanoparticles were fabricated with NSL (nanosphere diameter = 390 nm, metal thickness = 60 nm) and incubated in 1 mM MUA for 48 hrs. The sample was thoroughly rinsed with ethanol. Then, the extinction spectrum of MUA-functionalized Ag nanoparticles was collected in  $\text{N}_2$  and shown in Figure 3.3 (black solid line). The extinction maximum was found to be 565.5 nm. The nanoparticles were then incubated in 200  $\mu\text{M}$  camphor buffer solution for 30

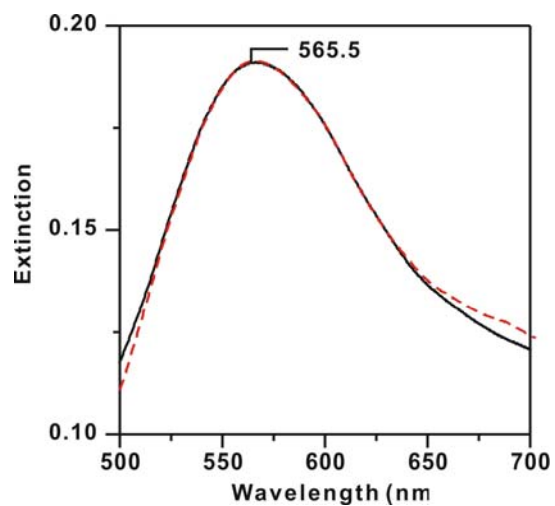


**Figure 3.3** Camphor adsorption to MUA

functionalized Ag nanoparticles. Black solid line is the extinction spectrum of MUA-functionalized Ag nanoparticles in  $N_2$  before exposure to camphor; while red dashed line is after exposure to camphor. All the spectra were measured in  $N_2$ .

mins and rinsed with MQ water. After the sample was dried with  $N_2$ , an extinction spectrum was measured and shown in Figure 3.3 (red dashed line). The extinction maximum stayed at the same wavelength at 565.5 nm. The constant LSPR position after introducing camphor to MUA-functionalized Ag nanoparticles indicates that camphor is unlikely to replace or adsorb to MUA.

### 3.3.3.2. Camphor-bound CYP101 Adsorption to MUA

Two sets of experiments have been performed following two different protocols. Figure 3.4A and 3.4B illustrate the scheme of protocol A and B. Protocol A is a 2-step experimental procedure of CYP101 binding to MUA, then camphor binding to CYP101. Protocol B is a 1-step procedure of camphor-bound CYP101 binding to MUA. Figure 3.4C shows the extinction spectra at each step following protocol A. The initial LSPR of the MUA-functionalized Ag nanoparticles is located at 527.2 nm (solid black line) in  $N_2$ . After incubation in camphor-free CYP101, the LSPR shifts to 550.0 nm (blue dotted line). Lastly, after the sample was incubated in camphor solution, the LSPR blue-shifts by 8.5 nm to 541.5 nm (red dashed line) in  $N_2$ . This is a 14.3 nm red-shift compared to the initial LSPR. Figure 3.4D shows the extinction spectra at each step following protocol B. The initial LSPR of MUA-functionalized Ag nanoparticles is at 530.5 nm (black solid line) in  $N_2$ . After incubation in camphor-bound CYP101, the LSPR of the nanoparticles shift to 545.1 nm (red dashed line) in  $N_2$ . That is a 14.6 nm red-shift. In conclusion, adding camphor separately in the 2-step protocol A yields the same results as immobilizing the camphor-bound CYP101 onto the surface in the 1-step protocol B.

The two control experiments have demonstrated that adding camphor causes no displacement or dissociation of MUA or CYP101 on the surface. Therefore, the blue-shift in the LSPR resulting from camphor binding to CYP101 is due to the spectral change in the CYP101



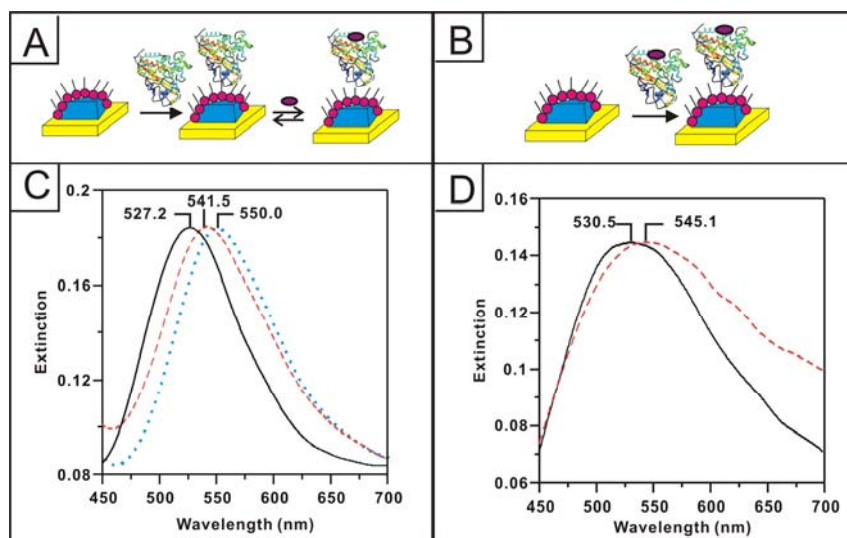


**Figure 3.4** The LSPR shifts experiments following two different protocols. (A) Schematic illustration of protocol A. (B) Schematic illustration of protocol B. (C) Extinction spectra of functionalized Ag nanoparticles at each step following protocol A. Black solid line is the LSPR of MUA-Ag nanoparticles. Blue dotted line is the LSPR of the sample after exposure to camphor-free CYP101. Red dashed line is the LSPR of the sample after exposure to camphor. (D) Extinction spectra of functionalized Ag nanoparticles at each step following protocol B. Black solid line is the LSPR of MUA-Ag nanoparticles. Red dashed line is the LSPR of the sample after exposure to camphor-bound CYP101. All the spectra were measured in  $N_2$ .

protein chromophore.

### 3.4 Conclusions

The tunability of the localized surface plasmon resonance has been successfully explored as a signal transduction mechanism for the detection of substrate binding. Indeed, this is the first demonstration that the binding of a small molecule (camphor) to a protein (CYP101( $\text{Fe}^{3+}$ )) can generate a LSPR spectral change. Amplified spectral response to substrate binding is achieved when the LSPR of the silver nanosensor is optimized to be close to the molecular resonance of the protein. This study demonstrates that strong coupling between the molecular resonance and the intrinsic LSPR of the nanoparticles results in an amplified LSPR shift that is modulated by substrate binding, providing further insight into possible uses of plasmon resonance spectroscopy. Application of this finding to the screening for inhibitors of human cytochrome P450s is under investigation based on these results. It is foreseeable that this discovery will provide guidance to the design and optimization of refractive index based sensing for biological targets with resonant chromophores.

## **Chapter Four**

### **Resonance Localized Surface Plasmon Spectroscopy: Sensing Substrate and Inhibitor**

#### **Binding to Cytochrome P450**

## 4.1 Introduction

The interaction between the metal nanoparticles and optical chromophores has been widely used in a variety of applications, such as in molecular plasmonic devices,<sup>115,160,172</sup> dye sensitized solar cells,<sup>105-107</sup> and biosensing and imaging applications.<sup>53,103,141,173,174</sup> The interaction between chromophore and metal nanoparticles (or thin films) is critical to the understanding of surface-enhanced spectroscopies, and improving the performance of chromophore/metal based devices. Recent progress has shown that localized surface plasmon resonance (LSPR) spectroscopy of metallic nanoparticles is a powerful tool to investigate the coupling between the chromophore's molecular resonances and the plasmon resonance modes of the nanoparticles.<sup>73,103,113,115</sup>

Localized surface plasmon resonance involves the collective oscillation of the conduction electrons in metallic nanostructures excited by electromagnetic radiation.<sup>2,4,7,8</sup> The LSPR wavelength of a given nanostructure is extremely sensitive to the local dielectric environment, so a shift in this wavelength upon analyte binding can be used in refractive index sensors.<sup>33,35,175,176</sup> Indeed, during the past few years, many LSPR sensors have been developed for chemical/biological targets.<sup>26,32,35,56,138,177</sup> Recently, LSPR sensors have been exploited for analytes with molecular resonances in the visible wavelength region.<sup>73,103,113</sup>

Based on previous experimental and theoretical studies, strong coupling of molecular chromophore and plasmon resonances is expected when molecules are adsorbed on metal nanostructures.<sup>73,103,112,114,115</sup> When chromophores adsorb on nanoparticles in monolayer concentrations, extinction from plasmon resonance excitation in the nanoparticle greatly exceeds that originating with the chromophore, although the interaction between the chromophore and plasmon is observable through the LSPR wavelength shift. In addition, the LSPR wavelength

shift induced by resonant adsorbates is strongly dependent on plasmon wavelength. As a result, the LSPR shift is sensitive to small changes in the resonances of the chromophore that are induced by binding of an additional analyte,<sup>103</sup> by chromophore dimerization<sup>73</sup> etc. In particular, recent studies demonstrate that LSPR wavelength shifts can be used to detect the spectral changes caused by the electronic structure changes around the heme center in cytochrome P450 proteins due to low molecular weight substrate binding.<sup>103</sup>

Cytochrome P450s are ubiquitous heme iron monooxygenases which activate dioxygen for insertion into an unactivated C-H bond and play important roles in human drug metabolism and hormonal biosynthesis.<sup>166</sup> Cytochrome P450s have interesting spectroscopic properties due to the unique molecular structure around the heme active site. The low spin six-coordinate P450 resting state has cysteine and water as axial ligands. On binding a substrate such as camphor, the water ligand is displaced and the low spin is converted to high spin P450. On the other hand, on binding, N-donor or O-donor inhibitors, the water ligation is replaced by an N-donor or O-donor atom and the resting ferric P450 remains low spin.<sup>170,171,178,179</sup> The spin state and the ligation around the iron center in P450 affect its spectroscopic properties.<sup>180,181</sup>

These spectroscopic properties of P450 have been well characterized. The optical spectrum of oxidized CYP101 (a member of the P450 super family isolated from *Pseudomonas Putida*) is that of a low-spin ferric hemeprotein with Soret maximum at 417 nm ( $\epsilon = 115,000 \text{ M}^{-1} \text{ cm}^{-1}$ ),  $\beta$ -Q band at 535 nm ( $\epsilon = 10,600 \text{ M}^{-1} \text{ cm}^{-1}$ ) and a more intense  $\alpha$ -Q band at 570 nm ( $\epsilon = 11,100 \text{ M}^{-1} \text{ cm}^{-1}$ ).<sup>31</sup> Upon addition of substrate, which can displace the coordinated water associated with heme-iron, the spin state of heme-iron changes from low-spin to high spin as monitored by the shift in the Soret band from 417 to 390 nm. There is a decrease in the intensity of the  $\alpha$ -Q band at 570 nm relative to  $\beta$ -Q band at 535 nm and the appearance of a charge

transfer band at 645 nm. The addition of ligands with nitrogen or oxygen donor atoms causes the Soret band to red shift. In particular, addition of imidazole red shifts the Soret band to 425 nm because imidazole is a  $\pi$ -donor to ferric porphyrins, donating electrons to the hole in the  $d_{xz}$ ,  $d_{yz}$  orbitals of the iron in the ferric state. The imidazole bound CYP101 has the Soret peak at 425 nm and the  $\alpha$ -Q band at 578 nm and the  $\beta$ -Q band at 541 nm.<sup>170,178</sup> The  $\beta$ -Q is more intense than the  $\alpha$ -Q band and therefore the binding of substrate (such as camphor) and inhibitor (such as imidazole) to CYP101 can be spectrally distinguished.<sup>30</sup>

In this work, we present the development of a LSPR sensor to detect substrate/inhibitor binding to cytochromes P450 and include a detailed study of the coupling between the Soret and Q bands of CYP101 to the LSPR wavelength of Ag nanoparticles and a comparison of the effect of substrate and inhibitor molecule binding to the immobilized CYP101.

## 4.2 Experimental Methods

### 4.2.1 Materials

Silver shot was purchased from Alfa Aesar (#11357 1-3 mm diameter, Premion®, 99.9999%). Tungsten vapor deposition boats were acquired from R.D. Mathis (Long Beach, CA). Polystyrene nanospheres with diameters of  $280 \pm 4$  nm,  $390 \text{ nm} \pm 19.5$  nm, were received as a suspension in water (Interfacial Dynamics Corporation, Portland or Duke Scientific, Palo Alto, CA) and were used without further treatment. Fisherbrand No. 2 glass coverslips with 18 mm diameters and the buffer salts ( $\text{KH}_2\text{PO}_4 \cdot 3\text{H}_2\text{O}$  and  $\text{KH}_2\text{PO}_4$ ) were obtained from Fisher Scientific (Pittsburgh, PA). (1R)-camphor, imidazole and 11-mercaptoundecanoic acid (11-MUA) were purchased from Sigma-Aldrich and used as received. For all steps of substrate preparation, water purified with cartridges from Millipore (Marlborough, MA) to a resistivity of  $18.2 \text{ M}\Omega \cdot \text{cm}^{-1}$  was

used. 1-ethyl-3-[3-dimethylaminopropyl]carbodiimide hydrochloride (EDC) was purchased from Pierce (Rockford, IL).

#### 4.2.2 Protein Expression and Purification

Recombinant wild-type P450cam protein was expressed in *Escherichia coli* and purified as reported<sup>182,183</sup> and stored at  $-80^{\circ}\text{C}$  at  $\sim 100\ \mu\text{M}$  concentration in 50 mM potassium phosphate buffer containing 150 mM potassium chloride salt (pH 7.4), 200  $\mu\text{M}$  camphor and 20 mM  $\beta$ -mercaptoethanol. Concentrations of CYP101 were determined using extinction coefficients  $\epsilon_{391} = 102\ \text{mM}^{-1}\cdot\text{cm}^{-1}$  (camphor-bound) or  $\epsilon_{417} = 115\ \text{mM}^{-1}\cdot\text{cm}^{-1}$  (substrate-free) in aqueous solution. The proteins were made substrate-free by passage through Superdex G-25 column.

#### 4.2.3 Glass Substrate Preparation

Glass substrates were cleaned in piranha solution (1:3 30%  $\text{H}_2\text{O}_2/\text{H}_2\text{SO}_4$ ) for one hour at  $80^{\circ}\text{C}$ . (*Warning: Piranha reacts violently with organic compounds and should be handled with caution.*) Samples were cooled to room temperature and were then rinsed profusely with deionized ( $18.2\ \text{M}\Omega\cdot\text{cm}$ ) water. Samples were then sonicated in 5:1:1  $\text{H}_2\text{O}/\text{NH}_4\text{OH}/30\%\ \text{H}_2\text{O}_2$  and thoroughly rinsed with water. The samples were stored in deionized ( $18.2\ \text{M}\Omega\cdot\text{cm}$ ) water prior to use.

#### 4.2.4 Nanoparticle Preparation

Nanosphere lithography (NSL)<sup>184</sup> was used to create monodisperse, surface-confined Ag nanoparticles. Polystyrene nanospheres ( $\sim 2.2\ \mu\text{L}$ ) were drop-coated onto the glass substrates and allowed to dry, forming a monolayer in a close-packed hexagonal formation, which served as a deposition mask. The samples were then transferred to the evaporation chamber. The pressure in the vacuum chamber was maintained below  $1 \times 10^{-5}$  Torr during the evaporation and a silver film was evaporated onto the slides. The deposition rate Ag was  $1.0 \sim 1.5\ \text{\AA}/\text{s}$ . A Leybold Inficon

XTM/2 quartz crystal microbalance (East Syracuse, NY) was used to measure the thickness of the Ag film deposited over the nanosphere mask,  $d_m$ . Following metal deposition, the samples were sonicated for 3-5 minutes in ethanol to remove the polystyrene nanosphere mask. The perpendicular bisector of the nanoparticles was varied by changing the diameter of the nanospheres used. The height of the nanoparticles was varied by depositing varying amounts of Ag onto the sample. These two parameters were varied to alter the LSPR peak position throughout the visible region of the spectrum as previously described.<sup>184</sup>

#### 4.2.5 Nanoparticle Solvent Annealing and Functional Immobilization

For each experiment, the sample was stabilized and functionalized in a home built flow cell. Immediately following nanospheres removal, the samples were placed in 1 mM of 11-MUA ethanol solution for 24 ~ 48 h. This time was determined to produce the repeatable and approximately full monolayer coverage of 11-MUA. After incubation, the nanoparticle samples were rinsed thoroughly with neat ethanol and dried by flowing N<sub>2</sub> gas through the sample cell. Samples were then activated using 10mM EDC and then they were incubated in 8  $\mu$ M CYP101 for 1 h. After incubation, the nanoparticle samples were rinsed with deionized (18.2 M $\Omega$ ·cm) water and dried by flowing N<sub>2</sub> gas through the sample cell. Finally, the samples were incubated in 200  $\mu$ M camphor buffer solution or 1 mM imidazole buffer solution for 30 mins. After incubation, the nanoparticle samples were rinsed with deionized (18.2 M $\Omega$ ·cm) water and dried by flowing N<sub>2</sub> gas through the sample cell.

#### 4.2.6 Ultraviolet-Visible Spectroscopy

Macroscopic UV-vis extinction measurements were collected using an Ocean Optics (Dunedin, FL) SD2000 fiber optically coupled spectrometer with a CCD detector and a Cary 300 Bio UV-vis spectrophotometer. All spectra in this study are macroscopic measurements



performed in standard transmission geometry with unpolarized light. The extinction spectra of the same sample acquired from the two spectrometers were calibrated. .

## 4.3 Results and Discussion

### 4.3.1 Coupling between P450 resonances and LSPR

The CYP101 UV-vis spectrum is shown in Figure 4.1. The substrate free CYP101 has a Soret band at 417 nm with extinction coefficient  $\epsilon = 115 \text{ mM}\cdot\text{cm}^{-1}$ , a less intense  $\alpha$ -Q band at 569 nm with  $\epsilon = 11.1 \text{ mM}\cdot\text{cm}^{-1}$  and  $\beta$ -Q band at 536 nm with  $\epsilon = 10.6 \text{ mM}\cdot\text{cm}^{-1}$ . To study the coupling of P450 resonances with plasmon resonance of the nanoparticles, nanoparticles with LSPR through 400 ~ 700 nm were fabricated by nanosphere lithography (NSL) by varying the nanosphere diameter and deposited metal thickness.<sup>32,35,36,138</sup> The nanoparticles were then functionalized with a self-assembled monolayer (SAM) of 11-mercaptoundecanoic acid (11-MUA). With the aid of 1-Ethyl-3-[3-dimethyl-aminopropyl] carbodiimide hydrochloride, the amine functional groups on the surface exposed arginine/lysine residues in cytochrome P450cam were covalently bound to the carboxyl terminated groups on 11-MUA.<sup>35</sup> The LSPR of the samples during each experimental step was monitored using UV-vis extinction spectroscopy in a  $\text{N}_2$  environment.

Figures 4.2A-D shows the representative spectra of MUA-functionalized nanoparticles and after CYP101 adsorption. Adsorption of CYP101 causes a red-shift in the LSPR of the nanoparticles. Previous work has demonstrated that the LSPR response of nanoparticles to resonant adsorbates is wavelength-dependent<sup>73,103,113</sup> Hence, a series of nanoparticles with different LSPR were fabricated with NSL and their response to binding CYP101 was explored.

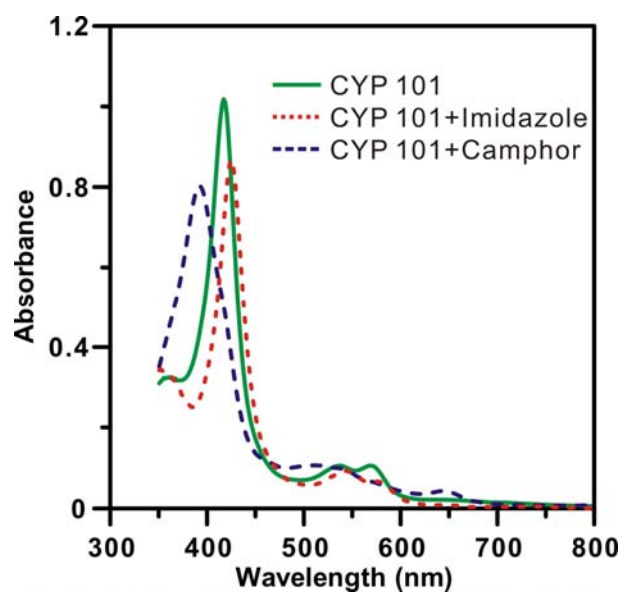


**Figure 4.1** UV-vis absorption spectrum of CYP101 (green solid line), imidazole-bound CYP101 (red dotted line) and camphor-bound CYP101 (blue dashed line).

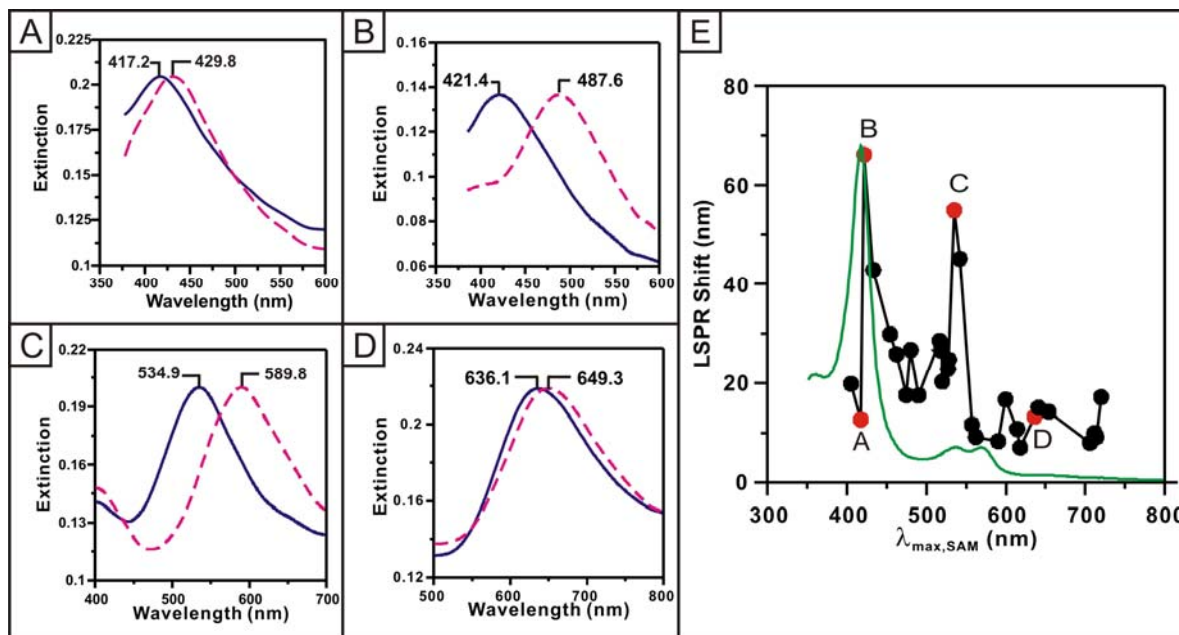


**Figure 4.2** Influence of CYP101 on the LSPR shift of 11-MUA SAM functionalized Ag nanoparticles and representative LSPR spectra. (A-D) LSPR spectra of Ag nanoparticles (associated with points A-D in Figure E) before (black line) and after CYP101 binding (red dotted line). Labeled are the LSPR peak positions of the spectra. (E) Wavelength-dependent LSPR shift induced by CYP101 vs. the LSPR wavelength of 11-MUA SAM functionalized Ag nanoparticles. Solid black line with filled dots is a plot of the LSPR shift (nm) vs. LSPR position of 11-MUA Ag nanoparticles. The green solid line is the absorption spectrum of the CYP101 (arbitrary scaling).

The LSPR shift induced by CYP101 versus LSPR of MUA-functionalized nanoparticles ( $\lambda_{\max, \text{SAM}}$ ) is plotted in Figure 4.2E. When  $\lambda_{\max, \text{SAM}}$  is displaced from the heme CYP101 resonance wavelengths ( $> 590$  nm), a average LSPR shift of  $\sim 11$  nm is observed when CYP101 binds to the nanoparticles. When  $\lambda_{\max, \text{SAM}}$  overlaps with the Soret band of CYP101 at 417 nm, a small LSPR shift of 12.6 nm was observed (spectra shown in Figure 4.2A), which is consistent with the previous studies<sup>73,103,113</sup>. When  $\lambda_{\max, \text{SAM}}$  is slightly to the red of the Soret band, an amplified LSPR shift as large as 66 nm was obtained (spectra shown in Figure 4.2B). The LSPR shift is amplified by 6 times compared to the average LSPR shift at off resonance wavelength. When  $\lambda_{\max, \text{SAM}}$  is shifted to the red of the Soret band, the LSPR shift gradually decreases to  $\sim 20$  nm.

An interesting phenomenon was observed that when  $\lambda_{\max, \text{SAM}}$  is close to the  $\beta$ -Q band of CYP101, the LSPR shift increases dramatically to 55 nm (spectra shown in Figure 4.2C). This behavior indicates that there is strong coupling between the  $\beta$ -Q band and LSPR excitation. Note that although the absorption coefficient of the  $\beta$ -Q band is 10 times smaller than that of the Soret band, the magnitude of the shift from the coupling between the  $\beta$ -Q band and LSPR is comparable to the shift induced by Soret band coupling. This is partly due to the wavelength dependence of the LSPR field enhancement, which even for nonresonant adsorbates leads to a linear increase in wavelength shift with plasmon resonance wavelength. For example, when a monolayer of benzenethiol molecules adsorb on Ag nanoparticles with different plasmon resonance wavelength, it leads to a  $\sim 35$  nm shift when the nanoparticles' LSPR is at 475 nm and a  $\sim 50$  nm LSPR shift at 725 nm.<sup>73</sup> However, when  $\lambda_{\max, \text{SAM}}$  is further red-shifted to the  $\alpha$ -Q band of CYP101, the LSPR shift is  $\sim 10$  nm, close to the average LSPR shift at off-resonance wavelengths. This behavior suggests that the  $\alpha$ -Q band is weaker relative to  $\beta$ -Q when CYP101

is adsorbed on the surface than in solution. The ratio of  $\alpha$ -Q/ $\beta$ -Q intensities is known to vary from one protein to another due to strong sensitivity of this ratio (which is determined by vibronic interactions) to small variations in the heme group excited state properties.<sup>185,186</sup>

#### 4.3.2 P450 LSPR Sensor Response to Low Molecular Weight Substrate and Inhibitor

The cytochrome P450 CYP3 enzyme family plays central role in drug metabolism. In particular, CYP3A4 is responsible for the metabolism of more than 50% of currently marketed drugs and is considered central focus of clinically manifested drug-drug interactions.<sup>168</sup> The binding of inhibitory drugs such as the antifungal drugs fluconazole, itraconazole, micafungin, miconazole, and voriconazole to cytochrome P450s in humans can dramatically modulate the activity of other therapeutics. The development of an ultrasensitive, label free detection method such as LSPR for detection of binding of the drug molecules to cytochrome P450s could have a significant impact on drug discovery research.<sup>166,187</sup>

Previous studies have shown that LSPR is sensitive to the electronic structure change in the adsorbed species.<sup>73,103</sup> When different drug molecules interact with P450 proteins, they induce a change in the absorption spectrum of P450. The wavelength of the Soret and Q bands of cytochrome P450s are determined by the ligand coordination of heme-iron. Figure 4.1 shows the UV-vis spectra of substrate-free CYP101 (green solid line), camphor-bound CYP101 (blue dashed line) and imidazole-bound CYP101 (red dotted line). From Figure 4.1, when the substrate molecule camphor binds to CYP101, it replaces the coordinated water and shifts the spin state of heme-iron to high spin. This binding induces the Soret band to shift to from 417 nm to 391 nm. When an inhibitor molecule with N-donor atoms such as imidazole (MW = 64.08 g/mol), binds to CYP101, there is electron donation from imidazole to heme-iron which induces a red shift in the Soret band from 417 nm to 425 nm.<sup>170,178,180,181,188</sup> The LSPR wavelength is

extremely sensitive to the electronic resonances of the adsorbates; therefore, one should be able to detect the above binding events by fabrication of LSPR sensors at appropriate wavelengths.

The LSPR sensing scheme is illustrated in Figure 4.3A. After P450 is immobilized on the nanoparticle surface, camphor/imidazole is further exposed to the protein. Figure 4.3C-D shows the spectra before and after camphor or imidazole binds to CYP101, respectively. When camphor binds to CYP101, it induces a blue shift in the LSPR; while when imidazole binds to CYP101, it induces a red shift in the LSPR. The blue/red LSPR shift response is consistent with the blue/red electronic resonance shifts induced by the binding of camphor/imidazole.

Since the LSPR response to resonant analyte is wavelength-dependent, samples with different LSPR wavelengths were tested. The LSPR response of the CYP101 receptor to camphor (blue squares) and imidazole (red dots) versus  $\lambda_{\text{max,SAM}}$  is summarized in Figure 4.3B. At wavelengths away from the Soret band resonance ( $\lambda_{\text{max,SAM}} > 460 \text{ nm}$ ), camphor induces an average blue shift of  $\sim 6 \text{ nm}$ . However when  $\lambda_{\text{max,SAM}}$  is slightly red of the P450 resonance, a blue shift as large as  $34 \text{ nm}$  (a factor of 5 amplification over the nonresonant result) is observed. As for imidazole, away from the Soret band resonance ( $\lambda_{\text{max,SAM}} > 460 \text{ nm}$ ), an average red shift of  $4.7 \text{ nm}$  is induced. However when  $\lambda_{\text{max,SAM}}$  is close to the P450 optical resonance, a 3X amplified LSPR shift of  $14.5 \text{ nm}$  is observed. Note that no significant shift on binding camphor or imidazole is observed at the Q-band wavelengths. This is consistent with the small wavelength changes seen in Fig. 1 for the Q-bands associated with camphor or imidazole binding.

The amplitude of the LSPR shift amplification is larger for camphor binding (5X) than for imidazole binding (3X). This can be described by analyzing the coupling of molecular

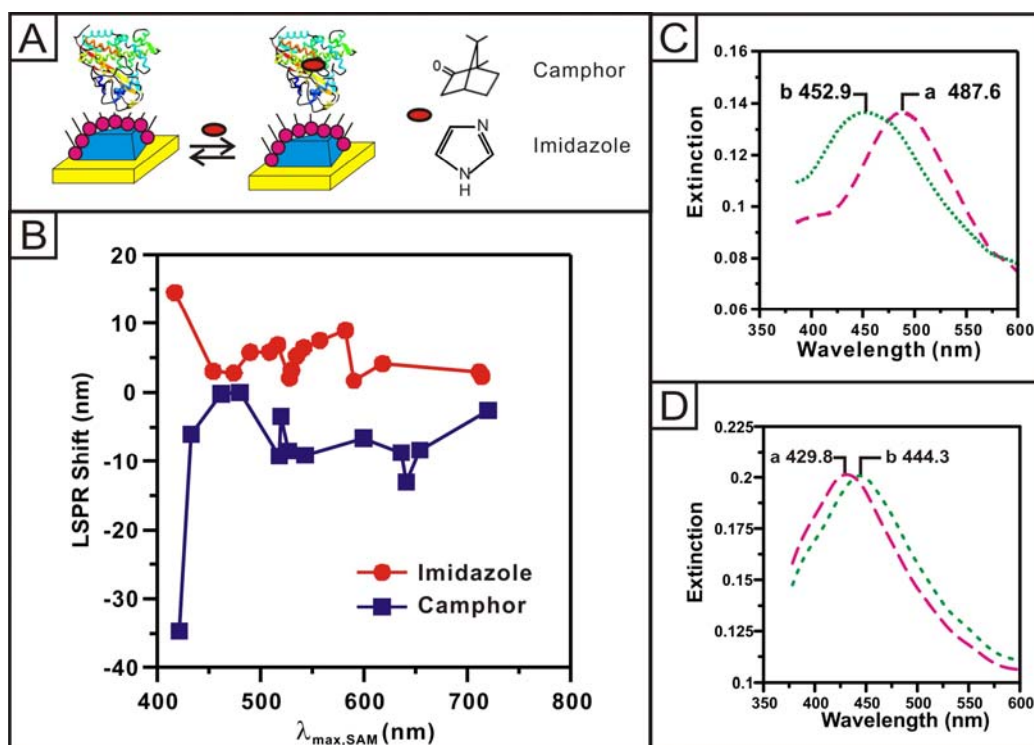


**Figure 4.3** (A) Schematic illustration of small molecule binding to CYP101 receptors on 11-MUA functionalized Ag nanoparticles. Inset shows the molecular structure of camphor and imidazole. (B) The wavelength-dependent LSPR shift induced by imidazole (red line with red dots) and camphor (blue line with squares). (C) Representative LSPR spectra of nanoparticles with CYP101 before (a, pink dashed line) and after (b, green dotted line) camphor binding. (D) Representative LSPR spectra of nanoparticles with CYP101 before (a, pink dashed line) and after (b, green dotted line) imidazole binding.

resonances with LSPR. When camphor binds to CYP101, the Soret band is blue-shifted by 27 nm (from 417 to 390 nm). Nanoparticles with LSPR wavelengths slightly red of the CYP101 resonance are strongly coupled to the Soret band of substrate free CYP101 where a large LSPR shift is expected upon protein binding to the nanoparticle. However, the same nanoparticles (with the absorption slightly red of the CYP101 417 nm resonance) do not couple strongly to camphor-bound CYP101 resonance at 390 nm where a relatively small LSPR shift is expected on binding camphor bound protein to the nanoparticle. Therefore, the net LSPR shift induced by camphor-bound CYP101 is much smaller than the LSPR shift caused by camphor-free CYP101. Thus, a large blue shift in the LSPR is observed at the CYP101 resonance wavelength when camphor binds to CYP101.

When imidazole binds to CYP101 there is an 8 nm red shift (from 417 to 425 nm) in its Soret band. The magnitude of the shift is much smaller than that for camphor, which means the electronic resonances of CYP101 and imidazole-bound CYP101 are closer. When nanoparticles couple strongly to imidazole-bound P450, they also couple strongly to free CYP101. Therefore, the difference between the LSPR shift induced by imidazole-bound CYP101 and free CYP101 is relatively small and only a relatively small red-shift is observed for imidazole binding.

#### **4.4. Conclusions**

The shifts in localized surface plasmon resonance wavelengths due to substrate binding have been demonstrated as a platform for signal transduction and the detection of low molecular weight molecule binding to cytochrome P450 proteins. The substrate free CYP101 shows an amplified LSPR shift from coupling of the Soret and Q bands of P450 with the LSPR. Amplified spectral response to substrate/inhibitor binding is achieved when the LSPR of the silver



nanosensor is optimized to be close to the Soret-band of the protein. The different binding mechanisms of substrate/inhibitor result in different spectral shifts, with camphor shifting blue and imidazole shifting red. The shift direction and magnitude is consistent with P450 spectral shift direction and magnitude.

This study demonstrates that the coupling between the molecular resonance and the intrinsic LSPR of the nanoparticles is determined by the orientation of the transition moment of the electronic resonance, providing further insight into possible uses of plasmon resonance spectroscopy. In addition, the extreme sensitivity of LSPR wavelength to adsorbate electronic transitions makes it possible to use this technique to detect low molecular weight adsorbates in relatively low coverage. Application of this finding to the screening for inhibitors of human cytochrome P450s is under investigation based on these results. This discovery will provide guidance to the design of plasmonic switches that can be turned on/off by small molecule binding events.

## **Chapter Five**

### **Wavelength-Scanned Surface-Enhanced Resonance Raman Excitation Spectroscopy of Tris(bipyridine)ruthenium(II) on Ag Nanoparticles**

## 5.1 Introduction

The localized surface plasmon resonance (LSPR) is one of the characteristic optical properties of noble metal nanostructures. It arises when light induces a collective oscillation in the conduction electrons.<sup>5,6,10</sup> The LSPR intensity, linewidth and wavelength are determined by the composition, size, and shape of the nanoparticles as well as being extremely sensitive to the surrounding dielectric medium.<sup>9,12,60,189-194</sup> A variety of chemical/biological sensors have been developed based on LSPR.<sup>32,35,138,147,173,176,195</sup> Recent investigations showed that when resonant molecules adsorb on nanoparticles, the strong coupling between the dye molecular resonance and LSPR leads to a LSPR wavelength shift that is dependent on the spectral overlap between the plasmon resonance of nanoparticles and the molecular resonance of the adsorbed species.<sup>73,103,113-116</sup> In particular, a very small LSPR shift is observed when the LSPR directly overlaps with the molecular resonance wavelength, and an amplified LSPR shift is observed when the LSPR is slightly to the red of the molecular resonance. By analyzing the wavelength-dependent LSPR wavelength shifts, one can study the electronic resonances of molecules that are adsorbed on a metallic surface under conditions where absorption by the molecules is too weak to be observed.<sup>73</sup>

When excited at the plasmon resonance wavelength of the noble metal nanostructures, significantly enhanced electromagnetic fields arise at the noble metal surface, and this is responsible for the major enhancement (the electromagnetic mechanism (EM)) in surface-enhanced Raman spectroscopy (SERS).<sup>3,4,81,86</sup> SERS and its mechanisms have been extensively studied by experiments and theories for the past 30 years.<sup>61,62,64,145,162,196-200</sup> For nanoparticles of the appropriate shape and size, the EM can give rise to enhancement factors up to  $10^8$ .<sup>29,143,201</sup> On the other hand, when excited at the analyte's electronic resonance frequency, the Raman

scattering intensity is enhanced by 10-100 comparing to off-resonance excitation, commonly referred to as resonance Raman enhancement.<sup>143,144,202</sup> Under certain conditions, the contribution from the EM and resonance Raman mechanisms can be combined, leading to surface enhanced resonant Raman (SERR) detection at single molecule level, where EM and resonant enhancement factors of  $10^{10-11}$  and  $10^4$  are achieved, respectively.<sup>65,203-212</sup>

The LSPR extinction and the frequency dependence of SERS intensity are closely related to each other. To study the correlation between the LSPR of nanoparticles and the SERS excitation profile, McFarland et. al. performed wavelength-scanned surface-enhanced Raman excitation spectroscopy (WS-SERES) studies of a monolayer of benzenethiol on Ag nanoparticles with varying LSPR.<sup>29</sup> WS-SERES profiles were taken at different wavelengths throughout the visible region of the electromagnetic spectrum. The experiments revealed that the maximum SERS enhancement factor occurred at excitation wavelengths that are higher in energy than the spectral location of the LSPR extinction maximum by  $\frac{1}{2}$  of the Raman Stokes shift of that band. This observation agrees with the SERS wavelength dependence predicted by the electromagnetic mechanism.

For resonant molecules, the SERS signal intensity is not only determined by EM enhancement from the nanoparticles, but is also affected by the molecular absorption. In this work, we explore the relationship between the SER excitation profile, LSPR of the nanoparticles and molecular resonance. Tris-(2,2'-bipyridine)-ruthenium(II) ( $\text{Ru}(\text{bpy})_3^{2+}$ ) is chosen as the surface-enhanced resonance Raman spectroscopy (SERRS) probe molecule.  $\text{Ru}(\text{bpy})_3^{2+}$  and its derivatives have been widely applied to a variety of molecular devices due to its a key role in the development of photochemistry,<sup>213-215</sup> electrochemistry,<sup>216,217</sup> photoelectrochemistry,<sup>218,219</sup> chemi- and electrochemi-luminescence.<sup>220-226</sup> The  $\text{Ru}(\text{bpy})_3^{2+}$  absorption spectrum has a major

ground state transition at 452 nm and a shoulder at 425 nm from a metal to ligand charge transfer transition<sup>227,228</sup>. It fluoresces at wavelengths greater than  $\sim 500$  nm which does not strongly interfere with its resonant Stokes Raman spectrum. SER(R)S activity of  $(\text{Ru}(\text{bpy})_3)^{2+}$  has been intensively studied over the past two decades, and its vibrational modes are clearly assigned.<sup>216,229-232</sup> When excited on and off resonance,  $\text{Ru}(\text{bpy})_3^{2+}$  has very different SERS and SERRS spectra that makes it easy to distinguish the resonance effect in SERS.

The work presented in this paper addresses two goals: (1) to present a more complete data set for the system of resonant molecules adsorbed on a nanostructured surface with tunable surface plasmon resonances; (2) to understand the relationship between laser excitation, molecular resonance, LSPR and SERS intensity. Three necessary experiments for these studies include: (1) Measurement of the surface coverage of  $\text{Ru}(\text{bpy})_3^{2+}$  on Ag nanoparticles to ensure it is one monolayer or less, so that the SERS measurements are performed only on molecules that are directly adsorbed to the surface. (2) Study the LSPR wavelength shift of Ag nanoparticles induced by a monolayer of  $\text{Ru}(\text{bpy})_3^{2+}$  to determine how the two electronic transitions of  $\text{Ru}(\text{bpy})_3^{2+}$  couple to the LSPR. (3) Measure the wavelength-scanned SERRS excitation profile of  $\text{Ru}(\text{bpy})_3^{2+}$  on the Ag nanoparticles while monitoring the correlated LSPR of the sample. This experiment reveals how LSPR and excitation wavelength influence SERRS intensity. In addition, theoretical studies using a quasi-static electrodynamics model are performed to study LSPR wavelength shift caused by a layer of  $\text{Ru}(\text{bpy})_3^{2+}$  and to predict how the EM enhancement together with the resonance enhancement lead to the experimental SERRS excitation profile.

## 5.2 Experimental Methods

### 5.2.1 Materials

Silver shot was purchased from Alfa Aesar (#11357 1-3mm diameter, Premion®, 99.9999%). Tungsten vapor deposition boats were acquired from R.D. Mathis (Long Beach, CA). Polystyrene nanospheres with diameters of  $280 \pm 4$  nm and  $390 \text{ nm} \pm 19.5$  nm were received as a suspension in water (Interfacial Dynamics Corporation, Portland or Duke Scientific, Palo Alto, CA) and were used without further treatment. Fisherbrand No. 2 glass coverslips with 18 mm diameters were obtained from Fisher Scientific (Pittsburgh, PA). For all steps of substrate preparation, deionized water was purified with cartridges from Millipore (Marlborough, MA) to a resistivity of  $18.2 \text{ M}\Omega\cdot\text{cm}$ . All the chemicals used were of reagent grade or better. Tetra-n-butylammonium hexafluorophosphate (TBAH) (Aldrich Chemical Co., Milwaukee, WI), and acetonitrile (Fisher Scientific, Fairlawn, VA) were used as purchased.  $\text{Ru}(\text{bpy})_3(\text{PF}_6)_2$  was prepared by using literature procedures.<sup>233</sup> The chemical structure and a electronic absorption spectrum of  $\text{Ru}(\text{bpy})_3^{2+}$  is given in Figure 5.1.

### 5.2.2 Nanoparticle Sample Preparation

Glass substrates were cleaned in piranha solution (1:3 30%  $\text{H}_2\text{O}_2/\text{H}_2\text{SO}_4$ ) for one hour at  $80^\circ\text{C}$ . (*Warning: Piranha reacts violently with organic compounds and should be handled with caution.*) Samples were cooled to room temperature and were then rinsed profusely with deionized water. Samples were then sonicated in 5:1:1  $\text{H}_2\text{O}/\text{NH}_4\text{OH}/30\% \text{H}_2\text{O}_2$  and thoroughly rinsed with water. The samples were stored in deionized water prior to use. Nanosphere lithography (NSL) was used to create monodisperse, surface-confined Ag nanoparticles. Polystyrene nanospheres ( $\sim 2.2 \mu\text{L}$ ) were drop-coated onto the glass substrates and allowed to dry, forming a monolayer in a close-packed hexagonal formation, which served as a deposition mask. The samples were then transferred to the evaporation chamber. The pressure in the

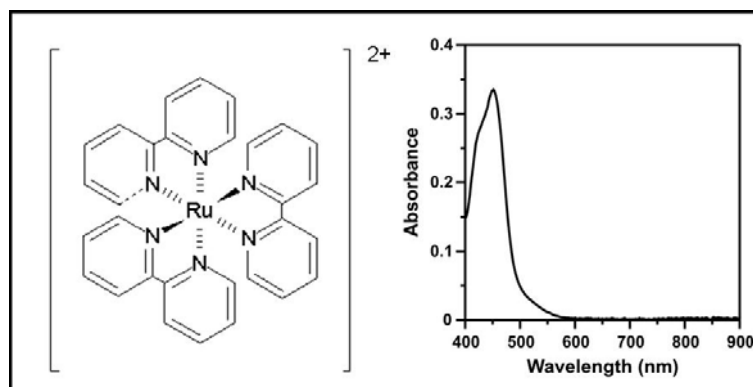


**Figure 5.1.** The structure (left) and absorption spectrum of  $\text{Ru}(\text{bpy})_3^{2+}$  (right). The absorption spectrum is 0.01 mM  $\text{Ru}(\text{bpy})_3(\text{PF}_6)_2$  in 0.1 M TBAH acetonitrile solution.

vacuum chamber was maintained below  $1 \times 10^{-5}$  Torr during the evaporation. A silver film was evaporated on the slides. The deposition rate Ag was  $1.0 \sim 1.5 \text{ \AA/s}$ . A Leybold Inficon XTM/2 quartz crystal microbalance (East Syracuse, NY) was used to measure the thickness of the Ag film deposited over the nanosphere mask,  $d_m$ . Following metal deposition, the samples were sonicated for 3-5 minutes in ethanol to remove the polystyrene nanosphere mask. The height of the nanoparticles was varied by depositing varying amounts of Ag onto the sample.

### 5.2.3 Electrochemistry of $\text{Ru}(\text{bpy})_3^{2+}$ coverage on Ag electrode

The homemade silver electrodes were masked with Torr-Seal from Varian, Inc. to expose an area of  $\sim 0.2 \text{ cm}^2$ . Prior to use, surfaces were polished with 0.3 and 0.05  $\mu\text{m}$  alumina successively (Buehler Ltd., Lake Bluff, IL) and sonicated in MQ water. A Ag wire was used as the quasi reference electrode, typically used in nonaqueous media. The BAS 100B/W electrochemical workstation was purchased from Bioanalytical Systems, Inc. (West Lafayette, IN). Solutions were deoxygenated with nitrogen for a minimum of 2 min prior to electrochemical experiments. A blanket of nitrogen, which was presaturated with solvent by passing it through a solvent saturator, was maintained in the electrochemical cell by continuous purging. The silver electrodes were incubated in 1.0 mM  $\text{Ru}(\text{bpy})_3^{2+}$  in acetonitrile for 10-60 min. Double potential step chronocoulometry measurements (DPSCC)<sup>234</sup> of the surface coverage of  $\text{Ru}(\text{bpy})_3^{2+}$  were made in 0.1 M TBAH in acetonitrile on those Ag electrodes by the application of a potential step wave form. The starting potential for the chronocoulometry measurement was -0.8 V. A potential step to -2 V past the  $3e^-$  reduction of  $\text{Ru}(\text{bpy})_3^{2+}$  for 250 ms duration was applied. The data were analyzed using Anson plots of the charge  $Q_f$  versus  $t^{1/2}$  for the forward step.

### 5.2.4 LSPR shift induced by $\text{Ru}(\text{bpy})_3^{2+}$ on Ag nanoparticles



Macro-scale UV-vis extinction measurements were collected using an Ocean Optics (Dunedin, FL) SD2000 fiber optically coupled spectrometer with a CCD detector. All spectra in this study are performed in standard transmission geometry with unpolarized light. Nanoparticles with various LSPR wavelengths were fabricated with NSL by varying the size of the nanospheres and the deposited metal thickness. The nanoparticles were solvent-annealed with methanol for 10-20 mins before exposed to  $\text{Ru}(\text{bpy})_3^{2+}$ . The nanoparticles were then incubated in 1 mM  $\text{Ru}(\text{bpy})_3^{2+}$  ethanol solution for 30 mins, then rinsed by excessive neat ethanol and dried in  $\text{N}_2$ . After introducing  $\text{Ru}(\text{bpy})_3^{2+}$ , the LSPR of the nanoparticle red shifts by different amount depending on the LSPR of the bare nanoparticles.

#### 5.2.5 SERS excitation profile of $\text{Ru}(\text{bpy})_3^{2+}$ on Ag nanoparticles

In order to perform correlated LSPR wavelength shift spectroscopy and WS-SERRES, it was necessary to perform LSPR micro-extinction on the inverted microscope such that the excitation profile was measured from the same spot on the sample due to sample heterogeneity. As such, the LSPR of the Ag nanoparticles before and after exposure to  $\text{Ru}(\text{bpy})_3^{2+}$  was measured with the micro-extinction setup without moving the sample. In-situ measurement of the LSPR spectrum was achieved by illuminating the sample with the microscope lamp and analyzing the transmitted light with a fiber-optically coupled miniature spectrometer (model SD2000, Ocean Optics, Dunedin, FL). SERR spectra of  $\text{Ru}(\text{bpy})_3^{2+}$  from the same spot were measured at different excitation wavelengths. Figure 5.2 shows a schematic of the instrumentation used for the WS-SERRES experiments. All optical measurements were performed using a Nikon Eclipse TE300 inverted microscope (Fryer Co., Huntley, IL) equipped with a 20X objective (XLWD, NA 0.5, *plan fluor*). Substrates were mounted on a piezoelectric

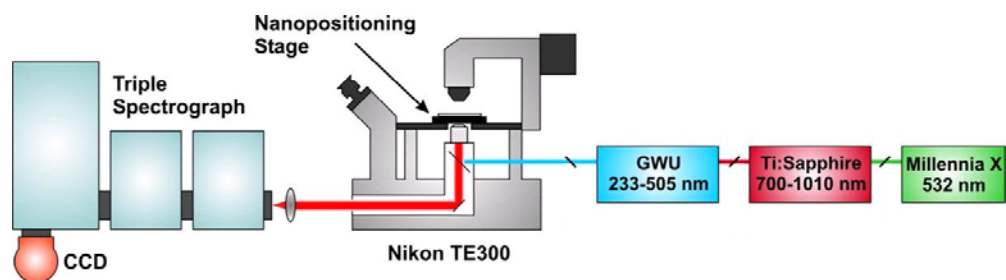


**Figure 5.2.** Schematic diagram of the WS SERES apparatus.

stage (model P-517.3CD, Polytech PI, Auburn, MA) to allow for sample positioning and raster- scanning during spectral acquisition. The light scattered by the samples was analyzed with a TriplePro three-stage spectrograph equipped with a liquid nitrogen-cooled, deep-depletion Spec-10:400BR CCD detector (Princeton Instruments, Trenton, NJ). The deep-depletion CCD detector was not necessary for this experiment, but since this apparatus is also used for near infrared SERS, it was chosen to prevent etaloning at those wavelengths. A color video camera was also attached to the front port of the microscope to facilitate laser alignment and positioning of the samples. Laser excitation was provided by a Spectra-Physics (Mountain View, CA) Millennia Xs ( $\lambda_{\text{ex}} = 532 \text{ nm}$ ) pumping a Spectra-Physics Tsunami with a GWU harmonic generator ( $\lambda_{\text{ex}} = 700\text{-}1000 \text{ nm}$ ,  $350\text{-}500\text{nm}$ ). The laser light from the tunable laser system was filtered using Pellin-Broca prisms to ensure monochromatic illumination of the sample. Furthermore, the SERRS intensity was normalized to the normal Raman scattering of cyclohexane following the procedure of McFarland et al<sup>29</sup> to correct for the instrument throughput, the detector quantum efficiency and the inherent  $\nu^4$  dependence on the Raman scattering cross-section. It is worthwhile to note that all illumination powers reported in this work were the laser powers incident on the microscope beam splitter, not the power incident on the sample. On the basis of experimental measurements, approximately 5-10% of the reported power is incident on the sample.

## 5.3 Results and Discussion

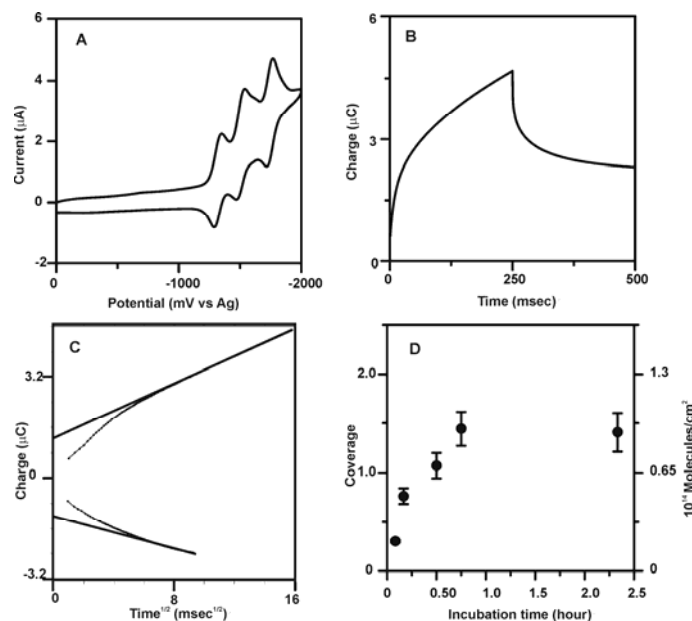
### 5.3.1 Electrochemistry of $\text{Ru}(\text{bpy})_3^{2+}$ coverage on Ag electrode

Figure 5.3A shows a cyclic voltammogram which results when a silver electrode is placed in a solution containing 1.0 mM  $\text{Ru}(\text{bpy})_3^{2+}$  and 0.10 M TBAH in acetonitrile.

$\text{Ru}(\text{bpy})_3^{2+}$  has three continuous one-electron reduction peaks on Ag electrodes. Good reversible behavior was observed for all three reductions. The reduction of  $\text{Ru}(\text{bpy})_3^{2+}$  to  $\text{Ru}(\text{bpy})_3^+$  occurs at about -1.3 V vs. Ag quasi reference electrode. The concentration of an electroactive species adsorbed on an electrode surface can be determined by DPSCC and Anson plots.<sup>234-236</sup> An example of the DPSCC data and Anson plots for the adsorption of  $\text{Ru}(\text{bpy})_3^{2+}$  on smooth Ag electrode is shown in Figure 5.3B and 5.3C. We determined that  $0.20 \times 10^{14}$  molecules/cm<sup>2</sup> were adsorbed on the smooth Ag electrode from 0.1 mM  $\text{Ru}(\text{bpy})_3(\text{PF}_6)_2$  and 0.1 M TBAH acetonitrile solution. Given the radius of  $\text{Ru}(\text{bpy})_3^{2+}$  of 0.7 nm,<sup>237</sup> the measured surface concentration translates to 0.3 monolayer of adsorbed  $\text{Ru}(\text{bpy})_3^{2+}$ . As the incubation time increase from 5 to 140 min, the surface coverage of  $\text{Ru}(\text{bpy})_3^{2+}$  adsorbate level off at  $\sim 0.94 \times 10^{14}$  molecules/cm<sup>2</sup> (Figure 5.3D). The error bars represent the standard deviation of at least three replicated DPSCC measurements, which may be mainly caused by various electrode surface area and roughness. From this measurement, we determined that a incubation for 30 min yields a monolayer coverage of  $\text{Ru}(\text{bpy})_3^{2+}$  on Ag surface ( $\sim 0.65 \times 10^{14}$  molecules/cm<sup>2</sup>); therefore, this incubation time was used in the following experiments.

### 5.3.2 LSPR shift induced by $\text{Ru}(\text{bpy})_3^{2+}$ on Ag nanoparticles

Previous studies demonstrate that the shift in the LSPR of nanoparticles induced by resonant adsorbates is highly dependent upon the spectral overlap between the LSPR and molecular resonance. To explore the effect of a monolayer of  $\text{Ru}(\text{bpy})_3^{2+}$  on the LSPR of Ag nanoparticles, nanoparticles with varying LSPR were fabricated with NSL and then incubated in 1 mM  $\text{Ru}(\text{bpy})_3^{2+}$  solution for 30 mins, followed by thoroughly rinsing. Figure 5.4 shows the plot of the LSPR shift induced by  $\text{Ru}(\text{bpy})_3^{2+}$  versus the LSPR position of bare Ag nanoparticles.



**Figure 5.3.** (A) Cyclic voltammogram of 0.10 mM  $\text{Ru}(\text{bpy})_3^{2+}$  in acetonitrile at a silver electrode with 0.10 M TBAH as the supporting electrolyte. The scan begins at 0 mV and first moves in the negative direction at 100 mV/sec. The three electron reductions of  $\text{Ru}(\text{bpy})_3^{2+}$  occur at -1347, -1539, and -1769 mV. (B) A representative double potential step chronocouloulogram in acetonitrile at the silver electrode with 0.10 M TBAH as the supporting electrolyte. Prior to the measurement, the electrode was incubated in 0.10 mM  $\text{Ru}(\text{bpy})_3^{2+}$  solution for 5min. Starting potential:-800 mV. Ending potential:-2000mV. Step width: 250 ms. (C) Anson plots of  $Q_f$  vs  $t^{1/2}$  (forward) and  $Q_r$  vs  $\theta$  (reverse) for (B). (D) The plot of  $\text{Ru}(\text{bpy})_3^{2+}$  adsorbate coverage vs incubation time. As the incubation time is increased from 5 to 140 min, the surface concentration increases from  $0.20 \times 10^{14}$  to  $0.94 \times 10^{14}$  molecules/cm<sup>2</sup>.

When  $\lambda_{\max}$  is blue of  $\text{Ru}(\text{bpy})_3^{2+}$  resonance, the LSPR shift is  $\sim 20$  nm. When  $\lambda_{\max}$  is close to the  $\text{Ru}(\text{bpy})_3^{2+}$  resonance at 452 nm, the LSPR is very small as 5 nm. As  $\lambda_{\max}$  is tuned to be slightly red of  $\text{Ru}(\text{bpy})_3^{2+}$  resonance at 453 nm, an amplified LSPR response of 50 nm was observed. Then the LSPR gradually decreased to 15 nm as  $\lambda_{\max}$  is located further to red of the  $\text{Ru}(\text{bpy})_3^{2+}$  resonance. The sharp transition of the LSPR shift from 5 nm to 50 nm within 10 nm of the molecular resonance was observed for a series of resonant molecules. The two transitions are polarized differently, therefore only the transition polarized perpendicular to the nanoparticle surface is strongly coupled with the LSPR. This phenomenon has been observed for nanoparticles covered with a molecular layer of  $\text{Fe}(\text{bpy})_3^{2+}$ .<sup>113</sup> In addition, theoretical predictions for an ellipsoidal particle coated with a layer of resonant molecules showed that the coupling between the plasmon resonance and molecular resonance depend on the orientation of the molecules on the surface.<sup>112</sup>

### 5.3.3. Kramers-Kronig Transformation and Refractive Index of $\text{Ru}(\text{bpy})_3^{2+}$

The LSPR shift is dependent on the refractive index of the surrounding medium of the nanoparticle. For non-resonant adsorbates, the LSPR wavelength shift ( $\Delta\lambda_{\max}$ ) can be estimated from the following empirical equation:<sup>138,147,148,238</sup>

$$\Delta\lambda_{\max} = m(n_{\text{ads}} - n_{\text{N}_2})(1 - e^{-2d/l_d}) \quad (5.1)$$

where  $m$  is the refractive index sensitivity of the nanoparticles ( $\sim 200$  nm/RIU),<sup>36,147</sup>  $n_{\text{ads}}$  is the real part of the refractive index of the adsorbate,  $n_{\text{N}_2}$  is the refractive index of the  $\text{N}_2$  surroundings (1.0),  $d$  is the molecular thickness (1.5 nm for  $\text{Ru}(\text{bpy})_3^{2+}$ ), and  $l_d$  is the characteristic electromagnetic field decay length of the nanoparticles (approximately 6 nm).<sup>147</sup>

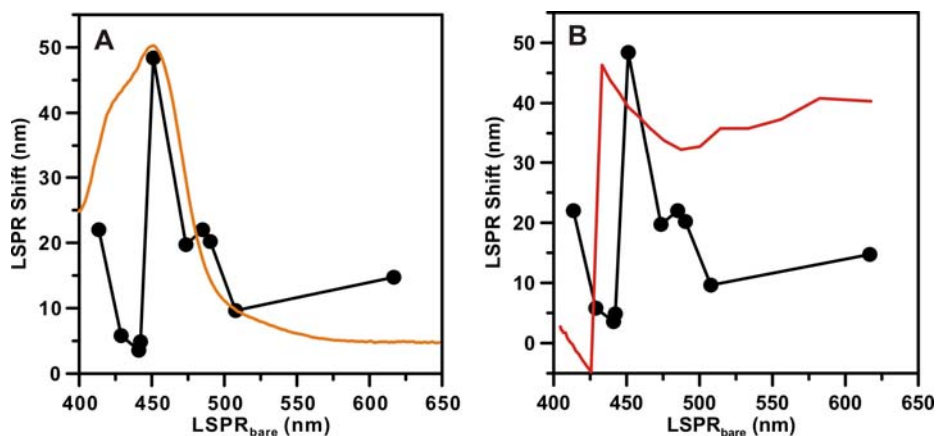


**Figure 5.4.** Effect of a monolayer of  $\text{Ru}(\text{bpy})_3^{2+}$  on the LSPR shift of Ag nanoparticles. (A) Wavelength-dependent LSPR shift induced by a monolayer of  $\text{Ru}(\text{bpy})_3^{2+}$  vs. the LSPR wavelength of bare Ag nanoparticles. Black line with filled dots is a plot of the LSPR shift (nm) vs. LSPR position of Ag nanoparticles. The orange line is the absorption spectrum of  $\text{Ru}(\text{bpy})_3^{2+}$  (arbitrary scaling). (B) Predicted LSPR shift (red line) using Eq. 1 and 2 and experimental LSPR shift (the solid black line with filled dots).

For resonant adsorbates, it has been demonstrated that  $\Delta\lambda_{\max}$  near molecular resonance can be estimated from the real part of the refractive index using a Kramers-Kronig transformation<sup>113,149</sup> and Eq 5.1. Using the same treatment as in the previous studies,  $n_{\text{ads}}$  is expressed as the sum of the nonresonant part of the refractive index ( $n_{\text{non,ads}}$ ) and the resonant contribution ( $\Delta n_{\text{res,ads}}$ ). From Eq. 5.1, the refractive index of the adsorbate layer can be estimated. Since the average  $\Delta\lambda_{\max}$  at off-molecular resonance wavelengths is 10 nm, the  $n_{\text{non,ads}}$  of  $\text{Ru}(\text{bpy})_2^{3+}$  is calculated to be  $\sim 1.1$ .

Using a Kramers-Kronig transformation,  $\Delta n_{\text{res,ads}}$  of  $\text{Ru}(\text{bpy})_2^{3+}$  was transformed from its solution absorption spectrum (Figure 5.1) using the following equation:<sup>10,149</sup>

$$\Delta n_{\text{res,ads}}(\omega) = \frac{c}{\pi} \int_0^\infty \frac{\Delta\alpha(\omega')}{(\omega')^2 - \omega^2} d\omega' \quad (5.2)$$

where  $\Delta\alpha$  is the change in the absorption coefficient ( $2.303 * A(\lambda)/T$  in which  $A(\lambda)$  is the molecular absorbance at a given wavelength and  $T$  is the effective molecular thickness),  $c$  is the speed of light,  $\lambda$  is the wavelength of light, and  $\omega$  is the angular frequency ( $2\pi c/\lambda$ ). The Kramers-Kronig transformation expresses the real part of the refractive indices as an integral of the absorption coefficients. From the LSPR shift measurements, only the electronic transition of  $\text{Ru}(\text{bpy})_3^{2+}$  at 452 nm couples strongly to the LSPR. To get the dielectric constant corresponding to electronic transition of  $\text{Ru}(\text{bpy})_3^{2+}$  at 452 nm, the absorption spectrum was deconvoluted with two Gaussian curves at 452 nm and 425 nm. Kramers-Kronig transformation was performed with the 452 nm Gaussian curve (Figure 5.5). Notice that the integral in this formula has a singularity, which was treated numerically by excluding the singular point in the integral. And in the Kramers-Kronig transformation, the integration is from 0 to infinite frequency where in the



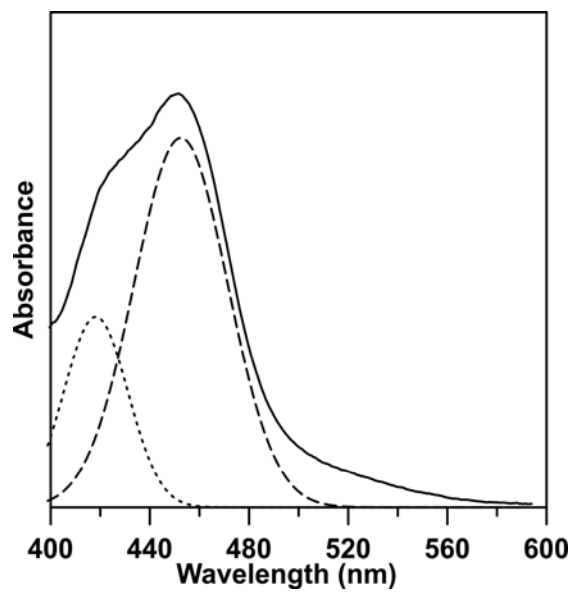


**Figure 5.5** Deconvolution of the absorption band of  $\text{Ru}(\text{bpy})_3^{2+}$  into two Gaussian curves at 452 and 425 nm (dashed lines).

experiments, only information of certain frequency ranges is available. In addition,  $\text{Ru}(\text{bpy})_2^{3+}$  has strong electronic resonances in the UV which will contribute significantly to its dielectric constants but are neglected in the current application. This treatment will lead to some uncertainty in the absolute value of the refractive indices.

#### 5.3.4 Theoretical modeling of LSPR shift

The LSPR wavelength shifts induced by a monolayer of resonant molecules were simulated by electrodynamics theory both numerically by the discrete dipole approximation (DDA) and analytically in the quasistatic limit.<sup>73,113</sup> These methods calculate the extinction of a bare nanoparticle and a nanoparticle with a layer of resonant molecules to get the  $\lambda_{\text{max}}$  shift. Results from both numerical and analytical methods agree well with the experimental data. Since the DDA method is computationally extensive, the quasistatic method is applied in this work. Briefly, in the quasistatic limit, the extinction cross section of a metallic spheroid is proportional to the imaginary part of its polarizability.

For a prolate spheroid oriented along the z direction ( $\frac{x^2 + y^2}{a^2} + \frac{z^2}{b^2} = 1$ ,  $a < b$ ), parallel to the direction of the applied electric field, in the quasistatic limit where the dimension of a spheroid is much smaller than the incident wavelength, the parallel component of the polarizability of the spheroid is<sup>10,72,239</sup>

$$\alpha = \frac{1}{3} f^3 \frac{\xi_0}{Q_1(\xi_0)} \left\{ \frac{\varepsilon_i - \varepsilon_o}{\varepsilon_i + \chi \varepsilon_o} \right\} \quad (5.3)$$

where  $\varepsilon_o$  is the dielectric constant of the medium outside the spheroid ( $\text{N}_2$  in this work),  $\varepsilon_i$  is the dielectric function of the spheroid (Ag in this work), and  $f$  is the focus of the spheroid given by:

$$f = (b^2 - a^2)^{1/2} \quad (5.4)$$

$\xi_0$  is the value of  $\xi$  at the spheroid surface where:

$$\xi_0 = \frac{1}{\sqrt{1 - \frac{a^2}{b^2}}} \quad (5.5)$$

$Q_1$  is a Legendre function of the second kind where:

$$Q_1(\xi_0) = \frac{\xi_0}{2} \ln\left(\frac{\xi_0 - 1}{\xi_0 + 1}\right) - 1 \quad (5.6)$$

and the function  $\chi$  is given by:

$$\chi = -1 + \frac{1}{(\xi_0^2 - 1)Q_1(\xi_0)} \quad (5.7)$$

The extinction crosssection ( $C_{ext}$ ) of a spheroid is proportional to the imaginary part of its porlarizability:

$$C_{ext} \propto \frac{1}{\lambda} \text{Im}(\alpha) \propto \frac{1}{\lambda} \text{Im}\left\{\frac{\varepsilon_i - \varepsilon_o}{\varepsilon_i + \chi\varepsilon_o}\right\} \quad (5.8)$$

For a spheroid coated with a layer, the parallel component of its polarizability becomes<sup>72</sup>

$$\alpha = \frac{f^3}{3} \left\{ \frac{\xi_0}{Q_1(\xi_0)} \frac{\varepsilon_i - \varepsilon_l}{\varepsilon_i + \chi\varepsilon_l} G - \frac{\xi_1}{Q_1(\xi_1)} (G - 1) \right\} \quad (5.9)$$

$$G = \frac{\xi_1 - \frac{Q_1(\xi_1)}{Q_1'(\xi_1)}}{\left( \xi_1 - \frac{\varepsilon_l}{\varepsilon_o} \frac{Q_1(\xi_1)}{Q_1'(\xi_1)} \right) + \frac{(1 - \frac{\varepsilon_l}{\varepsilon_o})(1 - \frac{\varepsilon_l}{\varepsilon_i})Q_1(\xi_1)}{\left( \frac{\varepsilon_l}{\varepsilon_i} Q_1'(\xi_o) - \frac{Q_1(\xi_o)}{\xi_o} \right)}} \quad (5.10)$$

where  $\varepsilon_l$  is the dielectric constant of the layer (Ru(bpy)<sub>3</sub><sup>2+</sup> for this work),  $\xi_0$  and  $\xi_1$  are the value of  $\xi$  at the inner and outer surface of the layered spheroid using spheroid coordinates. G is a

correction factor that comes from solving the LaPlace equation for the layered spheroid. The extinction cross section becomes:

$$C_{ext} \propto \frac{1}{\lambda} \text{Im} \left\{ \frac{\xi_0}{Q_1(\xi_0)} \frac{\varepsilon_i - \varepsilon_l}{\varepsilon_i + \chi \varepsilon_l} G - \frac{\xi_1}{Q_1(\xi_1)} (G-1) \right\} \quad (5.11)$$

To correct the static result for radiation damping and depolarization, we used the approach developed by Meier et.al.<sup>240</sup> for spheres and generalized by Zeman et. al. for spheroids.<sup>241</sup>

$$D = (1 - \frac{2}{3} i k^3 \alpha - k^2 \alpha / b)^{-1} \quad (5.12)$$

where  $k = \varepsilon_0^{1/2} \omega / c$ . Let  $\gamma_0 = \frac{\varepsilon_i - \varepsilon_o}{\varepsilon_i + \chi \varepsilon_o}$  for the bare spheroid and  $\gamma_1 = \frac{\varepsilon_i - \varepsilon_l}{\varepsilon_i + \chi \varepsilon_l}$  for the layered spheroid. The incorporation of Eq. 5.12 is accomplished by replacing  $\gamma_0$  and  $\gamma_1$  by  $D\gamma_0$  and  $D\gamma_1$  wherever it appears. Using Eq 5.8 and 5.11, we calculate the extinction of a bare Ag spheroid and that coated with a layer of  $\text{Ru(bpy)}_3^{2+}$  in  $\text{N}_2$ .

In the experiments, the NSL-fabricated nanoparticles are on a glass substrate. By assuming the nanoparticles are truncated tetrahedral with in-plane width of 65 nm and out-of-plane height of 50 nm, it is estimated that  $\sim 25\%$  of the nanoparticle surface is exposed to substrate. This effect is treated by an effective medium theory<sup>12</sup> where the dielectric constants of the layer are expressed as:  $\varepsilon_{l, \text{effect}} = \varepsilon_{mol} \cdot x + \varepsilon_o \cdot (1-x)$  where  $\varepsilon_{mol}$  is the dielectric function of the molecule, and  $x$  is the relative amount of the molecules in the layer which is 0.75 in this case. The effect of the glass substrate on the LSPR is not considered because from effective medium theory and previous work,<sup>37</sup> the substrate will result in a constant red shift in the nanoparticle LSPR. When comparing the difference in the LSPR of bare nanoparticles and nanoparticles with adsorbates, the constant red shift in the LSPR induced by substrate will be cancelled. For bare

nanoparticles,  $\epsilon_0$  is set to 1 for the dielectric constant of  $N_2$ . For the layered spheroid, the dielectric constant of the resonant layer of  $Ru(bpy)_3^{2+}$  was obtained from its absorption spectrum in solution using a Kramers-Kronig transformation described in section 5.3.3.

Figure 5.6 shows the calculated extinction spectra of bare (solid lines) and  $Ru(bpy)_3^{2+}$ -coated (dashed lines) Ag spheroids. Here the extinction wavelength of the Ag spheroid is varied by varying  $\chi$ . Each pair of spectra with the same colors is calculated using the same  $\chi$ . Notice that there is a dip in the extinction spectrum of the layered Ag spheroid due to  $Ru(bpy)_3^{2+}$  absorption, and the extinction splits into two bands. This extinction lineshape change has been reported by several groups with the experimental and theoretical studies for resonant molecule interacting with Au nanospheres or nanorods. However, in our experiments, no significant change is observed in the extinction of the Ag nanoparticles after  $Ru(bpy)_3^{2+}$  adsorption other than a wavelength shift. This indicates that in the experiments, the absorbance of  $Ru(bpy)_3^{2+}$  is relatively small compared to the extinction of the Ag nanoparticles; therefore, the effect of the  $Ru(bpy)_3^{2+}$  layer on the LSPR is to produce a spectral shift but not a lineshape change. In the modeling, this effect is much more significant in both the spectra shift and line shape change.

To simulate the LSPR wavelength shift, the semi-minor axis of the spheroid is chosen as 40 nm and the semi-major axis is varied to alter the shape factor  $\chi$ . This accounts for the varying LSPR of nanoparticles in the experiments. Figure 5.4B shows the predicted LSPR shift in comparison with the experimental results. The predicted LSPR shift curve captures the shape transition around the molecular resonance from a very small ( $< 10$  nm) to an amplified LSPR shift ( $\sim 50$  nm). However, the rapid change in  $\Delta\lambda_{\max}$  occurred at  $\sim 450$  nm in the experiments while the predicted change occurred at  $\sim 430$  nm. In addition, the magnitude of the predicted

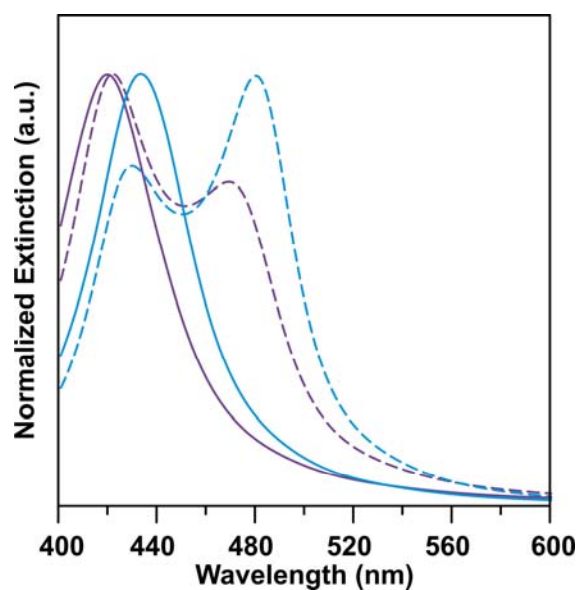


**Figure 5.6.** Calculated extinction spectra of bare Ag spheroid (solid lines) and Ag spheroid with  $\text{Ru}(\text{bpy})_3^{2+}$  (dashed lines) with varying  $\chi$  parameters. Each pair of spectra of the same color was calculated with the same  $\chi$ .

LSPR shift does not match the experimental data accurately. At a wavelength shorter than the molecular resonance, the predicted LSPR shift is negative. At an off-resonance wavelength ( $> 480$  nm), the predicted LSPR shift is much larger than the experimental data. This discrepancy has been seen in previous work<sup>73</sup> using a similar method because nanoparticles with a larger aspect ratio show a larger LSPR shift even if the layer has a dielectric constant that is constant with wavelength. In the experiments, the LSPR of the nanoparticles is tuned by both size and aspect ratio. Therefore, using only the aspect ratio to vary the nanoparticle LSPR overestimates the nanoparticle aspect ratio and leads to a LSPR shift that is larger than the experimental data. Furthermore, as discussed in section 5.3.3, the dielectric constants of  $\text{Ru}(\text{bpy})_3^{2+}$  obtained from Kramers-Kronig transformation have some uncertainty in the absolute value.

#### 5.3.5 SERS excitation profile of $\text{Ru}(\text{bpy})_3^{2+}$ on Ag nanoparticles

A representative SERRS spectrum of  $\text{Ru}(\text{bpy})_3^{2+}$  on Ag nanoparticles is shown in Figure 5.7. The peak at  $1487\text{ cm}^{-1}$  is the most enhanced band at resonant conditions. Figure 5.8 shows three excitation profiles for the  $1487\text{ cm}^{-1}$  peak of  $\text{Ru}(\text{bpy})_3^{2+}$ , each with an LSPR  $\lambda_{\text{max}}$  at different locations. The WS-SERRES profile in Figure 5.8A-B consists of 9 data points measured over the spectral range 420~497 nm. The LSPR  $\lambda_{\text{max}}$  of this substrate was measured to be 434.7 nm ( $23004\text{ cm}^{-1}$ ) with a monolayer of  $\text{Ru}(\text{bpy})_3^{2+}$ . Fitting a Gaussian line shape to the data reveals that the peak of the excitation profile,  $\lambda_{\text{ex,max}} = 445.1\text{ nm}$  ( $22467\text{ cm}^{-1}$ ) for the  $1487\text{ cm}^{-1}$  mode and  $\lambda_{\text{ex,max}} = 428.1\text{ nm}$  ( $23359\text{ cm}^{-1}$ ) for the  $1602\text{ cm}^{-1}$  mode. The WS-SERRES profile in Figure 5.8C-D consists of 9 data points measured over the spectral range 415-495 nm. The LSPR  $\lambda_{\text{max}}$  of this substrate was measured to be 465.2 ( $21496\text{ cm}^{-1}$ ) with a monolayer of  $\text{Ru}(\text{bpy})_3^{2+}$ . Fitting a Gaussian line shape to the data reveals that the peak of the excitation

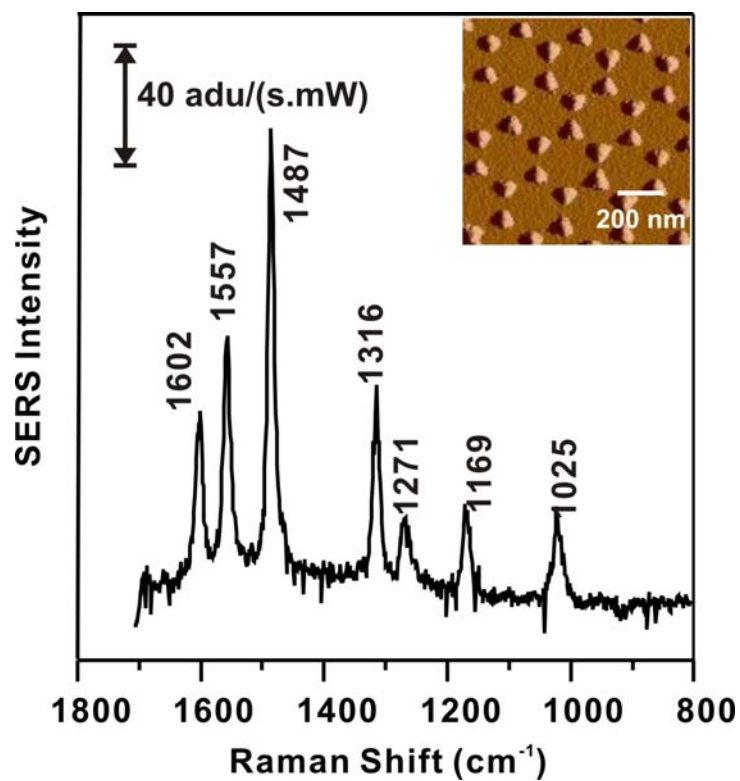


**Figure 5.7.** Representative SERS spectrum of  $\text{Ru}(\text{bpy})_3^{2+}$  on NSL-fabricated Ag nanoparticle substrate.  $\lambda_{\text{ex}} = 457.9 \text{ nm}$ , power = 0.131 mW, acquisition time = 60 s. An atomic force micrograph image of the sample is shown in the inset.



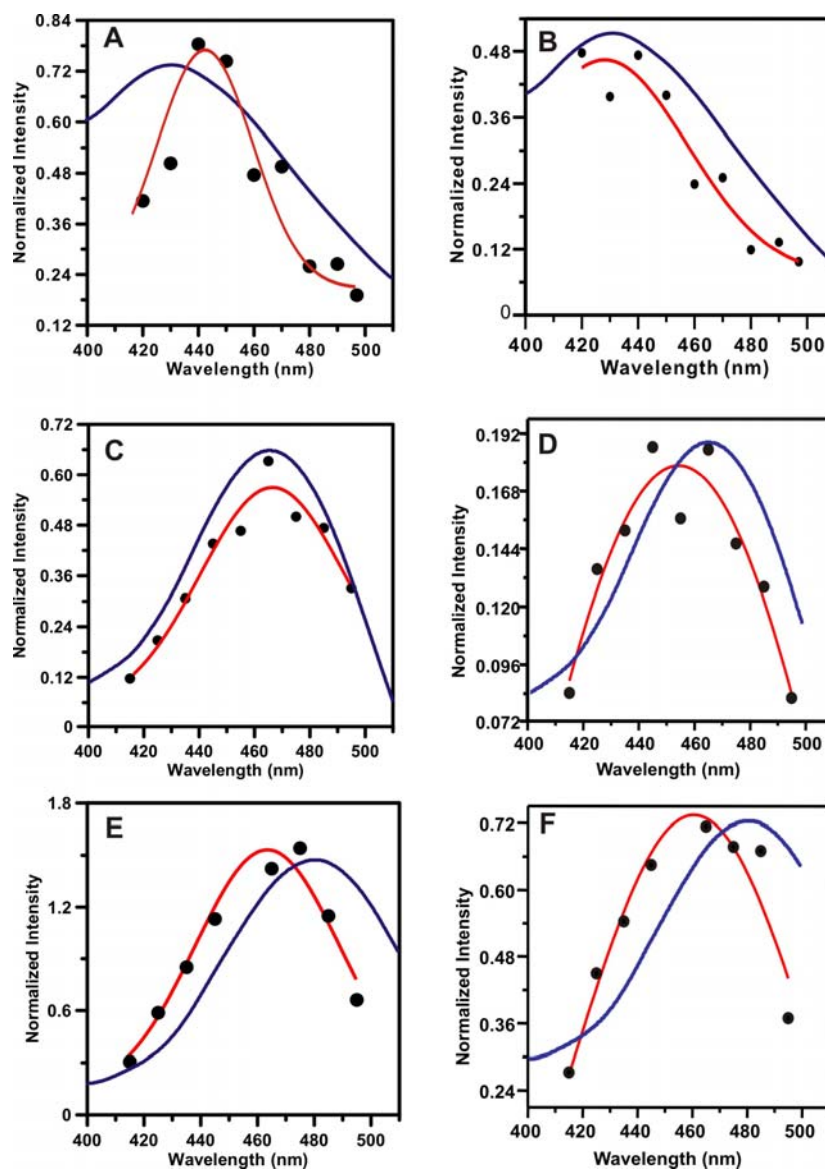


**Figure 5.8.** LSPR and surface-enhanced Raman excitation spectra of the  $1487\text{ cm}^{-1}$  peak (A, C and E) and  $1602\text{ cm}^{-1}$  peak (B, D and F) of  $\text{Ru}(\text{bpy})_3^{2+}$  with cyclohexane as intensity standard. (A-B) LSPR  $\lambda_{\text{max}} = 434.7\text{ nm}$ , profile fit maximum at (A)  $\lambda_{\text{ex,max}} = 445.1\text{ nm}$  and (B)  $\lambda_{\text{ex,max}} = 428.1\text{ nm}$ . (C-D) LSPR  $\lambda_{\text{max}} = 465.2\text{ nm}$ , profile fit maximum at (C)  $\lambda_{\text{ex,max}} = 466.4\text{ nm}$  and (D)  $\lambda_{\text{ex,max}} = 454.3\text{ nm}$ . (E-F) LSPR  $\lambda_{\text{max}} = 480.1\text{ nm}$ , profile fit maximum at (E)  $\lambda_{\text{ex,max}} = 464.1\text{ nm}$  and (F)  $\lambda_{\text{ex,max}} = 460.6\text{ nm}$ .

profile,  $\lambda_{\text{ex,max}} = 466.4 \text{ nm}$  ( $21441 \text{ cm}^{-1}$ ) for the  $1487 \text{ cm}^{-1}$  mode and  $454.3 \text{ nm}$  ( $22012 \text{ cm}^{-1}$ ) for the  $1602 \text{ cm}^{-1}$  mode. The WS-SERRES profile in Figure 5.8E-F consists of 8 data points measured over the spectral range 415-495 nm. The LSPR  $\lambda_{\text{max}}$  of this substrate was measured to be  $480.1 \text{ nm}$  ( $20829 \text{ cm}^{-1}$ ) with a monolayer of  $\text{Ru}(\text{bpy})_3^{2+}$ . Fitting a Gaussian line shape to the data reveals that the peak of the data reveals that the peak of the excitation profile,  $\lambda_{\text{ex,max}}$  is  $464.1 \text{ nm}$  ( $21547 \text{ cm}^{-1}$ ) for the  $1487 \text{ cm}^{-1}$  mode and  $460.6 \text{ nm}$  ( $21711 \text{ cm}^{-1}$ ) for the  $1602 \text{ cm}^{-1}$  mode.

According to McFarland et al, for a non resonant Raman scatterer adsorbed to a SERS active surface with well defined LSPR, the maximum excitation,  $\lambda_{\text{ex,max}}$ , occurs at higher energy than the LSPR extinction maximum,  $\lambda_{\text{max}}$ . The magnitude of the displacement is approximately half of the Raman Stokes shift.<sup>29</sup> This is in line with the theoretical predictions of the electromagnetic enhancement mechanism. As such, the different modes of a molecule will have maximum enhancement at different excitation frequencies. In this study, the molecule's electronic resonance is both resonant with the laser excitation frequency and with the oscillation frequency of the LSPR. This leads to deviation from the non-resonant case due to the resonance Raman effect. A previous report on a  $\text{Ru}(\text{bpy})_3^{2+}$  analogue,  $\text{Fe}(\text{bpy})_3^{2+}$ , shows that the  $1491 \text{ cm}^{-1}$  mode (corresponding to the  $1487 \text{ cm}^{-1}$  mode of  $\text{Ru}(\text{bpy})_3^{2+}$ ) undergoes a large resonance Raman enhancement biased towards the lower energy band of the electronic absorption spectrum (the high energy sideband does not contribute to resonance Raman enhancement), while the  $1607 \text{ cm}^{-1}$  mode (corresponding to the  $1602 \text{ cm}^{-1}$  mode of  $\text{Ru}(\text{bpy})_3^{2+}$ ) has a broad, weak resonance enhancement.<sup>242</sup> As a rough estimate, we note that the data for the  $1487 \text{ cm}^{-1}$  appears to be weighted towards the spectral location of the  $\text{Ru}(\text{bpy})_3^{2+}$  electronic absorption while the  $1602$

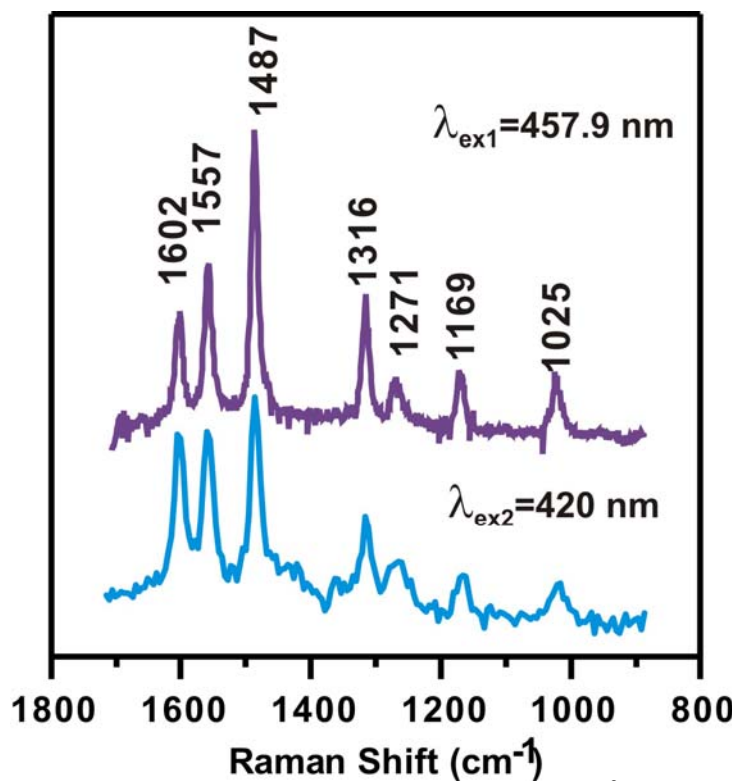


**Figure 5.9.** SERR spectra of  $\text{Ru}(\text{bpy})_3^{2+}$  on NSL-fabricated Ag nanoparticle substrate at two different excitation wavelengths.  $\lambda_{\text{ex1}} = 457.9 \text{ nm}$  (top purple curve).  $\lambda_{\text{ex2}} = 420 \text{ nm}$  (bottom blue curve).

$\text{cm}^{-1}$  mode resembles non-resonant behavior. Figure 5.9 shows two  $\text{Ru}(\text{bpy})_3^{2+}$  SERR spectra at different excitation frequencies. In the spectrum excited at lower energy close to the molecular resonance (top blue spectrum), the  $1487 \text{ cm}^{-1}$  to  $1602 \text{ cm}^{-1}$  mode intensity ratio is 2.5. This ratio changes to 1.2 as the excitation frequency is moved to higher energy and away from the molecular resonance (bottom purple spectrum). The same or an even more prominent phenomenon, where the  $1602 \text{ cm}^{-1}$  mode becomes more intense than the  $1487 \text{ cm}^{-1}$  mode, was reported previously,<sup>202</sup> and also for an analogue  $\text{Fe}(\text{bpy})_3^{2+}$ .<sup>242</sup> Since the  $1487 \text{ cm}^{-1}$  mode is more resonantly enhanced, we propose a theoretical model to understand the relationship between the LSPR, molecular resonance and its SERR excitation profile that involves the multiplication of EM and resonance enhancement mechanisms.

### 5.3.6 Theoretical modeling of SERRS excitation profile

Previous work by Kerker et al.<sup>71,243</sup> showed that the SERRS enhancement is proportional to the surface electromagnetic field at incident frequency and the Stokes shifted frequency, and the resonant Raman scattering tensor. The enhancement of the electric field is the ratio of the squared field ( $|E|^2$ ) to the square of the applied field ( $|E_0|^2$ ). Therefore, the EM enhancement is expressed as:

$$EF_{EM} = \frac{|E(\omega_0)|^2 |E(\omega_0 - \omega_{vib})|^2}{|E_0|^4} \quad (5.14)$$

where  $|E(\omega_0)|^2$ ,  $|E(\omega_0 - \omega_{vib})|^2$  are the square of the electromagnetic fields at the incident and Stokes shifted frequencies, respectively.

From the quasistatic theory model of a spheroid,<sup>68</sup> the average of the square of the electric field over the spheroid surface is expressed by the following equation derived by Zeman and Schatz:<sup>72</sup>

$$\langle |E|^2 \rangle = \langle |E_0|^2 \rangle \left\{ |1 - \gamma_0|^2 + \left[ \frac{2 \operatorname{Re}(1 - \gamma_0) \gamma_0^*}{Q_1(\xi_0)} + \frac{\gamma_0^2}{Q_1^2(\xi_0)(\xi_0^2 - 1)} \right] \left( \frac{-\sqrt{\xi_0^2 - 1} + \xi_0^2 \sin^{-1} \frac{1}{\xi_0}}{\sqrt{\xi_0^2 - 1} + \xi_0^2 \sin^{-1} \frac{1}{\xi_0}} \right) \right\} \quad (5.15)$$

$$\gamma = \frac{\varepsilon_i - \varepsilon_o}{\varepsilon_i + \chi \varepsilon_o} \quad (5.16)$$

In the present application, we use  $\chi$  as a parameter to tune the plasmon resonance wavelength of the spheroid to be at the plasmon resonances in the experiments (434, 465 and 480 nm) and calculate the EM enhancement for the three cases presented in Figure 5.8. In addition to the EM enhancement factor, many studies have shown that the resonant Raman enhancement profile at different excitation wavelength has the same line shape as the absorption spectrum of the molecule.<sup>144,242,244</sup> As discussed in the previous section, the report on  $\text{Fe}(\text{bpy})_3^{2+}$  shows that the  $1491 \text{ cm}^{-1}$  mode undergoes a resonance Raman enhancement with the line shape similar to the lower energy band of the electronic absorption spectrum and a maximum resonance enhancement of 40.<sup>143,242</sup> Therefore, we assume that the resonance Raman enhancement profile of  $\text{Ru}(\text{bpy})_3^{2+}$  has the same shape as the 452 nm band of its absorption spectrum with a maximum resonance enhancement of 40. We therefore multiplied the EM and resonant enhancement factors to get the WS-SERR excitation profile for each experiment. Figure 5.10 shows the three predicted SERRS excitation profiles of the  $1487 \text{ cm}^{-1}$  mode (where  $\omega_{\text{vib}}$  is set to be  $1487 \text{ cm}^{-1}$ ) for the three samples at different LSPR wavelengths. The experimental data and the Gaussian fitting are shown in the same plots for comparison. From Figure 5.10, the

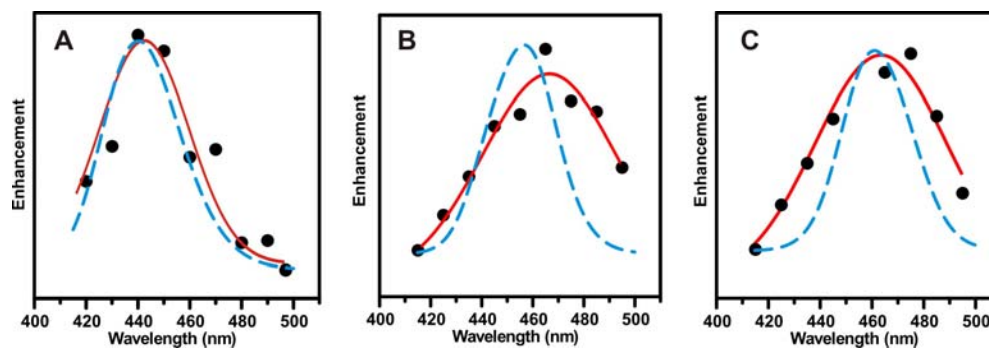


**Figure 5.10.** Predicted (blue dashed line) and experimental (black dots and red curve) surface-enhanced Raman excitation spectra of the  $1487\text{ cm}^{-1}$  peak. (A-C) correspond to three samples (A,C and E) in Figure 5.8.

predictions agree well with the experimental WS-SERR excitation profiles except for the width of the profiles, which probably arises because the shape of the nanoparticles in the theory and experiments differs. The results indicate that the WS-SERRES profiles involve multiplicative electromagnetic and resonance Raman enhancement.

When there is a resonant molecular layer on the spheroid, the expression for the average of the square of the electric field is slightly different from Eq 5.15. The correction factor  $|G|^2$  must be included and the expression for  $\gamma$  is different. For the layered spheroid, the average of the square of electric field over the surface within the layer ( $\xi_0 \leq \xi \leq \xi_1$ ) is<sup>72</sup>

$$\langle |E|^2 \rangle = |E_0|^2 |G|^2 \left\{ |B|^2 + \left[ \frac{2 \operatorname{Re}(B) A^*}{\xi} + \frac{|A|^2}{\xi^2 (\xi^2 - 1)} \right] \left( \frac{-\sqrt{\xi^2 - 1} + \xi^2 \sin^{-1} \frac{1}{\xi}}{\sqrt{\xi^2 - 1} + \xi^2 \sin^{-1} \frac{1}{\xi_0}} \right) \right\}^2 \quad (5.17)$$

$$A = \gamma_1 \frac{\xi_0}{Q_1(\xi_0)} \quad (5.18)$$

$$B = 1 - A \frac{Q_1(\xi)}{\xi} \quad (5.19)$$

When the layer is thin, the electric field within the layer does not change with different  $\xi$  values.

Therefore, we use the electric field at the outer surface to represent the average electric field in the layer. Figure 5.11 shows the  $\langle |E|^2 \rangle / |E_0|^2$  versus wavelength at the surface of the spheroid without (solid line) and with (dashed line) a layer of  $\text{Ru}(\text{bpy})_3^{2+}$  with the same size and aspect ratio. The absorption of the layer of  $\text{Ru}(\text{bpy})_3^{2+}$  leads to a decrease in the magnitude of  $\langle |E|^2 \rangle / |E_0|^2$  and a dip in the  $\langle |E|^2 \rangle / |E_0|^2$  profile. As stated in the section 5.3.4, this model overestimates the effect of the resonant layer the extinction spectral shape, leading to an extinction spectral change that was not observed in the experiments; we do not think that

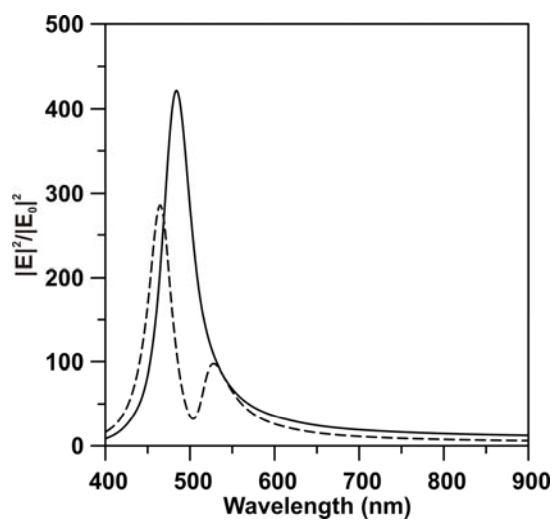


**Figure 5.11.** Calculated  $\langle |E|^2 \rangle / |E_0|^2$  of a bare Ag spheroid (solid lines) and Ag spheroid with  $\text{Ru}(\text{bpy})_3^{2+}$  (dashed lines) with the same  $\chi$  parameter.



including the absorbing layer in the electric field calculations gives valid results that can represent the electric field of the nanoparticles in the experiments. Therefore, a bare spheroid model is used to simulate the average electric field around the nanoparticles that are used in the experiments. However, from the calculation results in Figure 5.11, the layer of  $\text{Ru}(\text{bpy})_3^{2+}$  lead to a decrease in the magnitude of  $\langle |E|^2 \rangle / |E_0|^2$ . This effect was shown by Zeman et. al. in 1987 where a 0.1 coverage of the absorbed resonant molecular layer leads to a maximum SERRS enhancement and further increasing the coverage decreases the SERRS enhancement factor.<sup>72</sup>

### 5.3.7 An Example of SERRS EF Calculation

Since the magnitude of the intensity observed in the SERRS spectrum of  $\text{Ru}(\text{bpy})_3^{2+}$  can be interpreted as a multiplication of the normal Raman scattering cross section by the resonance Raman and EM enhancement, it is possible to write an expression for a decoupled SERRS enhancement factor. McFarland et al<sup>29</sup> gives an expression for the non-resonant EF for the case where the SERS and normal Raman analyte are the same molecule eliminating the need to normalize by differing cross-sections. In the present work, it is difficult to observe the magnitude of the resonance Raman intensity due to fluorescence. Therefore, the normal Raman intensity is given for a non-resonant molecule and the EF expression must include a cross-section normalization. The expression for the overall SERRS EF is:

$$\begin{aligned}
 EF_{SERRS} &= \frac{I_{SERRS,Ru} / (N_{SERRS,Ru} \cdot \sigma_{NR,Ru})}{I_{NR,Cyc} / (N_{NR} \cdot \sigma_{NR,Cyc})} \\
 &= \frac{I_{SERRS,Ru} / (N_{SERRS,Ru} \cdot \sigma_{RR,Ru})}{I_{NR,Cyc} / (N_{NR} \cdot \sigma_{NR,Cyc})} \cdot \frac{\sigma_{RR,Ru}}{\sigma_{NR,Ru}} = EF_{EM} \cdot EF_{RR}
 \end{aligned} \tag{5.13}$$

where I, N and  $\sigma$  are the intensities, number of and cross-sections of the resonance Raman (RR) and normal Raman (NR) analytes, respectively. By normalizing the observed SERRS intensity

to the resonant  $\text{Ru}(\text{bpy})_3^{2+}$  cross-section, the  $\text{EF}_{\text{SERS}}$  term only corresponds to EM enhancement. The measured intensities for the sample in Figure 5.8E were  $I_{\text{SERRS}} = 30.82 \text{ cts mW}^{-1} \text{ s}^{-1}$  for  $\text{Ru}(\text{bpy})_3^{2+}$   $1487 \text{ cm}^{-1}$  mode and  $I_{\text{NR}} = 20.82 \text{ cts mW}^{-1} \text{ s}^{-1}$  for cyclohexane  $1444.4 \text{ cm}^{-1}$  mode at  $\lambda_{\text{ex}} = 465 \text{ nm}$ . Comparing the intensity of the  $1487 \text{ cm}^{-1}$   $\text{Ru}(\text{bpy})_3^{2+}$  mode to the  $983 \text{ cm}^{-1}$   $\text{SO}_4^{2-}$  mode measured by Mallick et. al.<sup>202</sup>, and using the  $\text{SO}_4^{2-}$  cross section of  $14.8 \times 10^{-30}$  at  $\lambda_{\text{ex}} = 465 \text{ nm}$  as internal standard,<sup>245</sup> the resonant cross section of  $\text{Ru}(\text{bpy})_3^{2+}$  was determined to be  $\sigma_{\text{RRS}} = 4.4 \times 10^{-26} \text{ cm}^2 \text{ molecule}^{-1}$  at  $\lambda_{\text{ex}} = 465 \text{ nm}$ . The normal Raman cross section for the  $1444.4 \text{ cm}^{-1}$  cyclohexane mode was determined to be  $\sigma_{\text{NR}} = 9.37 \times 10^{-30} \text{ cm}^2 \text{ molecule}^{-1}$  at  $\lambda_{\text{ex}} = 465 \text{ nm}$ .after correcting for  $\nu^4$ .<sup>246</sup> The number of  $\text{Ru}(\text{bpy})_3^{2+}$  molecules present in the probe volume was determined to be  $N_{\text{SERRS}} = 1.8 \times 10^5$  assuming a surface coverage of  $0.65 \times 10^{14} \text{ molecules cm}^{-2}$  from the electrochemistry measurement, a  $4 \mu\text{m}^2$  laser spot size and only 7% coverage of nanoparticles resulting from NSL.<sup>39</sup> The number of cyclohexane molecules was estimated to be  $N_{\text{NR}} = 2.4 \times 10^{12}$ . This was found by assuming that the probe volume was a cylinder of  $100 \mu\text{m}$  in length with  $4 \mu\text{m}^2$  cross-section and using its bulk density of  $6.0 \times 10^{17} \text{ molecules cm}^{-2} \mu\text{m}^{-1}$ . Using these numbers, the EM EF was determined to be  $4.16 \times 10^3$ . Assuming that the resonant Raman EF is on the order of 40,<sup>143</sup> the overall EF observed here is  $1.66 \times 10^5$ .

## 5.4 Conclusions

In this work, we studied the contribution of electromagnetic and resonance enhancement to surface-enhanced resonant Raman intensity. A monolayer of  $\text{Ru}(\text{bpy})_3^{2+}$  molecules was adsorbed on nanoparticles with different localized surface plasmon resonance and the coupling

between molecular resonance and LSPR was probed by LSPR shift spectroscopy. One of the electronic transitions of  $\text{Ru}(\text{bpy})_3^{2+}$  is strongly coupled to the LSPR and leads to wavelength-dependent LSPR shifts. SERR spectra of  $\text{Ru}(\text{bpy})_3^{2+}$  were collected on three samples with different LSPR wavelengths for 400-500 nm Raman excitation wavelengths. Unlike non-resonant adsorbates,  $\text{Ru}(\text{bpy})_3^{2+}$  WS-SERR excitation profile peak positions depend on the relative spectral position of the LSPR and molecular resonance. Quasi-static electromagnetic simulations of the WS-SERR excitation profile based on multiplication of the EM and resonant enhancement factors showed good agreement with the experimental results.

## **Chapter Six**

### **Theoretical Study of Plasmonic Properties of Copper and Aluminum Nanoparticles**

#### **Fabricated by Nanosphere Lithography**

## 6.1 Introduction

It has been well characterized that the localized surface plasmon resonance (LSPR) of nanoparticles are determined by their composition, geometry and external dielectric medium.<sup>12,13,38,247</sup> Noble metal nanoparticles, in particular, Ag and Au, have been extensively studied and showed that they can support tunable plasmon resonances throughout the UV-vis-NIR region.<sup>59,248</sup> The requirement for LSPR is a large negative real and a small imaginary dielectric function, thus a number of other metals meet this criterion and in theory should support plasmon resonances for at least part of the UV-vis-NIR region.<sup>1,241,249,250</sup> Zeman and Schatz studied the electric field enhancement at different frequencies for nine metals (Li, Na, In, Ga, Cd, Zn, Ag, Au, Cu and Al).<sup>241</sup> The electric field enhancement is highly dependent on frequency so at certain desired frequencies, some metal exhibit larger field enhancement than others. It is worth studying the optical properties of metals other than Ag and Au to broaden the applicable area of plasmonics.

In this chapter, the optical properties of the copper<sup>9</sup> and aluminum nanoparticles fabricated by nanosphere lithography (NSL) were examined with classical electrodynamics calculations based on the discrete dipole approximation (DDA) method<sup>11,96,98</sup> and compared with experiments carried out by George H. Chan in the Department of Chemistry of Northwestern University. Since the Cu and Al are prone to oxidize, the affect of oxides on the optical properties are discussed as well. In all the DDA calculations, the shape of the nanoparticles is assumed to be truncated tetrahedral. The Cu dielectric constants are taken from *Handbook of Optical Constants of Solids*; Palik, E.D. The dominant oxidation product of copper metal at room temperature is Cu<sub>2</sub>O thus the dielectric function of Cu<sub>2</sub>O was used in the DDA

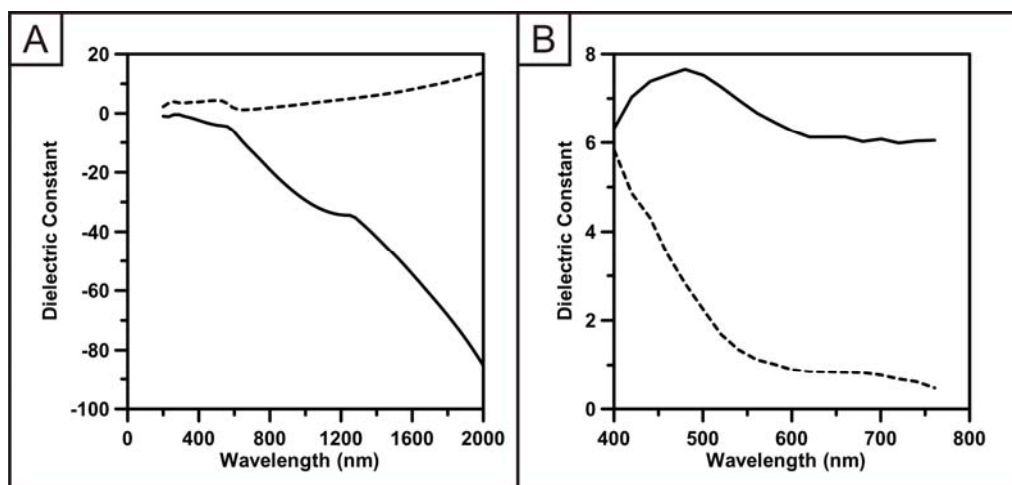


**Figure 6.1** Dielectric constants of Cu (A) and Cu<sub>2</sub>O (B). The solid line represents the real part and the dashed line represents the imaginary part.

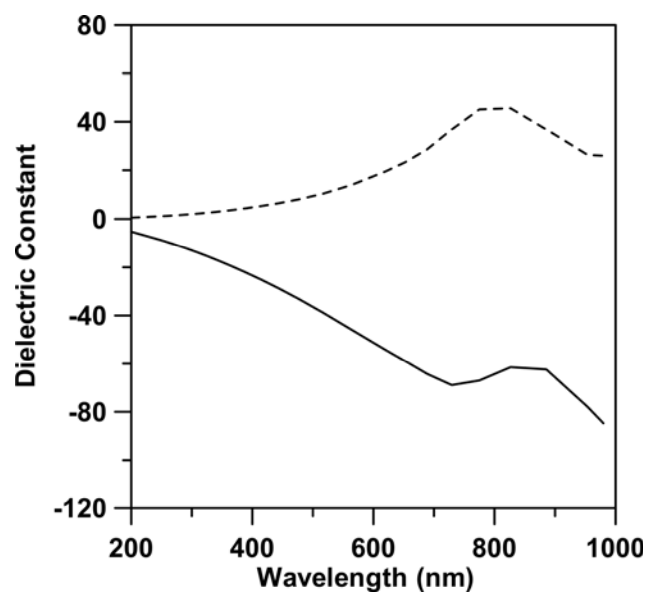


**Figure 6.2** Dielectric constants of Al. The solid line represents the real part and the dashed line represents the imaginary part.

simulations.<sup>251,252</sup> Figure 6.1A and B show the dielectric constants of Cu and Cu<sub>2</sub>O versus wavelength, respectively. Al dielectric constants are taken from the CRC Handbook of Chemistry and Physics (plotted in Figure 6.2) and the refractive index of Al<sub>2</sub>O<sub>3</sub> of 1.57 is taken from a recent paper by Whitney et al.<sup>91,253</sup> The effect of the glass substrate on the LSPR was treated using effective medium theory<sup>37</sup> in which the particles are assumed to be embedded in a homogeneous medium and the dielectric constant is a weighted average of that for glass and N<sub>2</sub>; the weighting is determined by the relative fractions of the particles that are exposed to each medium.

## 6.2 Plasmonic properties of Copper Nanoparticles

### 6.2.1 Effect of Copper Oxides on the LSPR of Copper Nanoparticles

From the dielectric constant of copper oxides in Figure 6.1 B, copper oxides absorb light in the visible wavelength range, therefore, would have significant effect on the LSPR of the copper nanoparticles. In Figure 6.3A, the spectrum in black illustrates the extinction spectrum of a NSL-fabricated Cu nanoparticle with a thin layer of copper oxides. With glacial acetic acid, copper oxides can be effectively removed while the underlying copper particle will not be attacked.<sup>254,255</sup> Representative LSPR spectra monitoring the process of copper oxides removal in glacial acetic acid are shown in pink, blue and green spectra in Figure 6.3A, consequently. And when dried in N<sub>2</sub>, the LSPR spectrum of the bare copper nanoparticles was recorded as the red spectrum in Figure 6.3A. These results indicate that copper oxides of different thickness have different effect on the LSPR of copper nanoparticles. The thicker the copper oxides are, the broader and weaker LSPR peaks are observed. The inset in Figure 6.3A is an AFM image of the



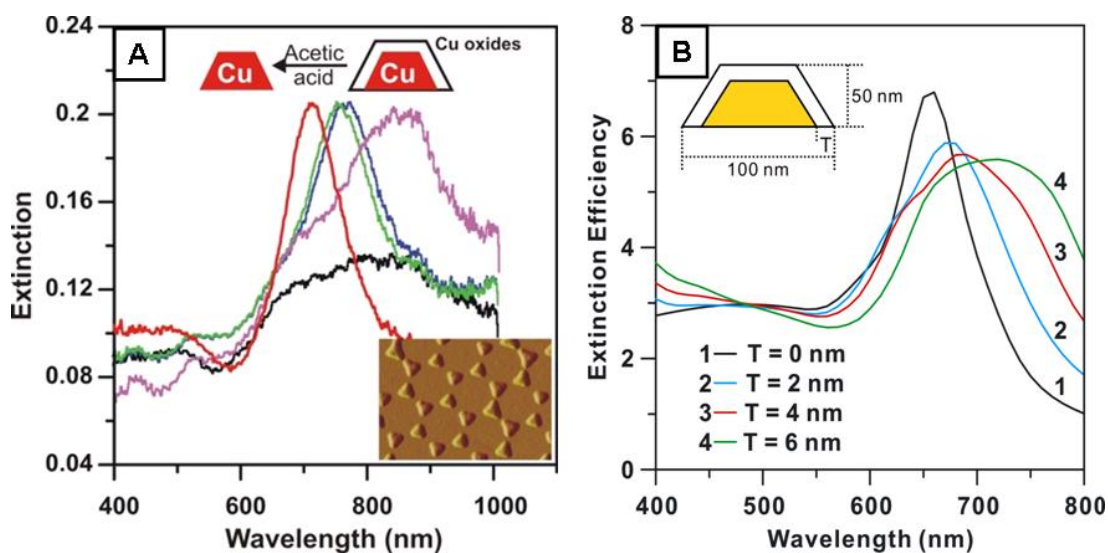


**Figure 6.3** (A) Extinction spectra of copper nananoparticles before treatment with glacial acetic acid in N<sub>2</sub> (black), during the treatment in real time in acetic acid (pink, blue, green) and after the treatment in N<sub>2</sub>. Inset is an AFM image of the copper nanoparticles. (B) DDA simulations of the effect of oxidation of copper (Cu<sub>2</sub>O) on a NSL Cu nanoparticle. Calculations were performed for a nanoparticle with a Cu core surrounded by a Cu<sub>2</sub>O shell. The inset shows a side view of the core-shell nanoparticle. The total height and width of the nanoparticle was fixed at 50 and 100 nm, respectively. The thicknesses (T) of the Cu<sub>2</sub>O shell were varied from 0 to 6 nm.

NSL-fabricated triangular copper nanoparticles.

To simulate the effect of copper oxides on copper nanoparticles, a core-shell geometry of the nanoparticle was constructed, i.e., a copper core surrounded with a shell of  $\text{Cu}_2\text{O}$  with schematic illustration shown in Figure 6.3B. In the calculations, the total height and width of the  $\text{Cu}_2\text{O}$  and Cu metal were fixed at 50 nm and 100 nm while the thickness of the  $\text{Cu}_2\text{O}$  shell was varied from 0 to 6 nm (Figure 6.3B). Spectrum 1 (black) depicts the LSPR spectrum for a bare copper metal nanoparticle. The LSPR peak has a well defined shape and shows a broad shoulder below 590 nm originating from the interband transitions of copper. In spectrum 2 (blue), the LSPR red shifts and the intensity decreases when a 2 nm layer of Cu is replaced by  $\text{Cu}_2\text{O}$ . As the thickness of  $\text{Cu}_2\text{O}$  increases, the LSPR peak red shifts and the intensity of the peak decrease until finally a broad peak is observed. These results mimic what is seen in Figure 6.3A quite accurately. Although the thickness of the copper oxide layer needed to match the experimental results is overestimated in the DDA simulations,<sup>256,257</sup> the calculations confirm that the presence of copper oxides can greatly affect the LSPR.

### 6.2.2 Tuning the LSPR of Copper Nanoparticles by Width and Height

The NSL technique allows for fabricating nanoparticles with various LSPR wavelengths by controlling the nanosphere diameter (D) (in-plane width of the particle) and deposited metal thickness (h) (out-of-plane height of the particle).<sup>39</sup>

To vary the in-plane-width of the nanoparticles, the height is fixed at  $h = 50$  nm, and different nanosphere diameters are used ( $D = 280, 390, 450, 500$ , and  $590$  nm). The relationship between the width of the nanoparticles and nanosphere diameters was previously studied by Haynes et. al.<sup>39</sup> The calculated and experimental extinction spectra are illustrated in Figure 6.4

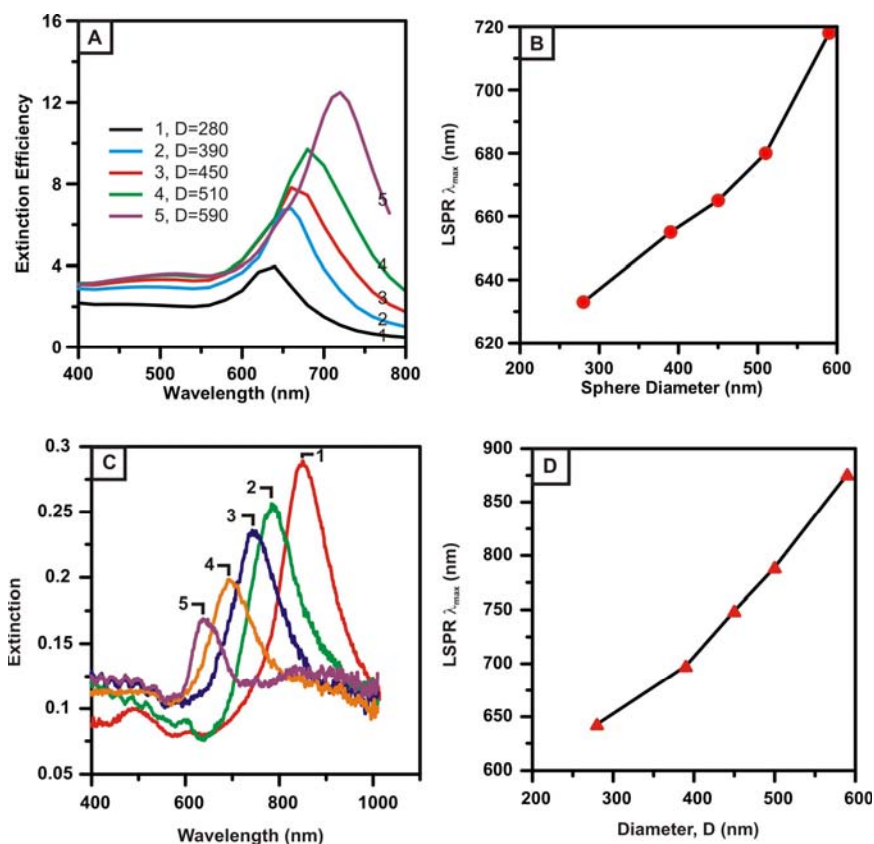


**Figure 6.4** (A) Extinction spectra of Cu nanoparticle with varying widths calculated by DDA. Spectrum 1 (black),  $D = 280$  nm,  $\lambda_{\max} = 635$  nm; spectrum 2 (blue),  $D = 390$  nm,  $\lambda_{\max} = 655$  nm; spectrum 3 (red),  $D = 450$  nm,  $\lambda_{\max} = 665$  nm; spectrum 4 (green),  $D = 510$  nm,  $\lambda_{\max} = 680$  nm; and spectrum 5 (purple),  $D = 590$  nm,  $\lambda_{\max} = 720$  nm. (B) LSPR  $\lambda_{\max}$  versus diameter is shown for the calculated results. (C) Extinction spectra of Cu nanoparticle arrays with varying widths after acetic acid treatment ( $D = 280 - 590$  nm;  $d_m = 50$  nm) measured with UV-vis spectroscopy. All spectra were collected in a  $N_2$  environment. Spectrum 1 (red),  $D = 590$  nm,  $\lambda_{\max} = 876$  nm; spectrum 2 (green),  $D = 500$  nm,  $\lambda_{\max} = 789$  nm; spectrum 3 (blue),  $D = 450$  nm,  $\lambda_{\max} = 750$  nm; spectrum 4 (orange),  $D = 390$  nm,  $\lambda_{\max} = 698$  nm, and spectrum 5 (purple),  $D = 280$  nm, and  $\lambda_{\max} = 643$  nm. (D) LSPR  $\lambda_{\max}$  versus diameter is shown for the experimental results.

A and C. Both the calculations and experiments show that the intensity of the LSPR peak increases as the nanosphere diameter becomes larger. As the LSPR approaches the interband transitions ( $E = 2.2$  eV corresponding to a wavelength of 560 nm) of Cu, a significant decrease in the intensity of the LSPR is observed. The calculated and experimental LSPR  $\lambda_{\max}$  as a function of nanosphere diameter are shown in Figure 6.4B and D, respectively. The calculations and experiments demonstrate similar trends but the overall LSPR  $\lambda_{\max}$  shift from nanosphere diameter change is smaller in the calculations. This discrepancy is likely due to differences between the fabricated and calculated particles shapes, as the truncated tetrahedron model is only a rough approximation to what is fabricated using NSL. In addition, the effective medium model for the substrate effects tends to underestimate the observed substrate effect for particles with high aspect ratios.

The LSPR  $\lambda_{\max}$  is also dependent upon the nanoparticle height. To study this dependence, the extinction spectra of copper nanoparticles with varying height from 20 ~ 70 nm were calculated, where the nanosphere diameter is fixed at  $D = 390$  nm. Figure 6.5A and C show the extinction spectra for different nanoparticle height predicted by DDA and measured with UV-vis spectroscopy, respectively. As the heights of the nanoparticle increases from 20 nm to 70 nm, a blue shift in the LSPR  $\lambda_{\max}$  is observed. The calculated and experimental LSPR  $\lambda_{\max}$  as a function of nanoparticle height are shown in Figure 6.5B and D, respectively. The experimental position of the LSPR  $\lambda_{\max}$  agrees at least qualitatively with the predictions of theory; though the predicted LSPR  $\lambda_{\max}$  shows smaller shift when height changes. The shift is larger for the shorter nanoparticles than is found in the measurements. For example, the predicted shift in  $\lambda_{\max}$  is 2 nm for a change in nanoparticle height from 60 to 70 nm, whereas the shift is 10 nm for a change of

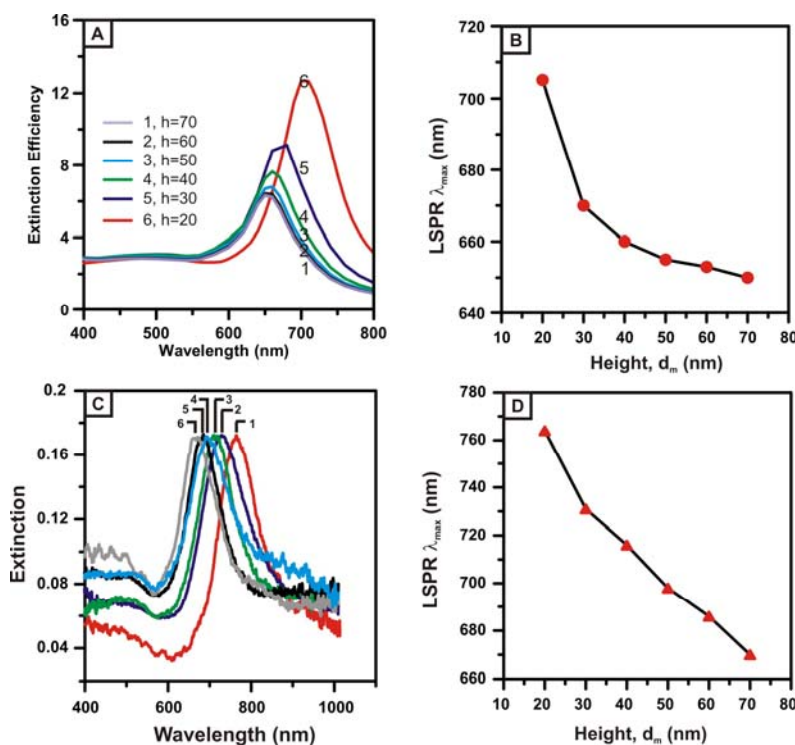


**Figure 6.5** (A) Extinction spectra of Cu nanoparticle with varying heights calculated by DDA. Spectrum 1 (grey),  $h = 70$  nm,  $\lambda_{\max} = 652$  nm; spectrum 2 (black),  $h = 60$  nm,  $\lambda_{\max} = 653$  nm; spectrum 3 (light blue),  $h = 50$  nm,  $\lambda_{\max} = 655$  nm; spectrum 4 (green),  $h = 40$  nm,  $\lambda_{\max} = 660$  nm; spectrum 5 (dark blue),  $h = 30$  nm,  $\lambda_{\max} = 670$  nm; and spectrum 6 (red),  $h = 20$  nm,  $\lambda_{\max} = 705$  nm. (B) LSPR  $\lambda_{\max}$  versus nanoparticle height ( $h$ ) is shown for calculated results. (C) Extinction spectra of the Cu nanoparticle arrays after acetic acid treatment ( $D = 390$  nm;  $h = 20 - 70$  nm) measured with UV-vis spectroscopy. All spectra were collected in a  $N_2$  environment. Spectrum 1 (red),  $h = 20$  nm,  $\lambda_{\max} = 764$  nm; spectrum 2 (dark blue),  $h = 30$  nm,  $\lambda_{\max} = 730$  nm; spectrum 3 (green),  $h = 40$  nm,  $\lambda_{\max} = 713$  nm; spectrum 4 (light blue),  $d_h = 50$  nm,  $\lambda_{\max} = 698$  nm; spectrum 5 (black),  $h = 60$  nm,  $\lambda_{\max} = 685$  nm; and spectrum 6 (light gray),  $h = 70$  nm,  $\lambda_{\max} = 670$  nm. (D) LSPR  $\lambda_{\max}$  versus nanoparticle height ( $h$ ) is shown for the experimental results.

the nanoparticle height from 30 to 40 nm. This behavior is consistent with theory, and in fact earlier theory studies concerning this were reported for Au triangular prisms.<sup>258</sup>

### 6.3 Plasmonic properties of Aluminum Nanoparticles

Aluminum is the third most abundant element by weight in the earth's crust and is very reactive with a high heat of combustion. When exposed to ambient conditions, aluminum metal rapidly oxidizes, and forms a thin surface oxide layer. This oxide layer prevents further attack by oxygen and passivates (protects) the surface. High-resolution transmission electron microscopy studies on aluminum nanoparticles indicate that the oxide layer is about ~2.5 nm thick and is part amorphous and part crystalline in nature.<sup>259</sup> Recently, there have been renewed interest in exploring the optical properties of Al<sup>260-267</sup> because it is capable of supporting surface plasmons in the UV and have been shown to be effective substrates for enhanced fluorescence and SERS.<sup>104,268-270</sup>

The dielectric constant of Al is shown in Figure 6.2. As described previously, materials that exhibit a large negative real and small positive imaginary dielectric function are capable of supporting surface plasmons. Thus, Al should be a plasmonic active element and should display LSPR properties in the UV-vis region. From an examination of the dielectric function of Al, it is clear that Al should display an LSPR that is tunable between 200 to 800 nm. In addition, a steep rise in the imaginary part of the dielectric function of Al at ~ 800 nm (1.5 eV) is attributed to interband transitions involving Al.

#### 6.3.1 Effect of Aluminum Oxides on the LSPR of Aluminum Nanoparticles

Aluminum is very reactive. When exposed to ambient conditions, aluminum metal

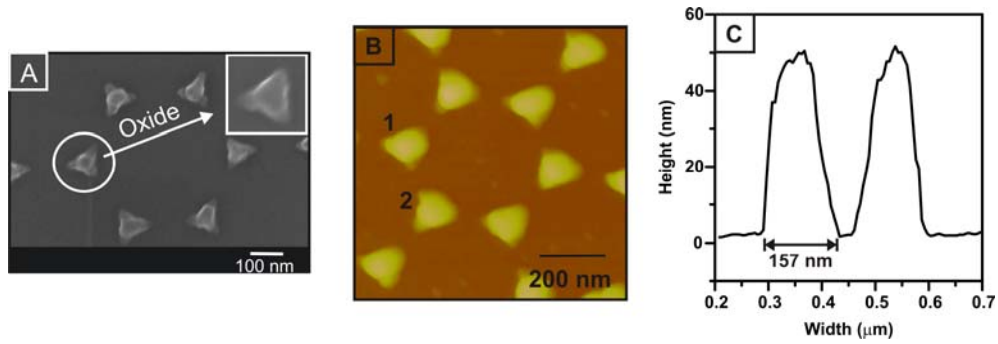


**Figure 6.6** (A) SEM image of Al nanoparticles on a Si substrate where  $D = 390$  nm and  $h = 50$  nm. (B) AFM image of the same size Al nanoparticles on a glass substrate. (C) AFM linescan profile of particle 1 and 2 in (B).

rapidly oxidizes, and forms a thin surface oxide layer. Unlike copper oxides, aluminum oxides are transparent in the UV-vis spectral range.<sup>90,91,253</sup> Therefore, aluminum oxides are not expected to have a significant effect on the peak shape of the LSPR of aluminum nanoparticles; rather a shift in the LSPR is expected. Figure 6.6 A shows the SEM of Al nanoparticles fabricated by NSL on a Si substrate where  $D = 390$  nm and  $h = 50$  nm. Upon closer examination of the SEM image, sharp contrast between the tips and the top base of the nanoparticle is observed, which suggests the presence of oxides of the tips of the nanoparticles. Figure 6.6 B and C shows the AFM image and linescan of the Al nanoparticles fabricated by NSL on a glass substrate where  $D = 390$  nm and  $h = 50$  nm. From the AFM linescan, the height of the nanoparticles is consistent with that measured with the quartz crystal microbalance. Note that the AFM linescan shape is similar to that of Ag nanoparticles fabricated by the same method. Therefore, the Al nanoparticle geometry is assumed to be truncated tetrahedral as that for Ag nanoparticles in the DDA calculations. Notice that the nanoparticle width is 157 nm from the AFM linescan, considering the AFM tip broadening effect of  $\sim 20$  nm,<sup>13</sup> the width of the nanoparticle is  $\sim 137$  nm. Comparing to Ag nanoparticles fabricated with the same nanosphere diameter, the width of Al nanoparticle is broadened by 1.5 times.<sup>13</sup> This is probably due to the dewetting properties of Al on glass surface is different from that of Ag because of differences in their surface melting temperatures. The same phenomenon was observed for Au previously.<sup>48</sup> Therefore, the geometry of the Al nanoparticle is similar but wider than the Ag nanoparticles. In order to get reasonable agreement with the experimental data, in the DDA calculations in section 6.3.2, the nanoparticle shape is still assumed to be truncated tetrahedral, while the width of the nanoparticle is 1.5-1.8 times of that calculated using the relationship between the width of the Ag



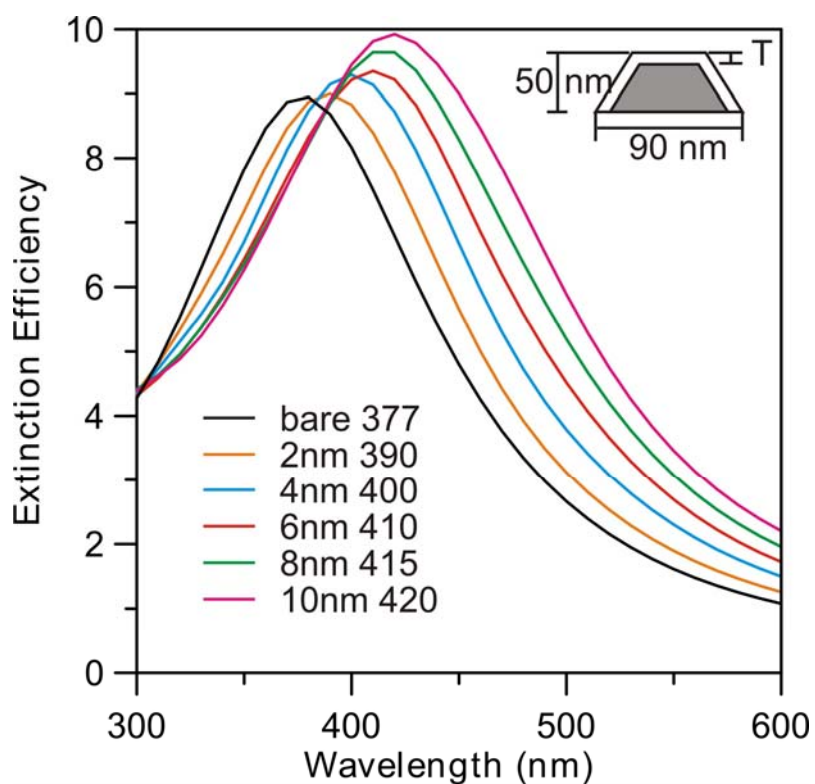


**Figure 6.7** DDA simulations of the effect of oxidation of aluminum ( $\text{Al}_2\text{O}_3$ ) on a NSL Al nanoparticle at room temperature. Calculations were performed for a nanoparticle with Al core surrounded an  $\text{Al}_2\text{O}_3$  shell. The inset shows a side view of the core-shell nanoparticle. The thicknesses (T) of the  $\text{Al}_2\text{O}_3$  shell were varied from 0 to 10 nm.

nanoparticle and nanosphere diameter developed in a previous work.<sup>39</sup>

Figure 6.7 shows theoretical calculations on the effect of oxidation on the LSPR of a single Al nanoparticle on a glass substrate surrounded by a  $N_2$  environment. The total height of the nanoparticle is 50 nm and the diameter is 90 nm. The addition of a 2 nm layer of  $Al_2O_3$  surrounding the Al nanoparticle ( $D = 390$  nm;  $d_m = 48$  nm of Al + 2 nm  $Al_2O_3$ ) leads to a red shift in the LSPR  $\lambda_{max}$  of  $\sim 13$  nm. As the amount of  $Al_2O_3$  was increased up to a thickness of 10 nm, no significant peak broadening or decrease in the extinction efficiency of the LSPR was observed in the calculated spectra as a result of the presence of an alumina oxide layer.

### 6.3.2 Tuning the LSPR of Aluminum Nanoparticles by Nanosphere Diameter

LSPR of nanoparticles is very sensitive to nanoparticle geometry. Figure 6.8A illustrates the predicted extinction spectra of the Al nanoparticle with a 2 nm Al oxide shell with varying width in a  $N_2$  environment on a glass substrate where the total height is fixed at 50 nm. Spectra 1-5 correspond to nanoparticle widths of 95 nm, 137 nm, 174 nm, 206 nm and 230 nm, respectively. As predicted from theory, an increase in the width of the nanoparticle leads to a red shift in the LSPR  $\lambda_{max}$  and broadening in the LSPR spectra. Figure 6.8 B shows the extinction spectra of NSL –fabricated Al nanoparticles at fixed height of 50 nm and varying nanosphere diameter of 280 (purple), 390 (blue), 410 (green), 500 (yellow) and 590 nm (red) measured with UV-vis spectroscopy. The calculated extinction spectra have similar LSPR lineshape as the experimental ones. From both the experimental results and calculations, when the nanoparticle LSPR approaches Al interband transitions at 1.5 eV (corresponding to  $\sim 800$  nm), the extinction spectrum is significantly broadened (yellow and red spectra in Figure 6.8 A and in Figure 6.8 B). The red spectra in Figure 6.8A and 6.8B are significantly broader than the other spectra; in

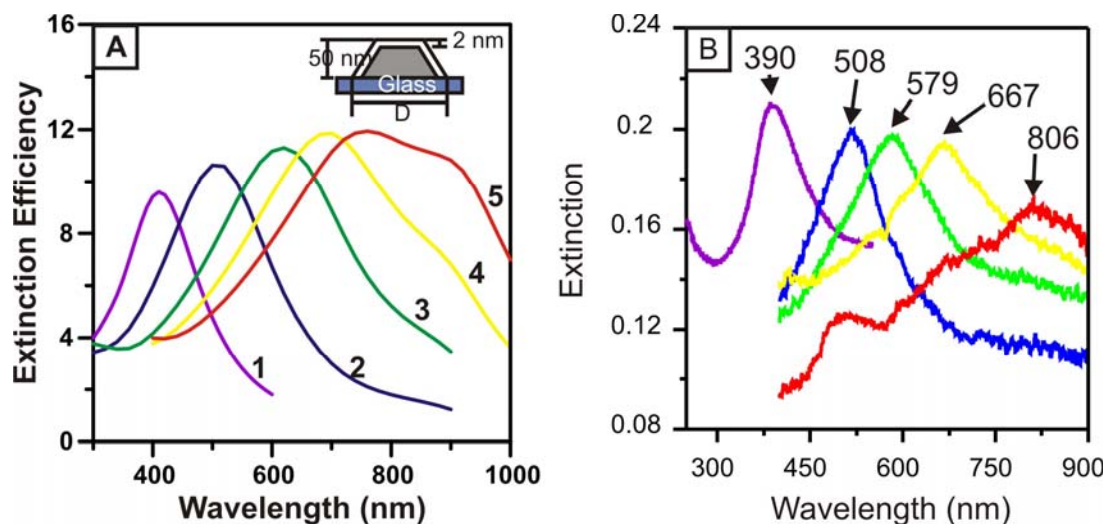


**Figure 6.8** (A) Extinction spectra of Al nanoparticle with varying widths calculated by DDA. Spectrum 1 (purple), width = 95 nm, spectrum 2 (blue), width = 136 nm; spectrum 3 (red), width = 174 nm; spectrum 4 (green), width = 206 nm; spectrum 5 (pink), width = 230 nm. (B) Extinction spectra of Al nanoparticle with varying widths measured with UV-vis spectroscopy. All spectra were collected in a  $N_2$  environment. Spectrum 1 (black),  $D = 280$  nm,  $\lambda_{\max} = 390$  nm; spectrum 2 (blue),  $D = 390$  nm,  $\lambda_{\max} = 508$  nm; spectrum 3 (green),  $D = 410$  nm,  $\lambda_{\max} = 579$  nm; spectrum 4 (yellow),  $D = 500$  nm,  $\lambda_{\max} = 667$  nm; and spectrum 5 (red),  $D = 590$  nm,  $\lambda_{\max} = 806$  nm.

addition, the calculated red spectrum in Figure 6.8B has  $\lambda_{\max}$  at  $\sim 760$  nm and shoulder at  $\sim 900$  nm. These results show that the Al interband transition greatly affect the LSPR band of Al nanoparticles. The same phenomenon was observed for Cu nanoparticles as shown in Figure 6.4 A and C.

### 6.3.3 Refractive Index Sensitivity of Aluminum Nanoparticles

As discussed in the previous chapters, LSPR of the nanoparticles is extremely sensitive to the external dielectric environment. The refractive index sensitivity (RI) of the Al nanoparticle arrays was investigated by DDA method. The extinction spectra of a single Al nanoparticle with 2 nm  $\text{Al}_2\text{O}_3$  (total width = 137 nm,  $h = 50$  nm) on a glass substrate were calculated in different dielectric environments. The environments are chosen as  $\text{N}_2$  (RI = 1.0),  $\text{H}_2\text{O}$  (RI = 1.33), ethanol (RI = 1.36), chloroform (RI = 1.45) and benzene (RI = 1.50). As shown in Figure 6.9A, the LSPR  $\lambda_{\max}$  shifts to lower energy when the dielectric constant of the environment increases. The extinction spectra of bare Al nanoparticles were also examined in different dielectric environments (spectra not shown). Figure 6.9 B shows the refractive index sensitivity of Al nanoparticle with 2 nm aluminum oxides (red line with circles) and bare Al nanoparticle (black line with triangles) in energy units (eV). The RI sensitivity of bare Al nanoparticle is 1.17 eV/RIU and that of Al nanoparticles with 2 nm oxides is 1.08 eV/RIU. The presence of 2 nm oxides does not significantly decrease the sensitivity of the Al nanoparticle. This result suggests that Al nanoparticles can potentially serve as UV LSPR sensing platforms.

### 6.3.4 Refractive Index Sensitivity Studied by Quasistatic Theory

As discussed in Chapter One, Two and Five, for an oblate spheroid in the quasistatic limit where the size of nanoparticle is smaller than the wavelength of light, the extinction cross section

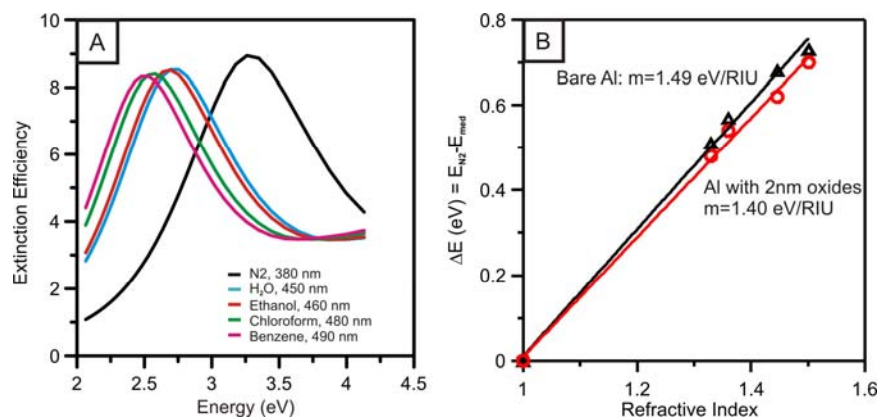


**Figure 6.9** (A) Extinction spectra of Al nanoparticle ( $D = 390$  nm,  $h = 50$  nm) on a glass substrate in different external environments calculated by DDA. Spectrum 1 (black), in N<sub>2</sub>,  $\lambda_{\text{max}} = 380$  nm; spectrum 2 (blue), in H<sub>2</sub>O,  $\lambda_{\text{max}} = 450$  nm; spectrum 3 (red), in ethanol,  $\lambda_{\text{max}} = 460$  nm; spectrum 4 (green), in chloroform,  $\lambda_{\text{max}} = 480$  nm; and spectrum 5 (pink), in benzene,  $\lambda_{\text{max}} = 490$  nm. (B) The change in  $\lambda_{\text{max}}$  (eV) versus the refractive index of the surroundings. Black line with triangles is for a bare Al nanoparticle and red line with circles is for Al nanoparticle with a 2 nm aluminum oxide layer.

$C_{ext}$  of a metallic spheroid in a homogenous medium is expressed by the following equation:<sup>10,68</sup>

$$C_{ext} \propto \frac{1}{\lambda} \text{Im} \left\{ \frac{\epsilon_m - \epsilon_o}{\epsilon_m + \chi \epsilon_o} \right\} \quad (6.1)$$

where  $\epsilon_m$  is the dielectric constant of metal,  $\epsilon_o$  is the dielectric constant of the surrounding medium, and  $\chi$  is a shape factor for the particle that has the value 2 for a sphere, and increases with increasing aspect ratio. When tuning  $\epsilon_o$ , we can calculate the RI sensitivity of the metals. Previous studies have revealed particles with LSPR  $\lambda_{\max}$  at longer wavelength have higher RI sensitivity than the particles with LSPR  $\lambda_{\max}$  at shorter wavelength. In order to compare the RI sensitivity of different metals,  $\chi$  is chosen differently for different metals so that their LSPR  $\lambda_{\max}$  are in similar wavelength range. Note that particles with larger aspect ratio have higher RI sensitivity; the method to choose  $\chi$  does not account this effect.

In this section, RI sensitivity of four metals is studied including Al, Ag, Au and Cu. The RI sensitivity of Al and Ag spheroid with LSPR  $\lambda_{\max}$  in UV wavelength range is calculated using Eq 6.1. Since Au and Cu interband transitions are at  $\sim 500$  nm and  $\sim 560$  nm, Au and Cu nanoparticles do not exhibit LSPR in UV wavelength range. Figure 6.10 A illustrates the RI sensitivity of Al (blue line with triangles) and Ag (red line with circles) spheroids. The parameter  $\chi$  is chosen as 15 for Al spheroid and 3 for Ag spheroid. The predicted RI sensitivity of Al spheroid is 126.0 nm/RIU while that of Ag spheroid is 66.1 nm/RIU. Even though that the aspect ratio of Al spheroid is much larger than that of Ag spheroid, for nanoparticles with LSPR  $\lambda_{\max}$  in UV wavelength range, Al nanoparticles are potentially better LSPR sensors than Ag nanoparticles, and have larger tunability of LSPR  $\lambda_{\max}$  in UV.

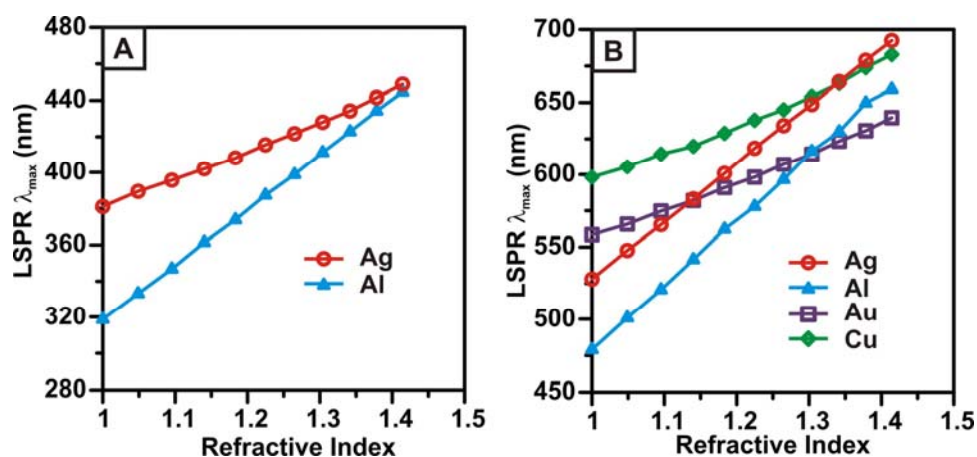


**Figure 6.10** (A) LSPR  $\lambda_{\max}$  of Ag and Al spheroid versus the refractive index of surroundings calculated by Eq. 6.1 with different  $\chi$  parameters. Red line with circles is for Ag and blue line with triangles is for Al. (B) LSPR  $\lambda_{\max}$  of Ag, Al, Au and Cu spheroid versus the refractive index of surroundings calculated by Eq. 6.1 with different  $\chi$  parameters. Red line with circles is for Ag, blue line with triangles is for Al, purple line with squares is for Au and green line with diamonds is for Cu.

For the visible wavelength range, the RI sensitivity of Al (blue line with triangles), Ag (red line with curves), Au (purple line with squares) and Cu (green line with diamonds) spheroids was calculated and plotted in Figure 6.10 B. The parameter  $\chi$  was chosen as 35, 10, 5 and 5 for Al, Ag, Au and Cu spheroids, respectively. The RI sensitivities of the Al, Ag, Au and Cu spheroids are 442.8 nm/RIU, 398.6 nm/RIU, 196.1 nm/RIU and 203.6 nm/RIU. The RI sensitivity of Al and Ag nanoparticles are comparable considering the aspect ratio of the Al spheroid is much larger than that of the Ag spheroid. Ag nanoparticles have larger LSPR tunability than Al nanoparticles in visible wavelength range. Al and Ag spheroids with a higher aspect ratio have a larger RI sensitivity than Au and Cu spheroids with lower aspect ratio. Au and Cu spheroids with the same aspect ratio have similar RI sensitivity. In the same dielectric environment, LSPR  $\lambda_{\max}$  of Au spheroid is at shorter wavelength comparing to Cu spheroid.

#### 6.3.5 LSPR of Al, Ag, Au and Cu NSL-Nanoparticles with Similar Geometry

NSL technique allows for fabricating nanoparticles of similar geometry with different materials. Figure 6.11A shows the first experimental comparison of the LSPR of the Al, Ag, Au, and Cu in  $N_2$  for a similar size and shape fabricated by NSL on a glass substrate where  $D = 390$  nm and  $h$  decreases from 50 nm. The order of LSPR  $\lambda_{\max}$  is Au (787 nm) > Cu (698 nm) > Ag (639 nm) > Al (598 nm). The LSPR peak of Al is broader than the noble metals because of the larger positive value of the imaginary part of its dielectric function in the visible region. The extinction spectra of the Al, Ag, Au, and Cu truncated tetrahedral particles (width = 90 nm,  $h = 50$  nm) were calculated by the DDA method and plotted in Figure 6.11B. The simulated LSPR  $\lambda_{\max}$  of the nanoparticles is also Au (665 nm) > Cu (655 nm) > Ag (610 nm) > Al (377 nm). However, the predicted LSPR  $\lambda_{\max}$  are at shorter wavelengths for all four metals, and the deviations of the Au and Al nanoparticle results from experiments are much larger than for the



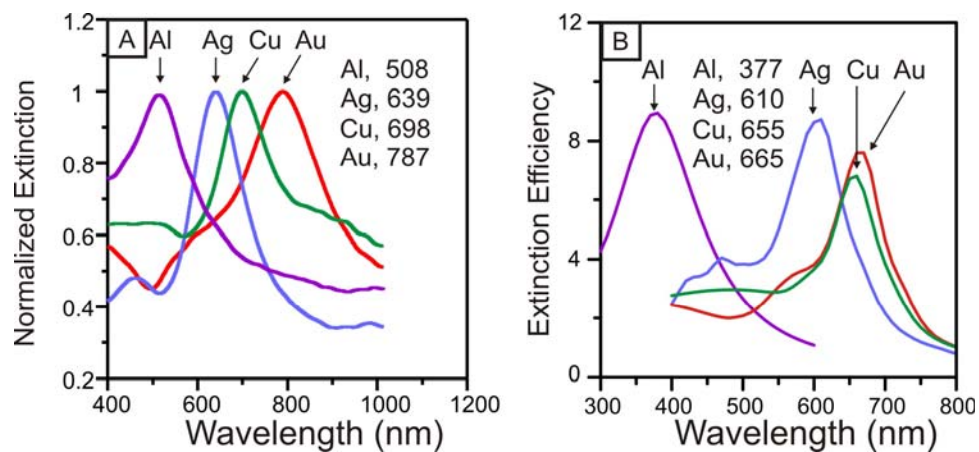


**Figure 6. 11** Comparison of the LSPR of Cu, Ag, Au, and Al for a similar size and shape obtained from experiment (A) and DDA calculations (B) ( $D = 390$  nm;  $h = 50$  nm; glass substrate;  $N_2$  environment).

Ag and Cu nanoparticles. This latter result probably arises because the truncated tetrahedral geometry assumption is not accurate for the Au and Al NSL-nanoparticles due to diffusion after deposition. Furthermore, for the Al nanoparticles, the effect of the ununiformly distributed oxide layer on the nanoparticle surface was not considered in the calculation. An interesting phenomenon was observed for the Cu and Au nanoparticles. As discussed in section 6.3.4, for Cu and Au spheroids with the same aspect ratio, the LSPR  $\lambda_{\max}$  of the Cu spheroid is at longer wavelength than the Au spheroid. However in the truncated tetrahedral particle case, the LSPR  $\lambda_{\max}$  is reversed such that the Cu nanoparticle LSPR  $\lambda_{\max}$  is at a shorter wavelength than the Au nanoparticle. This shows how nanoparticle shape plays an important role in determining the LSPR  $\lambda_{\max}$  of materials with similar dielectric properties in certain wavelength ranges.

## 6.4 Conclusions

The plasmonic properties of copper and aluminum nanoparticles fabricated by NSL are studied by UV-vis spectroscopy and electrodynamics theory. For copper nanoparticles, the presence of copper oxides layer greatly affect the LSPR, as demonstrated by both experiments and theory. By treatment with glacial acetic acid, the Cu oxides can be effectively removed. The LSPR of the Cu nanoparticles can be tuned by the in-plane width and out-of-plane height of the nanoparticles in the visible-NIR wavelength range. Theoretical predictions and experimental evidence show that aluminum nanoparticle arrays fabricated by NSL are capable of supporting surface plasmons in the UV-vis region. It has been demonstrated that the presence of a thin aluminum oxide layer leads to a red shift in the Al LSPR, while it does not significantly change the LSPR peak shape and intensity. The LSPR of Al nanoparticles can be tuned by the width of the nanoparticles. An electrodynamics study of the refractive index sensitivity of Al

nanoparticles shows that Al nanoparticles can be used as a UV LSPR sensing platform and as substrates for surface-enhance spectroscopies in the UV range. The RI sensitivity of Al, Ag, Au and Cu nanoparticles was calculated by quasistatic theory. Al nanoparticles have higher RI sensitivity in the UV than Ag nanoparticles. Au and Cu nanoparticles have similar RI sensitivity in visible, but smaller than the RI sensitivity of Ag nanoparticles. The LSPR of Cu, Ag, Au, and Al nanoparticles for a similar size and shape was compared in Figure 6.11; the LSPR  $\lambda_{\text{max}}$  show  $\text{Au} > \text{Cu} > \text{Ag} > \text{Al}$ . The versatility of the NSL technique allows for exploring the optical properties of more metals in the future.

## References:

- (1) Bohren, C. F.; Huffman, D. R. *Absorption and Scattering of Light by Small Particles*; John Wiley & Sons: New York, 1983.
- (2) Kreibig, U.; Vollmer, M. *Cluster Materials*; Springer-Verlag: Heidelberg, Germany, 1995; Vol. 25.
- (3) Schatz, G. C.; Young, M. A.; Van Duyne, R. P. Electromagnetic mechanism of SERS, *Topics in Applied Physics* **2006**, *103*, 19-46.
- (4) Schatz, G. C.; Van Duyne, R. P. In *Handbook of Vibrational Spectroscopy*; Chalmers, J. M., Griffiths, P. R., Eds.; Wiley: New York, 2002; Vol. 1, p 759-774.
- (5) Kreibig, U., Vollmer, M. *Optical Properties of Metal Clusters*; Springer-Verlag: Heidelberg, 1995; Vol. 25.
- (6) Kreibig, U. In *Handbook of Optical Properties*; Hummel, R. E., Wissmann, P., Eds.; CRC Press: Boca Raton, 1997; Vol. II, p 145-190.
- (7) Kreibig, U.; Gartz, M.; Hilger, A.; Hovel, H. In *Advances in Metal and Semiconductor Clusters*; Duncan, M. A., Ed.; JAI Press Inc.: Stamford, 1998; Vol. 4, p 345-393.
- (8) Willets, K. A.; Van Duyne, R. P. Localized surface plasmon resonance spectroscopy and sensing, *Annual Review of Physical Chemistry* **2007**, *58*, 267-297.
- (9) Chan, G. H.; Zhao, J.; Hicks, E. M.; Schatz, G. C.; Van Duyne, R. P. Plasmonic Properties of Copper Nanoparticles Fabricated by Nanosphere Lithography, *Nano Letters* **2007**, *7*, 1947-1952.
- (10) Huffman, C. F. B. a. D. R. *Absorption and Scattering of Light by Small Particles*; Wiley Interscience: New York, 1983.
- (11) Jensen, T.; Kelly, L.; Lazarides, A.; Schatz, G. C. Electrodynamics of noble metal nanoparticles and nanoparticle clusters, *Journal of Cluster Science* **1999**, *10*, 295-317.
- (12) Jensen, T. R.; Duval, M. L.; Kelly, K. L.; Lazarides, A. A.; Schatz, G. C.; Van Duyne, R. P. Nanosphere lithography: Effect of the external dielectric medium on the surface plasmon resonance spectrum of a periodic array of silver nanoparticles, *Journal of Physical Chemistry B* **1999**, *103*, 9846-9853.
- (13) Jensen, T. R.; Malinsky, M. D.; Haynes, C. L.; Van Duyne, R. P. Nanosphere Lithography: Tunable Localized Surface Plasmon Resonance Spectra of Silver Nanoparticles, *Journal of Physical Chemistry B* **2000**, *104*, 10549-10556.

- (14) Kelly, K. L.; Coronado, E.; Zhao, L.; Schatz, G. C. The Optical Properties of Metal Nanoparticles: The Influence of Size, Shape, and Dielectric Environment, *Journal of Physical Chemistry B* **2003**, *107*, 668-677.
- (15) Kelly, K. L.; Jensen, T. R.; Lazarides, A. A.; Schatz, G. C. Modeling metal nanoparticles optical properties, *Metal Nanoparticles* **2002**, 89-118.
- (16) Yguerabide, J.; Yguerabide, E. E. Light-scattering submicroscopic particles as highly fluorescent analogs and their use as tracer labels in clinical and biological applications - I. Theory, *Analytical Biochemistry* **1998**, *262*, 137-156.
- (17) Maier, S. A.; Brongersma, M. L.; Kik, P. G.; Meltzer, S.; Requicha, A. A. G.; Koel, B. E.; Atwater, H. A. Plasmonics - A route to nanoscale optical devices (vol 13, pg 1501, 2001), *Advanced Materials* **2003**, *15*, 562-562.
- (18) Maier, S. A.; Kik, P. G.; Atwater, H. A.; Meltzer, S.; Harel, E.; Koel, B. E.; Requicha, A. A. G. Local detection of electromagnetic energy transport below the diffraction limit in metal nanoparticle plasmon waveguides, *Nature Materials* **2003**, *2*, 229-232.
- (19) Smolyaninov, I. I.; Hung, Y.-J.; Davis, C. C. Surface plasmon dielectric waveguides, *Applied Physics Letters* **2005**, *87*, 241106/1-241106/3.
- (20) Krenn, J. R. Nanoparticle waveguides. Watching energy transfer, *Nature Materials* **2003**, *2*, 210-211.
- (21) Barnes, W. L.; Dereux, A.; Ebbesen, T. W. Surface plasmon subwavelength optics, *Nature* **2003**, *424*, 824-830.
- (22) Ozbay, E. Plasmonics: Merging photonics and electronics at nanoscale dimensions, *Science* **2006**, *311*, 189-193.
- (23) Vasseur, J. O.; Akjouj, A.; Dobrzynski, L.; Djafari-Rouhani, B.; El Boudouti, E. H. Photon, electron, magnon, phonon and plasmon mono-mode circuits, *Surface Science Reports* **2004**, *54*, 1-156.
- (24) Lezec, H. J.; Degiron, A.; Devaux, E.; Linke, R. A.; Martin-Moreno, L.; Garcia-Vidal, F. J.; Ebbesen, T. W. Beaming light from a subwavelength aperture, *Science* **2002**, *297*, 820-822.
- (25) Pettinger, B.; Ren, B.; Picardi, G.; Schuster, R.; Ertl, G. Nanoscale probing of adsorbed species by tip-enhanced Raman spectroscopy, *Physical Review Letters* **2004**, *92*, -.
- (26) McFarland, A. D.; Van Duyne, R. P. Single silver nanoparticles as real-time optical sensors with zeptomole sensitivity, *Nano Letters* **2003**, *3*, 1057-1062.

- (27) Dieringer, J. A.; McFarland, A. D.; Shah, N. C.; Stuart, D. A.; Whitney, A. V.; Yonzon, C. R.; Young, M. A.; Zhang, X. Y.; Van Duyne, R. P. Surface enhanced Raman spectroscopy: new materials, concepts, characterization tools, and applications, *Faraday Discuss.* **2006**, *132*, 9-26.
- (28) Zhang, X. Y.; Zhao, J.; Whitney, A. V.; Elam, J. W.; Van Duyne, R. P. Ultrastable substrates for surface-enhanced Raman spectroscopy: Al<sub>2</sub>O<sub>3</sub> overlayers fabricated by atomic layer deposition yield improved anthrax biomarker detection, *Journal of the American Chemical Society* **2006**, *128*, 10304-10309.
- (29) McFarland, A. D.; Young, M. A.; Dieringer, J. A.; Van Duyne, R. P. Wavelength-scanned surface-enhanced Raman excitation spectroscopy, *Journal of Physical Chemistry B* **2005**, *109*, 11279-11285.
- (30) Cao, Y. C.; Jin, R.; Mirkin, C. A. Nanoparticles with Raman spectroscopic fingerprints for DNA and RNA detection, *Science* **2002**, *297*, 1536-1540.
- (31) Yonzon Chanda, R.; Haynes Christy, L.; Zhang, X.; Walsh Joseph, T., Jr.; Van Duyne Richard, P. A glucose biosensor based on surface-enhanced Raman scattering: improved partition layer, temporal stability, reversibility, and resistance to serum protein interference, *Analytical Chemistry* **2004**, *76*, 78-85.
- (32) Haes, A. J.; Chang, L.; Klein, W. L.; Van Duyne, R. P. Detection of a biomarker for Alzheimer's disease from synthetic and clinical samples using a nanoscale optical biosensor, *Journal of the American Chemical Society* **2005**, *127*, 2264-2271.
- (33) Zhao, J.; Zhang, X. Y.; Yonzon, C. R.; Haes, A. J.; Van Duyne, R. P. Localized surface plasmon resonance biosensors, *Nanomedicine* **2006**, *1*, 219-228.
- (34) Brockman, J. M.; Nelson, B. P.; Corn, R. M. Surface plasmon resonance imaging measurements of ultrathin organic films, *Annual Review of Physical Chemistry* **2000**, *51*, 41-63.
- (35) Haes, A. J.; Van Duyne, R. P. A Nanoscale Optical Biosensor: Sensitivity and Selectivity of an Approach Based on the Localized Surface Plasmon Resonance Spectroscopy of Triangular Silver Nanoparticles, *Journal of the American Chemical Society* **2002**, *124*, 10596 - 10604.
- (36) Malinsky, M. D.; Kelly, K. L.; Schatz, G. C.; Van Duyne, R. P. Chain Length Dependence and Sensing Capabilities of the Localized Surface Plasmon Resonance of Silver Nanoparticles Chemically Modified with Alkanethiol Self-Assembled Monolayers, *Journal of the American Chemical Society* **2001**, *123*, 1471-1482.
- (37) Malinsky, M. D.; Kelly, K. L.; Schatz, G. C.; Van Duyne, R. P. Nanosphere Lithography: Effect of Substrate on the Localized Surface Plasmon Resonance Spectrum of Silver Nanoparticles, *Journal of Physical Chemistry B* **2001**, *105*, 2343-2350.

- (38) Link, S.; Wang, Z. L.; El-Sayed, M. A. Alloy Formation of Gold-Silver Nanoparticles and the Dependence of the Plasmon Absorption on Their Composition, *J. Phys. Chem. B* **1999**, *103*, 3529-3533.
- (39) Haynes, C. L.; Van Duyne, R. P. Nanosphere lithography: A versatile nanofabrication tool for studies of size-dependent nanoparticle optics, *Journal of Physical Chemistry B* **2001**, *105*, 5599-5611.
- (40) Metraux, G. S.; Mirkin, C. A. Rapid thermal synthesis of silver nanoprisms with chemically tailorable thickness, *Advanced Materials (Weinheim, Germany)* **2005**, *17*, 412-415.
- (41) Jin, R.; Cao, Y. C.; Hao, E.; Metraux, G. S.; Schatz, G. C.; Mirkin, C. A. Controlling Anisotropic Nanoparticle Growth Through Plasmon Excitation, *Nature* **2003**, *425*, 487-490.
- (42) Hulteen, J. C.; Treichel, D. A.; Smith, M. T.; Duval, M. L.; Jensen, T. R.; Van Duyne, R. P. Nanosphere lithography: Size-tunable silver nanoparticle and surface cluster arrays, *Journal of Physical Chemistry B* **1999**, *103*, 3854-3863.
- (43) Hulteen, J. C.; Van Duyne, R. P. Nanosphere Lithography: A Materials General Fabrication Process for Periodic Particle Array Surfaces, *Journal of Vacuum Science and Technology A* **1995**, *13*, 1553-1558.
- (44) Sherry, L. J.; Chang, S.-H.; Schatz, G. C.; Van Duyne, R. P.; Wiley, B. J.; Xia, Y. Localized Surface Plasmon Resonance Spectroscopy of Single Silver Nanocubes, *Nano Letters* **2005**, *5*, 2034-2038.
- (45) Sherry, L. J.; Jin, R.; Mirkin, C. A.; Schatz, G. C.; Van Duyne, R. P. Localized Surface Plasmon Resonance Spectroscopy of Single Silver Triangular Nanoprisms, *Nano Letters* **2006**, *6*, 2060-2065.
- (46) Xu, G.; Chen, Y.; Tazawa, M.; Jin, P. Surface Plasmon Resonance of Silver Nanoparticles on Vanadium Dioxide, *Journal of Physical Chemistry B* **2006**, *110*, 2051-2056.
- (47) Pinchuk, A.; Hilger, A.; von Plessen, G.; Kreibig, U. Substrate effect on the optical response of silver nanoparticles, *Nanotechnology* **2004**, *15*, 1890-1896.
- (48) Huang, W.; Qian, W.; El-Sayed, M. A. The Optically Detected Coherent Lattice Oscillations in Silver and Gold Monolayer Periodic Nanoprism Arrays: The Effect of Interparticle Coupling, *Journal of Physical Chemistry B* **2005**, *109*, 18881-18888.
- (49) Zhao, L.; Kelly, K. L.; Schatz, G. C. The Extinction Spectra of Silver Nanoparticle Arrays: Influence of Array Structure on Plasmon Resonance Wavelength and Width, *Journal of Physical Chemistry B* **2003**, *107*, 7343-7350.

- (50) Haynes, C. L.; McFarland, A. D.; Zhao, L.; Van Duyne, R. P.; Schatz, G. C.; Gunnarsson, L.; Prikulis, J.; Kasemo, B.; Kaell, M. Nanoparticle Optics: The Importance of Radiative Dipole Coupling in Two-Dimensional Nanoparticle Arrays, *Journal of Physical Chemistry B* **2003**, *107*, 7337-7342.
- (51) Gunnarsson, L.; Rindzevicius, T.; Prikulis, J.; Kasemo, B.; Kaell, M.; Zou, S.; Schatz, G. C. Confined Plasmons in Nanofabricated Single Silver Particle Pairs: Experimental Observations of Strong Interparticle Interactions, *Journal of Physical Chemistry B* **2005**, *109*, 1079-1087.
- (52) Fang, S.; Lee, H. J.; Wark, A. W.; Kim, H. M.; Corn, R. M. Determination of ribonuclease H surface enzyme kinetics by surface plasmon resonance imaging and surface plasmon fluorescence spectroscopy, *Analytical Chemistry* **2005**, *77*, 6528-6534.
- (53) Lee, H. J.; Nedelkov, D.; Corn, R. M. Surface plasmon resonance imaging measurements of antibody arrays for the multiplexed detection of low molecular weight protein biomarkers, *Analytical Chemistry* **2006**, *78*, 6504-6510.
- (54) Li, Y.; Lee, H. J.; Corn, R. M. Detection of protein biomarkers using RNA aptamer microarrays and enzymatically amplified surface plasmon resonance imaging, *Analytical Chemistry* **2007**, *79*, 1082-1088.
- (55) Seferyan, H. Y.; Zadoyan, R.; Wark, A. W.; Corn, R. A.; Apkarian, V. A. Diagnostics of spectrally resolved transient absorption: Surface plasmon resonance of metal nanoparticles, *Journal of Physical Chemistry C* **2007**, *111*, 18525-18532.
- (56) Yonzon, C. R.; Jeoungf, E.; Zou, S. L.; Schatz, G. C.; Mrksich, M.; Van Duyne, R. P. A comparative analysis of localized and propagating surface plasmon resonance sensors: The binding of concanavalin a to a monosaccharide functionalized self-assembled monolayer, *Journal of the American Chemical Society* **2004**, *126*, 12669-12676.
- (57) Wiley, B. J.; Im, S. H.; Li, Z.-Y.; McLellan, J.; Siekkinen, A.; Xia, Y. Maneuvering the Surface Plasmon Resonance of Silver Nanostructures through Shape-Controlled Synthesis, *Journal of Physical Chemistry B* **2006**, *110*, 15666-15675.
- (58) Wiley, B. J.; Xiong, Y.; Li, Z.-Y.; Yin, Y.; Xia, Y. Right Bipyramids of Silver: A New Shape Derived from Single Twinned Seeds, *Nano Letters* **2006**, *6*, 765-768.
- (59) Nehl, C. L.; Liao, H.; Hafner, J. H. Optical Properties of Star-Shaped Gold Nanoparticles, *Nano Letters* **2006**, *6*, 683-688.
- (60) Jin, R.; Cao, Y.; Mirkin, C. A.; Kelly, K. L.; Schatz, G. C.; Zheng, J. G. Photoinduced conversion of silver nanospheres to nanoprisms, *Science* **2001**, *294*, 1901-1903.



- (61) Jeanmaire, D. L.; Van Duyne, R. P. Surface Raman spectroelectrochemistry. Part I. Heterocyclic, aromatic, and aliphatic amines adsorbed on the anodized silver electrode, *Journal of Electroanalytical Chemistry and Interfacial Electrochemistry* **1977**, *84*, 1-20.
- (62) Nie, S.; Emory, S. R. Probing single molecules and single nanoparticles by surface-enhanced Raman scattering, *Science* **1997**, *275*, 1102-1106.
- (63) Moskovits, M. Surface-Enhanced Spectroscopy, *Reviews of Modern Physics* **1985**, *57*, 783-826.
- (64) Kneipp, K.; Wang, Y.; Kneipp, H.; Perelman, L. T.; Itzkan, I.; Dasari, R.; Feld, M. S. Single molecule detection using surface-enhanced Raman scattering (SERS), *Physical Review Letters* **1997**, *78*, 1667-1670.
- (65) Dieringer, J. A.; Lettan, R. B.; Scheidt, K. A.; Van Duyne, R. P. A frequency domain existence proof of single-molecule surface-enhanced Raman Spectroscopy, *Journal of the American Chemical Society* **2007**, *129*, 16249-16256.
- (66) Haes, A. J.; Zou, S.; Schatz, G. C.; Van Duyne, R. P. Nanoscale Optical Biosensor: Short Range Distance Dependence of the Localized Surface Plasmon Resonance of Noble Metal Nanoparticles, *Journal of Physical Chemistry B* **2004**, *108*, 6961-6968.
- (67) Haes, A. J.; Zou, S.; Schatz, G. C.; Van Duyne, R. P. A Nanoscale Optical Biosensor: The Long Range Distance Dependence of the Localized Surface Plasmon Resonance of Noble Metal Nanoparticles, *Journal of Physical Chemistry B* **2004**, *108*, 109-116.
- (68) Mie, G. Contributions to the Optics of Turbid Media, Especially Colloidal Metal Solutions, *Annalen der Physik (Weinheim, Germany)* **1908**, *25*, 377-445.
- (69) Kerker, M. *The Scattering of Light and Other Electromagnetic Radiation*; Academic: New York, 1969.
- (70) Voshchinnikov, N. V.; Farafonov, V. G. Optical properties of spheroidal particles, *Astrophys. Space Sci.* **1993**, *204*, 19-86.
- (71) Wang, D. S.; Kerker, M. Enhanced Raman-Scattering by Molecules Adsorbed at the Surface of Colloidal Spheroids, *Physical Review B* **1981**, *24*, 1777-1790.
- (72) Zeman, E. J.; Carron, K. T.; Schatz, G. C.; Vanduyne, R. P. A Surface Enhanced Resonance Raman-Study of Cobalt Phthalocyanine on Rough Ag Films - Theory and Experiment, *Journal of Chemical Physics* **1987**, *87*, 4189-4200.

- (73) Zhao, J.; Jensen, L.; Sung, J. H.; Zou, S. L.; Schatz, G. C.; Van Duyne, R. P. Interaction of plasmon and molecular resonances for rhodamine 6G adsorbed on silver nanoparticles, *Journal of the American Chemical Society* **2007**, *129*, 7647-7656.
- (74) Frens, G. Controlled Nucleation for Regulation of Particle-Size in Monodisperse Gold Suspensions, *Nature-Physical Science* **1973**, *241*, 20-22.
- (75) Hao, E.; Kelly, K. L.; Hupp, J. T.; Schatz, G. C. Synthesis of Silver Nanodisks Using Polystyrene Mesospheres as Templates, *Journal of the American Chemical Society* **2002**, *124*, 15182-15183.
- (76) Song, J. H.; Kim, F.; Kim, D.; Yang, P. D. Crystal overgrowth on gold nanorods: Tuning the shape, facet, aspect ratio, and composition of the nanorods, *Chemistry-a European Journal* **2005**, *11*, 910-916.
- (77) Kim, F.; Song, J. H.; Yang, P. D. Photochemical synthesis of gold nanorods, *Journal of the American Chemical Society* **2002**, *124*, 14316-14317.
- (78) Sun, Y. G.; Xia, Y. N. Shape-controlled synthesis of gold and silver nanoparticles, *Science* **2002**, *298*, 2176-2179.
- (79) Xu, H. X.; Bjerneld, E. J.; Kall, M.; Borjesson, L. Spectroscopy of single hemoglobin molecules by surface enhanced Raman scattering, *Physical Review Letters* **1999**, *83*, 4357-4360.
- (80) Michaels, A. M.; Nirmal, M.; Brus, L. E. Surface enhanced Raman spectroscopy of individual rhodamine 6G molecules on large Ag nanocrystals, *Journal of the American Chemical Society* **1999**, *121*, 9932-9939.
- (81) Xu, H. X.; Aizpurua, J.; Kall, M.; Apell, P. Electromagnetic contributions to single-molecule sensitivity in surface-enhanced Raman scattering, *Physical Review E* **2000**, *62*, 4318-4324.
- (82) Haes, A. J.; Zhao, J.; Zou, S. L.; Own, C. S.; Marks, L. D.; Schatz, G. C.; Van Duyne, R. P. Solution-phase, triangular Ag nanotriangles fabricated by nanosphere lithography, *Journal of Physical Chemistry B* **2005**, *109*, 11158-11162.
- (83) Henzie, J.; Shuford, K. L.; Kwak, E. S.; Schatz, G. C.; Odom, T. W. Manipulating the optical properties of pyramidal nanoparticle arrays, *Journal of Physical Chemistry B* **2006**, *110*, 14028-14031.
- (84) Odom, T. W.; Henzie, J.; Babayan, Y.; Greyson, E. C.; Kwak, E. S. Optical properties of surface-patterned nanostructures, *Talanta* **2005**, *67*, 507-513.

- (85) Hao, E.; Li, S.; Bailey, R. C.; Zou, S.; Schatz, G. C.; Hupp, J. T. Optical Properties of Metal Nanoshells, *Journal of Physical Chemistry B* **2004**, *108*, 1224-1229.
- (86) Hao, E.; Schatz, G. C. Electromagnetic Fields Around Silver Nanoparticles and Dimers, *Journal of Chemical Physics* **2004**, *120*, 357-366.
- (87) Hicks, E. M.; Zou, S.; Schatz, G. C.; Spears, K. G.; Van Duyne, R. P.; Gunnarsson, L.; Rindzevicius, T.; Kasemo, B.; Kaell, M. Controlling Plasmon Line Shapes through Diffractive Coupling in Linear Arrays of Cylindrical Nanoparticles Fabricated by Electron Beam Lithography, *Nano Letters* **2005**, *5*, 1065-1070.
- (88) Shumaker-Parry, J. S.; Rochholz, H.; Kreiter, M. Fabrication of crescent-shaped optical antennas, *Advanced Materials* **2005**, *17*, 2131-+.
- (89) Haynes, C. L.; McFarland, A. D.; Smith, M. T.; Hulteen, J. C.; Van Duyne, R. P. Angle-resolved nanosphere lithography: Manipulation of nanoparticle size, shape, and interparticle spacing, *Journal of Physical Chemistry B* **2002**, *106*, 1898-1902.
- (90) Whitney, A. V.; Elam, J. W.; Stair, P. C.; Van Duyne, R. P. Toward a thermally robust operando surface-enhanced Raman Spectroscopy substrate, *Journal of Physical Chemistry C* **2007**, *111*, 16827-16832.
- (91) Whitney, A. V.; Elam, J. W.; Zou, S. L.; Zinovev, A. V.; Stair, P. C.; Schatz, G. C.; Van Duyne, R. P. Localized surface plasmon resonance nanosensor: A high-resolution distance-dependence study using atomic layer deposition, *Journal of Physical Chemistry B* **2005**, *109*, 20522-20528.
- (92) Whitney, A. V.; Myers, B. D.; Van Duyne, R. P. Sub-100 nm Triangular Nanopores Fabricated with the Reactive Ion Etching Variant of Nanosphere Lithography and Angle-Resolved Nanosphere Lithography, *Nano Letters* **2004**, *4*, 1507-1511.
- (93) Hicks, E. M.; Zhang, X. Y.; Zou, S. L.; Lyandres, O.; Spears, K. G.; Schatz, G. C.; Van Duyne, R. P. Plasmonic properties of film over nanowell surfaces fabricated by nanosphere lithography, *Journal of Physical Chemistry B* **2005**, *109*, 22351-22358.
- (94) Kwak, E. S.; Henzie, J.; Chang, S. H.; Gray, S. K.; Schatz, G. C.; Odom, T. W. Surface plasmon standing waves in large-area subwavelength hole arrays, *Nano Letters* **2005**, *5*, 1963-1967.
- (95) Purcell, E. M.; Pennypacker, C. R. Scattering and absorption of light by nonspherical grains, *The Astrophysics Journal* **1973**, *186*, 705-714.
- (96) Draine, B. F., J. Discrete-Dipole Approximation for Scattering Calculations, *Journal of the Optical Society of America. A* **1994**, *11*, 1491-1499.

- (97) Goodman, J. J.; Draine, B. T.; Flatau, P. J. Application of the fast Fourier transformation techniques to the discrete dipole approximation, *Optics Letters* **1991**, *16*, 1198-1200.
- (98) Kelly, K. L.; Lazarides, A. A.; Schatz, G. C. Computational electromagnetics of metal nanoparticles and their aggregates, *Computing in Science & Engineering* **2001**, *3*, 67-73.
- (99) Zou, S.; Schatz, G. C. Metal nanoparticle array waveguides: Proposed structures for subwavelength devices, *Physical Review B: Condensed Matter and Materials Physics* **2006**, *74*, 125111/1-125111/5.
- (100) Zhao, L.; Zou, S.; Hao, E.; Schatz, G. C. Electrodynamics in computational chemistry, *Theory Appl. Comput. Chem.: First Forty Years FIELD Full Journal Title: Theory and Applications of Computational Chemistry: The First Forty Years* **2005**, 47-65.
- (101) Brevnov, D. A.; Bungay, C. Diameter-Dependent Optical Constants of Gold Mesoparticles Electrodeposited on Aluminum Films Containing Copper, *Journal of Physical Chemistry B* **2005**, *109*, 14529-14535.
- (102) Turner, A. P. F. Biochemistry - Biosensors sense and sensitivity, *Science* **2000**, *290*, 1315-1317.
- (103) Zhao, J.; Das, A.; Zhang, X.; Schatz, G. C.; Sligar, S. G.; Van Duyne, R. P. Resonance surface plasmon spectroscopy: Low molecular weight substrate binding to cytochrome P450, *Journal of the American Chemical Society* **2006**, *128*, 11004-11005.
- (104) Bharadwaj, P.; Anger, P.; Novotny, L. Nanoplasmonic enhancement of single-molecule fluorescence, *Nanotechnology* **2007**, *18*, -.
- (105) Gratzel, M. Photoelectrochemical cells, *Nature* **2001**, *414*, 338-344.
- (106) Gratzel, M. Dye-sensitized solid-state heterojunction solar cells, *Mrs Bulletin* **2005**, *30*, 23-27.
- (107) Martinson, A. B. F.; McGarrah, J. E.; Parpia, M. O. K.; Hupp, J. T. Dynamics of charge transport and recombination in ZnO nanorod array dye-sensitized solar cells, *Physical Chemistry Chemical Physics* **2006**, *8*, 4655-4659.
- (108) Oregan, B.; Gratzel, M. A Low-Cost, High-Efficiency Solar-Cell Based on Dye-Sensitized Colloidal TiO<sub>2</sub> Films, *Nature* **1991**, *353*, 737-740.
- (109) Ishikawa, K.; Wen, C. J.; Yamada, K.; Okubo, T. The photocurrent of dye-sensitized solar cells enhanced by the surface plasmon resonance, *Journal of Chemical Engineering of Japan* **2004**, *37*, 645-649.

- (110) Morfa, A. J.; Rowlen, K. L.; Reilly, T. H.; Romero, M. J.; van de Lagemaat, J. Plasmon-enhanced solar energy conversion in organic bulk heterojunction photovoltaics, *Applied Physics Letters* **2008**, *92*, -.
- (111) Pillai, S.; Catchpole, K. R.; Trupke, T.; Green, M. A. Surface plasmon enhanced silicon solar cells, *Journal of Applied Physics* **2007**, *101*, -.
- (112) Ambjornsson, T.; Mukhopadhyay, G.; Apell, S. P.; Kall, M. Resonant coupling between localized plasmons and anisotropic molecular coatings in ellipsoidal metal nanoparticles, *Physical Review B* **2006**, *73*, 085421-1-10.
- (113) Haes, A. J.; Zou, S.; Zhao, J.; Schatz, G. C.; Van Duyne, R. P. Localized surface plasmon resonance spectroscopy near molecular resonances, *Journal of the American Chemical Society* **2006**, *128*, 10905-10914.
- (114) Wiederrecht, G. P.; Wurtz, G. A.; Hranisavljevic, J. Coherent coupling of molecular excitons to electronic polarizations of noble metal nanoparticles, *Nano Letters* **2004**, *4*, 2121-2125.
- (115) Wurtz, G. A.; Evans, P. R.; Hendren, W.; Atkinson, R.; Dickson, W.; Pollard, R. J.; Zayats, A. V.; Harrison, W.; Bower, C. Molecular plasmonics with tunable exciton-plasmon coupling strength in J-aggregate hybridized Au nanorod assemblies, *Nano Letters* **2007**, *7*, 1297-1303.
- (116) Liu, G. L.; Long, Y. T.; Choi, Y.; Kang, T.; Lee, L. P. Quantized plasmon quenching dips nanospectroscopy via plasmon resonance energy transfer, *Nature Methods* **2007**, *4*, 1015-1017.
- (117) Kelley, A. M. A molecular spectroscopic description of optical spectra of J-aggregated dyes on gold nanoparticles, *Nano Letters* **2007**, *7*, 3235-3240.
- (118) In *Handbook of Optical Constants of Solids*; Palik, E. D., Ed.; Academic Press: New York, 1985, p 350-356.
- (119) Agostiano, A.; Mavelli, F.; Milano, F.; Giotta, L.; Trotta, M.; Nagy, L.; Maroti, P. PH-sensitive fluorescent dye as probe for proton uptake in photosynthetic reaction centers, *Bioelectrochemistry* **2004**, *63*, 125-128.
- (120) Beletskii, A.; Cooper, M.; Sriraman, P.; Chiriac, C.; Zhao, L. H.; Abbot, S.; Yu, L. M. High-throughput phagocytosis assay utilizing a pH-sensitive fluorescent dye, *Biotechniques* **2005**, *39*, 894-897.
- (121) Briggs, M. S.; Burns, D. D.; Cooper, M. E.; Gregory, S. J. A pH sensitive fluorescent cyanine dye for biological applications, *Physical Chemistry Chemical Physics* **2000**, *2*, 2323-2324.

- (122) Kuwana, E.; Liang, F.; Sevick-Muraca, E. M. Fluorescence lifetime spectroscopy of a pH-sensitive dye encapsulated in hydrogel beads, *Biotechnology Progress* **2004**, *20*, 1561-1566.
- (123) Song, A.; Parus, S.; Kopelman, R. High-performance fiber optic pH microsensors for practical physiological measurements using a dual-emission sensitive dye, *Analytical Chemistry* **1997**, *69*, 863-867.
- (124) Antoine, M. D.; Devanathan, S.; Patonay, G. Spectroscopic Studies of a Polarity-Sensitive Pyrenyl Dye, *Microchemical Journal* **1992**, *45*, 36-43.
- (125) Boyer, A. E.; Devanathan, S.; Patonay, G. Determination of Cmc of Surfactants Using Polarity Sensitive Aryl Dye, *Analytical Letters* **1991**, *24*, 701-723.
- (126) Huber, C.; Werner, T.; Krause, C.; Wolfbeis, O. S. Novel chloride-selective optode based on polymer-stabilised emulsions doped with a lipophilic fluorescent polarity-sensitive dye, *Analyst* **1999**, *124*, 1617-1622.
- (127) Mohr, G. J.; Wolfbeis, O. S. Effects of the polymer matrix on an optical nitrate sensor based on a polarity-sensitive dye, *Sensors and Actuators B-Chemical* **1996**, *37*, 103-109.
- (128) Dahne, L.; Horvath, A.; Weiser, G. Influence of Aggregation on the Optical-Spectra of a Polymethine Dye in Single-Crystals, *Chemical Physics* **1995**, *196*, 307-316.
- (129) Diaz-Flores, L. L.; Horley, P. P.; Gonzalez-Hernandez, J.; Perez-Bueno, J. J.; Vorobiev, Y. V.; Gorley, P. M. Molecular aggregation and shape effects in the optical spectra of organic dye molecules in SiO<sub>2</sub> and SiO<sub>2</sub>-PMMA matrices, *Journal of Physics and Chemistry of Solids* **2003**, *64*, 2409-2415.
- (130) Martinez, V. M.; Arbeloa, F. L.; Prieto, J. B.; Arbeloa, I. L. Characterization of rhodamine 6G aggregates intercalated in solid thin films of laponite clay. 2 - Fluorescence spectroscopy, *Journal of Physical Chemistry B* **2005**, *109*, 7443-7450.
- (131) Lipscomb, J. D.; Gunsalus, I. C. Structural Aspects of Active-Site of Cytochrome P-450Cam, *Drug Metabolism and Disposition* **1973**, *1*, 1-5.
- (132) Shimomura, M.; Honma, A.; Kondo, S.; Shinohara, E.; Tajima, N.; Koshiishi, K. Design of Ion Sensor-Based on Langmuir-Blodgett-Films Having Potential-Sensitive Dye - Effect of Surface-Treatment of Solid Substrate on Potassium-Ion Sensing, *Sensors and Actuators B-Chemical* **1993**, *14*, 629-631.
- (133) Dunham, P.; Babiartz, P.; Israel, A.; Zerial, A.; Weissmann, G. Membrane-Fusion - Studies with a Calcium-Sensitive Dye, Arsenazoi, in Liposomes, *Proceedings of the National Academy of Sciences of the United States of America* **1977**, *74*, 1580-1584.

- (134) Ellis, A. L.; Mason, J. C.; Lee, H. W.; Streckowski, L.; Patonay, G.; Choi, H.; Yang, J. J. Design, synthesis, and characterization of a calcium-sensitive near infrared dye, *Talanta* **2002**, *56*, 1099-1107.
- (135) Zollinger, H. *Color Chemistry: Syntheses, Properties and Applications of Organic Dyes and Pigments* 3rd ed.; Wiley-VCH: Weinheim, Germany, 2001.
- (136) Fraser, S. E. Crystal gazing in optical microscopy, *Nature Biotechnology* **2003**, *21*, 1272-1273.
- (137) Hutter, E.; Fendler, J. H. Exploitation of localized surface plasmon resonance, *Advanced Materials* **2004**, *16*, 1685-1706.
- (138) Riboh, J. C.; Haes, A. J.; McFarland, A. D.; Yonzon, C. R.; Van Duyne, R. P. A nanoscale optical biosensor: Real-time immunoassay in physiological buffer enabled by improved nanoparticle adhesion, *Journal of Physical Chemistry B* **2003**, *107*, 1772-1780.
- (139) Dahlin, A.; Zach, M.; Rindzevicius, T.; Kall, M.; Sutherland, D. S.; Hook, F. Localized surface plasmon resonance sensing of lipid-membrane-mediated biorecognition events, *Journal of the American Chemical Society* **2005**, *127*, 5043-5048.
- (140) Zhao, J.; Das, A.; Zhang, X. Y.; Schatz, G. C.; Sligar, S. G.; Van Duyne, R. P. Resonance surface plasmon spectroscopy: Low molecular weight substrate binding to cytochrome P450, *Journal of the American Chemical Society* **2006**, *128*, 11004-11005.
- (141) Lin, H. Y.; Chen, C. T.; Chen, Y. C. Detection of phosphopeptides by localized surface plasma resonance of titania-coated gold nanoparticles immobilized on glass substrates, *Analytical Chemistry* **2006**, *78*, 6873-6878.
- (142) Futamata, M.; Maruyama, F.; Ishikawa, M. Adsorbed sites of individual molecules on Ag nanoparticles in single molecule sensitivity-surface-enhanced Raman scattering, *Journal of Physical Chemistry B* **2004**, *108*, 13119-13127.
- (143) Haynes, C. L.; Van Duyne, R. P. Plasmon-sampled surface-enhanced Raman excitation spectroscopy, *Journal of Physical Chemistry B* **2003**, *107*, 7426-7433.
- (144) Hildebrandt, P.; Stockburger, M. Surface-Enhanced Resonance Raman-Spectroscopy of Rhodamine-6G Adsorbed on Colloidal Silver, *Journal of Physical Chemistry* **1984**, *88*, 5935-5944.
- (145) Emory, S. R.; Haskins, W. E.; Nie, S. M. Direct observation of size-dependent optical enhancement in single metal nanoparticles, *Journal of the American Chemical Society* **1998**, *120*, 8009-8010.

(146) Soper, S. A.; Nutter, H. L.; Keller, R. A.; Davis, L. M.; Shera, E. B. The Photophysical Constants of Several Fluorescent Dyes Pertaining to Ultrasensitive Fluorescence Spectroscopy, *Photochemistry and Photobiology* **1993**, 57, 972-977.

(147) Haes, A. J.; Hall, W. P.; Chang, L.; Klein, W. L.; Van Duyne, R. P. A localized surface plasmon resonance biosensor: First steps toward an assay for Alzheimer's disease, *Nano Letters* **2004**, 4, 1029-1034.

(148) Jung, L. S.; Campbell, C. T.; Chinowsky, T. M.; Mar, M. N.; Yee, S. S. Quantitative Interpretation of the Response of Surface Plasmon Resonance Sensors to Adsorbed Films, *Langmuir* **1998**, 14, 5636-5648.

(149) Kronig, R. d. L.; Kramers, H. A. Theory of absorption and dispersion in x-ray spectra, *Zeitschrift fuer Physik* **1928**, 48, 174-9.

(150) Martinez, V. M.; Arbeloa, F. L.; Prieto, J. B.; Lopez, T. A.; Arbeloa, I. L. Characterization of Rhodamine 6G aggregates intercalated in solid thin films of Laponite clay. 1. Absorption spectroscopy, *Journal of Physical Chemistry B* **2004**, 108, 20030-20037.

(151) Martinez, V. M.; Arbeloa, F. U.; Prieto, J. B.; Lopez, T. A.; Arbeloa, I. L. Characterization of supported solid thin films of laponite clay. Intercalation of rhodamine 6G laser dye, *Langmuir* **2004**, 20, 5709-5717.

(152) Noginov, M. A.; Vondrova, M.; Williams, S. M.; Bahoura, M.; Gavrilenko, V. I.; Black, S. M.; Drachev, V. P.; Shalaev, V. M.; Sykes, A. Spectroscopic studies of liquid solutions of R6G laser dye and Ag nanoparticle aggregates, *Journal of Optics a-Pure and Applied Optics* **2005**, 7, S219-S229.

(153) Dare-Doyen, S.; Doizi, D.; Guilbaud, P.; Djedaini-Pilard, F.; Perly, B.; Millie, P. Dimerization of xanthene dyes in water: Experimental studies and molecular dynamic simulations, *Journal of Physical Chemistry B* **2003**, 107, 13803-13812.

(154) Reisfeld, R.; Zusman, R.; Cohen, Y.; Eyal, M. The Spectroscopic Behavior of Rhodamine 6G in Polar and Non-Polar Solvents and in Thin Glass and Pmma Films, *Chemical Physics Letters* **1988**, 147, 142-147.

(155) Kasha, M. Energy transfer mechanisms and the molecular exciton model for molecular aggregates, *Radiation Research* **1963**, 20, 55-70.

(156) Kasha, M.; Rawls, H. R.; El-Bayoumi, M. A. Exciton model in molecular spectroscopy, *Pure and Applied Chemistry* **1965**, 11, 371-92.

(157) Ruiz Ojeda, P.; Katime Amashta, I. A.; Ramon Ochoa, J.; Lopez Arbeloa, I. Excitonic treatment and bonding of aggregates of Rhodamine 6G in ethanol, *Journal of the Chemical Society, Faraday Transactions 2: Molecular and Chemical Physics* **1988**, 84, 1-8.



- (158) Scientific Computing & Modelling NV: 2005.
- (159) Velde, G. T.; Bickelhaupt, F. M.; Baerends, E. J.; Guerra, C. F.; Van Gisbergen, S. J. A.; Snijders, J. G.; Ziegler, T. Chemistry with ADF, *Journal of Computational Chemistry* **2001**, *22*, 931-967.
- (160) Becke, A. D. Density-Functional Exchange-Energy Approximation with Correct Asymptotic-Behavior, *Physical Review A* **1988**, *38*, 3098-3100.
- (161) Perdew, J. P. Density-Functional Approximation for the Correlation-Energy of the Inhomogeneous Electron-Gas, *Physical Review B* **1986**, *33*, 8822-8824.
- (162) Jensen, L.; Schatz, G. C. Resonance Raman scattering of rhodamine 6G as calculated using time-dependent density functional theory, *Journal of Physical Chemistry A* **2006**, *110*, 5973-5977.
- (163) Adhikesavalu, D. N.; Mastropaolo, D.; Camerman, A.; Camerman, N. Two rhodamine derivatives: 9-[2-(ethoxycarbonyl)phenyl]-3,6-bis-(ethylamino)-2,7-dimethylxanthylium chloride monohydrate and 3,6-diamino-9-[2-(methoxycarbonyl)-phenyl]xanthylium chloride trihydrate, *Acta Crystallographica Section C-Crystal Structure Communications* **2001**, *57*, 657-659.
- (164) Yonzon, C. R.; Jeoung, E.; Zou, S. L.; Schatz, G. C.; Mrksich, M.; Van Duyne, R. P. A comparative analysis of localized and propagating surface plasmon resonance sensors: The binding of concanavalin a to a monosaccharide functionalized self-assembled monolayer, *Journal of the American Chemical Society* **2004**, *126*, 12669-12676.
- (165) Schlichting, I.; Berendzen, J.; Chu, K.; Stock, A. M.; Maves, S. A.; Benson, D. E.; Sweet, B. M.; Ringe, D.; Petsko, G. A.; Sligar, S. G. The catalytic pathway of cytochrome P450cam at atomic resolution, *Science* **2000**, *287*, 1615-1622.
- (166) *Cytochrome P450: Structure, Function, and Mechanism*; 3<sup>rd</sup> ed.; Kluwer Academic/Plenum: New York, 2005.
- (167) Guengerich, F. P. Reactions and Significance of Cytochrome-P-450 Enzymes, *Journal of Biological Chemistry* **1991**, *266*, 10019-10022.
- (168) Guengerich, F. P. Cytochrome P-450 3A4: regulation and role in drug metabolism, *Annual review of pharmacology and toxicology* **1999**, *39*, 1-17.
- (169) Spatzenegger, M.; Jaeger, W. Clinical Importance of Hepatic Cytochrome-P450 in Drug-Metabolism, *Drug Metabolism Reviews* **1995**, *27*, 397-417.
- (170) Sligar, S. G. Coupling of Spin, Substrate, and Redox Equilibria in Cytochrome P450, *Biochemistry* **1976**, *15*, 5399-5406.

(171) Denisov, I. G.; Makris, T. M.; Sligar, S. G.; Schlichting, I. Structure and Chemistry of Cytochrome P450, *Chemical Reviews* **2005**, *105*, 2253-2277.

(172) Leroux, Y. R.; Lacroix, J. C.; Chane-Ching, K. I.; Fave, C.; Felidj, N.; Levi, G.; Aubard, J.; Krenn, J. R.; Hohenau, A. Conducting polymer electrochemical switching as an easy means for designing active plasmonic devices, *Journal of the American Chemical Society* **2005**, *127*, 16022-16023.

(173) Fujii, E.; Koike, T.; Nakamura, K.; Sasaki, S.; Kurihara, K.; Citterio, D.; Iwasaki, Y.; Niwa, O.; Suzuki, K. Application of an absorption-based surface plasmon resonance principle to the development of SPR ammonium ion and enzyme sensors, *Analytical Chemistry* **2002**, *74*, 6106-6110.

(174) Kurihara, K.; Nakamura, K.; Hirayama, E.; Suzuki, K. An absorption-based surface plasmon resonance sensor applied to sodium ion sensing based on an ion-selective optode membrane, *Analytical Chemistry* **2002**, *74*, 6323-6333.

(175) Jensen, T. R.; Schatz, G. C.; Van Duyne, R. P. Nanosphere Lithography: Surface plasmon resonance spectrum of a periodic array of silver nanoparticles by UV-vis extinction spectroscopy and electrodynamic modeling, *Journal of Physical Chemistry B* **1999**, *103*, 2394-2401.

(176) Kreibig, U.; Gartz, M.; Hilger, A. Mie resonances. Sensors for physical and chemical cluster interface properties., *Ber. Bunsen-Ges.* **1997**, *101*, 1593-1604.

(177) Qi, Z. M.; Honma, I.; Zhou, H. S. Humidity sensor based on localized surface plasmon resonance of multilayer thin films of gold nanoparticles linked with myoglobin, *Optics Letters* **2006**, *31*, 1854-1856.

(178) Dawson, J. H.; Andersson, L. A.; Sono, M. Spectroscopic Investigations of Ferric Cytochrome P-450-Cam Ligand Complexes - Identification of the Ligand Trans to Cysteinate in the Native Enzyme, *Journal of Biological Chemistry* **1982**, *257*, 3606-3617.

(179) Das, A.; Grinkova, Y. V.; Sligar, S. G. Redox potential control by drug binding to cytochrome p450 3A4, *Journal of the American Chemical Society* **2007**, *129*, 13778-13779.

(180) Loew, G. H.; Harris, D. L. Role of the heme active site and protein environment in structure, spectra, and function of the cytochrome p450s, *Chemical Reviews* **2000**, *100*, 407-419.

(181) Harris, D.; Loew, G. Mechanistic Origin of the Correlation between Spin-State and Spectra of Model Cytochrome-P450 Ferric Heme-Proteins, *Journal of the American Chemical Society* **1993**, *115*, 5799-5802.

(182) Gunsalus, I. C.; Wagner, G. C. Bacterial P-450cam methylene monooxygenase components: Cytochrome m, putidaredoxin, and putidaredoxin reductase, *Methods in Enzymology* **1978**, 52, 166-188.

(183) Makris, T. M.; von Koenig, K.; Schlichting, I.; Sligar, S. G. Alteration of P450 Distal Pocket Solvent Leads to Impaired Proton Delivery and Changes in Heme Geometry, *Biochemistry* **2007**, 46, 14129-14140.

(184) Haynes, C. L.; Van Duyne, R. P. Nanosphere Lithography: A Versatile Nanofabrication Tool for Studies of Size-Dependent Nanoparticle Optics., *Journal of Physical Chemistry B* **2001**, 105, 5599-5611.

(185) Eaton, W. A.; Hochstrasser, R. M. Single-Crystal Spectra of Ferrimyoglobin Complexes in Polarized Light, *Journal of Chemical Physics* **1968**, 49, 985-995.

(186) Eaton, W. A.; Hofrichter, J. Polarized Absorption and Linear Dichroism Spectroscopy of Hemoglobin, *Methods in Enzymology* **1981**, 76, 175-261.

(187) Zlokarnik, G.; Grootenhuis, P. D. J.; Watson, J. B. High throughput P450 inhibition screens in early drug discovery, *Drug Discovery Today* **2005**, 10, 1443-1450.

(188) Hanson, L. K.; Eaton, W. A.; Sligar, S. G.; Gunsalus, I. C.; Gouterman, M.; Connell, C. R. Origin of Anomalous Soret Spectra of Carboxycytochrome P-450, *Journal of the American Chemical Society* **1976**, 98, 2672-2674.

(189) Kidwai, M.; Bansal, V.; Saxena, A.; Aerry, S.; Mozumdar, S. Cu-Nanoparticles: efficient catalysts for the oxidative cyclization of Schiff's bases, *Tetrahedron Lett.* **2006**, 47, 8049-8053.

(190) Kraus, W. A.; Schatz, G. C. Plasmon resonance broadening in small metal particles, *Journal of Chemical Physics* **1983**, 79, 6130-9.

(191) Kraus, W. A.; Schatz, G. C. Plasmon resonance broadening in spheroidal metal particles, *Chemical Physics Letters* **1983**, 99, 353-7.

(192) Sung, J.; Hicks, E. M.; Van Duyne, R. P.; Spears, K. G. Nanoparticle spectroscopy: Dipole coupling in two-dimensional arrays of L-shaped silver nanoparticles, *Journal of Physical Chemistry C* **2007**, 111, 10368-10376.

(193) Sung, J.; Hicks, E. M.; Van Duyne, R. P.; Spears, K. G. Nanoparticle Spectroscopy: Plasmon Coupling in Finite-Sized Two-Dimensional Arrays of Cylindrical Silver Nanoparticles, *Journal of Physical Chemistry C* **2008**, 112, 4091-4096.

- (194) Zou, S.; Schatz, G. C. Narrow plasmonic/photonic extinction and scattering line shapes for one and two dimensional silver nanoparticle arrays,*Journal of Chemical Physics* **2004**, *121*, 12606-12612.
- (195) Okamoto, T.; Yamaguchi, I.; Kobayashi, T. Local plasmon sensor with gold colloid monolayers deposited upon glass substrates,*Optics Letters* **2000**, *25*, 372-374.
- (196) Zhao, L.; Jensen, L.; Schatz, G. C. Pyridine-Ag<sub>20</sub> Cluster: A Model System for Studying Surface-Enhanced Raman Scattering,*Journal of the American Chemical Society* **2006**, *128*, 2911-2919.
- (197) Schatz, G. C. THEORETICAL-STUDIES OF SURFACE ENHANCED RAMAN-SCATTERING,*Accounts of Chemical Research* **1984**, *17*, 370-376.
- (198) Dick, L. A.; McFarland, A. D.; Haynes, C. L.; Van Duyne, R. P. Metal Film over Nanosphere (MFON) Electrodes for Surface-Enhanced Raman Spectroscopy (SERS): Improvements in Surface Nanostructure Stability and Suppression of Irreversible Loss,*Journal of Physical Chemistry B* **2002**, *106*, 853-860.
- (199) Kerker, M.; Wang, D. S.; Chew, H. Surface Enhanced Raman-Scattering (SERS) by Molecules Adsorbed at Spherical-Particles,*Applied Optics* **1980**, *19*, 3373-3388.
- (200) Oldenburg, S. J.; Westcott, S. L.; Averitt, R. D.; Halas, N. J. Surface enhanced Raman scattering in the near infrared using metal nanoshell substrates,*Journal of Chemical Physics* **1999**, *111*, 4729-4735.
- (201) Zhang, X.; Young, M. A.; Lyandres, O.; Van Duyne, R. P. Rapid detection of an anthrax biomarker by surface-enhanced Raman spectroscopy,*Journal of the American Chemical Society* **2005**, *127*, 4484-4489.
- (202) Mallick, P. K.; Danzer, G. D.; Strommen, D. P.; Kincaid, J. R. Vibrational-Spectra and Normal-Coordinate Analysis of Tris(Bipyridine)Ruthenium(Ii),*Journal of Physical Chemistry* **1988**, *92*, 5628-5634.
- (203) Bizzarri, A. R.; Cannistraro, S. Statistical analysis of intensity fluctuations in single molecule SERS spectra,*Physical Chemistry Chemical Physics* **2007**, *9*, 5315-5319.
- (204) Doering, W. E.; Nie, S. M. Single-molecule and single-nanoparticle SERS: Examining the roles of surface active sites and chemical enhancement,*Journal of Physical Chemistry B* **2002**, *106*, 311-317.
- (205) Emory, S. R.; Jensen, R. A.; Wenda, T.; Han, M. Y.; Nie, S. M. Re-examining the origins of spectral blinking in single-molecule and single-nanoparticle SERS,*Faraday Discussions* **2006**, *132*, 249-259.

- (206) Etchegoin, P. G.; Meyer, M.; Le Ru, E. C. Statistics of single molecule SERS signals: is there a Poisson distribution of intensities?, *Physical Chemistry Chemical Physics* **2007**, *9*, 3006-3010.
- (207) Futamata, M. Single molecule sensitivity in SERS: importance of junction of adjacent Ag nanoparticles, *Faraday Discussions* **2006**, *132*, 45-61.
- (208) Kneipp, K.; Kneipp, H. Detection, identification, and tracking of biomolecules at the single molecule level using SERS, *Biophysical Journal* **2005**, *88*, 365a-365a.
- (209) Kneipp, K.; Kneipp, H.; Bohr, H. G. Single-molecule SERS spectroscopy, *Surface-Enhanced Raman Scattering: Physics and Applications* **2006**, *103*, 261-277.
- (210) Moskovits, M.; Tay, L. L.; Yang, J.; Haslett, T. SERS and the single molecule, *Optical Properties of Nanostructured Random Media* **2002**, *82*, 215-226.
- (211) Otto, A.; Bruckbauer, A.; Chen, Y. X. On the chloride activation in SERS and single molecule SERS, *Journal of Molecular Structure* **2003**, *661*, 501-514.
- (212) Vlckova, B.; Pavel, I.; Sladkova, M.; Siskova, K.; Slouf, M. Single molecule SERS: Perspectives of analytical applications, *Journal of Molecular Structure* **2007**, *834*, 42-47.
- (213) Gleria, M.; Minto, F.; Beggiato, G.; Bortolus, P. Photochemistry of Tris(2,2'-Bipyridine)Ruthenium(II) in Chlorinated Solvents, *Journal of the Chemical Society-Chemical Communications* **1978**, 285-285.
- (214) Sato, H.; Kawasaki, M.; Haga, M.; Kasatani, K.; Ban, T.; Suenaga, H.; Kitamura, N. Photochemistry in the Premicellar Region - the Study of Electron-Transfer in the Tris(2,2'-Bipyridine)Ruthenium(II) - 1,1'-Dimethyl-4,4'-Bipyridinium System by the Emission Lifetime Measurement, *Nippon Kagaku Kaishi* **1984**, 51-59.
- (215) White, H. S.; Becker, W. G.; Bard, A. J. Photochemistry of the Tris(2,2'-Bipyridine)Ruthenium(II) Peroxydisulfate System in Aqueous and Mixed Acetonitrile Water Solutions - Evidence for a Long-Lived Photoexcited Ion-Pair, *Journal of Physical Chemistry* **1984**, *88*, 1840-1846.
- (216) Stacy, A. M.; Vanduyne, R. P. Surface Enhanced Raman and Resonance Raman-Spectroscopy in a Non-Aqueous Electrochemical Environment - Tris(2,2'-Bipyridine)Ruthenium(II) Adsorbed on Silver from Acetonitrile, *Chemical Physics Letters* **1983**, *102*, 365-370.
- (217) Pichot, F.; Beck, J. H.; Elliott, C. M. A series of multicolor electrochromic ruthenium(II) trisbipyridine complexes: Synthesis and electrochemistry, *Journal of Physical Chemistry A* **1999**, *103*, 6263-6267.

(218) Elbicki, J. M.; Morgan, D. M.; Weber, S. G. Photoelectroanalytical Chemistry - Electrochemical Detection of a Photochemistry Active Species, Tris(2,2'-Bipyridine)Ruthenium(II), *Analytical Chemistry* **1985**, 57, 1746-1751.

(219) Elliott, C. M.; Freitag, R. A.; Blaney, D. D. Electrochemistry, Spectroelectrochemistry, and Photochemistry of a Series of New Covalently Linked Tris(2,2'-Bipyridine)Ruthenium(II) Diquat Complexes, *Journal of the American Chemical Society* **1985**, 107, 4647-4655.

(220) Tokel, N. E.; Bard, A. J. Electrogenenerated Chemiluminescence .9. Electrochemistry and Emission from Systems Containing Tris(2,2'-Bipyridine)Ruthenium(II) Dichloride, *Journal of the American Chemical Society* **1972**, 94, 2862-&.

(221) Han, H. Y.; He, Z. K.; Zeng, Y. Chemiluminescence determination of tetracyclines using a tris(2,2'-bipyridine)ruthenium(II) and potassium permanganate system, *Analytical Sciences* **1999**, 15, 467-470.

(222) Jiang, Q. H.; Sun, S. G.; Hakansson, M.; Langel, K.; Ylinen, T.; Suomi, J.; Kulmala, S. Electrochemiluminescence and chemiluminescence of a carboxylic acid derivative of ruthenium(II) tris-(2,2'-bipyridine) chelate synthesized for labeling purposes, *Journal of Luminescence* **2006**, 118, 265-271.

(223) Knight, A. W.; Greenway, G. M. Relationship between structural attributes and observed electrogenerated chemiluminescence (ECL) activity of tertiary amines as potential analytes for the tris(2,2'-bipyridine)ruthenium(II) ECL reaction - A review, *Analyst* **1996**, 121, R101-R106.

(224) Miao, W. J.; Choi, J. P.; Bard, A. J. Electrogenenerated chemiluminescence 69: The tris(2,2'-bipyridine)ruthenium(II), (Ru(bpy)<sub>3</sub>)(2+)/tri-n-propylamine (TPrA) system revisited - A new route involving TPrA(center dot+) cation radicals, *Journal of the American Chemical Society* **2002**, 124, 14478-14485.

(225) Morita, H.; Konishi, M. Electrogenenerated chemiluminescence derivatization reagents for carboxylic acids and amines in high-performance liquid chromatography using tris(2,2'-bipyridine)ruthenium(II), *Analytical Chemistry* **2002**, 74, 1584-1589.

(226) Sato, Y.; Uosaki, K. Electrochemical and Electrogenenerated Chemiluminescence Properties of Tris(2,2'-Bipyridine)Ruthenium(II)-Tridecanethiol Derivative on Ito and Gold Electrodes, *Journal of Electroanalytical Chemistry* **1995**, 384, 57-66.

(227) Belser, P.; Daul, C.; Vonzelewsky, A. On the Assignment of the Mlct Transition in the Ru(Bpy)<sub>3</sub>(2+) Complex Ion, *Chemical Physics Letters* **1981**, 79, 596-598.

(228) Kalyanasundaram, K. Photophysics, Photochemistry and Solar-Energy Conversion with Tris(Bipyridyl)Ruthenium(II) and Its Analogs, *Coordination Chemistry Reviews* **1982**, *46*, 159-244.

(229) Virdee, H. R.; Hester, R. E. Surface-Enhanced Raman-Spectra of  $[\text{Ru}^{\text{II}}(\text{Bpy})_3]^{2+}$  and Electrochemically Generated  $[\text{Ru}^{\text{II}}(\text{Bpy})_3]^{2+}$  on a Silver Electrode, *Journal of Physical Chemistry* **1984**, *88*, 451-455.

(230) Basu, A.; Gafney, H. D.; Streckas, T. C. Resonance Raman-Spectra of Ruthenium(II) Complexes of Bipyridine and Substituted Bipyridines - Ground-State and Excited-State Properties, *Inorganic Chemistry* **1982**, *21*, 2231-2235.

(231) Srnova-Sloufova, I.; Vlckova, B.; Snoeck, T. L.; Stufkens, D. J.; Matejka, P. Surface-enhanced Raman scattering and surface-enhanced resonance Raman scattering excitation profiles of Ag-2,2'-bipyridine surface complexes and of  $[\text{Ru}(\text{bpy})_3]^{2+}$  on Ag colloidal surfaces: Manifestations of the charge-transfer resonance contributions to the overall surface enhancement of Raman scattering, *Inorganic Chemistry* **2000**, *39*, 3551-3559.

(232) Bradley, P. G.; Kress, N.; Hornberger, B. A.; Dallinger, R. F.; Woodruff, W. H. Vibrational Spectroscopy of the Electronically Excited-State .5. Time-Resolved Resonance Raman-Study of Tris(Bipyridine)Ruthenium(II) and Related Complexes - Definitive Evidence for the Localized Mlct State, *Journal of the American Chemical Society* **1981**, *103*, 7441-7446.

(233) Fussarydel, O.; Zhang, H. T.; Hupp, J. T.; Leidner, C. R. Electrochemical Assembly of Metallopolymeric Films Via Reduction of Coordinated 5-Chlorophenanthroline, *Inorganic Chemistry* **1989**, *28*, 1533-1537.

(234) Anson, F. C. Innovations in Study of Adsorbed Reactants by Chronocoulometry, *Analytical Chemistry* **1966**, *38*, 54-&.

(235) Anson, F. C.; Christie, J. H.; Osteryou. Ra A Study of Adsorption of Cadmium(2) on Mercury from Thiocyanate Solutions by Double Potential-Step Chronocoulometry, *Journal of Electroanalytical Chemistry* **1967**, *13*, 343-&.

(236) Christie, J. H.; Osteryou. Ra; Anson, F. C. Application of Double Potential-Step Chronocoulometry to Study of Reactant Adsorption Theory, *Journal of Electroanalytical Chemistry* **1967**, *13*, 236-&.

(237) Chaignon, F.; Torroba, J.; Blart, E.; Borgstrom, M.; Hammarstrom, L.; Odobel, F. Distance-independent photoinduced energy transfer over 1.1 to 2.3 nm in ruthenium trisbipyridine-fullerene assemblies, *New Journal of Chemistry* **2005**, *29*, 1272-1284.

(238) Haes, A. J.; Zou, S. L.; Zhao, J.; Schatz, G. C.; Van Duyne, R. P. Localized surface plasmon resonance spectroscopy near molecular resonances, *Journal of the American Chemical Society* **2006**, *128*, 10905-10914.

- (239) Gersten, J.; Nitzan, A. Electromagnetic Theory of Enhanced Raman-Scattering by Molecules Adsorbed on Rough Surfaces, *Journal of Chemical Physics* **1980**, *73*, 3023-3037.
- (240) Meier, M.; Wokaun, A. Enhanced Fields on Large Metal Particles - Dynamic Depolarization, *Optics Letters* **1983**, *8*, 581-583.
- (241) Zeman, E. J.; Schatz, G. C. An Accurate Electromagnetic Theory Study of Surface Enhancement Factors for Ag, Au, Cu, Li, Na, Al, Ga, In, Zn, and Cd, *Journal of Physical Chemistry* **1987**, *91*, 634-643.
- (242) Clark, R. J. H.; Turtle, P. C.; Strommen, D. P.; Streusand, B.; Kincaid, J.; Nakamoto, K. Resonance Raman-Spectra and Excitation Profiles of Tris(Alpha-Diimine) Complexes of Iron(II), *Inorganic Chemistry* **1977**, *16*, 84-89.
- (243) Kerker, M. Founding-Fathers of Light-Scattering and Surface-Enhanced Raman-Scattering, *Applied Optics* **1991**, *30*, 4699-4705.
- (244) Clark, R. J. H.; Hempleman, A. J.; Tocher, D. A. Infrared, Resonance Raman, and Excitation Profile Studies of  $\text{Os}_2(\text{O}_2\text{CCH}_3)_4\text{Cl}_2$  and  $\text{Os}_2(\text{O}_2\text{CCD}_3)_4\text{Cl}_2$  - the Assignment of the Osmium Osmium Stretching Vibration for a Complex Involving an Osmium Osmium Multiple Bond, *Journal of the American Chemical Society* **1988**, *110*, 5968-5972.
- (245) Dudik, J. M.; Johnson, C. R.; Asher, S. A. Wavelength Dependence of the Preresonance Raman Cross-Sections of  $\text{CH}_3\text{CN}$ ,  $\text{SO}_4^{2-}$ ,  $\text{ClO}_4^-$ , and  $\text{NO}_3^-$ , *Journal of Chemical Physics* **1985**, *82*, 1732-1740.
- (246) Trulson, M. O.; Mathies, R. A. Raman Cross-Section Measurements in the Visible and Ultraviolet Using an Integrating Cavity - Application to Benzene, Cyclohexane, and Cacodylate, *Journal of Chemical Physics* **1986**, *84*, 2068-2074.
- (247) Huang, W. Y.; Qian, W.; El-Sayed, M. A. Coherent vibrational oscillation in gold prismatic monolayer periodic nanoparticle arrays, *Nano Letters* **2004**, *4*, 1741-1747.
- (248) Murray, W. A.; Suckling, J. R.; Barnes, W. L. Overlayers on Silver Nanotriangles: Field Confinement and Spectral Position of Localized Surface Plasmon Resonances, *Nano Letters* **2006**, *6*, 1772-1777.
- (249) Cline, M. P.; Barber, P. W.; Chang, R. K. Surface-Enhanced Electric Intensities on Transition-Metal and Noble-Metal Spheroids, *Journal of the Optical Society of America B: Optical Physics* **1986**, *3*, 15-21.
- (250) Creighton, J. A.; Eadon, D. G. Ultraviolet Visible Absorption-Spectra of the Colloidal Metallic Elements, *Journal of the Chemical Society, Faraday Transactions* **1991**, *87*, 3881-3891.



- (251) Derin, H.; Kantarli, K. Optical characterization of thin thermal oxide films on copper by ellipsometry, *Applied Physics A* **2002**, 75, 391-395.
- (252) Wieder, H.; Czanderna, A. W. The oxidation of copper films to CuO<sub>0.67</sub>, *Journal of Physical Chemistry* **1962**, 66, 816-21.
- (253) *CRC Handbook of Chemistry and Physics*; 69 ed. Boca Raton, FL, 1989.
- (254) Chavez, K. L.; Hess, D. W. A novel method of etching copper oxide using acetic acid, *J. Electrochem. Soc.* **2001**, 148, G640-G643.
- (255) *Metals Handbook*; 2nd ed. Materials Park, OH, 1998.
- (256) Yanase, A.; Komiyama, H. Insitu Observation of Oxidation and Reduction of Small Supported Copper Particles Using Optical-Absorption and X-Ray-Diffraction, *Surf. Sci.* **1991**, 248, 11-19.
- (257) Yanase, A.; Matsui, H.; Tanaka, K.; Komiyama, H. Optical Observation of Oxidation and Reduction of Small Supported Copper Particles, *Surf. Sci.* **1989**, 219, L601-L606.
- (258) Shuford, K. L.; Ratner, M. A.; Schatz, G. C. Multipolar excitation in triangular nanoprisms, *Journal of Chemical Physics* **2005**, 123, 114713-1-114713-8.
- (259) Ramaswamy, A. L.; Kaste, P. A 'nanovision' of the physiochemical phenomena occurring in nanoparticles of aluminum, *J. Energ. Mater.* **2005**, 23, 1-25.
- (260) Boyd, G. T.; Rasing, T.; Leite, J. R. R.; Shen, Y. R. Local-Field Enhancement on Rough Surfaces of Metals, Semimetals, and Semiconductors with the Use of Optical 2nd-Harmonic Generation, *Physical Review B: Condensed Matter* **1984**, 30, 519-526.
- (261) Ctistis, G.; Patoka, P.; Wang, X.; Kempa, K.; Giersig, M. Optical Transmission through Hexagonal Arrays of Subwavelength Holes in Thin Metal Films, *Nano Letters* **2007**, 7, 2926-2930.
- (262) Gao, Y.; Lopezrios, T. Raman-Scattering of Pyridine Coadsorbed with Al on Quenched Ag Films - Evidence of Raman Enhancement in the Pores, *Surface Science* **1988**, 198, 509-523.
- (263) Liao, P. F.; Stern, M. B. Surface-Enhanced Raman-Scattering on Gold and Aluminum Particle Arrays, *Optics Letters* **1982**, 7, 483-485.
- (264) Lopez-Rios, T.; Gao, Y.; Vuye, G. Influence of Al Submonolayers on Surface-Enhanced Raman-Scattering of Pyridine on Ag Surfaces, *Chemical Physics Letters* **1984**, 111, 249-253.

- (265) Lopez-Rios, T.; Pettenkofer, C.; Pockrand, I.; Otto, A. Enhanced Raman-Scattering from Aluminum Films,*Surface Science* **1982**, *121*, L541-L544.
- (266) Srituravanich, W.; Fang, N.; Sun, C.; Luo, Q.; Zhang, X. Plasmonic Nanolithography,*Nano Letters* **2004**, *4*, 1085-1088.
- (267) Tillin, M. D.; Sambles, J. R. A Surface Plasmon-Polariton Study of the Dielectric-Constants of Reactive Metals - Aluminum,*Thin Solid Films* **1988**, *167*, 73-83.
- (268) Dorfer, T.; Schmitt, M.; Popp, J. Deep-UV surface-enhanced Raman scattering,*Journal of Raman Spectroscopy* **2007**, *38*, 1379-1382.
- (269) Malicka, J.; Gryczynski, I.; Gryczynski, Z.; Lakowicz, J. R. Surface Plasmon-Coupled Ultraviolet Emission of 2,5-Diphenyl-1,3,4-oxadiazole,*Journal of Physical Chemistry B* **2004**, *108*, 19114-19118.
- (270) Ray, K.; Chowdhury, M. H.; Lakowicz, J. R. Aluminum Nanostructured Films as Substrates for Enhanced Fluorescence in the Ultraviolet-Blue Spectral Region,*Analytical Chemistry* **2007**, *79*, 6480-6487.
- (271) Myszka, D. G.; Rich, R. L. Implementing surface plasmon resonance biosensors in drug discovery,*Pharmaceutical Science & Technology Today* **2000**, *3*, 310-317.
- (272) Heyse, S.; Stora, T.; Schmid, E.; Lakey, J. H.; Vogel, H. Emerging techniques for investigating molecular interactions at lipid membranes,*Biochimica et Biophysica Acta (BBA) - Reviews on Biomembranes* **1998**, *1376*, 319-338.
- (273) Matthew A. Cooper Advances in membrane receptor screening and analysis,*Journal of Molecular Recognition* **2004**, *17*, 286-315.
- (274) Rebecca L. Rich, D. G. M. Survey of the year 2006 commercial optical biosensor literature,*Journal of Molecular Recognition* **2007**, *20*, 300-366.
- (275) Rebecca L. Rich, D. G. M. Survey of the year 2005 commercial optical biosensor literature,*Journal of Molecular Recognition* **2006**, *19*, 478-534.
- (276) Cooper, M. A. Non-optical screening platforms: the next wave in label-free screening?,*Drug Discovery Today* **2006**, *11*, 1068-1074.
- (277) Tollin, G.; Salamon, Z.; Hruby, V. J. Techniques: Plasmon-waveguide resonance (PWR) spectroscopy as a tool to study ligand-GPCR interactions,*Trends in Pharmacological Sciences* **2003**, *24*, 655-659.

(278) Crespi, C. L.; Miller, V. P.; Penman, B. W. Microtiter Plate Assays for Inhibition of Human, Drug-Metabolizing Cytochromes P450, *Analytical Biochemistry* **1997**, *248*, 188-190.

(279) Zlokarnik, G.; Grootenhuys, P. D. J.; Watson, J. B. High throughput P450 inhibition screens in early drug discovery, *Drug Discovery Today* **2005**, *10*, 1443-1450.

(280) White, R. E. High-Throughput Screening in Drug Metabolism and Pharmacokinetic Support of Drug Discovery, *Annual Review of Pharmacology and Toxicology* **2000**, *40*, 133-157.

(281) Guengerich, F. P. U.-h. w. s. c. s. a. B. W.-D. T.-B. e. a. d. c. Cytochrome P-450 3A4: regulation and role in drug metabolism, *Annual Review Of Pharmacology And Toxicology* **1999**, *39*, 1-17.

(282) Scott, E. E.; Halpert, J. R. Structures of cytochrome P450 3A4, *Trends Biochem Sci* **2005**, *30*, 5-7.

(283) Guengerich, F. P. Cytochrome p450 and chemical toxicology, *Chem Res Toxicol* **2008**, *21*, 70-83.

(284) Dawson, J.; Andersson, L.; Sono, M. Spectroscopic investigations of ferric cytochrome P-450-CAM ligand complexes. Identification of the ligand trans to cysteinate in the native enzyme, *J. Biol. Chem.* **1982**, *257*, 3606-3617.

(285) Ahlstrom, M. M.; Zamora, I. Characterization of Type II Ligands in CYP2C9 and CYP3A4, *J Med Chem* **2008**, *51*, 1755-1763.

(286) Tamm, L. K.; McConnell, H. M. Supported phospholipid bilayers, *Biophys. J.* **1985**, *47*, 105-113.

(287) Wagner, M. L.; Tamm, L. K. Tethered Polymer-Supported Planar Lipid Bilayers for Reconstitution of Integral Membrane Proteins: Silane-Polyethyleneglycol-Lipid as a Cushion and Covalent Linker, *Biophys. J.* **2000**, *79*, 1400-1414.

(288) Knoll, W.; Frank, C. W.; Heibel, C.; Naumann, R.; Offenhausser, A.; Ruhe, J.; Schmidt, E. K.; Shen, W. W.; Sinner, A. Functional tethered lipid bilayers, *J Biotechnol* **2000**, *74*, 137-58.

(289) Sinner, E. K.; Knoll, W. Functional tethered membranes, *Curr Opin Chem Biol* **2001**, *5*, 705-11.

(290) Rigaud, J.-L.; Pitard, B.; Levy, D. Reconstitution of membrane proteins into liposomes: application to energy-transducing membrane proteins, *Biochimica et Biophysica Acta (BBA) - Bioenergetics* **1995**, *1231*, 223-246.

- (291) Leitz, A. J.; Bayburt, T. H.; Barnakov, A. N.; Springer, B. A.; Sligar, S. G. Functional reconstitution of Beta2-adrenergic receptors utilizing self-assembling Nanodisc technology, *Biotechniques* **2006**, *40*, 601-2, 604, 606.
- (292) Bayburt, T. H.; Grinkova, Y. V.; Sligar, S. G. Assembly of single bacteriorhodopsin trimers in bilayer nanodiscs, *Arch Biochem Biophys* **2006**, *450*, 215-22.
- (293) Boldog, T.; Grimme, S.; Li, M.; Sligar, S. G.; Hazelbauer, G. L. Nanodiscs separate chemoreceptor oligomeric states and reveal their signaling properties, *Proc Natl Acad Sci U S A* **2006**, *103*, 11509-14.
- (294) Nath, A.; Atkins, W. M.; Sligar, S. G. Applications of phospholipid bilayer nanodiscs in the study of membranes and membrane proteins, *Biochemistry* **2007**, *46*, 2059-69.
- (295) Alami, M.; Dalal, K.; Lelj-Garolla, B.; Sligar, S. G.; Duong, F. Nanodiscs unravel the interaction between the SecYEG channel and its cytosolic partner SecA, *EMBO J* **2007**, *26*, 1995-2004.
- (296) Baas, B. J.; Denisov, I. G.; Sligar, S. G. Homotropic cooperativity of monomeric cytochrome P450 3A4 in a nanoscale native bilayer environment, *Archives of Biochemistry and Biophysics Highlight section: Methodologies for the measurement of the macular pigment* **2004**, *430*, 218-228.
- (297) Shaw, A. W.; Pureza, V. S.; Sligar, S. G.; Morrissey, J. H. The local phospholipid environment modulates the activation of blood clotting, *J Biol Chem* **2007**, *282*, 6556-63.
- (298) Marin, V. L.; Bayburt, T. H.; Sligar, S. G.; Mrksich, M. Functional assays of membrane-bound proteins with SAMDI-TOF mass spectrometry, *Angew Chem Int Ed Engl* **2007**, *46*, 8796-8.
- (299) Domanski, T. L.; Liu, J.; Harlow, G. R.; Halpert, J. R. Analysis of Four Residues within Substrate Recognition Site 4 of Human Cytochrome P450 3A4: Role in Steroid Hydroxylase Activity and [alpha]-Naphthoflavone Stimulation, *Archives of Biochemistry and Biophysics* **1998**, *350*, 223-232.
- (300) Hosea, N. A.; Miller, G. P.; Guengerich, F. P. Elucidation of Distinct Ligand Binding Sites for Cytochrome P450 3A4, *Biochemistry* **2000**, *39*, 5929-5939.
- (301) Gillam, E. M. J.; Baba, T.; Kim, B. R.; Ohmori, S.; Guengerich, F. P. Expression of Modified Human Cytochrome P450 3A4 in Escherichia coli and Purification and Reconstitution of the Enzyme, *Archives of Biochemistry and Biophysics* **1993**, *305*, 123-131.

(302) Denisov, I. G.; Baas, B. J.; Grinkova, Y. V.; Sligar, S. G. Cooperativity in cytochrome P450 3A4: linkages in substrate binding, spin state, uncoupling, and product formation, *J Biol Chem* **2007**, *282*, 7066-76.

(303) Denisov, I. G.; Grinkova, Y. V.; Lazarides, A. A.; Sligar, S. G. Directed self-assembly of monodisperse phospholipid bilayer Nanodiscs with controlled size, *Journal of the American Chemical Society* **2004**, *126*, 3477-87.

(304) Denisov, I. G.; Grinkova, Y. V.; Baas, B. J.; Sligar, S. G. The ferrous-dioxygen intermediate in human cytochrome P450 3A4. Substrate dependence of formation and decay kinetics, *J Biol Chem* **2006**, *281*, 23313-8.

(305) Das, A.; Grinkova, Y. V.; Sligar, S. G. Redox potential control by drug binding to cytochrome P450 3A4, *J Am Chem Soc* **2007**, *129*, 13778-9.

## **Appendix A**

### **Detection of Drug binding to Human Cytochrome P450-3A4 in Nanodisc using Resonant Localized Surface Plasmon Resonance**

## A.1 Introduction

In the drug discovery process, the sensing of molecular interactions between a drug molecule and protein is very important. There is increasing demanding for the development of sensitive, label-free, array-based protein analysis for high-throughput drug discovery. The progress in these directions not only require new concepts in sensors but also require superior surface conjugation techniques and development of novel fluidic devices.

One of the cornerstone in drug discovery research is the need for ultrasensitive detection of drug interactions with membrane proteins which are the targets of most of the currently marketed therapeutic targets.<sup>271-277</sup> In particular, detection of drug binding to membrane bound human cytochrome P450s is important for understanding the interaction between the drug and the protein.<sup>278-280</sup> CYP3A4 is one of the most important enzymes in Cytochrome P450 family in drug and xenobiotics metabolism in the human body and is involved in drug-drug interactions.<sup>281</sup> CYP3A4 is prone to inhibition because of its broad substrate specificity and promiscuous open active site.<sup>282</sup> The inhibition of CYP3A4 by one drug can modify the pharmacokinetic profile of another drug leading to the variations of efficacy or toxicity of the drugs.<sup>283</sup> Hence, there is the potential risk of drug-drug interactions. Therefore, it is important to discover inhibitors and substrates in early drug discovery process. On the basis of spectral changes which CYP3A4 undergoes on binding drugs, the drugs can be classified into three types: type I (which shows blue shift in the Soret at 415 nm), type II (red shift in Soret) and those drugs which do not show any shift in Soret.<sup>284</sup> Most of the type II drug molecules are reversible mechanistic inhibitors which bind directly to the heme iron atom.<sup>285</sup> Moreover, CYP3A4 and other membrane bound cytochrome P450s such as aromatase are produced in low-yield using heterologous expression

systems. Therefore, a high-throughput optical detection of drug binding to CYP3A4 using low concentration of protein will be an important initial step in drug discovery.

Membrane bound proteins in general and CYP3A4 in particular are inherently insoluble or prone to aggregation and oligomerization in aqueous solution. There has been substantial advance in the development of techniques that allow the analysis of membrane associated ligand receptor in model native-like lipid bilayer environment.<sup>286-290</sup> Recently, Nanodiscs have been used to solubilize and functionally stabilize CYP3A4 and other membrane proteins.<sup>291-296</sup> Nanodiscs are essentially segments of phospholipid bilayer surrounded by a protein belt. This protein belt in the Nanodisc controls the dimension of the Nanodisc (Figure A.1A and C). Previously, Nanodisc has been shown to be a viable platform to stabilize membrane proteins maintaining full functionality, for surface based applications. These stabilized membrane proteins in Nanodisc have been coupled successfully with surface based detection schemes such as SPR<sup>297</sup> and SAMDI<sup>298</sup> (self-assembled monolayer MALDI). The Nanodiscs typically have diameter of 10 nm and height of 5.5 nm hence, one advantage Nanodiscs have over tethered bilayer as a model phospholipid bilayer is that they can provide the lipid bilayer mimic for the membrane protein which is within the sensing volume of the nanoparticle sensors.

Based on the work discussed in Chapter Three and Four, one can develop nanoparticle-based sensors combining resonance localized surface plasmon resonance spectroscopy and Nanodisc to detect different types of drug binding to human membrane CYP3A4 in Nanodisc. Figure A.1B shows the representative UV-vis spectra of CYP3A4 Nanodisc, and with two types of drugs, which are similar to the system of camphor and imidazole with CYP101 discussed in Chapter Four. The preliminary results will be presented in the following sections.



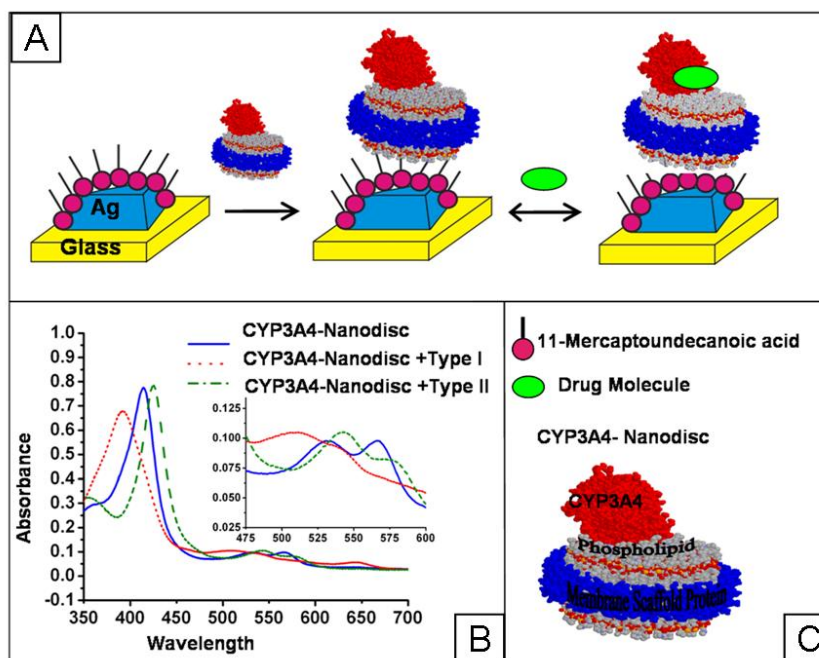


**Figure A.1:** (A) Schematic representation of CYP3A4-Nanodisc immobilized Ag nanobiosensor, followed by binding of drug molecule. The Ag nanoparticles are fabricated using NSL (nanosphere lithography) on a glass substrate. (B) UV-vis absorption spectra of CYP3A4-Nanodisc in the following states: (1) low spin substrate free ferric state of with a Soret band at 415 nm (blue solid line) (2) high spin type I drug bound ferric state with a Soret band at 391 nm (red dotted line) and (3) low spin type II drug bound ferric state with Soret band at 425 nm. The inset shows the detailed changes in the Q-bands region. (C) Schematic notations of 11-MUA, CYP3A4-Nanodisc and drug.

## **A.2. Experimental Methods**

### A.2.1 Materials

Silver shot was purchased from Alfa Aesar (#11357 1-3 mm diameter, Premion®, 99.9999%). Tungsten vapor deposition boats were acquired from R.D. Mathis (Long Beach, CA). Polystyrene nanospheres with diameters of  $280 \pm 4$  nm were received as a suspension in water (Interfacial Dynamics Corporation, Portland) and were used without further treatment. Fisherbrand No. 2 glass coverslips with 18 mm diameters and the buffer salts ( $\text{KH}_2\text{PO}_4 \cdot 3\text{H}_2\text{O}$  and  $\text{KH}_2\text{PO}_4$ ) were obtained from Fisher Scientific (Pittsburgh, PA). For all steps of substrate preparation, water purified with cartridges from Millipore (Marlborough, MA) to a resistivity of  $18.2 \text{ M}\Omega \cdot \text{cm}^{-1}$  was used. 1-ethyl-3-[3-dimethylaminopropyl]carbodiimide hydrochloride (EDC) was purchased from Pierce (Rockford, IL).

Sodium cholate, bromocriptine (BC), erythromycin (ERY), testosterone, lovastatin, androstene-dione, alpha-naphthoflavone, nifedipine, ketoconazole, itraconazole, tranlycypromine, diclofenac, terfenadine and Amberlite (XAD-2) were purchased from Sigma. CHAPS is from Anatrace, Inc. (Maumee, OH), Emulgen 913 from Karlan Research Products Corp. (Santa Rosa, CA); and POPC (1-Palmitoyl-2-Oleoyl-*sn*-Glycero-3-Phosphocholine) from Avanti Polar Lipids Inc. (Alabaster, AL). All other chemicals (> ACS Grade) are purchased from Fisher and were used without further purification.

### A.2.2 Ultraviolet-Visible Spectroscopy

Macroscale UV-vis extinction measurements were collected using an Ocean Optics (Dunedin, FL) SD2000 fiber optically coupled spectrometer with a CCD detector and a Cary 300 Bio UV-vis spectrophotometer. All spectra in this study are macroscopic measurements performed in standard transmission geometry with unpolarized light. The extinction spectra of the same sample acquired from the two spectrometers have been tested to be consistent.

### A.2.3 Expression and Purification of CYP3A4 Nanodiscs

Cytochrome P450 3A4 (CYP3A4) with a C- terminal histidine tag was expressed from the NF-14 construct in the PCWori+ vector as previously described.<sup>296,299-302</sup> The CYP3A4 in NF-14 pCW Ori+ vector was a generous gift from Dr. F. P. Guengerich (Vanderbilt University, Nashville, TN). CYP3A4 was expressed and purified from *Escherichia coli* as previously described with minor modifications.<sup>296</sup>

Human CYP3A4 was assembled into Nanodiscs using the membrane scaffold protein MSP1D1(-).<sup>303</sup> MSP1D1(-) is MSP1D1 with the poly (histidine) tag removed as described previously.<sup>296</sup> Briefly, the purified CYP3A4 from the *E. coli* expression system in 0.1% Emulgen 913 was mixed with the disk reconstitution mixture containing MSP1D1(-), POPC, and sodium cholate present in 1:65:130 molar ratios. The detergents (cholate and emulgen) were removed by treatment with Amberlite (XAD-2), to initiate the self assembly process. The resultant mixture was then purified using Ni-NTA column to remove the empty Nanodiscs followed by size exclusion chromatography to obtain homogenous CYP3A4-Nanodiscs.

The result of this self-assembly reaction is monomeric CYP3A4 incorporated into a 10 nm discoidal POPC bilayer stabilized by the encircling amphipathic membrane scaffold protein belt. The CYP3A4-Nanodiscs were prepared in a substrate-free form and kept at 4°C. For long term storage, the preparations were flash frozen and stored in -80°C in the presence of 10% glycerol. Expression and purification of CYP3A4-Nanodisc was evaluated by SDS-PAGE as described before.<sup>304</sup>

The CYP3A4-Nanodisc concentration was measured by UV–VIS spectroscopy using a CARY BIO 300 spectrophotometer as described previously. CYP3A4-Nanodisc was in 100 mM potassium phosphate buffer (pH 7.4). The CYP3A4-Nanodiscs were evaluated for binding to the

substrate bromocriptine (BC) before every experiment to test the functional integrity of the protein used in the experiments.<sup>305</sup>

#### A.2.4 Substrate Binding to CYP3A4 Nanodiscs

The substrate binding spectra was measured using a Cary Bio 300 UV–Vis spectrophotometer (Varian, Lake Forest, CA) in dual-beam mode. CYP3A4-Nanodisc at O.D of 0.1 was added to the sample cuvette with a total volume of 120  $\mu$ L in each. The stocks of various drug molecules in different solvents were prepared between 10mM to 20 mM stocks. A small aliquot of the drug stock was added to the protein solution keeping the concentration of the organic (ethanol, methanol or chloroform) solubilizing solvent concentration below 1.5%. The spectra were measured between 350 and 700 nm and corrected for dilution factor. The spectra are reported in the supplementary material.<sup>304</sup>

#### A.2.5 Nanoparticle Fabrication and Functional Immobilization

Ag nanoparticles were fabricated by nanosphere lithography as described in the previous chapters. For each experiment, the sample was stabilized and functionalized in a home built flow cell. Immediately following nanospheres removal, the samples were placed in 1 mM of 11-MUA ethanol solution for 24 ~ 48 h. This time was determined to produce the repeatable and approximately full monolayer coverage of 11-MUA. After incubation, the nanoparticle samples were rinsed thoroughly with neat ethanol and dried by flowing N<sub>2</sub> gas through the sample cell. Samples were then activated using 10mM EDC and then they were incubated in 1 $\mu$ M CYP3A4-Nanodisc for 1 h. After incubation, the nanoparticle samples were rinsed with MQ water and dried by flowing N<sub>2</sub> gas through the sample cell. Finally, the samples were incubated in 200  $\mu$ M drug compounds in buffer solution for 30 mins. After incubation, the nanoparticle samples were rinsed with MQ water and dried by flowing N<sub>2</sub> gas through the sample cell.

## A.3 Results and Discussions

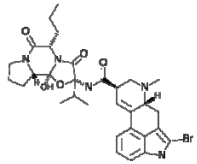
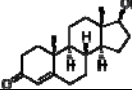
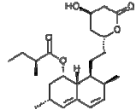
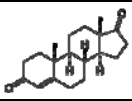
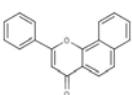
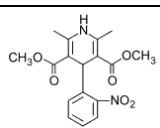
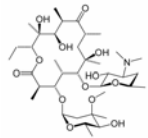
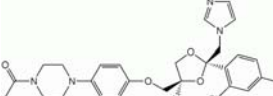
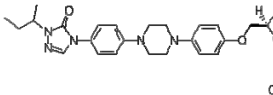
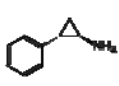
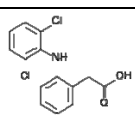
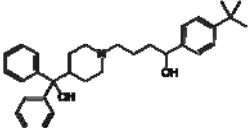
### A.3.1 Drug Binding to CYP3A4-ND

Drug binding to CYP3A4 in Nanodiscs was monitored using UV-Vis absorption spectroscopy (350–700 nm). The substrate free CYP3A4 in Nanodisc is low spin and has a Soret band at 415 nm, a less intense  $\alpha$ -Q band at 567 nm and  $\beta$ -Q band at 532 nm. Upon addition of various drug molecules, the binding to CYP3A4 gives rise to two characteristic types of spectral change. The spectral changes observed are indicative of substrate interaction with CYP3A4 and represents the primary mode of substrate binding to CYP3A4 for enzymatic hydroxylation.<sup>284</sup>

One class of spectral change (termed as type I) occurs when the substrate binding leads to the displacement of water from the sixth coordination site of the heme macrocycle in CYP3A4 and the spin state of heme-iron changes from low-spin to high spin. The spectral changes as shown in Figure A1 B are monitored by the shift in the Soret band from 415 to 391 nm. There is a decrease in the intensity of the  $\alpha$ -Q band relative to  $\beta$ -Q band. Moreover, there is blue shift of the  $\alpha$ -Q band from 568 to 540 nm and the  $\beta$ -Q band from 533 to 511 nm and the appearance of a charge transfer band at 645 nm. Type I drugs are mostly substrates to CYP3A4 for enzymatic hydroxylation.

The other class of spectral change (termed as type II) happens when the ligands with nitrogen, oxygen or sulfur donor atoms directly coordinate with the heme-iron. As the ligand field is stronger, than water there is formation of a low spin complex with red shifted Soret and Q-bands compared to the substrate free. Especially on binding nitrogen donors such as those containing imidazole, azole, amine groups, the Soret red shifts from 415 nm to 423 nm and the Q-bands shift from 568 to 576 nm and 533 to 542 nm as shown in Figure 1B. In general, the type

**TABLE A.1** Drug name, structure, binding type to CYP3A4 and spectral change they produce on binding CYP3A4 Nanodisc.

	Drug Name	Structure	Binding Type to CYP3A4	Direction of LSPR Shift	Amount of LSPR shift
1	Bromocriptine (dopamine agonist)		Type I	Blue	(-) 8 nm
2	Testosterone (Steroid Hormone)		Type I	Blue	(-) 7 nm
3	Lovastatin (Lipid Lowering)		Type I	Blue	(-) 4 nm
4	Androstene-dione (Steroid Hormone)		Type I	Blue	(-) 6 nm
5	Alpha-naphthoflavone (Flavonoid prototype)		Type I	Blue	(-) 8 nm
6	Nifedipine (Calcium Channel Blocker)		Type I	Blue	----
7	Erythromycin (Macrolide Antibiotic)		Type I	Blue	(-) 1.6 nm
8	Ketoconazole (Antifungal Drug)		Type II	Red	(+) 4 nm
9	Itraconazole (Antifungal Drug)		Type II	Red	-----
10	Tranlycypromine (Monoamine oxidase Inhibitor)		Type II	Red	(+) 2 nm
11	Diclofenac (Anti-inflammatory)		Type II	Red	(+) 5 nm
12	Terfenadine (Antihistamine)		Type II	Red	-----

II drugs are strong ligands to the heme iron atom which decreases the redox potential of the CYP3A4. This decrease in redox potential of CYP3A4 is associated with difficulty in reduction of the CYP3A4-drug complex by its redox partner cytochrome P450 reductase. This is thought to be the general mechanism of inhibition by type II drugs. The type II inhibitors become even more strong inhibitors if in addition to coordinating with the iron atom, they are also lipophilic and bind easily to the lipid bilayer membrane. Table A.1 summarizes the drug binding type and the spectral change they produce on binding CYP3A4 Nanodisc.

### A.3.2 LSPR Coupling of CYP3A4-Nanodisc to Silver Nanoparticle

The coupling of the CYP3A4 resonances with plasmon resonance of the silver nanoparticles was studied. For this, nanoparticles were fabricated around 500-600 nm using nanosphere lithography as previously described. The nanoparticles were then functionalized with a self-assembled monolayer (SAM) of 11-MUA. The nanoparticles were then incubated in 0.5  $\mu$ M CYP3A4-Nanodisc. With the aid of EDC, CYP3A4-Nanodisc were covalently bound to the carboxyl terminated groups on 11-MUA (schematic illustrated in Figure A.1A). The LSPR of the samples during each experimental step was monitored using UV-vis extinction spectroscopy in a N<sub>2</sub> environment as shown in Figure A.2D-F. As shown in Figure 2D-F, the typical LSPR shift is ~35 nm on binding CYP3A4-ND to the nanoparticle with LSPR maxima around 500-600 nm range.

### A.3.3 Drug Binding to CYP3A4-Nanodisc monitored using Localized Surface Plasmon Resonance

CYP3A4 is responsible for the metabolism of more than 50% of currently marketed drugs and is considered central focus of clinically manifested drug-drug interactions. Many of

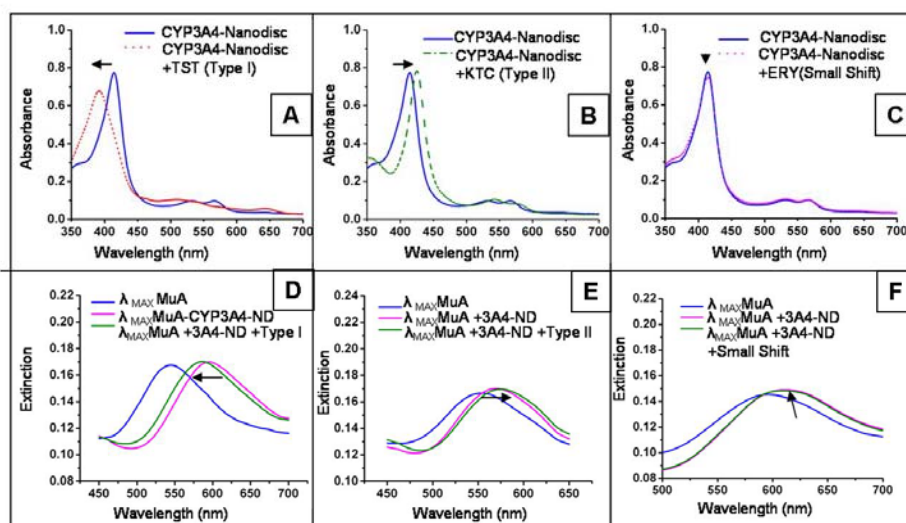


**Figure A.2 (Top panel)** (A) (B) (C) UV-vis absorption spectrum of CYP3A4-Nanodisc with testosterone (TST) bound (type I substrate), Ketoconazole (KTC) bound (Type II drug) and Erythromycin (ERY) bound (shows a very small type I shift). **(Bottom panel)** UV-vis extinction spectra of each step in the surface modification of NSL fabricated Ag nanoparticles for the different drug molecules. (D) For testosterone (representative type I substrate) binding,  $\lambda_{\text{max},\text{MuA}} = 547 \text{ nm}$ ,  $\lambda_{\text{max},\text{CYP3A4-ND}} = 596 \text{ nm}$ , and  $\lambda_{\text{max},\text{CYP3A4-ND-Type I}} = 589 \text{ nm}$  (blue shift). The direction of shift is same as in top panel A. (E) For ketoconazole (representative type II substrate),  $\lambda_{\text{max},\text{MuA}} = 553 \text{ nm}$ ,  $\lambda_{\text{max},\text{CYP3A4-ND}} = 566 \text{ nm}$ , and  $\lambda_{\text{max},\text{CYP3A4-ND-KTC}} = 570 \text{ nm}$  (red shift). The direction of shift is same as top panel B. (F) For erythromycin binding,  $\lambda_{\text{max},\text{MuA}} = 591 \text{ nm}$ ,  $\lambda_{\text{max},\text{CYP3A4-ND}} = 610 \text{ nm}$  and  $\lambda_{\text{max},\text{CYP3A4-ND-ERY}} = 609 \text{ nm}$ . All extinction measurements were collected in a  $\text{N}_2$  environment. A typical concentration of  $100 \mu\text{M}$  drug molecule was used to saturate all the binding sites.



the nitrogen containing xenobiotics inhibit CYPs and they also produce a typical type II spectral characteristic as discussed before. Membrane bound CYPs are produced in low yield using heterologous expression systems. Hence for rapid drug screening in the initial stage of drug discovery, it will be useful to distinguish between type I and type II drugs using low concentration of membrane protein.

CYP3A4-Nanodiscs are coupled to the silver nanoparticle surface. At the wavelength of monitoring of ~500-600 nm, the average LSPR shift on binding CYP3A4-Nanodisc is 35-40 nm. Figure A.2 shows three representative spectra of the drug molecules which were tested for binding to CYP3A4-Nanodisc. The top panels show the shift in the spectrum on binding the drug molecules to the protein in solution. The bottom panels show the LSPR shift in the spectrum on binding the drug molecules to the proteins on the nanoparticle surface. In Figure A.2D-F, the UV-vis extinction spectra of each step in the surface modification of NSL fabricated Ag nanoparticles for the different drug molecules are shown. Figure A.2D shows the LSPR maxima for testosterone binding. The thiol modified nanoparticle has  $\lambda_{\text{max,MuA}} = 547$  nm. On binding CYP3A4 Nanodisc,  $\lambda_{\text{max,CYP3A4-ND}}$  is 596 nm. Further on binding testosterone (representative type I substrate), the  $\lambda_{\text{max,CYP3A4-ND-TypeI}}$  is blue shifted to 589 nm. The change in the LSPR maxima on binding testosterone is (-) 7 nm. The direction of shift is similar to the direction in which the Soret and the Q-bands shift on binding the testosterone drug molecules in Figure A.2A. Several other type I drugs were tested (see table 1), all of them shifted the LSPR maxima to blue wavelength on binding to CYP3A4-ND immobilized on the surface of the nanoparticle. Hence, it can be concluded that type I drug binding can be detected on nanoparticle surface using effectively femtomoles of proteins on the surface.

In Figure A.2E, Ketoconazole (representative type II drug) is detected with the LSPR of the nanoparticle. The nanoparticle is modified with muA has  $\lambda_{\max, \text{MuA}} = 553 \text{ nm}$ . On binding CYP3A4-ND the  $\lambda_{\max, \text{CYP3A4-ND}} = 566 \text{ nm}$ . On binding ketoconazole, the red shifted  $\lambda_{\max, \text{CYP3A4-ND-KTC}} = 570$ . The change in the LSPR maxima of the nanoparticle on binding ketoconazole is (+) 4 nm. The direction of shift is similar to the direction in which the Soret and the Q-bands shift on binding the ketoconazole drug molecules in Figure A.2B. Other type II drugs when they bind to CYP3A4-Nanodisc on nanoparticle surface also produce red shift. Usually this shift is in the order of 2 nm (see table 2). The extent of red shift on binding type II drug is less than that those observed for type I drug molecules. The LSPR shifts observed are manifestation of nanoparticle and protein chromophore coupling hence if the protein spectra changes due to drug binding then only the LSPR peaks will shift.

Another interesting case is that of erythromycin which on binding to the protein produces minimal change in the protein spectra as shown in Figure A.2C. On binding erythromycin to CYP3A4-ND, the LSPR maxima are the following:  $\lambda_{\max, \text{MuA}} = 591 \text{ nm}$ ,  $\lambda_{\max, \text{CYP3A4-ND}} = 610 \text{ nm}$  and  $\lambda_{\max, \text{CYP3A4-ND-ERY}} = 609 \text{ nm}$ . The LSPR peak is blue shifted by (-) 1 nm. This shows that there is some correlation between amount of spectral change produced on drug binding to the protein in solution and to the drug binding to the protein on the surface of the nanoparticle.

From Table A.1 and Figure A.2 it is concluded that it is possible to detect and distinguish between the binding of type I and type II drugs to CYP3A4-Nanodisc. The direction of LSPR shift is consistent with the shifts observed in the protein spectra on binding type I and II drugs. At the LSPR wavelengths used in these studies, for type I drugs the blue shift is  $\sim 6\text{-}8\text{ nm}$  and for type II drugs the red shift is  $\sim 2\text{-}4 \text{ nm}$ .

In the future, more drug molecules will be tested to realize rapid drug screening using LSPR and Nanodisc technique. Fabrication of a LSPR chip with microfluidic channels will further lower the required CYP3A4-Nanodisc sample volume.

# Jing Zhao

Department of Chemistry  
Northwestern University  
2145 Sheridan Road  
Evanston, IL 60208-3113  
Tel.: 847-467-4983/847-491-2952  
Mobile: 224-805-0491  
Email: j-zhao4@northwestern.edu

---

## EDUCATION

Ph.D candidate in Physical/Analytical Chemistry Department of Chemistry, Northwestern University	09/2003 ~ 06/2008 Advisor: Prof. Richard P. Van Duyne Prof. George C. Schatz
BS in Chemical Physics Department of Chemical Physics, University of Science and Technology of China, P. R. China	09/1997 ~ 07/2002 Advisor: Prof. Jinlong Yang

## EXPERIENCE

Research Assistant Department of Chemistry, Northwestern University	09/2003 ~ 06/2008
<ul style="list-style-type: none"><li>✧ Fabricated metallic nanostructures by lithographic methods and vapor deposition.</li><li>✧ Characterized the optical and structural properties of metallic.</li><li>✧ Explored the coupling between the localized surface plasmon resonance (LSPR) of the nanoparticles and the molecular resonances of the adsorbates.</li><li>✧ Applied electromagnetic theory and density functional theory to reveal the adsorbate-induced change in the plasmon resonance wavelength of the nanoparticles.</li><li>✧ Developed biological and chemical sensors based on LSPR and surface-enhanced Raman spectroscopy.</li></ul>	
Teaching Assistant Department of Chemistry, Northwestern University	01/2004 ~ 03/2006
<ul style="list-style-type: none"><li>✧ General Chemistry</li><li>✧ Thermodynamics</li><li>✧ Physical Chemistry</li><li>✧ Quantum Mechanics</li></ul>	

## SKILLS

**Nanoparticle Fabrication**

- ✧ Nanosphere lithography
- ✧ High vacuum thermo and electron-beam deposition
- ✧ Chemical synthesis of Au and Ag nanoparticles

**Characterization of nanoparticles and biological systems**

- ✧ UV-Vis spectroscopy, FT-IR
- ✧ Raman and Surface-enhanced Raman spectroscopy
- ✧ MALDI-TOF MS
- ✧ Dark-field scattering spectroscopy of single nanoparticles
- ✧ Atomic force microscopy
- ✧ Scanning Electron Microscope

**Computational skills**

- ✧ Electromagnetic modeling using Mie theory and Discrete Dipole Approximation method
- ✧ Quantum chemistry package GAMESS
- ✧ Computer programming using Fortran, Matlab, Mathcad, Maple, Hyper Chem
- ✧ Experience in Linux RedHat Operating System, parallel Linux clusters

**AWARDS**

Chinese Government Award for Outstanding Self-Financed Students Aboard	02/2008
Nanoscale Science & Engineering Center Outstanding Research Award	08/2007
SPIE Scholarship in Optical Science and Engineering	08/2007
Phi Lambda Upsilon Gelewitz Award	05/2007
Great Lake Chinese American Chemical Society Student Poster Award	05/2007
MRS Graduate Student Silver Award	04/2007
SPIE Newport Spectra-Physics Research Excellence Travel Award	08/2006

**AFFILIATIONS**

American Chemistry Society	Society for Applied Spectroscopy
Materials Research Society	Phi Lambda Upsilon (PLU) Chemistry Honorary
The International Society for Optical Engineering (SPIE)	

**ACTIVITIES**

- Northwestern University Chemistry Department “All Scout Nano Event” Spring, 2007 and 2008
- Nanoscale Science and Engineering Center Research Experience for Teachers Program Mentor, Summer 2007

- Nanoscale Science and Engineering Center Undergraduate Research Program Mentor, Spring 2006
- Northwestern Point Person for International Friendship Program, 04/2004~04/2005
- Head of Society Department of Chinese Students and Scholars Association, 04/2004~04/2005

## **PUBLICATIONS AND PATENT APPLICATIONS**

1. **Zhao, J.**; Das, A.; Schatz, G. C.; Sligar, S. G.; Van Duyne, R. P. J. Phys. Chem. C, submitted (2008)
2. **Zhao, J.**; Pinchuk, A. O.; McMahon, J. M.; Li, S.; Ausman, L. K.; Atkinson, A. L.; Schatz, G. C., Acc. Chem. Res., submitted (2008)
3. Camden, J.P.; Dieringer, J. A.; **Zhao, J.**; Van Duyne, R. P., Acc. Chem. Res., submitted (2008)
4. Anker, J.A.; Hall, W.P.; Lyandres, O; Shan, N.C.; **Zhao, J.**; Van Duyne, R.P., Nat. Mat., in press (2008).
5. Sung, J.; Kosuda, K. M.; **Zhao, J.**; Spears, K. G.; Van Duyne, R. P. , J. Phys. Chem. C (2008), 112, 5707.
6. **Zhao, J.**; Sherry, L. J.; Schatz, George C.; Van Duyne, R. P. IEEE Journal of Selected Topics Quantum Electronics, in press (2008).
7. **Zhao, J.**; Jensen, L.; Sung, J.; Zou, S.; Schatz, George C.; Van Duyne, R. P. J. Am. Chem. Soc. (2007), 129, 7647.
8. Chan, G. H.; **Zhao, J.**; Hicks, E. M.; Schatz, G. C.; Van Duyne, R. P. Nano Lett. (2007), 7, 1947.
9. Yonzon, C. R.; Zhang, X.; **Zhao, J.**; Van Duyne, R. P. Spectroscopy (2007), 22, 42.
10. Willets, K. A.; Hall, W. P.; Sherry, L. J.; Zhang, X.; **Zhao, J.**; Van Duyne, R. P. In Nanobiotechnology: Concepts, Methods and Perspectives; Mirkin C. A., Niemeyer C. M. Eds.; Wiley-VCH; New York, 2007; pp. 159-173.
11. **Zhao, J.**; Das, A.; Zhang, X.; Schatz, G. C.; Sligar, S. G.; Van Duyne, R. P. J. Am. Chem. Soc. (2006), 128, 11004. (*Patent application NU 26096*)
12. Haes, A. J.; Zou, S.; **Zhao, J.**; Schatz, G. C.; Van Duyne, R. P. J. Am. Chem. Soc. (2006), 128, 10905. (*Patent application NU 26091*)
13. Zhang, X.; **Zhao, J.**; Whitney, A. V.; Elam, J. W.; Van Duyne, R. P. J. Am. Chem. Soc. (2006), 128, 10304. (*Patent application NU 26092*)
14. **Zhao, J.**; Zhang, X.; Yonzon, C. R.; Haes, A. J.; Van Duyne, R. P. Nanomedicine (2006), 1, 219.
15. **Zhao, J.**; Zhang, X.; Haes, A. J.; Zou, S.; Schatz, G. C.; Van Duyne, R. P. Proceedings of SPIE-The International Society for Optical Engineering (2006), 63231B/1-63231B/13.
16. Zhang, X.; Whitney, A. V.; **Zhao, J.**; Hicks, E. M.; Van Duyne, R. P. Journal of Nanoscience and Nanotechnology (2006), 6, 1920.
17. Willets, K. A.; Whitney, A. V.; **Zhao, J.**; Van Duyne, Richard P. PMSE Preprints (2006), 95 1000.
18. **Zhao, J.**; Haes, A. J.; Zhang, X.; Zou, S.; Hicks, E. M.; Schatz, G. C.; Van Duyne, R. P.

Mat. Res. Soc. Symp. Proc. (2006), 900E, 0900-O13-08.1--0900-O13-08.6.

19. Zhang, X.; Hicks, E. M.; **Zhao, J.**; Schatz, G. C.; Van Duyne, R. P. Nano Lett. (2005), 5, 1503.
20. Haes, A.J.; **Zhao, J.**; Zou, S.; Own, C. S.; Marks, L. D.; Schatz, G. C.; Van Duyne, R. P. J. Phys. Chem. B (2005), 109, 11158.

## **PRESENTATIONS**

1. **Zhao, J.**; Dieringer, J. A.; Zhang, X.; Schatz, G. C.; Van Duyne, R. P., "Surface-enhanced Resonance Raman Excitation Spectroscopy (SERES) of Tris-(2,2'-bipyridine)-ruthenium(II) on Noble Metal Surfaces" *Oral presentation at 235rd ACS National Meeting, New Orleans, LA, United States, April 6-10, 2008.*
2. **Zhao, J.**; Schatz, G. C.; Van Duyne, R. P. "Localized surface plasmon resonance sensor for small molecule binding to proteins." *Poster presentation at 2007 Chemical Sensors & Interfacial Design Gordon Research Conference, Newport, RI, United States, July 29-Aug 3, 2007.*
3. **Zhao, J.**; Schatz, G. C.; Van Duyne, R. P. "Localized surface plasmon resonance biosensor for substrate binding to cytochrome P450 proteins." *Oral presentation at 2007 MRS Spring Meeting, San Francisco, CA, United States, April 9-13, 2007.*
4. **Zhao, J.**; Jensen, L.; Schatz, G. C.; Van Duyne, R. P.. "Localized surface plasmon resonance study of Rhodamine 6G on noble metal surface." *Poster presentation at 233rd ACS National Meeting, Chicago, IL, United States, March 25-29, 2007.*
5. **Zhao, J.**; Zhang, X.; Haes, A. J.; Zou, S.; Schatz, G. C.; Van Duyne, R. P.. "Localized surface plasmon and molecular resonance: fundamental study and application." *Oral presentation at 2006 SPIE Optics & Photonics, San Diego, CA, Aug 13-17, 2006 (Invited paper).*
6. **Zhao, J.**; Haes, A. J.; Zhang, X.; Zou, S.; Hicks, E. M.; Schatz, G. C.; Van Duyne, R. P. "Alkanethiol Mediated Release of Surface Bond Nanoparticles Fabricated by Nanosphere Lithography." *Oral presentation at 2005 MRS Fall Meeting, Boston, MA, United States, Nov 28-Dec 2, 2005.*